



HAL
open science

Impact detection and classification for safe physical Human-Robot Interaction under uncertainties

Nolwenn Briquet-Kerestedjian

► **To cite this version:**

Nolwenn Briquet-Kerestedjian. Impact detection and classification for safe physical Human-Robot Interaction under uncertainties. Automatic. Université Paris Saclay (COMUE), 2019. English. NNT : 2019SACL038 . tel-02278822

HAL Id: tel-02278822

<https://theses.hal.science/tel-02278822>

Submitted on 4 Sep 2019

HAL is a multi-disciplinary open access archive for the deposit and dissemination of scientific research documents, whether they are published or not. The documents may come from teaching and research institutions in France or abroad, or from public or private research centers.

L'archive ouverte pluridisciplinaire **HAL**, est destinée au dépôt et à la diffusion de documents scientifiques de niveau recherche, publiés ou non, émanant des établissements d'enseignement et de recherche français ou étrangers, des laboratoires publics ou privés.

Impact detection and classification for safe physical Human-Robot Interaction under uncertainties

Thèse de doctorat de l'Université Paris-Saclay
préparée à CentraleSupélec

École doctorale n°580
Sciences et Technologies de l'Information et de la Communication (STIC)
Spécialité de doctorat : Automatique

Thèse présentée et soutenue à Gif-sur-Yvette, le 10 Juillet 2019, par

Nolwenn Briquet-Kerestedjian

Composition du Jury :

M. David FILLIAT Professeur (HDR), ENSTA ParisTech	Président
M. Richard BEAREE Professeur (HDR), Arts et Métiers ParisTech	Rapporteur
M. Vincent PADOIS Chargé de recherche (HDR), Inria Bordeaux Sud-Ouest	Rapporteur
M. Michel KINNAERT Professeur, Ecole Polytechnique de Bruxelles	Examineur
Mme Pauline MAURICE Chercheuse postdoctorale, Inria Nancy Grand-Est	Examinatrice
M. Pedro RODRIGUEZ-AYERBE Professeur (HDR), CentraleSupélec-L2S	Directeur de thèse
M. Mathieu GROSSARD Ingénieur-chercheur (HDR), CEA-LIST	Co-encadrant de thèse
Mme Maria MAKAROV Enseignante-chercheuse, CentraleSupélec-L2S	Co-encadrante de thèse
M. Arne WAHRBURG Principal scientist, ABB Corporate Research Center Germany	Invité

À toi, puisque de toutes façons “aucun échec n’aurait été toléré” ...

Remerciements

Je souhaite tout d'abord remercier l'ensemble des membres du jury : David Filliat, pour avoir accepté de présider ce jury ; Richard Bearee, déjà présent à ma soutenance de mi-thèse, et Vincent Padois, pour leurs retours et points de vue très intéressants ; Michel Kinnaert et Pauline Maurice qui ont contribué, par leurs remarques pertinentes lors de la soutenance, à enrichir encore les perspectives de ces travaux.

Je tiens à remercier particulièrement mon directeur de thèse Pedro Rodriguez-Ayerbe, pour tous les échanges riches d'enseignement que nous avons pu avoir, sa manière de vérifier les conclusions obtenues en les évaluant sous un autre angle (réflexe que je vais adopter maintenant), et enfin pour avoir supporté mon parler parfois un peu franc ! Je remercie chaleureusement Mathieu Grossard et Maria Makarov, pour tous leurs conseils avisés, leur soutien dans les moments difficiles et leurs encouragements dans toutes mes démarches (Allemagne, Canada !). Je n'aurais pas pu souhaiter une meilleure équipe d'encadrement. I would also like to thank Arne Wahrburg, first of all for having endured 2h30 of defense in French, but above all for having made the collaboration with ABB possible which has enriched this thesis work and my personal experience.

Je souhaite également remercier Yann Perrot, chef du Service de Robotique Interactive du CEA-LIST pour m'avoir accueillie il y a 5 ans au sein du laboratoire. Je remercie également Didier Dumur, chef du département Automatique de CentraleSupélec, pour m'avoir permise de mener cette thèse dans de bonnes conditions.

J'aimerais remercier très chaleureusement tous les collègues du CEA. Merci à tous d'avoir contribué à la bonne humeur générale au sein du laboratoire, c'était un vrai plaisir d'échanger avec chacun d'entre vous. Merci à Frédéric Collédani pour m'avoir donné l'opportunité d'intégrer le laboratoire en travaillant sur Judith (dans la boue jusqu'aux chevilles ou par 40°C !). Merci à Benoit Perochon pour sa patience lors de la construction du banc d'essai ! Merci aussi à Elodie, Martine, Dominique S., Faiza, pour leur bienveillance et leur sourire toujours chaleureux. Je ne peux pas citer tout le monde mais je remercie chacun d'entre vous !

Je remercie également tous les professeurs et doctorants/docteurs du département Automatique de CentraleSupélec. Sorin, Cristina ($\times 2$), merci pour votre bonne humeur ambiante. Mes docteurs roumains préférés, Ion et Andreea, merci pour le soutien au coude-à-coude pendant ces 3 ans.

Cette thèse n'aurait pas été la même sans mes amis du CEA-LIST, qui sont maintenant bien plus que des amis du travail. MC (désolé), à Toulouse ou ailleurs, tu resteras ma sœur de cœur. Ma petite Vaiyee, pour ne pas faire dans les sentiments je dirai simplement ♡. Alex et Antho, merci pour les belles personnes que vous êtes, généreux et toujours présents, le cœur sur la main. Merci à tous les trois de m'avoir acceptée comme pièce rapportée dans le bureau 10 ! Ma Susie, merci pour ce que tu es, tellement spontanée et attentionnée. Emeline, je garde un très bon souvenir de ces matinées efficaces à la Permanence et de ces après-midi perdues à discuter !

Benoit M., si ta capacité à relativiser si facilement pouvait être un peu plus contagieuse ! Merci notamment pour m'avoir sauvé plusieurs fois avec Git ☺ Benoit B. et Anaïs, à nos déjeuners à la Guichetta ou à l'aérodrome ! Je n'oublie bien sûr pas tous les autres: Juan-Miguel, Ugo, Katleen, Djibril, José, Titouan, Selma, Laura, merci à vous tous.

Je n'en serais pas ici aujourd'hui sans ma famille. Mes frères, sœur, beau-frère et belles-sœurs, qui heureusement sont là pour pouvoir se serrer les coudes tous ensemble. Mes neveux Hélycia et Envel qui sont comme des petites bulles d'amour et de bonheur à chaque fois que je les vois. Ma mère qui est toujours là dès que l'on a besoin d'elle et qui a toujours trouvé l'énergie pour me remotiver lorsque ça a été difficile. Mon père et Martine, pour leur soutien et leurs encouragements sans faille, je souhaite avoir la même volonté que vous de ne jamais faire les choses à moitié ! Notre papa Fred, qui nous a donné confiance en nous et nous a appris à être ambitieux, j'espère que tu serais fier aujourd'hui...

Last but not least, merci à toi Courosh d'avoir su être aussi patient et attentionné pendant ces 4 ans. Je pense que je me rappellerai longtemps de cette discussion sur la modélisation du contact jusqu'à 3 heures du matin...! Je m'excuse d'ailleurs ici-même que tu aies dû mille fois me rassurer/encourager/gronder/relire/changer les idées/entretenir, et ce surtout cette dernière année ! J'en profite pour remercier toute ta famille pour être tous si adorables avec moi, je n'ai jamais eu de si beau gâteau post-manuscrit ! Maintenant commence notre vie "hors-thèse" et j'ai hâte de voir ce qui nous attend, ensemble, au Canada.

Table of Contents

List of figures	v
List of tables	ix
List of symbols	xi
List of acronyms	xiii
Résumé étendu de la thèse	xv
1 Context and objectives	1
1.1 Introduction	2
1.1.1 Towards industry 4.0	2
1.1.2 Human-Robot Interaction	5
1.1.3 Safety requirements for collaborative robots	8
1.1.3.1 Safety standards and related studies	8
1.1.3.2 Injury risk reduction measures	14
1.2 Motivations	19
1.2.1 Problem statement	19
1.2.2 Contributions of the thesis	21
1.3 Outline	23
2 Modeling serial robot manipulators under uncertainties	25
2.1 Serial robot manipulator modeling	26
2.1.1 Notations	26
2.1.2 Force/torque transmission model	27
2.1.3 Dynamic models	28
2.1.3.1 Robots with rigid links and infinitely stiff joints (<i>rigid case</i>)	29
2.1.3.2 Robots with rigid links and elastic joints (<i>flexible case</i>)	31
2.2 Characterization of the associated uncertainties	34
2.2.1 Sources of uncertainties	34
2.2.2 Probability distribution of uncertainties	35
2.3 Parameter uncertainties	37
2.3.1 Dynamic model parameters estimation	37
2.3.1.1 Existing approaches	38
2.3.1.2 Methodology under consideration	39
2.3.1.3 Characterization of associated errors	42
2.3.2 State calculation	43

2.3.2.1	Existing approaches	43
2.3.2.2	Methodology under consideration	45
2.3.2.3	Characterization of associated errors	47
2.3.3	Geometric model parameters estimation	49
2.4	Conclusion	50
3	Design of impact detection strategies under model uncertainties	51
3.1	Related work	52
3.1.1	Impact detection strategies	52
3.1.2	Works explicitly addressing uncertainties	55
3.1.3	Positioning statement	57
3.2	Direct external torque estimation (DETE)	59
3.2.1	Residual generation	59
3.2.2	Residual evaluation	62
3.2.3	Illustration of the uncertainties contribution	66
3.2.3.1	Comparison of the parametric and numerical differentiation contributions	67
3.2.3.2	Validation of approximations	69
3.2.3.3	Interpretation of the error range	70
3.3	Disturbance observers design	71
3.3.1	State-space representations under uncertainties	71
3.3.1.1	Joint position and velocity observer (JPVO)	72
3.3.1.2	Generalized momentum observer (GMO)	74
3.3.2	Discretization and Kalman filter design	76
3.3.2.1	Sampled-time model for Kalman filter design	77
3.3.2.2	Sampled-time model for Kalman filter analysis	78
3.3.3	Evaluation of the estimated external torque	79
3.3.4	Discussion	84
3.4	Extension to robots with rigid links and elastic joints	87
3.4.1	Deficiencies of the rigid model	88
3.4.2	Extension of the direct external torque estimation (DETE)	89
3.4.3	Extension of the disturbance observers design	91
3.4.3.1	Extension of the joint position and velocity observer (JPVO)	91
3.4.3.2	Extension of the generalized momentum observer (GMO)	93
3.5	Qualitative comparison of the developed strategies	95
3.6	Conclusion	96
4	Experimental validation of impact detection strategies	99
4.1	Validation and characterization of detection performance	100
4.1.1	Description of the experiment	100
4.1.2	Preliminary analysis of disturbance observer settings	102
4.1.2.1	Analytical criteria for detection	105
4.1.2.2	Influence of the robot's modeling parameters	107

4.1.2.3	Influence of the disturbance model parameters	109
4.1.3	Experimental validation	114
4.1.3.1	Protocols and settings	114
4.1.3.2	Experimental results	116
4.2	Validation with regard to the energy transferred	120
4.2.1	Description of the experimental set-up	120
4.2.2	Evaluation of the results	121
4.3	Conclusion	125
5	Characterizing Human-Robot contact situations	127
5.1	Approaches for characterizing contact situations	128
5.1.1	Related work	128
5.1.2	Positioning statement	131
5.1.3	Case studies	133
5.2	Neural network approach	133
5.2.1	Input data	134
5.2.2	Neural network architecture	134
5.2.3	Training algorithm	136
5.2.4	Performance metrics	139
5.3	Case study 1: contact localization and user adaptability in contact intent classification	140
5.3.1	Data collection	140
5.3.2	Experiment A: results on the training candidate	142
5.3.3	Experiment B: results on test candidates	142
5.3.4	Discussion	144
5.4	Case study 2: generalization of contact intent classification	144
5.4.1	Data collection	145
5.4.2	Experiment A: results on the training candidates	148
5.4.3	Experiment B: results on test candidates from the same trajectory	149
5.4.4	Experiment C: results on test candidates from a new trajectory	153
5.4.5	Discussion	156
5.5	Conclusion	159
6	Conclusions and outlooks	161
6.1	Conclusions	161
6.1.1	Development of a quantitative methodology rendering explicit the contribution of uncertainties	162
6.1.2	Design of novel adaptive impact detection strategies explicitly taking into account the contribution of uncertainties (rigid and flexible cases)	162
6.1.3	Characterization of the contact intention and localization	163
6.2	Outlooks	163
6.2.1	Validation of the impact detection algorithms in the flexible case	163
6.2.2	A greater efficiency in impact detection	164

6.2.3	Further improvements in contact situations characterization	165
6.2.4	Towards a complete control scheme	165
Appendix A – Biomechanical constants of the human body		167
Appendix B – Applicative case of the ISYBOT prototype robot		169
B.1	Presentation of the robot	169
B.2	Geometric model parameters	170
B.3	Dynamic model parameters	171
B.3.1	Experimental protocol	172
B.3.2	Validation of the friction model	172
B.3.3	Results and associated uncertainties	173
B.3.4	Insights on the identification of flexible dynamic model parameters	176
B.4	State calculation	177
B.4.1	Position error distribution	177
B.4.2	Velocity error distribution	177
B.4.3	Acceleration error distribution	177
Appendix C – Further information on the characterization of Human-Robot contact situations		179
C.1	Experimental protocol	179
C.2	Experiment A: 1 candidate in the training	180
C.3	Experiment B: 3 candidates in the training	184
C.4	Experiment C: 3 trajectories in the training	188
Bibliography		193
List of publications		211

List of Figures

1	Exemple des quatre situations de contact et des potentielles réactions post-impact associées en contexte industriel.	xvi
2	Seuils fixes et adaptatifs pour la détection et l'évaluation des contacts.	xvii
3	Schéma explicatif de la structure du manuscrit	xviii
1.1	Unimate, invented by George Devol for General Motors in 1961 [Wallén 2008] . .	2
1.2	Production costs according to the volume and the type of automation of the workstation [Hägele 2002].	3
1.3	Harsh working conditions with high risk of developing work-related musculoskeletal disorders.	4
1.4	Description of the key components of the <i>smart factory</i> [Fostec & Company 2019].	4
1.5	Examples of remote (<i>top</i>) and proximal physical (<i>bottom</i>) Human-Robot interactions	5
1.6	Description of the different types of pHRI according to the degree of interaction between the robot and the human operator, in terms of shared workspace, process (P) and workpiece (W) [Helms 2002, Ministère du travail 2017].	6
1.7	Closed and open robot workspaces depending on the type of operation and the level of safety required.	7
1.8	Illustration of a spring-coupled two mass system	10
1.9	Definition of the extended Abbreviated Injury Scale [Haddadin 2013].	12
1.10	Examples of supervision systems	15
1.11	Actuators commonly used in robotics	18
1.12	Impact event pipeline and expected outputs from each phase [Haddadin 2017] . .	19
1.13	Example of the four contact situations in an industrial context and possible associated post-impact reactions.	20
1.14	Fixed versus adaptive thresholds in contact detection and evaluation.	21
1.15	Explanatory scheme of the thesis structure	23
2.1	Schematic representation of a 1-dimensional rigid transmission.	29
2.2	Schematic representation of a 1-dimensional elastic transmission.	31
2.3	Example of a continuous position and corresponding digital signal (sampled and quantified) obtained at a sampling time T_s with a sensor resolution r	45
2.4	Frequency responses of exact derivative and first-order low-pass filtered derivative with $\omega_c = 2\pi 10$ rad/s and $\omega_c = 2\pi 60$ rad/s for a sampling time of $T_s = 1$ ms. . .	46
3.1	Steps of an impact detection algorithm based on fault diagnosis	53
3.2	Band-pass filter for removing torques due to robot motion and noise [Song 2013]	55
3.3	Adaptive threshold using fuzzy logic [Sneider 1996]	57
3.4	Adaptive threshold defined by the maximum contribution of uncertainties	58
3.5	Block diagram of the residual generation step with exact and uncertain terms. .	59

3.6	Displacement of robot axis 3.	66
3.7	Uncertainties $\delta\tau^P$ and their associated error envelope under P1 and P2 conditions	67
3.8	Uncertainties $\delta\tau^D$ and their associated error envelope under D1 and D2 conditions	68
3.9	Comparison of $\delta\tau^P$ (under condition P1) and $\delta\tau^D$ (under condition D2).	69
3.10	Approximation error on $\delta\tau$ under (P1,D2) conditions.	70
3.11	Two interpretations of the residual evaluation step with the DETE method	70
3.12	Continuous models used for the Kalman filter design and analysis	77
3.13	Estimation of $\tau_{ext}(k)$ resulting from the Kalman filter design	78
3.14	Input-output formulation of $\hat{\tau}_{ext}(k)$ according to $\tau_{ext}(k)$, $\delta\tau(k)$ and $v(k)$	80
3.15	Case U1 — $A_{ext} = I$, $\Sigma_{ext} = I$	86
3.16	Case U2 — $A_{ext} = I$, $\Sigma_{ext} = I$	86
3.17	Case U1 — $A_{ext} = I$, $\Sigma_{ext} = 100I$	87
4.1	Picture of a recorded contact with the axis 2 in motion (in <i>yellow</i>) and the other axes locked (in <i>red</i>).	101
4.2	Force measured by the force/torque sensor in the direction perpendicular to the movement.	101
4.3	Illustration of the effects of an impact on several signals measured during two identical tests performed without and with contact.	101
4.4	Reference trajectory of robot axis 2 (<i>blue lines</i>) with the calculation time steps of the transfer functions matrices (<i>orange markers</i>).	103
4.5	Bode diagrams of $H_1^k(z)$, $H_2^k(z)$ and $H_3^k(z)$ for JPVO and GMO methods (computed at the 78 time instants represented in Figure 4.4).	105
4.6	Schematic response of $H_1^k(z)$ to a step input of amplitude Γ in the external torque $\tau_{ext}(k)$ (example of a first-order response).	106
4.7	Bode diagrams of $H_1^k(z)$ (<i>left</i>) and resulting settling time $t_{r_{5\%}}$ and minimum detectable torque Γ_{min} (<i>right</i>) under P0 , P1 and P2 conditions for JPVO and GMO methods (computed at the time instants represented in Figure 4.4).	108
4.8	Bode diagrams of $H_1^k(z)$ (<i>left</i>) and resulting settling time $t_{r_{5\%}}$ and minimum detectable torque Γ_{min} (<i>right</i>) under D0 , D1 and D2 conditions for JPVO and GMO methods (computed at the time instants represented in Figure 4.4).	110
4.9	Bode diagrams of $H_1^k(z)$ for JPVO and GMO methods under conditions A1 to A3 and $\Sigma 1$ to $\Sigma 3$ (computed at the time instants represented in Figure 4.4).	112
4.10	Settling time $t_{r_{5\%}}$ for JPVO and GMO methods under conditions A1 to A3 and $\Sigma 1$ to $\Sigma 3$ (computed at the time instants represented in Figure 4.4).	113
4.11	Minimum detectable torque Γ_{min} for JPVO and GMO methods under conditions A1 to A3 and $\Sigma 1$ to $\Sigma 3$ (computed at the time instants represented in Figure 4.4).	113
4.12	Evaluation by the bank of Kalman filters	115
4.13	Residual (estimation $\hat{\tau}_{ext}$ of the external torque) obtained in the rigid case with the DETE, the JPVO and the GMO (with disturbance model A1 , $\Sigma 3$) and its associated detection thresholds.	117
4.14	Alert signals (<i>dashed lines</i>) indicating the impact detection (<i>impact if > 0</i>) in relation with the applied force measured by the force/torque sensor (<i>solid black line</i>).	118

4.15	Analytical criteria for the DETE, the JPVO and the GMO (with disturbance model $A1, \Sigma3$).	119
4.16	Experimental set-up to reproduce human-robot impacts	120
4.17	Reference trajectory of the robot's end-effector (speed v_1)	121
4.18	Evolution of the force applied to the sliding carriage as measured by the force/torque sensor (<i>solid black lines</i>) and alert signals (<i>dashed lines</i>) indicating the detection of the impact for each method (<i>impact if > 0</i>).	122
4.19	Evolution of the force applied to the sliding carriage as a function of its displacement (<i>solid black lines</i>) and impact detection moments (<i>color crosses</i>) for each method.	124
5.1	Typical profiles of the external torque for collision and interaction in the time and frequency domains [Kouris 2016].	129
5.2	Evolution of the external torque in case of collision in the time and frequency domains at two consecutive time steps [Kouris 2018].	130
5.3	Illustration of the time window label and the resulting delay	135
5.4	Scheme of a basic feedforward neural network with one hidden layer	136
5.5	Designed neural network architecture.	137
5.6	Illustration of the sample-by-sample and situation-by-situation evaluations	139
5.7	ABB YuMi, a dual-arm collaborative manipulator with 7-DOF each arm used for collecting data to characterize the contact situation.	140
5.8	Pictures of the test bench: hand of a participant attached to the sliding carriage of the rail (<i>left</i>), force/torque sensor located on the steering wheel of the robot (<i>middle</i>), human-robot contact with the force/torque sensor at the interface (<i>right</i>).	147
5.9	Four rectilinear trajectories planned for the robot coming into contact with the participant's hand attached to the sliding carriage of the rail.	147
5.10	Interaction classification results when the test is carried out on the same trajectory as the one the network has been trained on.	150
5.11	Collision classification results when the test is carried out on the same trajectory as the one the network has been trained on.	151
5.12	Interaction classification results when the test is carried out on a different trajectory from the one(s) the network has been trained on.	154
5.13	Collision classification results when the test is carried out on a different trajectory from the one(s) the network has been trained on.	155
B.1	Prototype of the 6-DOF ISYBOT collaborative robot	169
B.2	Illustration of the attached frames of the ISYBOT prototype robot in the configuration $\mathbf{q} = (0\ 0\ 0\ 0\ 0\ 0)^T$	170
B.3	Validation of the Coulomb friction model on triangular trajectories of increasing frequency.	173
B.4	Validation of the identification of the rigid dynamic model parameters	174
B.5	Validation of the constant linear stiffness model for axis 2.	176
B.6	Empirical distribution of the mean-free error signals in position, velocity and acceleration for joint 2 (<i>histograms</i>).	178

List of Tables

1.1	Types of collaborative operation as reported in [ISO 10218-1: 2011, ISO 10218-2: 2011]	9
1.2	Example of collaborative robots available on the market	17
3.1	Summary of the proposed methods and corresponding sections	58
3.2	Comparison of the impact detection strategies developed <i>in the rigid case</i>	96
3.3	Comparison of the impact detection strategies developed <i>in the elastic-joint case</i>	97
4.1	Resulting trends for the observer-based strategies according to the various influential parameters.	114
5.1	Examples of force profiles recorded in <i>collision</i> and <i>interaction</i> contact situations with two different human subjects during <i>case study 2</i> .	132
5.2	Comparison of the two case studies conducted	133
5.3	Confusion matrix with performance metrics	139
5.4	Number of recorded samples of each category for <i>case study 1</i>	141
5.5	Classification results for the subject that contributed to training data generation	142
5.6	Classification results for test candidate 1: without prior experience with the classifier (<i>top</i>) and after adaptation to the classifier (<i>bottom</i>).	143
5.7	Classification results for test candidate 2: without prior experience with the classifier (<i>top</i>) and after adaptation to the classifier (<i>bottom</i>).	143
5.8	Number of recorded samples of each category for <i>case study 2</i>	148
5.9	Classification results for the 16 candidates combined when the neural network has been trained on their own recorded contacts.	149
5.10	Classification results for the 16 candidates combined when the neural network has been trained on 1 other candidate from the same trajectory as the test candidate.	152
5.11	Classification results for the 16 candidates combined when the neural network has been trained on 2 other candidates from the same trajectory as the test candidate.	152
5.12	Classification results for the 16 candidates combined when the neural network has been trained on 3 other candidates from the same trajectory as the test candidate.	153
5.13	Classification results for the 16 candidates combined when the neural network has been trained on candidates from 1 other trajectory.	156
5.14	Classification results for the 16 candidates combined when the neural network has been trained on candidates from 2 other trajectories.	156
5.15	Classification results for the 16 candidates combined when the neural network has been trained on candidates from 3 other trajectories.	156
5.16	Final results obtained for <i>case studies 1</i> and <i>2</i> depending on whether the same candidate and trajectory were considered for validation (=) or different ones (\neq).	158

A.1	Biomechanical constants of the human body from [ISO/TS 15066: 2016] (in grey: critical zone).	167
B.1	Table of the associated parameters of the ISYBOT prototype robot	170
B.2	Notations for the rigid dynamic model parameters of the ISYBOT prototype robot	171
B.3	Identified rigid dynamic model parameters of the ISYBOT prototype robot . . .	175

List of Symbols

Mathematical notations

s	Laplace variable
z	Discrete variable
$\mathbf{0}$	Matrix of zeros (dimensions are not explicitly specified for clarity reasons but can be deduced)
\mathbf{I}	Identity matrix (dimensions are not explicitly specified for clarity reasons but can be deduced)
$(\cdot)^T$	Matrix transpose

Other notation

$:=$	By definition
------	---------------

Robot-related parameters

n	Number of robot's (actuated) degrees of freedom
N	Number of robot's base parameters (N_r in rigid modeling, N_f in flexible modeling)
χ	Robot's base parameters
θ	Motor angular position vector after the reduction stage (<i>rad</i>)
q	Joint angular position vector (<i>rad</i>)
τ	Applied motor torque after the reduction stage (<i>Nm</i>)
τ_{ext}	External torque (<i>Nm</i>)
T_s	Sampling time (<i>s</i>)

Uncertainties-related parameters

\mathbf{a}	Any exact matrix or vector
\mathbf{a}_\star	Measured or estimated value of any matrix or vector \mathbf{a}
$\delta\mathbf{a}$	Error defined by $\delta\mathbf{a} = \mathbf{a}_\star - \mathbf{a}$
$\mathbf{a} \sim \mathcal{N}(\boldsymbol{\mu}, \boldsymbol{\sigma})$	\mathbf{a} follows a normal distribution with $\boldsymbol{\mu}$ -mean and $\boldsymbol{\sigma}$ -standard deviation
$\mathbf{a} \sim \mathcal{U}(\mathbf{a}, \mathbf{b})$	\mathbf{a} follows a uniform distribution with values in the interval $[\mathbf{a}, \mathbf{b}]$

List of Acronyms

ACE Accidental Contact with an uncertain Environment.

ACO Accidental Contact with a human Operator.

AIS Abbreviated Injury Scale.

CAD Computed-Aided Design.

CNNs Convolutional Neural Networks.

DDM Direct Dynamic Model.

DETE Direct External Torque Estimation.

DOB Disturbance OBserver.

DOF Degrees Of Freedom.

FDI Fault Detection and Isolation.

FDM Flexible Dynamic Model.

FFT Fast Fourier Transform.

FIO Fault Isolation Observer.

GMO Generalized Momentum Observer.

HRI Human-Robot Interaction.

ICE Intended Contact with an uncertain Environment.

ICO Intended Contact with a human Operator.

IDM Inverse Dynamic Model.

JPVO Joint Position and Velocity Observer.

LS Least-Squares.

PCA Principal Component Analysis.

PDF Probability Density Function.

pHRI physical Human-Robot Interaction.

PSD Power Spectral Density.

RDM Rigid Dynamic Model.

RNN Recurrent Neural Network.

SCSs Screw-Cable Systems.

SEAs Series Elastic Actuators.

SVM Support Vector Machine.

VSAs Variable Stiffness Actuators.

WLS Weighted Least-Squares.

Résumé étendu de la thèse

Introduction

Avec le développement de robots manipulateurs légers et des stratégies de commande associées, la robotique collaborative suscite depuis plusieurs années un intérêt croissant dans le cadre de l'Interaction Homme - Robot (HRI). Dans ce contexte, robot et opérateur humain évoluent dans le même espace de travail, soulevant ainsi de nouvelles problématiques liées à la sécurité de l'opérateur.

Pour atteindre le double objectif de sécurité et performance, différentes stratégies sont envisagées. Des techniques de surveillance de scène s'appuyant sur des capteurs extéroceptifs peuvent être utilisées afin d'adapter la trajectoire ou la vitesse du robot selon sa proximité avec l'opérateur. La conception mécanique des robots dédiés à l'interaction physique avec un opérateur humain est également reconsidérée de façon à réduire l'énergie transférée à l'opérateur durant le contact. Enfin, la détection d'éventuels impacts par des algorithmes de sécurité peut permettre de réagir au plus tôt et de manière appropriée selon les caractéristiques de l'impact. Ces algorithmes peuvent alors garantir une réaction sûre, rapide et efficace, du robot vis-à-vis des événements extérieurs en déclenchant par exemple une transition d'une loi de commande à une autre.

Ces travaux portent sur le développement de ces algorithmes à partir d'informations proprioceptives uniquement. En effet, l'utilisation d'un nombre minimal de capteurs pour la détection, et en particulier une dépendance moins grande aux capteurs d'effort voire leur absence, constitue un critère important dans un contexte industriel pour lequel intégration et coût sont deux contraintes fortes. Les stratégies de détection et de réaction nécessitent alors un modèle dynamique du système ce qui les rend sujettes au compromis entre sensibilité de détection et robustesse vis-à-vis des incertitudes de modélisation.

Problématique

Ces travaux de thèse s'inscrivent dans le contexte général de l'Interaction physique Homme - Robot (pHRI) en milieu industriel. Dans ce contexte, des contacts intentionnels ou accidentels peuvent survenir entre un robot et son environnement, qu'il s'agisse d'opérateurs humains évoluant dans le même espace de travail ou d'objets fixes ou mobiles présents à proximité. En particulier, les quatre situations de contact suivantes peuvent survenir:

- *Contact intentionnel avec un opérateur humain (ICO)*: ce cas peut se produire lorsque sur une ligne de production à petite échelle, le robot est polyvalent et fréquemment reconfiguré pour effectuer plusieurs tâches, ou encore si un opérateur intervient pour dérouter le robot en présence d'une pièce défectueuse,
- *Contact accidentel avec un opérateur humain (ACO)*: cette situation peut survenir si une personne est heurtée par le robot en se déplaçant à proximité,

- *Contact intentionnel avec un environnement incertain (ICE)*: durant l'exécution de sa tâche, le robot pourrait avoir à entrer en contact avec une pièce afin d'effectuer une action spécifique sur celle-ci,
- *Contact accidentel avec un environnement incertain (ACE)*: ce scénario peut se produire si une pièce inconnue est placée sur la trajectoire pré-programmée du robot.

Selon le type de situation identifié, des réactions spécifiques seraient à mettre en œuvre. La [Figure 1](#) suggère des exemples de ces quatre scénarios illustrés dans un contexte industriel, avec des stratégies post-impact adaptées. En outre, l'emplacement du contact sur le robot fournit un élément de contexte supplémentaire permettant, par exemple, de déplacer le robot selon une direction appropriée pour le libérer d'un contact accidentel.

Ces travaux mettent dans un premier temps l'accent sur la détection de l'impact. En s'appuyant sur les techniques de détection de défaut, les méthodes de détection d'impact proposent de générer un signal de surveillance reflétant l'occurrence d'un impact en étant non nul uniquement lorsqu'un contact survient sur le robot (voir [Figure 2](#)). En contrepartie de l'utilisation de capteurs proprioceptifs seuls, la connaissance de modèles liés au robot est nécessaire pour calculer le signal de surveillance. Cependant, ces modèles peuvent être sujets à des incertitudes de modélisation qui s'expriment par du bruit sur le signal de surveillance comme illustré dans la [Figure 2](#). Si aucune information supplémentaire n'est disponible ou supposée sur la structure des incertitudes, des seuils de détection fixes sont généralement utilisés pour détecter le contact [[Haddadin 2017](#)]. Néanmoins, le réglage de tels seuils peut s'avérer fastidieux en présence d'incertitudes de modélisation : si ces seuils sont trop faibles, l'algorithme peut déclencher des fausses alarmes, alors que s'ils sont réglés de façon à être supérieurs aux erreurs de modélisation, la sensibilité de détection est diminuée. Dans un second temps, l'étape de caractérisation des situations de contact est rendue difficile par la présence d'incertitudes de modélisation : le réglage de certains paramètres est réalisé à partir de données expérimentales soumises aux erreurs de modélisation, ce qui peut grandement affecter le succès de la classification.

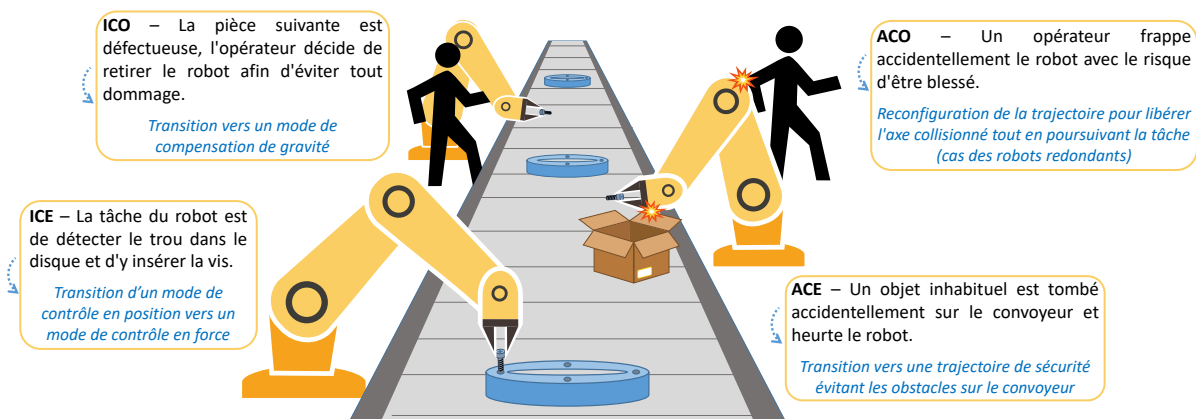


Figure 1: Exemple des quatre situations de contact et des potentielles réactions post-impact associées en contexte industriel.

Dans la littérature, plusieurs approches courantes utilisent le couple généré par la force appliquée au moment du contact et retranscrit au niveau des articulations du robot comme signal de surveillance [De Luca 2006, Haddadin 2017, Wahrburg 2018]. Le premier objectif de ces travaux de thèse consiste à reconsidérer ces approches en présence d'incertitudes de modélisation puis de comparer leurs performances de détection d'un point de vue théorique et expérimental. Le développement de stratégies adaptatives innovantes pour la détection d'impact en présence d'incertitudes constitue le second objectif de la thèse. Pour cela, les erreurs de modélisation seront traitées comme des bruits lors de la synthèse de filtres de Kalman visant à reconstruire le couple dû à l'impact. Un seuil de détection adaptatif tenant compte de la contribution maximale des incertitudes le long de la trajectoire du robot sera envisagé (voir Figure 2). Ainsi, toute contribution supplémentaire au-delà du seuil ne pourrait être due qu'à l'occurrence d'un contact, permettant ainsi sa détection. Une fois l'impact détecté, le troisième objectif porte sur la détermination de l'intention de l'opérateur au moment du contact (contact intentionnel ou accidentel) et sur la localisation de l'impact le long du bras du robot. Cette problématique est traitée comme un problème de classification à l'aide de techniques d'apprentissage, qui présentent l'avantage de déterminer intrinsèquement les critères utiles à la classification. L'adaptabilité de ces techniques d'apprentissage aux conditions de fonctionnement variables du robot constitue un aspect déterminant pour la pertinence de ces approches.

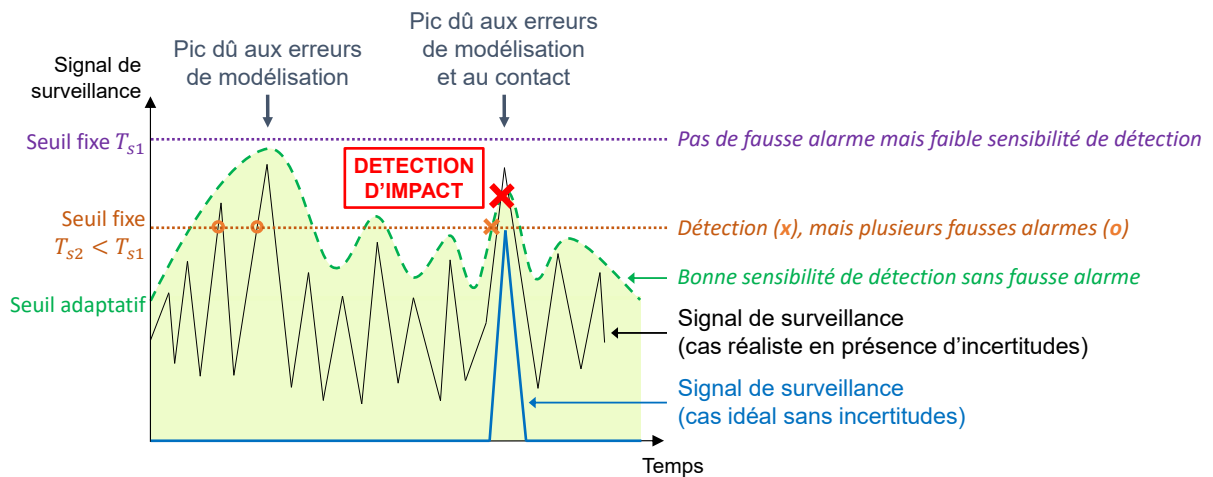


Figure 2: Seuils fixes et adaptatifs pour la détection et l'évaluation des contacts. Un seuil fixe peut être réglé de façon à être supérieur aux erreurs générées par les incertitudes de modélisation mais risque alors d'être relativement conservatif. S'il est plus faible, alors cela peut déclencher des fausses alarmes. Un seuil adaptatif pertinent permettrait de détecter correctement l'impact sans déclencher de fausses alarmes.

Structure du manuscrit

L'organisation de ce manuscrit est détaillée ci-après (voir Figure 3) :

Le chapitre 2 rappelle le formalisme utilisé pour la description des robots manipulateurs sériels. La détection d'impact intervenant dans un contexte dynamique, le modèle dynamique du robot

est présenté dans le cas de robots à corps rigides et à articulations infiniment rigides ou à articulations flexibles. Les sources potentielles d'incertitudes s'exprimant dans le modèle dynamique sont identifiées et, pour chaque type d'incertitudes, une méthodologie est proposée pour caractériser les erreurs induites. En particulier, les incertitudes de modélisation du robot prototype ISYBOT du CEA-LIST ont été caractérisées de façon quantitative en utilisant la méthodologie proposée.

Le [chapitre 3](#) aborde la problématique de la conception d'algorithmes de détection d'impact sous incertitudes en n'utilisant que des mesures proprioceptives. Dans ces travaux, deux catégories de méthodes de détection d'impact sont explorées : le couple extérieur responsable de l'impact est soit directement estimé à partir du modèle dynamique du robot, soit reconstruit à partir d'observateurs de perturbation et filtrage de Kalman. Pour chaque méthode, les erreurs induites par les incertitudes sont mises en évidence en propageant les erreurs provenant du modèle dynamique du robot. En utilisant la méthodologie développée dans le [chapitre 2](#), la contribution maximale des erreurs de modélisation présentes est calculée, générant ainsi un seuil de détection adaptatif qui dépend de la trajectoire du robot. Cette approche est développée dans le cas de robots à articulations infiniment rigides ou à articulations flexibles.

Le [chapitre 4](#) est dédié à la validation expérimentale des algorithmes de détection d'impact précédents appliqués au robot prototype ISYBOT. A partir d'un exemple illustratif d'une situation de contact entre le robot et un sujet humain, une étude préliminaire est menée pour examiner l'influence des erreurs de modélisation et des paramètres de réglage sur le temps et la sensibilité de détection. Les avantages et inconvénients des différentes méthodes étudiées, préalablement mis en évidence de manière théorique dans le [chapitre 3](#), sont confirmés expérimentalement. Enfin, l'énergie transférée au système collisionné est examinée selon le choix de l'algorithme de détection utilisé et les valeurs obtenues sont rapportées aux références données dans les normes robotiques.

Le [chapitre 5](#) propose de caractériser les situations de contact à l'aide de techniques d'apprentissage supervisé et plus particulièrement de réseaux de neurones. L'objectif consiste à déterminer l'intention humaine lors d'un contact avec le robot (intentionnelle ou accidentelle) et de localiser la zone de contact sur le bras du robot. Les performances de généralisation à plusieurs sujets humains et à différentes trajectoires du robot sont étudiées. Dans cette optique, deux études de cas sont réalisées à partir de données expérimentales collectées auprès d'un robot ABB YuMi et du robot prototype ISYBOT.

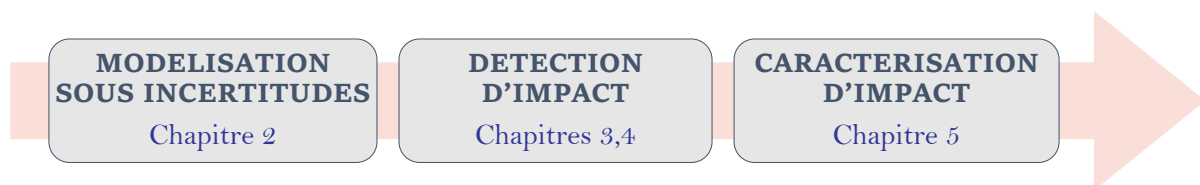


Figure 3: Schéma explicatif de la structure du manuscrit

Contributions de la thèse

Afin d'atteindre les objectifs précédents, quatre contributions principales ont été proposées :

Contribution 1 : développement d'une méthodologie quantitative rendant explicite la contribution des incertitudes

Etant donné que les méthodes de détection d'impact basées sur le modèle dynamique du robot sont soumises au compromis entre sensibilité de détection et robustesse aux incertitudes de modélisation, une analyse approfondie des erreurs induites par les incertitudes a été réalisée. En particulier, deux types d'erreurs ont été considérés : les erreurs sur les paramètres dynamiques du robot (calculées par identification expérimentale) et les erreurs induites par le calcul de l'état du robot (obtenu par différenciation numérique de la position mesurée). Dans chaque cas, une caractérisation stochastique de la distribution des erreurs a été proposée puis appliquée au prototype de robot ISYBOT.

Cette méthodologie quantitative, théorique et expérimentale, a été mise en œuvre sur plusieurs algorithmes de détection d'impact pour quantifier les effets induits par les incertitudes. En rendant explicite les erreurs générées par un algorithme de détection d'impact donné, la méthodologie développée a finalement permis de :

- clarifier les incertitudes en jeu et la façon dont elles affectent la détection,
- proposer de nouvelles stratégies de détection d'impact,
- comparer ces algorithmes en fonction du type et de la quantité d'incertitudes impliquées.

Contribution 2 : Conception de nouvelles stratégies de détection d'impact adaptatives tenant explicitement compte de la contribution des incertitudes (cas rigide)

De nouvelles stratégies de détection d'impact ont été conçues à partir de la méthodologie précédente. Pour cela, une approche probabiliste a été adoptée pour déterminer la contribution maximale des erreurs de modélisation à partir de leur formulation rendue explicite. Cette marge d'erreurs maximale constitue alors un seuil de détection d'impact pertinent, dépendant de la trajectoire du robot, du niveau d'incertitudes paramétriques, du bruit sur la mesure de position et de la méthode d'approximation numérique choisie pour le calcul de la vitesse et de l'accélération.

Deux types de stratégies ont été étudiés dans le cas de robots à corps rigides et à articulations infiniment rigides : le couple extérieur responsable de l'impact est soit directement estimé à partir du modèle dynamique du robot, soit reconstruit à partir d'observateurs de perturbation et filtrage de Kalman. En ce qui concerne cette dernière méthode, en plus de la technique largement utilisée basée sur la quantité de mouvement du robot, un autre observateur basé sur la position et la vitesse articulaires a été proposé. Ces trois stratégies ont d'abord été comparées de manière conceptuelle en fonction de la structure des incertitudes impliquées, puis une analyse fréquentielle a été menée afin de prédire certaines tendances selon les erreurs de modélisation et les paramètres de réglage. Enfin, ces algorithmes ont été validés hors ligne sur le robot prototype ISYBOT et des critères de caractérisation des performances de détection obtenues ont été proposés, tels que l'énergie transférée au système collisionné pendant le contact.

Contribution 3 : Conception de nouvelles stratégies adaptatives de détection d'impact prenant explicitement en compte de la contribution des incertitudes (cas flexible)

Lorsque des composants déformables sont présents dans la chaîne d'actionnement, des modèles spécifiques sont nécessaires pour prendre en compte l'effet des élasticités. Si des méthodes de détection d'impact développées dans le cas de robots à articulations rigides sont appliquées à des robots à articulations flexibles, alors des erreurs de modélisation supplémentaires sont introduites en raison de l'inadéquation du modèle proposé. Pour cette raison, l'approche précédente a été déclinée aux robots à corps rigides et articulations flexibles : en affinant le modèle dynamique du robot pour prendre en compte les élasticités articulaires, l'objectif est de réduire la contribution des erreurs de modélisation et ainsi améliorer les performances de détection. Pour chaque méthode de détection étudiées, deux variantes possibles ont été proposées selon que l'on tienne compte des incertitudes sur le modèle de frottement du moteur ou sur la raideur articulaire.

Contribution 4 : Caractérisation de l'intention du contact et localisation de l'impact sur le bras du robot

Après l'étape de détection d'impact, la phase de caractérisation vise à extraire des éléments de contexte liés au contact, afin de déclencher une réaction appropriée du robot qui, d'une part, ne mette pas en danger l'opérateur humain et, d'autre part, assure une transition efficace. Dans ces travaux, nous nous sommes concentrés sur la détermination de l'intention de l'opérateur lors du contact avec le robot (contact intentionnel ou accidentel) et sur la localisation de la zone du robot collisionnée.

Compte tenu de la complexité du problème due aux incertitudes de modélisation ainsi qu'à d'autres paramètres incertains liés à l'opérateur, une stratégie de classification par réseaux de neurones a été étudiée. Une structure de réseau "boîte grise" guidée par la physique du contact a été proposée pour accroître l'efficacité de la classification. Deux études de cas ont été menées afin d'évaluer la possibilité de généraliser à tout individu humain et à toute trajectoire du robot. Les résultats ont démontré que la localisation de la zone de contact sur le robot peut être très efficace avec des réseaux de neurones. La détermination de l'intention du contact s'avère toutefois plus fastidieuse puisqu'elle peut être liée à des caractéristiques propres au sujet humain qui manipule le robot (appréhension, sensibilité, anticipation, etc.). La généralisation à tout sujet humain ou à toute trajectoire du robot donne des résultats prometteurs, mais la généralisation aux deux facteurs simultanément semble limitée par la structure élémentaire du réseau neuronal considéré. L'adaptation d'un sujet humain à un classificateur entraîné sur une autre personne peut éventuellement constituer une approche alternative.

Perspectives

Ces résultats sont une étape de plus vers une collaboration sûre et efficace entre humains et robots. Plusieurs pistes peuvent être explorées suite à ces travaux de thèse et sont décrites ci-dessous.

Validation des algorithmes de détection d'impact dans le cas flexible

Les stratégies de détection d'impact ont été déclinées dans le cas flexible pour des robots à corps rigides et à articulations flexibles. Dans ce cas, le modèle dynamique du robot devrait être identifié de manière plus précise, entraînant une réduction des écarts-types sur les erreurs d'estimation des paramètres dynamiques. Cela permettrait non seulement d'obtenir une meilleure estimation du couple extérieur (qui serait exempte des erreurs liées à l'inadéquation du modèle rigide), mais aussi de réduire les marges d'erreur, et donc d'améliorer les performances de détection. Une extension de ces travaux consisterait donc à vérifier cette hypothèse en simulation et en expérimentation. Cela permettrait d'augmenter la dynamique du mouvement du robot sans risquer de stimuler les flexibilités puisque les effets induits seraient pris en compte, tout en assurant une détection sûre des impacts.

Une plus grande efficacité dans la détection des impacts

Tout d'abord, une validation en ligne et approfondie des algorithmes de détection d'impact est essentielle pour une utilisation future, en particulier sur des scénarios de fonctionnement réalistes (vitesses et accélérations du robot, instants et emplacements des contacts). L'analyse fréquentielle développée dans cette thèse ayant établi la relation entre les incertitudes de modélisation et les performances de détection attendues, l'étude pourrait être approfondie dans le cas d'une application industrielle ayant une tâche bien définie, par exemple :

- en adoptant l'approche inverse : sur la base d'exigences de sécurité à respecter pendant la tâche (a priori imposées par les normes robotiques), on pourrait s'intéresser aux leviers disponibles pour améliorer les performances de détection. L'étude de l'évolution des erreurs de modélisation selon la trajectoire du robot constituerait une première approche : la trajectoire pourrait alors être programmée selon un critère minimisant les erreurs induites par les incertitudes et donc augmentant les performances de détection. Dans le cas d'un robot redondant, certaines configurations du bras robotique pourraient éventuellement être privilégiées à cet égard. Une autre possibilité dans le cas des méthodes basées sur des observateurs de perturbation serait d'ajuster les paramètres du modèle de perturbation en fonction de l'énergie dissipée maximale autorisée par les normes. En effet, en s'appuyant sur la modélisation d'un système à deux masses reliées par un ressort, on pourrait préciser l'évolution de la force de contact et donc le modèle du couple extérieur considéré.
- en introduisant des éléments contextuels : jusqu'à présent dans ces travaux, un intervalle de confiance à 3σ a été considéré pour la détection (correspondant à un niveau de confiance de 99.7%), mais le réglage de ce paramètre pourrait être rendu plus précis afin d'éviter des performances de détection trop conservatrices. Une réduction locale de ce paramètre pourrait être envisagée, par exemple si l'on peut identifier des séquences de la tâche au cours desquelles un contact du robot avec son environnement est prévu. L'ajustement de ce paramètre pourrait également être déterminé par des techniques d'apprentissage ou par de la logique floue, en fournissant en entrées le couple extérieur estimé et la marge d'erreur associée liée aux incertitudes de modèle. La vitesse du robot peut également être un critère déterminant pour le réglage de ce paramètre.

Dans une perspective plus exploratoire, il serait intéressant de comparer les performances de détection obtenues avec les stratégies de détection proposées dans ces travaux (estimation directe du couple extérieur ou observateurs de perturbation) avec les techniques basées sur de l'apprentissage : ces dernières pourraient être utilisées en supplément afin de garantir une détection plus fine des impacts de faible amplitude (non détectés par les stratégies proposées dans ces travaux car confondus avec l'enveloppe des erreurs de modélisation). Cependant, s'appuyer uniquement sur de telles approches semble discutable à première vue puisqu'il n'y a aucun moyen de quantifier la performance attendue si ce n'est de façon heuristique, contrairement aux stratégies proposées, ce qui représente jusqu'alors un obstacle à la sécurité de l'opérateur.

Perfectionnement de la caractérisation des situations de contact

Afin d'améliorer la généralisation de la classification de l'intention de contact à tout individu humain et à toute trajectoire de robot, deux approches sont proposées :

- examiner d'autres choix d'entrées : le choix du couple extérieur estimé et de la vitesse du robot comme entrées du réseau de neurones est basé sur des considérations physiques, mais d'autres entrées peuvent être tout aussi pertinentes. En effet, si l'objectif est de conserver une structure de réseau relativement simple avec un nombre réduit de neurones, alors des entrées pré-traitées pourraient améliorer les résultats de la classification. À cette fin, une analyse en composantes principales (PCA) pourrait être utilisée pour déterminer les signaux pertinents.
- examiner d'autres structures de réseaux de neurones : des structures plus complexes peuvent être nécessaires pour traiter efficacement la complexité du problème. D'une part, des réseaux de neurones récurrents (RNNs) seraient appropriés pour prendre en compte l'évolution temporelle du couple extérieur, comme proposé dans [Kouris 2018] dans le cas d'une approche fréquentielle. D'autre part, des réseaux de neurones convolutifs (CNNs) permettraient d'extraire des caractéristiques liées au contact plus profondes. Toutefois, il convient de noter que des structures plus complexes nécessitent également des temps de traitement plus longs: la compatibilité avec une implémentation en temps réel sur le robot doit alors être examinée.

Ces avancées pourraient également permettre d'extraire plus d'informations sur la situation de contact, comme la rigidité de l'environnement collisionné pour distinguer par exemple entre un sujet humain et une pièce rigide.

Vers un schéma de commande complet

Les méthodes de détection et de caractérisation proposées dans ces travaux sont à intégrer dans un schéma de commande complet, qui incluerait également des stratégies post-impact. À cette fin, une loi de commande en impédance peut être envisagée pour la phase post-impact, qui est largement reconnue comme étant adaptée pour les situations d'interaction du robot avec son environnement.

Plus spécifiquement, une adaptation des gains de commande en impédance pourrait être considérée afin d'obtenir un comportement efficace durant la phase post-impact (vis-à-vis des objectifs de passivité et de transparence), et tenant compte des caractéristiques de l'impact détecté (intention, point de contact, amplitude des efforts, etc.). Dans ce contexte adaptatif, la question de la stabilité de la loi de commande devra être examinée.

Context and objectives

“ *It is not the strongest of the species that survives, nor the most intelligent, but rather the one most adaptable to change.* ”

Wrongly attributed to Charles Darwin (1963)

Contents

1.1	Introduction	2
1.1.1	Towards industry 4.0	2
1.1.2	Human-Robot Interaction	5
1.1.3	Safety requirements for collaborative robots	8
1.1.3.1	Safety standards and related studies	8
1.1.3.2	Injury risk reduction measures	14
1.2	Motivations	19
1.2.1	Problem statement	19
1.2.2	Contributions of the thesis	21
1.3	Outline	23

In an industrial context or for service applications involving human-robot collaboration, this thesis proposes new insights on the detection and characterization of contact situations between a robot and its environment without the use of extra sensors. The collided obstacles are of an unknown geometry and location in the environment and may occur at any point along the robot arm. The framework and challenges of this work are presented in this first chapter.

1.1 Introduction

1.1.1 Towards industry 4.0

Over the last centuries, technological evolution has made it possible for human beings to revolutionize their industry, reinventing it through the exploitation of new energy resources but also adapting it to their evolving needs and constraints. In particular, since the 18th century, mechanization and mass production have profoundly transformed the industry in its quest for greater productivity and competitiveness.

While the idea of automated beings was already generating fear and fascination in literature [Shelley 1818] and theater [Capek 1920], the first industrial robot to be deployed on an assembly line appeared in the 60's at the dawn of the third industrial revolution (see Figure 1.1). Defined as an automated and programmable system capable of moving in three or more directions [ISO 8373: 2012], industrial robots were conceived to perform repetitive tasks at high speed and with good accuracy. These tasks are precisely the ones that are likely to be the least attractive for human operators since they do not require any added value or particular skills. With a new division of labor, robotic automation has opened up new opportunities in industry (e. g. in the space, medical and military sectors), but also in service robotics.

Although the trend is towards ever-increasing automation of manufacturing processes, there are however other operations for which human dexterity and decision-making skills remain until now irreplaceable by a traditional industrial robot. Motivated by technological and economical reasons, in this case the human operator is kept in the loop as an experienced active agent but is assisted by a robotic system. This form of synergy takes advantage on the one hand of the robot's precision, repeatability and strength and on the other hand of the human expertise, perception and adaptation skills.



Figure 1.1: Unimate, invented by George Devol for General Motors in 1961 [Wallén 2008]

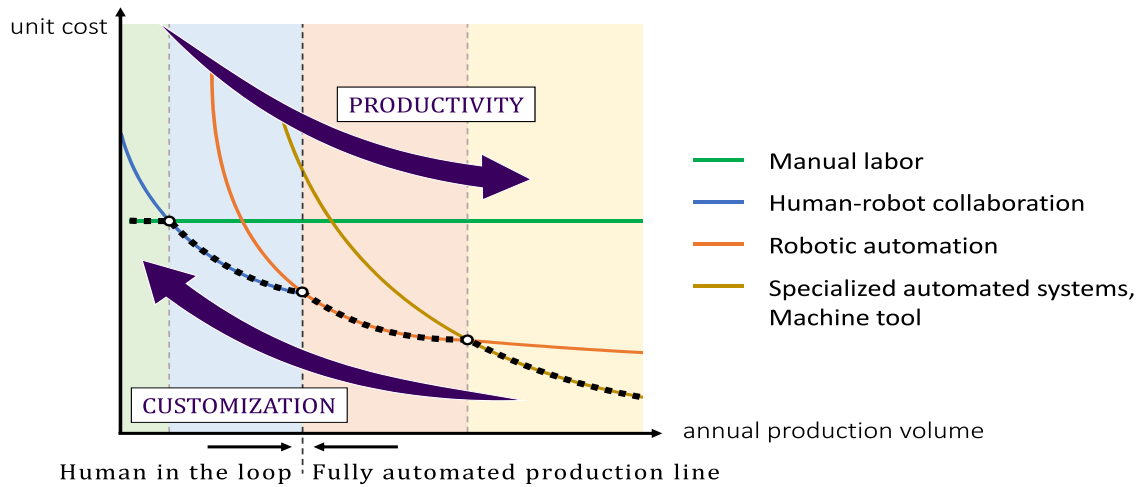


Figure 1.2: Production costs according to the volume and the type of automation of the workstation [Hägele 2002].

This working partnership is particularly suitable for tasks carried out on very variable products (e.g. agri-food industry), applications that require frequent interventions or reconfigurations (e.g. multiple product variants) or for any meticulous operation (e.g. surgical procedure). Small and medium-sized production plants have especially benefited from this first step towards automated processes since their volume of production does not usually justify the high costs of research and integration of a specialized robot (see Figure 1.2). The trend towards greater product customization and shorter product life cycles also explain this search for flexibility in manufacturing processes. As a physical assistance system, collaborative robots have also found a particular interest in reducing work-related musculoskeletal disorders due for instance to repetitive gestures, excessive effort or non-ergonomic posture maintained over time (see Figure 1.3). These disorders can lead to significant compensation costs for companies (in 2017, work-related musculoskeletal disorders represented more than 87% of the occupational diseases in France [Assurance Maladie 2017]).

In the attractive concept of *collaborative robotics*, cobots (for *collaborative robots*) are generally recognized for their versatility and intuitive programming as they benefit from the latest advances in robotics, just as traditional industrial robots could be if they were designed in this way. What really distinguishes a collaborative robot from a traditional robot is the *collaborative application*. The latter defines the compatibility between a human and a robot to collaborate under safe conditions in an unstructured environment, that is not totally known and potentially variable. This new framework is made possible by recent advances in the fields of mechanics, electronics, materials and computer science, associated with progress in computational capabilities. They have been beneficial to robotics by increasing robot capabilities in perception (advanced instrumentation and sensors), information processing (improved microprocessors and algorithms) and actuation (enhanced actuators and materials). With a broader awareness of its environment, the robot's actions can be appropriately derived from what it perceives through external stimuli and no longer from a pre-established implemented program.



(a) In public works, painful working posture and discomfort caused by noise and vibrations of tools.



(b) In the food industry, handling of cutting tools with high hygiene and temperature constraints.



(c) In the car industry, working with arms raised on elevated production lines at a sustained pace.

Figure 1.3: Harsh working conditions with high risk of developing work-related musculoskeletal disorders.

This pursuit of flexibility and efficiency in manufacturing processes is part of the strategy of what some call the *industry 4.0*. Within the *smart factories*, all means of production have to be connected together, including robot and human operator (see Figure 1.4). They form a network of cyber-physical systems¹ that use information and communication technologies to allow their interaction in real time. In the case of robotics, many interconnections are being explored, for example with virtual and augmented reality, big data or artificial intelligence, driven by fantasies but at the same time framed by ethical principles.

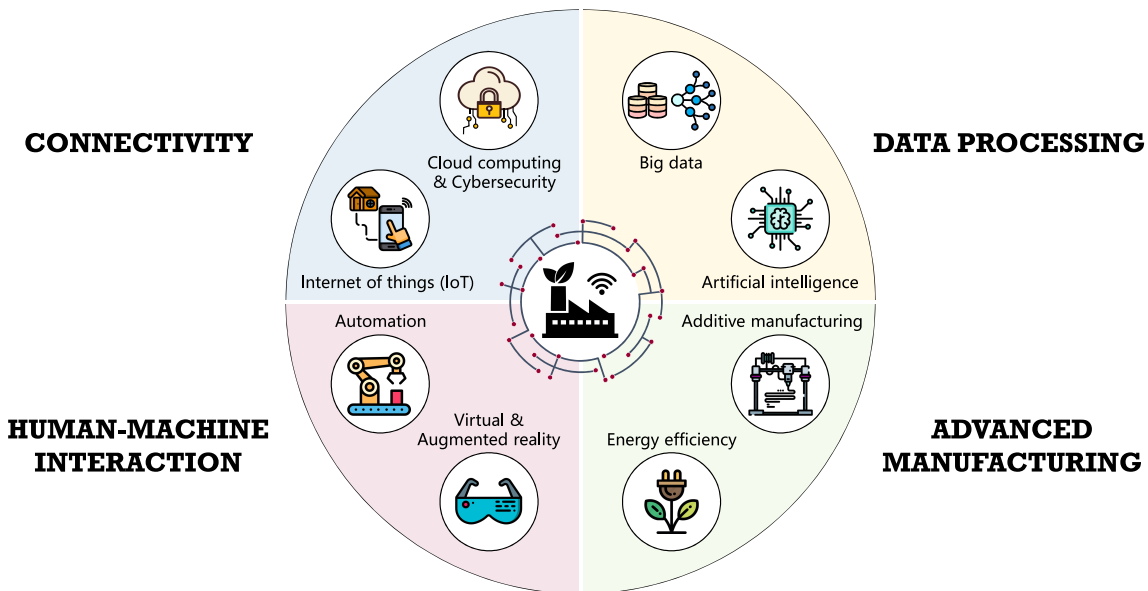


Figure 1.4: Description of the key components of the *smart factory* [Fostec & Company 2019]: the industry of the future will benefit from advances in each of these areas, which, when interconnected, offer greater flexibility and efficiency in the manufacturing processes.

¹The term *cyber-physical systems* refers to engineered systems that are built from, and depend upon, the seamless integration of computation and physical components [National Science Foundation 2019].

1.1.2 Human-Robot Interaction

During the human-robot collaborative application, the two agents interact through a form of communication called *Human-Robot Interaction (HRI)*. These interactions may be classified into three categories, depending on the proximity between the robot and the human and the nature of the information exchanged:

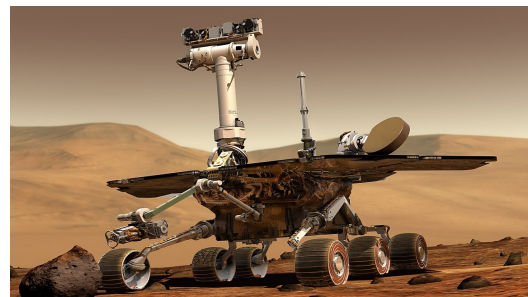
Remote Human-Robot Interaction (also called *teleoperation* or *telem Manipulation*) refers to applications where a human operates on the robot remotely, this separation occurring in space (e. g. in [Figure 1.5a](#)) or time (e. g. with exploration robots due to inaccessible access conditions as in [Figure 1.5b](#)). Interaction is achieved through a control interface which can take various forms, from remote controls to joystick, teach pendant and haptic device but also including virtual reality interfaces.

Cognitive Human-Robot Interaction deals with social factors between robots and humans, based on an interpretation of verbal attributes (voice commands, speech recognition, natural-language processing) or non-verbal information (gesture recognition, head and eye gaze tracking, bio-signals activity).

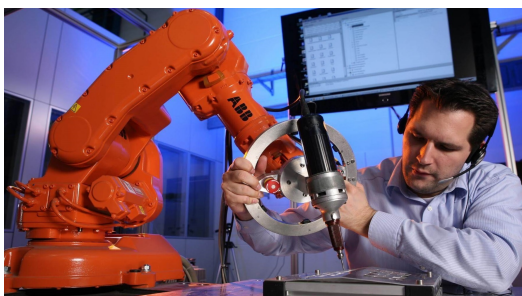
Physical Human-Robot Interaction is characterized by the spatial proximity between the robot and the operator that share a common workspace, named the *collaborative workspace*. Then the operator has the possibility to be in physical contact with the robot in operation under certain conditions, either to perform tasks together (e. g. programming by demonstration in [Figure 1.5c](#)) or for physical assistance (e. g. exoskeleton in [Figure 1.5d](#)).



(a) Teleoperation with an haptic control interface



(b) Exploration on Mars with *Opportunity* rover



(c) Programming the trajectory by demonstration



(d) Posture assistance for carrying heavy loads

Figure 1.5: Examples of remote (*top*) and proximal physical (*bottom*) Human-Robot interactions

Varying degrees of physical Human-Robot Interaction (pHRI)

In this work, we will focus on pHRI. In this case, the work cell is designed in accordance with the required degree of interaction between the operator and the robot for the task completion. In particular, four scenarios of human-robot physical collaboration have been identified in [Helms 2002], with increasing degrees of interaction from scenario 1 to 4 (see Figure 1.6):

Scenario 1. *Coexistence*: robot and human operator operate independently on separate workpieces and tasks without any safety fence to separate them (shared workspace, separate process in time or space, separate workpiece). In this case, the spatial proximity between the two agents mainly allows the operator to intervene quickly in the event of a fault or to change the robot's operation mode.

Scenario 2. *Alternating cooperation*: robot and human operator work sequentially on the same workpiece (shared workspace, separate process in time, common workpiece).

Scenario 3. *Simultaneous cooperation*: robot and human operator operate on separate tasks to manufacture the same workpiece at the same time, but do not necessarily have physical contact (shared workspace, separate process in space, common workpiece).

Scenario 4. *Physical assistance*: the robot and the operator work on a single workpiece by performing the task together (common workspace, process and workpiece). The robot's purpose is to relieve the operator either in the performance of his or her gesture (e.g. constrained trajectory for motion guiding, tremor filtering) or the task (e.g. amplified effort exerted or felt, weight compensation of the tool or load).

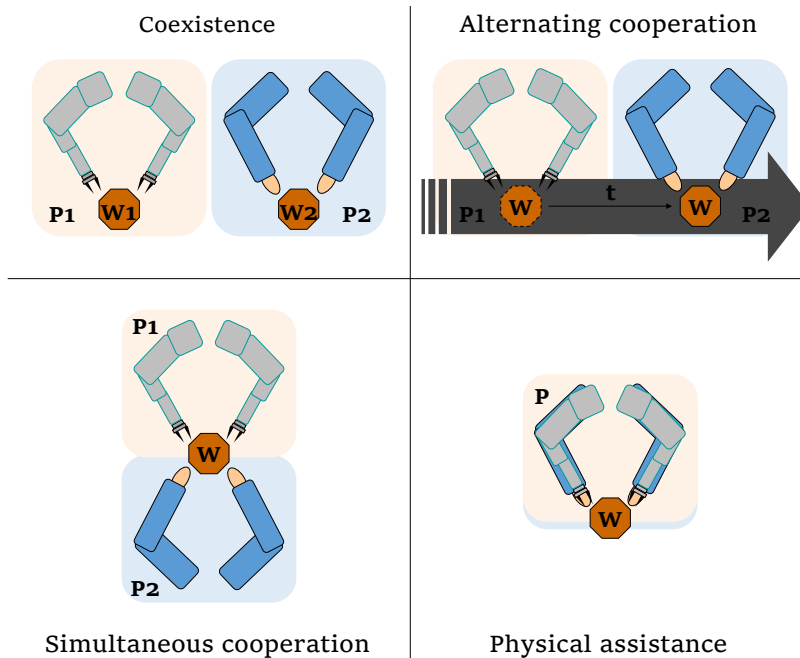


Figure 1.6: Description of the different types of pHRI according to the degree of interaction between the robot and the human operator, in terms of shared workspace, process (P) and workpiece (W) [Helms 2002, Ministère du travail 2017].

In the first three scenarios, the robot motion can be pre-programmed or programmed by prior demonstration, then it evolves autonomously in normal operating mode. In the last case, either the robot follows the operator's motion (e. g. exoskeleton), or the robot leads the movement and the operator intervenes punctually to adjust its trajectory for example. These situations are not mutually exclusive: depending on the task requirements, the robotic system can be designed to be able to implement several of these operating modes.

Consequently, physical interaction between the robot and the human operator may occur occasionally if during most of the task robot and human operator work independently but have to interact at specific times (scenarios 1 to 3), or may be permanent if the operator is supposed to work continuously in contact with the robot (scenario 4). In [Bicchi 2008], the former case is referred to as *hands-off pHRI* and the latter one as *hands-on pHRI*. In this thesis, the focus is on *hands-off* interactions: robot and human operator share the same workspace and contacts between them can punctually occur, whether intentional or undesired.

In any of these collaborative situations, we are facing new challenges that do not exist with traditional industrial robots. So far, the line of defense has been to take all measures to impose a segregation between robots and human operators by installing the robots in a closed work cell as shown in Figure 1.7a. These cells are usually equipped with a large number of sensors to monitor the entry of people so that, if necessary, any power can be instantly cut off from the robot, thus minimizing the risk of possibly dangerous situation to occur. Since pHRI brings workers and robots together in a shared workspace as illustrated in Figure 1.7b, the conventional protection systems established for industrial robotics no longer apply. To guarantee the operator's safety at all times, including during interaction phases, it is necessary to implement specific safety criteria.



(a) Traditional industrial robot in closed environment, delimited by safety fences and signs prohibiting access to any human individual during robot operation.



(b) Collaborative operation with a robot working alongside a human operator in an open environment, without any physical separation.

Figure 1.7: Closed and open robot workspaces depending on the type of operation and the level of safety required.

1.1.3 Safety requirements for collaborative robots

As stated by Asimov's first law [Asimov 1950], "*a robot may not injure a human being or, through inaction, allow a human being to come to harm*". With the desire to remove barriers between robots and operators, a natural demand for a clear set of safety measures has been required by robot manufacturers, integrators and end-users. Thus specific standards and studies² were established to reduce the risks of accidents and injuries during the collaborative application, followed by the implementation of new risk reduction measures.

1.1.3.1 Safety standards and related studies

Until 2006, a human in the vicinity of a robot in operation was not allowed for safety reasons. In this case, the most commonly used solution was to install a physical safety barrier around the robot, which prevented unauthorized persons from entering the robot's workspace and could initiate the robot's shutdown.

Standard currently in application

Originally, the first international standard concerning industrial robot safety and introducing the concept of collaborative application was published in 2006 with ISO 10218 regulation, followed by the American adaptation ANSI/RIA R15.06 in 2009. More recent versions [ISO 10218-1: 2011, ISO 10218-2: 2011, ANSI R15.06 2012] were subsequently available in 2011 and 2012. Concerning ISO 10218, it has been divided into two parts. The first part [ISO 10218-1: 2011], which is mainly addressed to robot manufacturers, deals with technical specifications to guide the design of robot intrinsic safety devices. The second part [ISO 10218-2: 2011] is rather addressed to robot integrators by focusing on the safety requirements within the industrial robotic cell.

These standards specify new regulations for the collaborative operation, which is defined at this stage as *a state in which purposely designed robots work in direct cooperation with a human within a defined workspace*. The task performed by the robot system (described by the combination of the robot arm, the control scheme, the end-effector and the workpiece) and the workspace in which it evolves are considered as a whole that must fulfill the necessary conditions for a safe collaborative operation. To specify these conditions, four fundamental and non-exclusive types of collaborative operations have been identified and are reported in Table 1.1:

²Any robotic application is generally subject to standards on safety of machinery in industry such as [ISO 12100: 2010, ISO 13850: 2015, ISO 13855: 2010, IEC 60204-1: 2016], however in this thesis the focus is on specific standards for collaborative robotics operations. In addition, only risks induced by a physical contact with the robot are examined, although human operators are exposed to other potential risks (e.g risks related to electricity, fluids under pressure, pinching of hands or feet, falling parts, etc.).

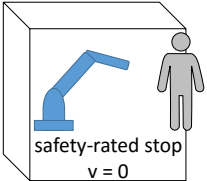
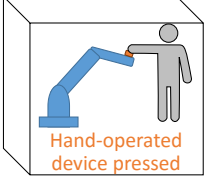
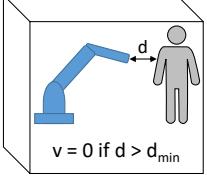
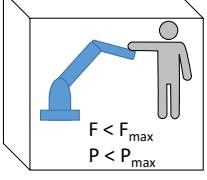
Safety-rated monitored stop	
<p><i>No robot motion while operator is in the collaborative workspace (either the operator or the robot system may move, but not both at the same time).</i></p>	
Hand guiding	
<p><i>Robot motion only through direct input of the operator with an hand-operated device (both the person and the robot may move at the same time but the motion is controlled by the operator).</i></p>	
Speed and separation monitoring	
<p><i>Robot motion only when separation distance above a minimum protective separation distance d_{min} (operator and robot may move at the same time only at a sufficiently safe distance).</i></p>	
Power and force limiting by inherent design or control	
<p><i>In case of contact, the robot can only produce harmless situations for the operator through the limitation of its speed, power, efforts or torque (operator and human can move at the same time).</i></p>	

Table 1.1: Types of collaborative operation as reported in [ISO 10218-1: 2011, ISO 10218-2: 2011]

Although the first three modes allow the spatial proximity of the robot and the operator, their physical contact is allowed only when the robot is stopped or hand-guided by the operator. Only the fourth mode allows their physical contact while the robot moves autonomously. In all cases, a risk assessment must be conducted conscientiously by the robot integrator to secure the operating conditions for a specific workspace and a defined task. Indeed, the collaborative robot can only be safe for a given application in a defined working environment, but it cannot be considered indiscriminately safe under all conditions. The risk is assessed according to the combination of its potential severity, its likelihood of occurrence and the operator's ability to escape from the hazard [Marvel 2015]. This determines the appropriate security mode taking into account the task requirements. Thus, some robot manufacturers have equipped their robots with safety options such as KUKA's *Safe Operation and Safe Handling* and ABB's *SafeMove* that performs safety monitoring of robot motion, tool and standstill supervision as well as speed limitation.

Limitations of existing safety standards and additional in-depth studies

In its original version of 2006, ISO 10218 standard specified that the presence of the human in the collaborative workspace required one of the following limitations to be fulfilled:

- Maximum robot end-effector velocity is 0.25 m.s^{-1} ,
- Maximum static force is 150 N ,
- Maximum dynamic power is 80 W .

However, some studies have shown that these conditions were ill-adapted and that the problem was poorly addressed [Haddadin 2009, Haddadin 2013]. Indeed, no characteristics of the robot such as its mass, its payload or its control schemes were considered. Thus the same limitations were applied to a lightweight compliant robot system as to a high payload standard industrial robot. In addition, a robot with a sharp tool at its end would be allowed to exert a force up to 150 N in the same way as an object with a rounded tip, and this regardless of which part of the human body is impacted.

Demonstration of these deficiencies

Let us consider a 1-dimensional mass-spring-mass model for the impact between a human and a robot as illustrated in Figure 1.8. We denote m_R and m_H the contribution of the robot mass (due to its inertia and payload) and the human effective mass (which depends on the actual mass of the body region in contact and its effects being connected to other body regions as defined in Appendix A) respectively. The connection between the two bodies is modeled by a linear spring of stiffness k . The two masses move at a speed \dot{x}_R and \dot{x}_H for the robot and the human respectively and come into contact across a surface area A (see Figure 1.8).

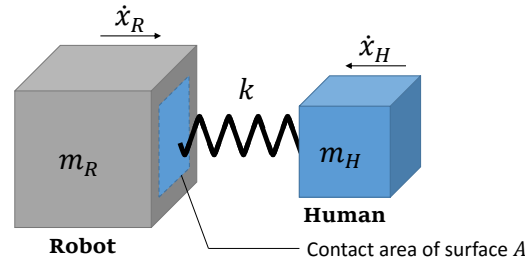


Figure 1.8: Illustration of a spring-coupled two mass system

Denoting $x(t) = x_R(t) - x_H(t)$ the relative position between the center of mass of the human and the robot, the dynamic equation of motion gives:

$$x(t) = \frac{\dot{x}_0}{\omega_0} \cos\left(\omega_0 t - \frac{\pi}{2}\right) \quad (1.1)$$

with $\omega_0 = \sqrt{\frac{k}{\mu}}$ the natural frequency, $\mu = \frac{m_R m_H}{m_R + m_H}$ the reduced mass, and assuming that $x(0) = 0$ and $\dot{x}(0) = \dot{x}_0$.

Then the contact force is given by:

$$F(t) = -\sqrt{k\mu}\dot{x}_0 \cos\left(\omega_0 t - \frac{\pi}{2}\right) \quad (1.2)$$

In equation (1.2), it is clearly noticeable that the contact force $F(t)$ depends on the mass of the two bodies involved through μ , as well as on the contact stiffness k (which is mainly the stiffness of the human body part in contact in the case of a highly stiff robot). The shape of the contact area A must also be taken into account because, for a same contact force, the resulting pressure on the human skin differs. Since these factors influence the impact force, they must be taken into account when assessing the dangerousness of the contact.

As a consequence, these limitations have since been removed in the revised versions of ISO 10218 in 2011 and 2012. Nevertheless, there was still a lack of quantitative limitations and differentiation according to the contact circumstances. A large number of studies coming from research laboratories in this emerging field has been conducted to propose further insights on an efficient evaluation of the safety during collaborative operations. A change of perspective has been undertaken, considering human injuries as the central element for achieving a quantitative safety assessment.

First, [Haddadin 2009] has drawn a "safety tree" that has given the direction towards a more differentiated classification of injury mechanisms. The case of constrained and unconstrained contacts together with the dependency on contact geometry and on robot mass and speed has been raised in [Haddadin 2008b, Haddadin 2008c, Haddadin 2012]. In addition, [Ogorodnikova 2009] has proposed several danger criteria to indicate the level of risk during an interaction with a robot. In particular, several biomechanical analyses have been conducted to evaluate the applicability of injury severity criteria from the automotive field to collaborative robots [Oberer 2007, Haddadin 2007, Haddadin 2010b]. However, the Head Injury Criterion (HIC) [Versace 1971], which is the most commonly used index in the automotive industry, has proved to be insufficient to describe low severity injury such as those induced by collaborative robots, due to robot speeds which are significantly lower than in automobile crash testing [Haddadin 2009]. Indeed, for robots operating in industrial context at typical speeds up to $\approx 2 \text{ m.s}^{-1}$, blunt head impacts without clamping are very unlikely to be life-threatening regardless of the robot weight. However, other serious injuries, such as fractures of facial and cranial bones, may already occur at moderate speeds and appear to be a more relevant injury severity. Therefore the Abbreviated Injury Scale (AIS), which is a well-established injury classification for injuries ranging from minor to fatal [Civil 1988], has been extended to differentiate between superficial³ injuries of lower severity [Haddadin 2013] (see Figure 1.9). Nevertheless, this classification is independent of the location of the human body part impacted.

In addition to understanding the basic mechanisms of injury levels in humans, it is also of interest to consider pain tolerance and characterize it according to the body area. Pain onset thresholds have been measured on healthy adults subjects on several body areas [Suita 1995, Yamada 1997].

³The term *superficial* is the official term, although it may be misleading in the context of robotics since even superficial injury is already unacceptable.

	AIS	SEVERITY	TYPE OF INJURY	INJURY EXAMPLE		
Potential injuries for industrial robots	0	None	None	/		
	Worst case scenario allowed for collaborative/service robots	1. A	Minor	Superficial injury, class 1	Contusion (bruise)	Extension
		1. B	Minor	Superficial injury, class 2	Abrasion	
		1. C	Minor	Superficial injury, class 3	Contusion (crush, severe bruise, hematoma)	
		1. D	Minor	Superficial injury, class 4	Superficial/minor laceration (incised wound/cut)	
		1. E ≡ 1	Minor	Superficial injury, class 5	Laceration, gash, superficial avulsion	AIS
	2	Moderate	Recoverable	Nerve contusion, linear fraction		
	3	Serious	Possibly recoverable	Small brain contusion		
	4	Severe	Not fully recoverable without care	Complex basal skull fracture		
	5	Critical	Not fully recoverable with care	Diffuse axonal injury		
6	Fatal	Unsurvivable	Separation of brainstem			

Figure 1.9: Definition of the extended Abbreviated Injury Scale [Haddadin 2013]. While industrial robots can cause minor to fatal injuries e.g. in the event of safety equipment failure, severe risks must be avoided for collaborative or service robots, as physical contact can be both necessary and crucial. Since in this case only superficial injuries are allowed at most, a more precise description of low injury scenarios is achieved by splitting up AIS = 1 into five categories.

Further investigations were carried out to determine various impact-related quantities that are relevant for causing contusion in human soft tissue [Desmoulin 2011, Behrens 2014]. In particular, threshold values in forces and pressures were measured before the onset of pain at several points of the human body and have since been considered appropriate to limit the effects of physical contact [Unfallversicherung 2009, Melia 2015]. In [Povse 2010], the pain intensity has been proven experimentally to be directly related to the impact-energy density, which is defined as the amount of energy absorbed by the human body area during contact. More recently, [Vemula 2018] has proposed refining this metrics by considering power flux density, which allows the influence of contact duration to be taken into account and results in a more inclusive indicator.

New technical specification ISO/TS 15066

The comprehensive and in-depth study from the above-mentioned literature on the severity of human body injuries, which combined the efforts of industrial research groups, academic community and standardization organizations, has resulted in the release of the technical specification ISO/TS 15066 in 2016 [ISO/TS 15066: 2016]. It provides additional guidelines to meet previous standards but has to be consulted in conjunction with the safety requirements described in ISO 10218. In particular, the possible types of contact between the robot's moving parts and a human subject are classified as:

- Transient contact: a part of the human body is impacted by a moving part of the robot system but the human can recoil or retract from the robot without being clamped or trapped, which results in a short contact time;
- Quasi-static contact: a person's body part is trapped between a moving part of the robot and another fixed or moving part of the work cell (e.g. clamping or crushing situations).

According to this new technical specification, the risk assessment aims at determining the threshold values to be applied (e. g. in forces, torques, velocities, momentum, mechanical power, axis ranges or space ranges), by considering: the effective payload, the total mass of robot's moving parts, the area and geometry of the robot surface in contact, the exposed human body regions, the origin of contact events (intentional action, undesired contact), the probability or frequency of occurrence, the type of contact event (quasi-static or transient) and all the other quantities that can characterize the physical contact event.

Based on the previously stated studies that measured pain sensitivity thresholds, quantitative biomechanical limits are given informatively into standard ISO/TS 15066 to guide the integrator during the robot limitations evaluation. For the 29 body areas tested (see [Appendix A](#)), pressure and force limits for quasi-static contacts were established by measuring pain onset thresholds. Transient limit values in force and pressure are obtained by considering that, according to the previously conducted analyses, they can be at least twice as great as quasi-static values. Both quantities are of interest because one or the other can be the limiting factor depending on the situation.

Energy criterion and speed limitation

The mass-spring-mass model illustrated in [Figure 1.8](#) is considered in ISO/TS 15066 to model the human-robot contact. A fully inelastic contact situation is assumed, which represents the worst case scenario: the total kinetic energy is not conserved but is fully or partially dissipated during the contact. More specifically, the technical specification considers that the total kinetic energy of the human-robot system is transformed into elastic potential energy within the spring. Assuming that the latter accounts for the stiffness of the human body region in contact (see [Appendix A](#)), the maximum allowable amount of energy absorbed by the human body is given by:

$$E_{max} = \frac{\min(F_{max}^2, A^2 p_{max}^2)}{2k} \quad (1.3)$$

where F_{max} and p_{max} are the maximum permissible contact force and pressure, whose values are given in [\[ISO/TS 15066: 2016\]](#) for different areas of the human body.

Finally, by definition of the kinetic energy transferred after impact, the maximum allowable relative velocity should be limited to:

$$|\dot{x}|_{max} = \sqrt{\frac{2 E_{max}}{\mu}} \quad (1.4)$$

Nevertheless, in the general case this does not directly inform on the robot speed limitation since the contribution of the human velocity remains unpredictable. Example of applications of these guidelines can be found in [\[Matthias 2016, Rosenrauch 2017\]](#). In [\[Vemula 2018\]](#), the human-robot impact model is refined by considering a linear spring-damper system that has been validated based on collision tests with human subjects.

Finally, more differentiated guidelines are proposed in the technical specification ISO/TS 15066 for risk and hazard assessment during a collaborative operation, which shall be incorporated in a future updated version of the standards. Security requirements are given by considering the whole process, including the robot system, but also the task to be performed and the collaborative workspace. Quantitative thresholds for the adjustment of the robot safety limitations are given for informational purposes, depending on the exposure of a particular area of the human body to be in contact with the robot. Safety maps evaluating the dangerousness of a robotic arm within its workspace are proposed in the literature in light of this technical specification [Nakamoto 2017, Mansfeld 2018]. In order to guarantee these new limitations inherent to collaborative operations, specific injury risk reduction measures are deployed.

1.1.3.2 Injury risk reduction measures

Before the coexistence of the human and the robot in the same workspace, safety devices were mostly external, such as safety light curtains to detect the operator's entry. In collaborative robotics, operators and robots work in an open environment without fences, thus other risk reduction measures have to be integrated to ensure the operator safety at any time. For this purpose, the design of collaborative robots is specifically adapted to allow an intrinsically safe pHRI. A *compliant* robot behavior is sought, which means that the robot has to react in a soft and flexible way to any contact within its environment. To this end, one can distinguish between supervision systems that aim to avoid any contact with the operator or to adapt the robot's motion and trajectory according to their proximity (*pre-impact phase*), passive safety design that guarantees a first level of safety in the event of an impact through the robot mechanical design (*impact phase*), and active safety strategies that refer to the design of impact detection and reaction algorithms (*post-impact phase*).

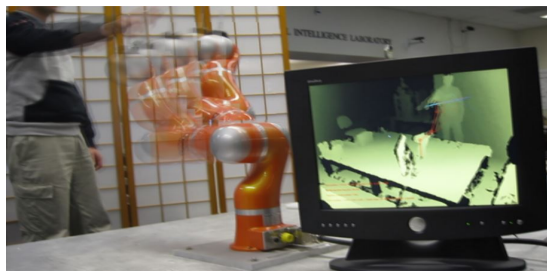
Supervision systems

Before the occurrence of an impact, a technique for monitoring the collaborative workspace can be used to control at any time the proximity between the robot and the human operator and initiate a safe robot reaction in case of potential dangerous situation. A wide range of additional external sensors can be used, with even more efficiency when combined with other technologies: RGB camera, stereo camera systems, Kinect sensors (Figure 1.10a), motion capture systems (Figure 1.10c), infra-red proximity sensors, capacitive sensors, lidar scanners. Some of them (e.g. lasers) allow to generate a 3D range map of the environment (Figure 1.10b). When the robot environment is known with a relatively good accuracy, it can also be reproduced in a virtual environment that will be updated in real time according to the information received by the other sensors [Zube 2015].

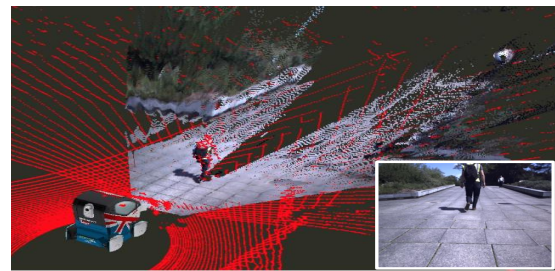
Whatever the technique used, pre-impact strategies consist in calculating at each moment a safety criterion which will be compared with a threshold value in order to determine the robot reaction to be adopted for avoiding the impact or adapting the robot motion to minimize the

impact effects (e. g. in case of intended contact). The reaction strategy can be simply based on the separation distance between the robot and the operator and result in solving an optimization problem at every time step to generate a trajectory towards the robot goal that avoids any collision with the human [Wang 2018]. In [Tan 2009], safety working areas are defined and the robot velocity is adapted according to the proximity with the operator (see Figure 1.10d). In other cases, a danger index is monitored, such as the product of factors affecting the impact force in [Kulić 2005] or the kinetic energy of the robotic system in [Meguenani 2016, Joseph 2018]. Alternative approaches incorporate the prediction of human behavior [Mainprice 2013].

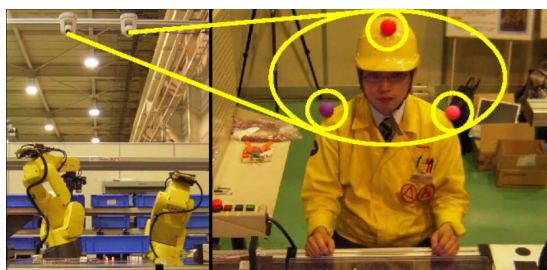
In some situations, this approach is neither sufficient nor appropriate, for example because of temporary obstruction of the field of vision, robustness to working conditions or low sampling rate of vision systems. In other cases, safety of the installation must be guaranteed at a higher level, then redundant safety devices are recommended. Also, relative motions between the robot and human can be very fast and difficult to predict due to the high speed inherent to human movements. For these reasons, the use of exteroceptive sensors⁴ may not be sufficient to limit the risk of human injury, thus passive safety design and active safety control shall be added as additional security measures.



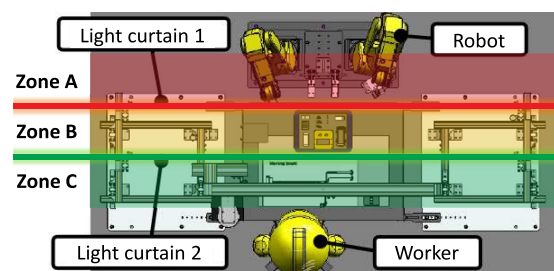
(a) A depth image from a Kinect camera is monitoring a lightweight KUKA LWR IV robot sharing its workspace with a human [Flacco 2012a].



(b) Real-time fusion of stereo camera and 3D lidar scanner data integrated on an autonomous vehicle to form a dense depth map [Maddern 2016].



(c) Two IP cameras track the color marks on the head and shoulders of the human operator to prevent any dangerous contact with the robot at these locations [Tan 2009].



(d) Two light curtains divide the working space into three zones where the robot speed is increasingly reduced as the human is detected in an area close to the robot [Tan 2009].

Figure 1.10: Examples of supervision systems

⁴ *Exteroceptive sensors* provide measurements in relation to the robot's environment (e. g. cameras, end-effector force/torque sensors), whereas *proprioceptive sensors* provide measurements of the robot's internal state (e. g. actuator current sensors, motor and joint position sensors, joint torque sensors).

Passive safety design

A first influencing factor for passive safety measures is the contact geometry: since pressure is one of the critical factors in limiting the risk of injury (see equation (1.3)), increasing the contact surface area would reduce the hazard. As studied in [Vemula 2018], the robot's external surface radius of curvature is thus of particular interest: rounded edges and corners on the robot are generally preferred, as evidenced by the design of collaborative robots commonly available on the market (e.g. YuMi, IIWA, Sawyer or CEA-LIST robots in Table 1.2).

In addition, numerous passive safety measures are adopted to limit the energy stored by the robot and hence the part that can potentially be transferred to the operator in the event of contact. There are two ways to achieve this: either by reducing the kinetic energy of the robot, or by integrating components into the robot that will absorb a portion of the energy.

Apart from reducing the robot's speed, one option to reduce its kinetic energy is to minimize the moving masses [Haddadin 2008b, Haddadin 2008c, Mansfeld 2017]. This is the reason why collaborative robots are generally lightweight robots (see robot weights in Table 1.2). Also, some transmissions allow their actuators to be positioned at the robot base (e.g. Screw-Cable Systems (SCSs) as illustrated in Figure 1.11a), further reducing the inertia in motion.

Regardless of the collided area of the human body, if the robot stiffness is non-infinitely high (e.g. in case of deformable structure or impedance control law), then part of its kinetic energy will be transformed into mechanical deformation energy, thus avoiding being transferred to the operator. Therefore, robot areas that are the most exposed to potential contacts are often covered with a soft visco-elastic material [Park 2011] (e.g. commercial robots in Table 1.2).

Furthermore, robots using stiff actuators to achieve the precision, stability and bandwidth required for an accurate position control tend to have several disadvantages in collision situations, such as a lack of compliance, additional friction, increasing reflected inertia and backlash. Ideally, a robot with high rigidity would be desirable for high positioning accuracy and dynamics, but without sacrificing contact sensitivity. Therefore, Series Elastic Actuators (SEAs) with mechanical compliant elements such as belts, cables or gears were integrated into the actuation system to achieve a compromise between precision and safety [Pratt 1995]. For example, Harmonic drive[®], based on the deformable Flexspline, is a mechanical gear system commonly used in robotics since it allows high reduction ratios while presenting low backlash (see Figure 1.11b). SCSs is another technology that provides shock tolerance and low friction levels (see Figure 1.11a). In addition, the reduction ratio of SCSs is very small compared to Harmonic drive[®], which minimizes the influence of actuator-side inertia (due to the squared reduction ratio in its expression converted at the output-side), and therefore also tends to decrease the apparent inertia. With SEAs, the inertia of the link and that of the heavier motor are coupled through the elastic joint, which consequences on safety in pHRI are highlighted in [Haddadin 2010a]. Moreover, mechanical elasticities tend to make position-tracking more complex and cause increased oscillations due to vibrations, thus reducing the robot's performances. Variable Stiffness Actuators (VSAs) extend the SEAs concept with adaptive compliance technology that allows the actuator's passive elastic stiffness and damping to be mechanically adjusted during its motion [Wolf 2016].

Collaborative Robot	Characteristics	Actuation system Force/torque instrumentation
ABB – YuMi 	$m_r = 38$ kg $m_p = 0.5$ kg per arm $l = 559$ mm	7 DOF per arm Harmonic drive [®] gear system Joint torque measurement through motor current sensors
FANUC – CR-35iA 	$m_r = 990$ kg $m_p = 35$ kg $l = 1813$ mm	6 DOF Harmonic drive [®] gear system Force/torque sensor at the base
KUKA – IIWA 7 R800, IIWA 14 R820 	$m_r = 22/30$ kg resp. $m_p = 7/14$ kg resp. $l = 800/820$ mm resp.	7 DOF Harmonic drive [®] gear system Joint torque sensors
RETHINK ROBOTICS – Sawyer 	$m_r = 19$ kg $m_p = 4$ kg $l = 1260$ mm	7 DOF Harmonic drive [®] gear system Joint torque sensors and wrist camera
UNIVERSAL ROBOTS – UR3, UR5, UR10 	$m_r = 15/15/17$ kg resp. $m_p = 3/5/10$ kg resp. $l = 500/850/1300$ mm resp.	6 DOF Harmonic drive [®] gear system Joint torque measurement through motor current sensors, force/torque sensor at the end-effector
CEA-LIST – Prototype of ISYBOT robot 	$m_r = 59$ kg $m_p = 8$ kg $l = 1200$ mm	6 DOF Screw-cable actuators Joint torque measurement through motor current sensors

Table 1.2: Example of collaborative robots available on the market^a

^aDOF stands for Degrees Of Freedom. Variable m_r denotes the robot weight, m_p its payload and l its maximum reachable distance. Sources: [ABB 2019, FANUC 2018, KUKA 2017, Rethink Robotics 2018, Universal Robots 2017, Robotiq 2018].

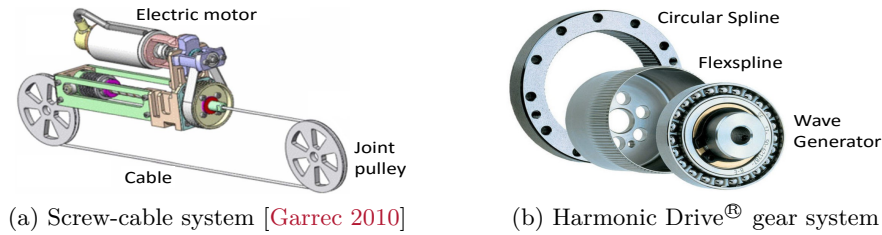


Figure 1.11: Actuators commonly used in robotics

Active safety strategies

The purpose of the impact detection phase is to determine a binary output indicating whether there is an impact occurrence on the robot or not. The earlier the impact is detected, the sooner the robot will be able to react in order to minimize the energy dissipated during the post-impact phase. Additional sensors can be embedded in the robot to this end. Spreading tactile sensors along the robot body, such as with an artificial skin, is a first solution [Mittendorfer 2015]. Force/torque sensors can also be integrated, either at the robot base [Geffard 2000] (e.g. CR-35iA robot) or wrist [Lu 2005] (e.g. UR robots), although in this latter case the forces applied upstream on the arm will not be detectable. Some techniques exploit the vibration characteristics generated by impacts using accelerometers [Min 2019]. Another possibility relies on the use of joint torque sensors (e.g. KUKA-DLR LWR [De Luca 2006], YuMi, IIWA and Sawyer robots). When actuators have good backdrivable properties such as the SCSs in Figure 1.11a, friction levels are characteristically low enough to ensure force transmission with high efficiency [Garrec 2010] (e.g. ISYBOT prototype robot). Thus any external force applied to the robot will be reliably transmitted up to the drive motor currents, allowing contact detection over the entire arm. By being sensitive to external contacts even in absence of additional sensor, robots with such technology can be inherently safe for pHRI.

In order for the robot to react in the most appropriate way after the detection, the maximum amount of information about the physical contact event should be gathered (see Figure 1.12). Especially, the determination of the contact link, and more precisely of the exact contact point, are useful inputs for the reaction strategy on the one hand and for reconstructing the amplitude and direction of the applied force on the other hand [De Luca 2012]. Contextual elements can also be obtained by classifying contact situations: contact intent (accidental or intentional), colliding environment (soft or stiff), type of impact (transient, repetitive, quasi-static), etc.

Finally, during the reaction phase, the robot should react purposefully in response to the contact characteristics previously determined. For instance, if the detected contact has been classified as accidental and quasi-static with a soft environment (e.g. operator's hand), stopping the robot, which is the simplest reaction to a contact, is probably not the most appropriate strategy in this case since the operator would risk being trapped by the robot. Similarly, if an interaction with a rather soft environment is recognized, then it probably suggests an intention from the operator to start a specific physical collaboration, then the robot's post-impact reaction should not be to recover its original task. Some examples of collision reaction strategies can be found in [Haddadin 2008a, De Luca 2008, Parusel 2011].

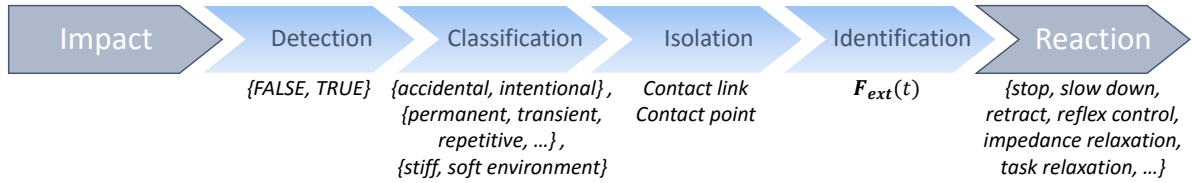


Figure 1.12: Impact event pipeline and expected outputs from each phase [Haddadin 2017]

This brief review of possible measures and strategies to reduce the risk of human injury highlights the specific design of collaborative robots to ensure a safe pHRI. In particular, the characteristics of the robot actuators and the choice of sensor technologies is essential for the implementation of successful active impact detection and reaction strategies.

1.2 Motivations

1.2.1 Problem statement

In view of the previously stated context, this thesis falls within the general framework of physical Human-Robot Interaction in an industrial environment. In particular, *hands-off* operations in *power and force limiting* mode are considered: typically, a robot and a human operator share the same collaborative workspace, thus intentional or accidental contacts between them can occur. For a broader scope, other contacts between the robot and its environment can be included, which are different from those with a human operator but which may also occur during the execution of the robot's task. More precisely, the following four contact situations may occur:

- *Intended Contact with a human Operator (ICO)*: this situation may occur when on a small-scale production line, the robot is versatile and frequently reconfigured by the human operator to perform several tasks, or during human intervention to inform the robot about the presence of a defective part,
- *Accidental Contact with a human Operator (ACO)*: this can happen if a person walks close by the robot and is hit during the robot motion,
- *Intended Contact with an uncertain Environment (ICE)*: this refers to a scenario where during the performance of its task, the robot must come into contact with a workpiece in order to perform a specific action on it,
- *Accidental Contact with an uncertain Environment (ACE)*: this case may arise if an undesired part is placed on the robot's programmed path.

Depending on the type of situation determined, specific reactions would have to be implemented. Figure 1 suggests examples of these four contact scenarios illustrated in an industrial context, with appropriate post-impact strategies. In addition, the location of the contact on the robot arm provides an additional context element allowing, for example, to move the robot in an appropriate direction to release it from an accidental contact.

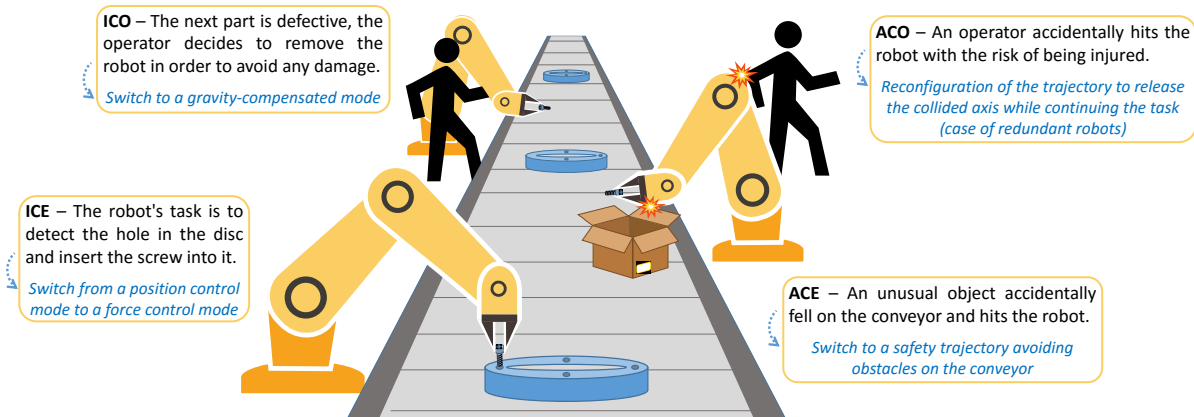


Figure 1.13: Example of the four contact situations in an industrial context and possible associated post-impact reactions.

This thesis addresses the challenge of enhancing safety during pHRI operations through active safety algorithms. More specifically, the focus is on impact detection and classification through the use of proprioceptive information only. Indeed, in an industrial context, cost and integration constraints can be quite significant and limiting, and the use of additional sensors such as force/torque sensors can be relatively expensive. It also requires their integration to be taken into account from the design phase of the robot. Besides, monitoring the motor torques (through the motor currents if mechanical backdrivability properties are sufficiently acceptable or using joint torque sensors) gives reliable information on the external forces applied to the robot.

Based on fault detection techniques, impact detection methods propose to generate a monitoring signal reflecting the occurrence of an impact by being non-zero only when an external wrench is applied on the robot (see Figure 1.14). In return for the use of proprioceptive sensors only, the knowledge of robot models is necessary to calculate the monitoring signal. However, these models may be subject to modeling uncertainties that may result in noise on the monitoring signal as illustrated in Figure 1.14. If no additional information is available or assumed on the structure of the uncertainties, fixed detection thresholds are generally used for detecting the contact [Haddadin 2017]. Nevertheless, adjusting fixed thresholds can be tedious in presence of modeling uncertainties: if they are set too small, the algorithm may trigger false alarms, while if they are set to be higher than the modeling errors, the detection sensitivity is reduced. In addition, the contact characterization step is made difficult by the presence of modeling uncertainties: the adjustment of certain parameters is based on experimental data subject to modeling errors, which can greatly affect the success of the classification.

In the literature, several common approaches use the torque generated by the external wrench applied and transmitted to the robot joints as a monitoring signal [De Luca 2006, Haddadin 2017, Wahrburg 2018]. The first objective of this thesis is to reconsider these approaches in the presence of modeling uncertainties and then to compare their detection performance from a theoretical and experimental point of view. The development of innovative adaptive strategies for impact detection in the presence of uncertainties is the second objective of the thesis. For this

purpose, modeling errors will be treated as noises when designing Kalman filters to reconstruct the torque due to the impact. An adaptive detection threshold taking into account the maximum contribution of uncertainties along the robot's trajectory will be considered (see Figure 2). Thus, any additional contribution beyond the threshold could only be due to the occurrence of a contact, thus allowing its detection. Once the impact has been detected, the third objective is to determine the operator's intention at the time of contact (intentional or accidental contact) and to locate the impact along the robot arm. This problem is treated as a classification problem using learning techniques, which have the advantage of intrinsically determining the relevant features for classification. The adaptability of these learning techniques to the variable operating conditions of the robot is a decisive aspect for the relevance of such approaches.

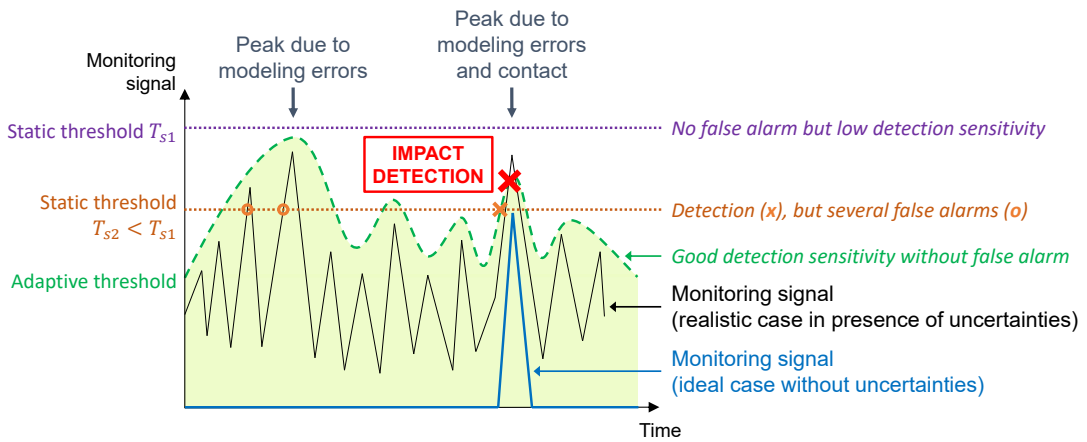


Figure 1.14: Fixed versus adaptive thresholds in contact detection and evaluation. A fixed threshold can be tuned higher than the modeling uncertainties but is likely to be conservative, or lower which may trigger false alarms. A convenient adaptive threshold would correctly detect the impact without triggering false alarms.

1.2.2 Contributions of the thesis

The following four contributions were completed in this thesis to meet the previous objectives:

Contribution 1: Development of a quantitative methodology rendering explicit the contribution of uncertainties

Since the impact detection algorithms are based on the dynamic model of the robot, special attention is paid to the uncertainties in this model. In this work, we assume that model uncertainties are the main source of errors, and more specifically model uncertainties on the robot's dynamic parameters and state. For each of these contributions, a stochastic approach is followed to quantitatively characterize the induced errors, which are then treated as random noises of given probabilistic distribution. These errors are propagated through the robot's dynamic model and a structured formulation of the total resulting errors induced by the uncertainties and depending on the robot's trajectory is proposed.

Contribution 2: Design of novel adaptive impact detection strategies explicitly taking into account the contribution of uncertainties (rigid case)

The previous methodology is applied to several impact detection strategies, in the case of robots with infinitely stiff joints and links as a first approach. For each strategy, a structured and quantified expression of the errors induced by the uncertainties is derived. In order to efficiently isolate the dynamic effects of the impacts, the maximal error range due to modeling errors is investigated: it represents a threshold above which any additional contribution within the monitoring signal could only be due to an external contact, thus allowing its detection (adaptive threshold in Figure 1.14). The objective is therefore to obtain a structured formulation of the uncertainties-induced errors involved in a given impact detection algorithm in order to provide an adaptive detection threshold, based on the amount of modeling errors and depending on the robot's trajectory.

This approach has been derived for several impact detection algorithms that use the torque generated by the external wrench applied as a monitoring signal, making it possible to compare them in terms of detection sensitivity and rapidity.

Contribution 3: Design of novel adaptive impact detection strategies explicitly taking into account the contribution of uncertainties (flexible case)

When deformable components are present in the actuation chain, specific models are required to take into account the effect of the induced elasticities. If methods developed in the case of rigid robots are applied to robots with elastic joints, additional modeling errors are introduced due to the inadequacy of the proposed model. That is the reason why the previous approach has been derived in the case of robots with rigid links and elastic joints: by refining the dynamic model of the robot taking into account joint elasticities, the objective is to reduce the contribution of modeling errors and thus improve the sensitivity of detection to an impact.

Contribution 4: Characterization of the contact intention and localization on the robot arm

An appropriate reaction strategy for the robot manipulator depends on a correct classification of the contact situation. The objective is to extract useful contextual information from the available proprioceptive measurements, and in particular the intention of the contact (accidental or intentional) and the location of the impact on the robot arm. To do this, supervised learning techniques through the use of neural networks are investigated. Indeed, the benefit of multi-layer neural networks to extract features of increasing complexity and their simple extendability to an increased number of classification outputs by only re-labeling the training data render them a versatile tool for contact situation classification. The challenge of generalizing beyond training data, which is an important aspect in robotics for such approaches, has been investigated.

1.3 Outline

The organization of this thesis is detailed hereafter (see [Figure 1.15](#)):

[Chapter 2](#) recalls the formalism used for the description of serial robot manipulators. As the subsequent impact detection intervenes in a dynamic context, the focus is on the robot's dynamic model that is presented in the case of robots with infinitely stiff joints and in the case of robots with elasticities in the joints. The potential sources of uncertainties in the dynamic model are identified, and for each type of uncertainty, a methodology is proposed to characterize the induced errors. In particular, the modeling uncertainties of the ISYBOT prototype robot of the CEA-LIST have been quantitatively characterized using this methodology.

[Chapter 3](#) addresses the issue of designing impact detection algorithms under uncertainties using only proprioceptive measurements. In this work, two categories of impact detection methods are explored: direct estimation of external torque and disturbance observer-based approaches. For each method, the uncertainties-induced errors are highlighted by propagating the errors arising from the robot's dynamic model. Using the methodology developed in [Chapter 2](#), the envelope characterizing their maximum contribution is derived, resulting in an adaptive detection threshold that depends on the robot's trajectory. This approach is developed for robots with infinitely stiff joints and for robots with elasticities in the joints.

[Chapter 4](#) is dedicated to the experimental validation of the previous algorithms redesigned under uncertainties on the ISYBOT prototype robot. On an illustrative example of human-robot contact, a preliminary study is conducted to examine the influence of tuning parameters on the detection time and sensitivity. The pros and cons of the different methods studied, theoretically highlighted through the previous analysis, are confirmed experimentally. Finally, the energy transferred to the collided system is examined for the proposed detection algorithms and the values obtained are related to the references given in the robotic standards.

[Chapter 5](#) proposes to characterize contact situations using supervised learning techniques through the use of neural networks. More specifically, the objective is to classify the human intention when coming into contact with the robot as intended or undesired and to localize the contact area on the robot arm. The generalizability of this classification to several human subjects and robot trajectories is studied. To this end, two case studies are carried out using experimental data collected from an ABB YuMi robot and the ISYBOT prototype robot.

Finally, [Conclusions and outlooks](#) end this thesis.

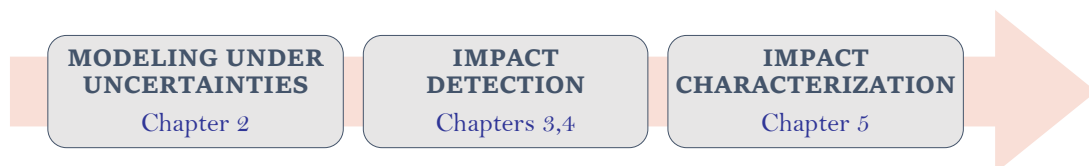


Figure 1.15: Explanatory scheme of the thesis structure

Modeling serial robot manipulators under uncertainties

“ *Essentially, all models are wrong, but some are useful.* ”

George E.P. Box (1987)

Contents

2.1	Serial robot manipulator modeling	26
2.1.1	Notations	26
2.1.2	Force/torque transmission model	27
2.1.3	Dynamic models	28
2.1.3.1	Robots with rigid links and infinitely stiff joints (<i>rigid case</i>)	29
2.1.3.2	Robots with rigid links and elastic joints (<i>flexible case</i>)	31
2.2	Characterization of the associated uncertainties	34
2.2.1	Sources of uncertainties	34
2.2.2	Probability distribution of uncertainties	35
2.3	Parameter uncertainties	37
2.3.1	Dynamic model parameters estimation	37
2.3.1.1	Existing approaches	38
2.3.1.2	Methodology under consideration	39
2.3.1.3	Characterization of associated errors	42
2.3.2	State calculation	43
2.3.2.1	Existing approaches	43
2.3.2.2	Methodology under consideration	45
2.3.2.3	Characterization of associated errors	47
2.3.3	Geometric model parameters estimation	49
2.4	Conclusion	50

This chapter begins by introducing the robotic modeling formalism that will be used for the subsequent design of impact detection and classification algorithms. Section 2.1 recalls the main models describing serial robot manipulators and their motion. In particular, since impact detection intervenes in a dynamic context, the dynamic model of robots with infinitely stiff joints and links is highlighted (*rigid case*). As collaborative robots are characterized by more flexible mechanical construction through their actuation and transmission system, a dynamic model taking into account elasticities in the joints is presented (*flexible case*).

Thereafter, the uncertainties stemming from the robot dynamic models are investigated in Section 2.2 since they may lead to false alarms and misclassifications during the impact detection and classification steps. The different potential sources of errors are identified and a stochastic approach is adopted to approximate uncertainties by random variables of given probabilistic distribution.

For this work, parameter uncertainties are considered as the main source of errors regarding the robot dynamic motion. The contribution of each category of uncertain parameters involved in the robot dynamic models is analyzed in Section 2.3. The emphasis is put on the dynamic model parameters and the motor and joint coordinates in position, velocity and acceleration: depending on the method adopted to obtain them, different errors will be generated. For each of these two types of parameters, the technique used in this thesis for their computation is presented, then a specific methodology is proposed to characterize the random distribution of errors induced by the associated uncertainties.

2.1 Serial robot manipulator modeling

2.1.1 Notations

A serial robot manipulator is considered as a simple open kinematic chain with bodies (or links) connected end-to-end by actuated joints. Bodies can be rigid or deformable structures and joints can be prismatic or revolute. In this work, only the case of robots with rigid bodies and revolute joints is considered.

The n robot's links are numbered from 0 to n with the first link being the robot base and link n the terminal link. In this work, all the n joints are supposed actuated by n motors, to form a n -Degrees Of Freedom (DOF) robot. Any joint $j \in \llbracket 1..n \rrbracket$ connects link $j - 1$ to link j and the variable measuring the rotation of the following link j with respect to the previous one $j - 1$ is denoted q_j . The vector $\mathbf{q} = (q_1 \dots q_n)^T \in \mathbb{R}^n$ forms the *joint coordinates* and describes the robot configuration in the *joint space*. A particular point of interest is the robot endpoint on the last link, defined as the *end-effector* where a tool is usually attached. Its situation in the *Cartesian space* (also called the *operational space*) in terms of position and orientation is described by the *operational coordinates* denoted $\mathbf{E} \in \mathbb{R}^6$.

The robot is assumed to evolve in a fixed frame of reference \mathcal{R}_0 attached to the robot base. A frame \mathcal{R}_j is assigned to each link j according to the Khalil-Kleininger convention (also called the modified Denavit-Hartenberg convention) detailed in [Khalil 2004]. The spatial arrangement of these frames is completely described by the geometric Denavit-Hartenberg parameters: localization of a frame \mathcal{R}_j relative to its previous frame \mathcal{R}_{j-1} is determined as a composition of rotations and translations depending on these parameters and represented by the homogeneous transformation matrix ${}^{j-1}\mathbf{T}_j \in \mathbb{R}^{4,4}$ [Khalil 2004].

The robot motion can be described through different models commonly used in robotics:

- the geometric and kinematic models, that describe the mapping from joint space to Cartesian space at the position and velocity levels respectively,
- the force/torque transmission model and the dynamic models, that define the relation between the applied forces and the resulting torques along the arm, and the ensuing motion of the industrial manipulator.

In the following, only models directly related to impact detection and classification are presented, that is the force/torque transmission model in Section 2.1.2 and the dynamic models in Section 2.1.3. The interested reader can refer to [Khalil 2004] for other models that are not presented as part of the scope of this thesis.

2.1.2 Force/torque transmission model

When the robot manipulator comes into contact with its environment, an external wrench $\mathbf{F}_{ext} = (F_x \ F_y \ F_z \ T_x \ T_y \ T_z)^T \in \mathbb{R}^6$ is generated. This wrench can be applied at the end-effector or anywhere on the robot structure, the contact point on the robot arm being designated as C in the general case. F_x, F_y, F_z and T_x, T_y, T_z represent respectively the force and torque components applied to point C .

The impacting wrench \mathbf{F}_{ext} induces an external torque $\boldsymbol{\tau}_{ext} \in \mathbb{R}^n$ at the joint level, which are related by:

$$\boldsymbol{\tau}_{ext} = \mathbf{J}_C(\mathbf{q})^T \mathbf{F}_{ext} \quad (2.1)$$

where $\mathbf{J}_C(\mathbf{q})$ is the Jacobian matrix computed at the contact point C according to the robot kinematic model (the interested reader can refer to [Khalil 2004] for further details on the computation of the Jacobian matrix). It should be noted that $\mathbf{J}_C(\mathbf{q})$ and \mathbf{F}_{ext} must be expressed in the same frame (usually the reference frame \mathcal{R}_0). According to equation (2.1), $\boldsymbol{\tau}_{ext}$ can be viewed as a projection of \mathbf{F}_{ext} on each robot joint through the Jacobian matrix.

Remark 2.1 *The external torque $\boldsymbol{\tau}_{ext}$ will be affected only by wrenches that do not belong to the kernel of $\mathbf{J}_C(\mathbf{q})^T$. The observability of an external wrench at the joint torque level therefore depends on the robot configuration and the direction of the impacting wrench. More details about the force/torque transmission can be found in [Walker 1994, Khalil 2004].*

Remark 2.2 When the Jacobian matrix is expressed at a point C that is located on link j , its last $n - j$ columns are identically null. Therefore, the last $n - j$ components of $\boldsymbol{\tau}_{ext}$ will be zero when a wrench is applied on link j :

$$J_C(\mathbf{q}) = \begin{pmatrix} * & \dots & * & 0 & 0 \\ * & \dots & * & 0 & 0 \\ \vdots & \dots & \vdots & \vdots & \vdots \\ * & \dots & * & 0 & 0 \end{pmatrix} \quad \Longrightarrow \quad \boldsymbol{\tau}_{ext} = \begin{pmatrix} * & \dots & * & 0 & 0 \end{pmatrix}^T$$

2.1.3 Dynamic models

In the literature, several approaches have been proposed for the definition of the robot dynamic model. Among these, we can mention the Euler-Lagrange formalism detailed in [Spong 2006] which is based on the Lagrangian equation with the kinetic and potential energies computed for the multi-body robot considered as a whole. Another approach called the Newton-Euler method is described in [Khalil 2010] and relies on the dynamic equations written recursively for each link. These approaches differ in their physical interpretation and their computational efficiency but produce the same resulting model, that is presented in the case of robots with infinitely stiff joints in Section 2.1.3.1 and considering elastic joints in Section 2.1.3.2. Note that the robot dynamic model, which provides the joint torques in terms of the joint positions, velocities and accelerations, is also called the *Inverse Dynamic Model (IDM)* as opposed to the *Direct Dynamic Model (DDM)* that describes the joint accelerations in terms of the joint positions, velocities and torques [Khalil 2004].

The following notations are used throughout the thesis:

- $\boldsymbol{\tau}_{mot} \in \mathbb{R}^n$ is the vector of applied motor torques before the reduction stage. In case of direct-current motors, $\boldsymbol{\tau}_{mot}$ can be directly deduced from the measurement of motor currents $\mathbf{i}_{mot} \in \mathbb{R}^n$ by $\boldsymbol{\tau}_{mot} = \mathbf{K}_{em} \mathbf{i}_{mot}$, where $\mathbf{K}_{em} \in \mathbb{R}^{n,n}$ is the diagonal matrix of the electromagnetic torque constants of the motors,
- $\boldsymbol{\theta}_{mot} \in \mathbb{R}^n$ denotes the rotor positions measuring the rotation of the motor shaft before the reduction stage. It can be obtained from the motor position sensors,
- $\mathbf{R}_{red} \in \mathbb{R}^{n,n}$ is defined as the matrix containing the reduction ratios $R_{red_j} > 1$ for each motor transmission j . \mathbf{R}_{red} can be non-diagonal in case of coupled axes,
- The vector of applied motor torques and motor positions after the reduction stage, denoted $\boldsymbol{\tau} \in \mathbb{R}^n$ and $\boldsymbol{\theta} \in \mathbb{R}^n$ respectively, are deduced from $\boldsymbol{\tau} = \boldsymbol{\eta} \mathbf{R}_{red}^T \boldsymbol{\tau}_{mot}$ and $\boldsymbol{\theta} = \mathbf{R}_{red}^{-1} \boldsymbol{\theta}_{mot}$ where $\boldsymbol{\eta} \in \mathbb{R}^{n,n}$ is the diagonal matrix of the gears transmission efficiency,
- $\mathbf{q} \in \mathbb{R}^n$ is the vector of joint positions, which can be known from position sensors if integrated at the robot joints.

In the following, only variables after the reduction stage (*joint side*) are used. Time dependence is omitted in the equations for the sake of simplicity. In addition, we consider that the electromagnetic torque constants \mathbf{K}_{em} , the reduction matrix \mathbf{R}_{red} and the gears transmission efficiency η are perfectly characterized.

2.1.3.1 Robots with rigid links and infinitely stiff joints (*rigid case*)

In this section, transmission chains are considered as perfectly rigid and without mechanical backlash. A schematic representation of the actuation chain is illustrated in Figure 2.1. The motor shafts and the links being rigidly connected, the joint and motor positions after the reduction stage are equal: $\mathbf{q} = \boldsymbol{\theta}$.

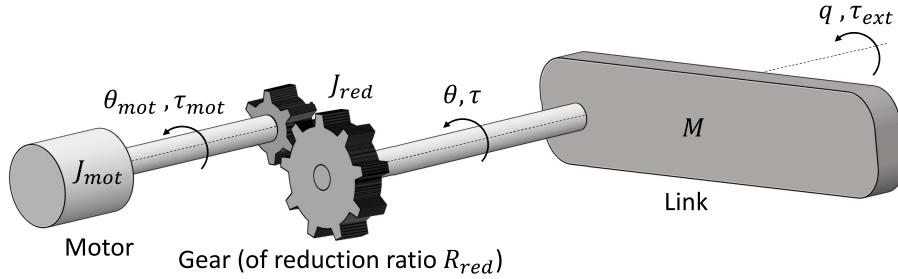


Figure 2.1: Schematic representation of a 1-dimensional rigid transmission with J_{mot} the motor inertia (before the reduction stage), J_{red} the gear inertia and M the link inertia (both after the reduction stage).

In the case of Euler-Lagrange formalism, the robot dynamic model is obtained by deriving the robot kinetic energy and considering gravity as the only source of potential energy and friction as the only dissipative forces. Therefore, the *Rigid Dynamic Model (RDM)* for a robot with rigid links and infinitely stiff joints is defined by:

$$\mathbf{M}_r(\mathbf{q})\ddot{\mathbf{q}} + \mathbf{C}(\mathbf{q}, \dot{\mathbf{q}})\dot{\mathbf{q}} + \mathbf{G}(\mathbf{q}) + \boldsymbol{\tau}_f = \boldsymbol{\tau} + \boldsymbol{\tau}_{ext} \quad (2.2)$$

With:

- $\mathbf{M}_r(\mathbf{q}) \in \mathbb{R}^{n,n}$ the rigid inertia matrix such as $\mathbf{M}_r(\mathbf{q}) = \mathbf{M}(\mathbf{q}) + \mathbf{J}_m$. The matrix $\mathbf{M}(\mathbf{q}) \in \mathbb{R}^{n,n}$ contains the inertial terms derived from the link and motor masses and from the link inertia tensors. The matrix $\mathbf{J}_m \in \mathbb{R}^{n,n}$ is a constant matrix collecting the actuators inertia after the reduction stage. More specifically, we can define $\mathbf{J}_m = \mathbf{R}_{red}^T \mathbf{J}_{mot} \mathbf{R}_{red} + \mathbf{J}_{red}$ with $\mathbf{J}_{mot}, \mathbf{J}_{red} \in \mathbb{R}^{n,n}$ the inertia matrices of the rotors and the gears respectively,
- $\mathbf{C}(\mathbf{q}, \dot{\mathbf{q}}) \in \mathbb{R}^{n,n}$ the matrix such as $\mathbf{C}(\mathbf{q}, \dot{\mathbf{q}})\dot{\mathbf{q}}$ captures the torque induced by Coriolis and centrifugal forces,
- $\mathbf{G}(\mathbf{q}) \in \mathbb{R}^n$ the torque related to gravity effects,

- $\boldsymbol{\tau}_f \in \mathbb{R}^n$ the torque induced by friction forces. A large number of studies on friction models exists in the literature as described in [Armstrong H elouvry 1994]. One of the most common is the Coulomb friction model taking into account stiction and Stribeck phenomena and depending only on velocity. However, more refined models have been proposed, e. g. Dahl, Bliman-Sorine or Lund-Grenoble (LuGre) models [Olsson 1998]. In addition, it is commonly observed that the friction phenomenon depends on different parameters, in particular on load and temperature [Hamon 2010, Bittencourt 2012, Bagge Carlson 2015].

Nevertheless, as a first approximation and without loss of generality, a Coulomb friction model is adopted in the following (see the experimental validation of the friction model for the application case of the ISYBOT prototype robot in Appendix B – Section B.3.2). Therefore $\boldsymbol{\tau}_f$ is expressed as:

$$\boldsymbol{\tau}_f = \mathbf{F}_v \dot{\mathbf{q}} + \mathbf{F}_s \text{sign}(\dot{\mathbf{q}}) \quad (2.3)$$

where $\mathbf{F}_v, \mathbf{F}_s \in \mathbb{R}^{n,n}$ are matrices of viscous and dry friction coefficients respectively and $\text{sign}(\cdot)$ is the function such as:

$$\text{sign}(x) = \begin{cases} 1 & \text{if } x > 0, \\ 0 & \text{if } x = 0, \\ -1 & \text{if } x < 0. \end{cases} \quad (2.4)$$

To completely describe the robot dynamic behavior, n sensor measurements are required in the rigid case. Since $\mathbf{q} = \boldsymbol{\theta}$, position motor sensors can be used. However, if their accuracy is not sufficient, joint position sensors with good resolution could be used in addition by integrating them into the joints provided that the mechanical design of the robot allows it.

Properties of the RDM [Khalil 2004]

Property 2.1 *The inertia matrix $\mathbf{M} \in \mathbb{R}^{n,n}$ is symmetric and positive definite.*

Property 2.2 *The Coriolis and centrifugal matrix \mathbf{C} is not unique. Nonetheless, a convenient form is obtained using the Christoffel symbols c_{ijk} , such as for each element C_{ij} of matrix \mathbf{C} :*

$$C_{ij} = \sum_{k=1}^n c_{ijk} \dot{q}_k \quad \text{with} \quad c_{ijk} = \frac{1}{2} \left[\frac{\partial M_{ij}}{\partial q_k} + \frac{\partial M_{ik}}{\partial q_j} - \frac{\partial M_{jk}}{\partial q_i} \right] \quad (2.5)$$

For this particular choice of definition, the matrix $\dot{\mathbf{M}} - 2\mathbf{C}$ is skew-symmetric. Using Property 2.1 and given that \mathbf{J}_m is constant, the following relation holds:

$$\dot{\mathbf{M}}_r(\mathbf{q}) = \dot{\mathbf{M}}(\mathbf{q}) = \mathbf{C}(\mathbf{q}, \dot{\mathbf{q}}) + \mathbf{C}^T(\mathbf{q}, \dot{\mathbf{q}}) \quad (2.6)$$

Remark 2.3 *Certain impact detection methods rely on the use of the generalized momentum $\mathbf{p} \in \mathbb{R}^n$, defined as:*

$$\mathbf{p}(\mathbf{q}, \dot{\mathbf{q}}) = \mathbf{M}_r(\mathbf{q}) \dot{\mathbf{q}} \quad (2.7)$$

For this purpose and using equation (2.6), the RDM defined in equation (2.2) can be rewritten as:

$$\dot{\mathbf{p}} - \mathbf{C}^T(\mathbf{q}, \dot{\mathbf{q}})\dot{\mathbf{q}} + \mathbf{G}(\mathbf{q}) + \boldsymbol{\tau}_f = \boldsymbol{\tau} + \boldsymbol{\tau}_{ext} \quad (2.8)$$

2.1.3.2 Robots with rigid links and elastic joints (*flexible case*)

Deformable components of the actuation chain such as transmission belts, cables or gears, may be responsible for elasticities in the joints. The joint elasticity is modeled by a lumped elasticity which connects the motor to the link as illustrated in Figure 2.2 [Spong 1987, Khalil 2000b]. As a first approximation, the lumped elasticity of the j^{th} joint can be considered as linear of constant stiffness K_j . Thus, since the rotor is no longer rigidly connected to the link, the dynamics of the two bodies differ but remain coupled by the deformable component. The joint deformation is given by the time-varying displacement $\mathbf{q} - \boldsymbol{\theta}$ between the link position and the rotation of the driving actuator.

Consequently, Euler-Lagrange and Newton-Euler formalisms are modified by distinguishing the dynamic contributions coming from the motor and the link sides. In the case of Euler-Lagrange formalism, the contribution of elasticities is integrated by considering the elastic potential energy related to a spring deformation: $\frac{1}{2}(\mathbf{q} - \boldsymbol{\theta})^T \mathbf{K}(\mathbf{q} - \boldsymbol{\theta})$ with $\mathbf{K} \in \mathbb{R}^{n,n}$ the constant diagonal matrix of joint stiffnesses. To describe both motor and joint dynamics, the model dimension is increased to $2n$.

In the following, only the *reduced* formulation of the Flexible Dynamic Model (FDM) is presented. The interested reader can refer to [De Luca 2016] for further details on the *complete* FDM.

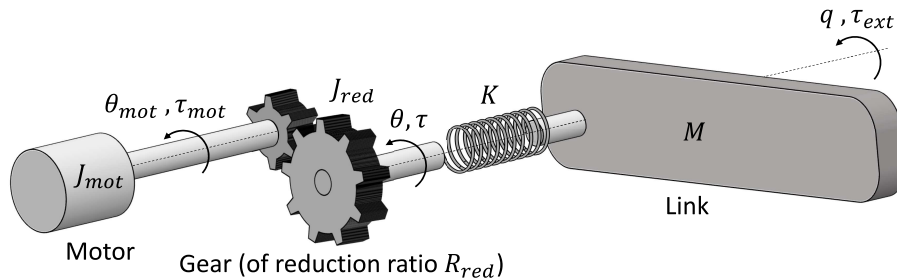


Figure 2.2: Schematic representation of a 1-dimensional elastic transmission with K the elastic stiffness.

Reduced flexible dynamic model

The following assumptions are required to determine the complete FDM [De Luca 2016]:

Hypothesis 2.1 *The deformations are mainly concentrated in the joints. They are small enough to be limited to the linear elastic domain.*

Hypothesis 2.2 *The rotors of the motors are considered as uniform bodies which move only in rotation and without eccentricity. As a consequence, the rotor inertia matrix and the gravity term in the flexible dynamic model do not depend on the angular position of the rotors. More specifically, the rotor inertia matrix is constant and diagonal, and the gravity term depends only on the link position.*

The following additional assumption is required to deduce the reduced FDM:

Hypothesis 2.3 *The angular velocity of the rotors is only due to their own spinning, and is not driven by the rotation of the upstream axes. It is equivalent as considering that for large reduction ratios (of the order 100-150), the contributions of the inertial couplings between the motors and the links can be neglected in comparison with their own inertia [De Luca 2016].*

By considering as negligible the inertial couplings between the motors and the links, the *reduced FDM* for a robot with rigid links and elastic joints is given by:

$$M(\mathbf{q})\ddot{\mathbf{q}} + C(\mathbf{q}, \dot{\mathbf{q}})\dot{\mathbf{q}} + \mathbf{G}(\mathbf{q}) + \boldsymbol{\tau}_{fa} + \boldsymbol{\tau}_k = \boldsymbol{\tau}_{ext} \quad (2.9a)$$

$$J_m\ddot{\boldsymbol{\theta}} + \boldsymbol{\tau}_{fm} - \boldsymbol{\tau}_k = \boldsymbol{\tau} \quad (2.9b)$$

With:

- $\boldsymbol{\tau}_{fa}, \boldsymbol{\tau}_{fm} \in \mathbb{R}^n$ describing friction torques from joint and motor sides respectively. For both origins, a Coulomb friction model is adopted:

$$\boldsymbol{\tau}_{fa} = \mathbf{F}_{va} \dot{\mathbf{q}} + \mathbf{F}_{sa} \text{sign}(\dot{\mathbf{q}}) \quad (2.10)$$

$$\boldsymbol{\tau}_{fm} = \mathbf{F}_{vm} \dot{\boldsymbol{\theta}} + \mathbf{F}_{sm} \text{sign}(\dot{\boldsymbol{\theta}}) \quad (2.11)$$

where $\mathbf{F}_{va}, \mathbf{F}_{vm}$ are the matrices of viscous friction coefficients (respectively at joint and motor sides) and $\mathbf{F}_{sa}, \mathbf{F}_{sm}$ those of dry friction coefficients (respectively at joint and motor sides),

- $\boldsymbol{\tau}_k \in \mathbb{R}^n$ defining the elastic torque induced by the joint elasticities, such as:

$$\boldsymbol{\tau}_k = \mathbf{K}(\mathbf{q} - \boldsymbol{\theta}) - \boldsymbol{\tau}_{k0} \quad (2.12)$$

where $\boldsymbol{\tau}_{k0}$ refers to a preload torque.

The n equations (2.9a) are referred to as the *link equations*, while the n equations (2.9b) are known as the *motor equations*. Both sets of equations are coupled through the elastic torque τ_k . Since the model dimension is $2n$, the same number of sensor measurements is required to fully describe the robot dynamic behavior in the flexible case. Motor and joint position sensors are a first solution (e.g. ISYBOT prototype robot), while in other cases torque sensors are integrated at the joints to directly measure the elastic torque τ_k (e.g. KUKA-DLR LWR [De Luca 2006]). The link positions \mathbf{q} could then be inferred using equation (2.12) and the motor positions $\boldsymbol{\theta}$.

Remarks about the FDM

Remark 2.4 *A weaker formulation of the FDM can be obtained by summing the two equations (2.9a) and (2.9b):*

$$M(\mathbf{q})\ddot{\mathbf{q}} + C(\mathbf{q}, \dot{\mathbf{q}})\dot{\mathbf{q}} + G(\mathbf{q}) + \tau_{fa} + \mathbf{J}_m\ddot{\boldsymbol{\theta}} + \tau_{fm} = \boldsymbol{\tau} + \boldsymbol{\tau}_{ext} \quad (2.13)$$

Indeed, in this case the elastic contribution disappears and, when compared to the RDM, it simply amounts to distinguishing between motor and joint contributions for inertia and friction effects. In a similar way as in the rigid case and for the purpose of ultimately designing impact detection algorithms, the FDM can be rewritten using the generalized momentum defined in the flexible case as:

$$\mathbf{p}(\mathbf{q}, \dot{\mathbf{q}}, \dot{\boldsymbol{\theta}}) = M(\mathbf{q})\dot{\mathbf{q}} + \mathbf{J}_m\dot{\boldsymbol{\theta}} \quad (2.14)$$

This yields:

$$\dot{\mathbf{p}} - C^T(\mathbf{q}, \dot{\mathbf{q}})\dot{\mathbf{q}} + G(\mathbf{q}) + \tau_{fa} + \tau_{fm} = \boldsymbol{\tau} + \boldsymbol{\tau}_{ext} \quad (2.15)$$

Remark 2.5 *In the limit case where $K_j \rightarrow \infty$ (infinitely stiff joint) for each joint j , there is no elastic deformation thus $\boldsymbol{\theta} \rightarrow \mathbf{q}$. Then the FDM in equation (2.9) merges with the RDM in equation (2.2). Properties (2.1-2.3) remain valid in the flexible case as an extension of the rigid case.*

Remark 2.6 *For visco-elastic joints, elasticities can be modeled by a damped spring, introducing a damping term depending on the derivation of the joint deformation, i. e. $\dot{\mathbf{q}} - \dot{\boldsymbol{\theta}}$, into the left-hand side of equations (2.9a) and (2.9b).*

Remark 2.7 *Non-linear effects inherent to elastic components may be observed. More detailed models of elastic joints have therefore been proposed: non-linear stiffness and hysteresis models in case of Harmonic drive[®] [Dhaouadi 2003, Liu 2017], polynomial stiffness with a piece-wise elastic torque model for cable-based transmissions [Fichera 2017], online estimation of the elastic stiffness for variable stiffness actuators [Flacco 2012b]. However, as a first approximation with the small deformation hypothesis (Hypothesis 2.1), a constant stiffness is considered in the following.*

2.2 Characterization of the associated uncertainties

The performance of certain techniques that rely on the robot dynamic model, such as advanced control schemes or impact detection strategies, depends to a large extent on the precise knowledge of its components. In this section, the potential sources of uncertainties and their characterization are investigated based on the theory of Uncertainty Quantification (UQ) [Barth 2011, Smith 2013]. In a general way, this field aims to answer the following questions:

Q1 Can the physical process be reproduced by a mathematical model and which inputs does it depend on ?

Q2 Given a mathematical model and inputs, how accurately is the estimated output and what are the uncertainties affecting it ?

Q3 Given a mathematical model, inputs and uncertainties, can the error in the numerical solution be reliably quantified ?

2.2.1 Sources of uncertainties

Uncertainties-induced errors can arise in the modeling, simulation and experimental phases. Their sources can be classified into three categories [Roy 2011]:

Parameter uncertainties refer to the values of the input parameters that may not be accurately known or available. Section 2.3 is dedicated to this type of uncertainties, which is considered to be responsible for the main contribution of errors in our study.

Modeling uncertainties arise from the lack of knowledge of underlying physical phenomena that are not captured by the dynamic model. Indeed, even if accurate values of the input parameters are known, the mathematical modeling may be insufficient to describe the detailed dynamic behavior of the robot. This may come from:

- Approximations and assumptions: on the robot geometry, the friction model at low speed, the hypotheses of the FDM, some neglected non-linear phenomena,
- Dependencies on inputs that are either uncontrolled or unspecified: friction dependency on temperature and load, influence of the room temperature and pressure, evolution of parameters according to mechanical constraints and wear of the structure.

Numerical uncertainties deal with roundoff errors or truncations coming from:

- Measurement errors: calibration errors, measurement noises (from position sensors and current measurements),
- Computing errors: discretization and convergences errors, machine precision,
- Roundoff errors: rounding of conventionally used constants (e.g. standard gravity).

In this thesis, we are interested in the uncertainties generating errors on the measured or estimated quantities that will be propagated during the computation of the robot's dynamic model. The main causes identified are parameter uncertainties and measurement noise, although other types of errors may be present but their contribution is assumed to be small in comparison. In order to quantify the effects of these uncertainties, the following section defines the most common probability distributions for the induced errors.

2.2.2 Probability distribution of uncertainties

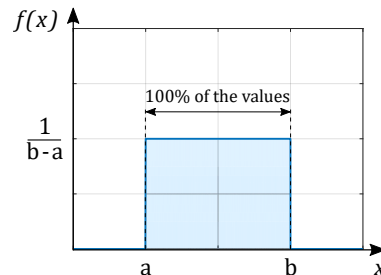
For this thesis, a *probabilistic approach* is sought, which consists in modeling the uncertainties effects as randomly-distributed noises and proposing a quantified characterization of their distribution based on the *probability theory*. Other approaches could be used for characterizing uncertainties, such as the fuzzy set theory which models uncertainties through fuzzy sets with membership functions [Klir 1995, Mendel 2001]. For instance, in [Song 2005], this technique is used for the control of a robot arm manipulator under uncertainties.

The stochastic model of a given type of uncertainty can be defined using data collected from repeated samples of similar experiments. Considering the form of the uncertainty distribution and the statistical characteristics extracted (e.g. arithmetic mean, standard deviation), a probability distribution is then assumed. Two types of laws are commonly used in probability theory to characterize uncertainties and will be detailed hereinafter: uniform (or rectangular) distribution and normal (or Gaussian) distribution. Others probability distributions may also be encountered, such as: exponential, Rayleigh, U-quadratic, triangular distributions, etc.

Uniform distribution

This distribution is adapted when the quantity of interest has the same probability of occurrence over a defined range: all outcomes are equally likely to occur. In this case, the probability distribution is characterized by the minimum and maximum boundaries a and b , and the Probability Density Function (PDF) of the continuous uniform distribution is:

$$f(x) = \begin{cases} \frac{1}{b-a} & \text{if } a \leq x \leq b, \\ 0 & \text{otherwise.} \end{cases}$$



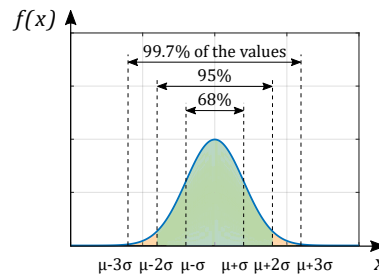
A random variable X following a uniform distribution with values in the interval $[a, b]$ is denoted $X \sim \mathcal{U}(a, b)$. The expected value of the distribution is $E[X] = (a + b)/2$ and the variance is $V[X] = (b - a)^2/12$.

The uniform distribution is used when no prior information is known about the parameter distribution (e. g. because it is unmeasurable), except its boundaries. The interval analysis relies on the uniform distribution by considering ranges of plausible values for the uncertain parameters and propagating the uncertainty intervals through a given mathematical model [Moore 1979, Jaulin 2001]. This approach is particularly convenient to evaluate the influence of tolerances and clearances and to deal with bounded roundoff errors. In particular, several works investigate the consequences of joint tolerances design, described by their upper and lower bounds, on the robot kinematic model [Merlet 2004, Wu 2007].

Normal distribution

This distribution is very common to describe the distribution of experimentally measured data. In this case, the probability distribution is characterized by the arithmetic mean value μ and the standard deviation σ , and the PDF of the continuous normal distribution is:

$$f(x) = \frac{1}{\sqrt{2\pi\sigma^2}} e^{-\frac{(x-\mu)^2}{2\sigma^2}}$$



A random variable X following a normal distribution with these characteristics is denoted $X \sim \mathcal{N}(\mu, \sigma)$. The expected value of the distribution is $E[X] = \mu$ and the variance is $V[X] = \sigma^2$.

The normal law is of first interest in probability theory since the *central limit theorem* establishes that the normalized sum of independent and/or identically distributed random variables approaches the normal distribution as the number of variables in the sum increases [Petrov 1995, Johnson 2004]. Consequently, an experimental measurement error will follow a normal distribution, providing that it results from many independent random errors. Generally, the average error is zero, but otherwise it may reflect a permanent bias in the measurement. For this reason, measurement errors in physical experiments are often modeled by a normal distribution. In the context of robotics, this approach is used for instance to model uncertain spatial representations for mobile robots [Smith 1990, Elfes 1990] or for robot grasping [Jiang 2012, Li 2016].

In the following, since we have assumed that parameter uncertainties represent the main source of errors, we examine in more detail the parameters involved in the robot dynamic model that can be sources of uncertainty. With regard to the determination of a probability law, a normal distribution is preferred in order to eventually design impact detection algorithms using Kalman filtering.

2.3 Parameter uncertainties

Among parameter uncertainties, two major contributions are identified: on the one hand, the robot dynamic model parameters and, on the other hand, the motor and joint positions and their derivatives. This section provides a review of existing methods for their determination and a methodology for quantifying the induced errors. Finally, the case of geometric model parameters is examined.

2.3.1 Dynamic model parameters estimation

At first, we assume a priori that the robot geometry is consistent with the nominal Computed-Aided Design (CAD) and that the manufacturing and assembly processes are accurate and generate few errors. Methods to refine the robot's geometric model are explained in more detail in Section 2.3.3.

The rigid dynamic model parameters of link and actuator j are divided into three categories. The notations used in the following are taken from [Khalil 2004].

1. The inertial parameters of the link:

- the mass of the link, including the actuators located on it, denoted M_{m_j} ,
- the elements of the inertia matrix \mathbf{I}_j of link j with respect to frame \mathcal{R}_j , such as:

$$\mathbf{I}_j = \begin{pmatrix} XX_j & XY_j & XZ_j \\ XY_j & YY_j & YZ_j \\ XZ_j & YZ_j & ZZ_j \end{pmatrix} = \begin{pmatrix} \int (y^2 + z^2) dm & - \int xy dm & - \int xz dm \\ - \int xy dm & - \int (x^2 + z^2) dm & - \int yz dm \\ - \int xz dm & - \int yz dm & \int (x^2 + y^2) dm \end{pmatrix}$$

- the first moments of link j with respect to frame \mathcal{R}_j and denoted MX_j , MY_j , MZ_j , such as:

$$[MX_j; MY_j; MZ_j]^T = M_{m_j} [XG_j; YG_j; ZG_j]^T$$

with XG_j , YG_j , ZG_j the Cartesian coordinates of the center of gravity G_j of link j in the frame \mathcal{R}_j .

2. The actuator inertia expressed at the joint side J_{m_j} ,

3. The friction parameters of the link: F_{v_j} and F_{s_j} for the viscous and dry friction parameters respectively.

For the flexible dynamic model parameters, the friction contributions from the joint (F_{va_j} , F_{sa_j}) and the motor (F_{vm_j} , F_{sm_j}) sides are distinguished and they are both expressed at the joint side. The elastic-joint stiffness K_j is an additional dynamic model parameter, together with the preload torque τ_{k0_j} .

For each joint j , these parameters are combined in the vectors ζ_{r_j} and ζ_{f_j} in the rigid and flexible cases respectively:

$$\zeta_{r_j} = [M_{m_j} \ XX_j \ XY_j \ XZ_j \ YY_j \ YZ_j \ ZZ_j \ MX_j \ MY_j \ MZ_j \ J_{m_j} \ F_{v_j} \ F_{s_j}]^T \quad (2.16)$$

$$\zeta_{f_j} = [M_{m_j} \ XX_j \ XY_j \ XZ_j \ YY_j \ YZ_j \ ZZ_j \ MX_j \ MY_j \ MZ_j \ F_{va_j} \ F_{sa_j} \ K_j \ \tau_{k0_j} \ J_{m_j} \ F_{vm_j} \ F_{sm_j}]^T \quad (2.17)$$

Finally, the dynamic parameters of a robot with n links are represented by the vectors ζ_r and ζ_f in the rigid and flexible cases respectively, such that:

$$\zeta_r = [\zeta_{r_1}^T \ \zeta_{r_2}^T \ \dots \ \zeta_{r_n}^T]^T \quad (2.18)$$

$$\zeta_f = [\zeta_{f_1}^T \ \zeta_{f_2}^T \ \dots \ \zeta_{f_n}^T]^T \quad (2.19)$$

2.3.1.1 Existing approaches

Several methods can be considered to obtain the dynamic model parameters. These methods differ in their implementation and post-processing time, in the instrumentation required and in the available results.

A first method consists in carrying out measurements for each individual body on a test bench before assembling the robot (or by disassembling it) as in [Armstrong 1986], but this approach can be tedious and requires very precise results. Another practice relies on the nominal CAD model of the robot, which allows to retrieve the complete inertial parameters. However, the 3D model of the robot is not always given by the robot manufacturer or certain approximations on the assembly are made, such as neglected mechanical parts or cable routine, which can be subject to errors.

In other cases, the experimental identification of the dynamic model parameters provides the most accurate values for the robot as it is actually assembled. For this purpose, the input/output behavior of the robot is collected during planned trajectories and the dynamic parameters are estimated by minimizing the difference between a given mathematical model and its computation in function of the measured robot variables. A large variety of methods exist and the choice of a suitable technique can be guided according to: the experimental setup (offline or online [Flacco 2011], open- or closed-loop [Gautier 2013b], robot instrumentation [Janot 2011], multivariable or monovariable axis-by-axis [Pham 2001]), the identification method (time-domain or frequency-domain [Makarov 2012], parametric or nonparametric [Camoriano 2016], black-box or gray-box approaches [Wernholt 2011]), the purpose (control scheme, local use [Villagrossi 2013] or over the entire workspace) and the physical characteristics of the robot (linear or non-linear models, rigid or elastic joints [Albu-Schäffer 2001], friction models [Kermani 2007], axis coupling). Most of these techniques can be combined, offering a wide spectrum of possibilities.

For the following, the methodology based on an experimental identification of the dynamic model parameters is detailed since it was found to be the best trade-off between the ease of experimentation and the precision of the resulting values.

2.3.1.2 Methodology under consideration

Property 2.3 *The left-hand member of the RDM (equation (2.2)) and the FDM (equation (2.9)) can be rewritten in a linear form with respect to the physical parameters of the robot defined at the beginning of Section 2.3.1.*

In the rigid case, this leads to:

$$\phi_r(\mathbf{q}, \dot{\mathbf{q}}, \ddot{\mathbf{q}}) \chi_r = \boldsymbol{\tau} + \boldsymbol{\tau}_{ext} \quad (2.20)$$

where $\phi_r(\mathbf{q}, \dot{\mathbf{q}}, \ddot{\mathbf{q}}) \in \mathbb{R}^{n, N_r}$ is the rigid regression matrix and $\chi_r \in \mathbb{R}^{N_r}$ is the vector of the rigid base parameters. As described in [Gautier 1990, Khalil 2004], the base parameters constitute the minimum set of parameters that completely characterize the robot dynamic behavior. They are obtained from the dynamic model parameters ζ_r described previously by eliminating those that have no effect on the dynamic model and by linearly regrouping some others.

In the flexible case, it yields:

$$\phi_f(\mathbf{q}, \dot{\mathbf{q}}, \ddot{\mathbf{q}}, \boldsymbol{\theta}, \dot{\boldsymbol{\theta}}, \ddot{\boldsymbol{\theta}}) \chi_f = \begin{pmatrix} \boldsymbol{\tau}_{ext} \\ \boldsymbol{\tau} \end{pmatrix} \quad (2.21)$$

with $\phi_f(\mathbf{q}, \dot{\mathbf{q}}, \ddot{\mathbf{q}}, \boldsymbol{\theta}, \dot{\boldsymbol{\theta}}, \ddot{\boldsymbol{\theta}}) \in \mathbb{R}^{2n, N_f}$ the flexible regression matrix and $\chi_f \in \mathbb{R}^{N_f}$ the flexible base parameters.

More explicitly, it can be observed from equation (2.21) and from the reduced form of the FDM in equation (2.9) that:

$$\underbrace{\begin{pmatrix} \widetilde{\phi}_r(\mathbf{q}, \dot{\mathbf{q}}, \ddot{\mathbf{q}}) & D_{q-\theta} & -I & 0 & 0 & 0 \\ 0 & -D_{q-\theta} & I & D_{\ddot{\theta}} & D_{\dot{\theta}} & D_{\text{sign}(\dot{\theta})} \end{pmatrix}}_{\phi_f(\mathbf{q}, \dot{\mathbf{q}}, \ddot{\mathbf{q}}, \boldsymbol{\theta}, \dot{\boldsymbol{\theta}}, \ddot{\boldsymbol{\theta}})} \underbrace{\begin{pmatrix} \widetilde{\chi}_r \\ \chi_K \\ \chi_{\tau_{k0}} \\ \chi_{J_m} \\ \chi_{F_{vm}} \\ \chi_{F_{sm}} \end{pmatrix}}_{\chi_f} = \begin{pmatrix} \boldsymbol{\tau}_{ext} \\ \boldsymbol{\tau} \end{pmatrix} \quad (2.22)$$

where

- the motor-side contributions have been removed from $\phi_r(\mathbf{q}, \dot{\mathbf{q}}, \ddot{\mathbf{q}})$ and χ_r in the tilde notations $\widetilde{\phi}_r(\mathbf{q}, \dot{\mathbf{q}}, \ddot{\mathbf{q}})$ and $\widetilde{\chi}_r$,
- matrices $D_{q-\theta}$, $D_{\ddot{\theta}}$, $D_{\dot{\theta}}$ and $D_{\text{sign}(\dot{\theta})}$ are defined by $D_{var} = \text{diag}(var_1 \ var_2 \ \dots \ var_n) \in \mathbb{R}^{n, n}$ for $var \in \{q - \theta, \ddot{\theta}, \dot{\theta}, \text{sign}(\dot{\theta})\}$,
- the vectors of the associated parameters χ_K , $\chi_{\tau_{k0}}$, χ_{J_m} , $\chi_{F_{vm}}$ and $\chi_{F_{sm}}$ are defined by $\chi_{par} = [par_1 \ par_2 \ \dots \ par_n]^T$ for $par \in \{K, \tau_{k0}, J_m, F_{vm}, F_{sm}\}$.

Single elastic joint example

If we consider a single link rotating in the horizontal plane (hence without gravity) and actuated with a motor through an elastic joint coupling, and if we assume that Coriolis and centrifugal terms are negligible, then the FDM is reduced to:

$$M\ddot{q} + F_{va}\dot{q} + F_{sa}\text{sign}(\dot{q}) + K(q - \theta) - \tau_{k0} = \tau_{ext} \quad (2.23a)$$

$$J_m\ddot{\theta} + F_{vm}\dot{\theta} + F_{sm}\text{sign}(\dot{\theta}) - K(q - \theta) + \tau_{k0} = \tau \quad (2.23b)$$

where the same notation as in Figure 2.2 are used. Then the terms $\phi_f \in \mathbb{R}^{2,8}$ and $\chi_f \in \mathbb{R}^8$ of equation (2.21) are expressed as follows:

$$\phi_f = \begin{pmatrix} \ddot{q} & \dot{q} & \text{sign}(\dot{q}) & q - \theta & -1 & 0 & 0 & 0 \\ 0 & 0 & 0 & -(q - \theta) & 1 & \ddot{\theta} & \dot{\theta} & \text{sign}(\dot{\theta}) \end{pmatrix} \quad (2.24)$$

$$\chi_f = \left(M \quad F_{va} \quad F_{sa} \quad K \quad \tau_{k0} \quad J_m \quad F_{vm} \quad F_{sm} \right)^T \quad (2.25)$$

Note that other models than the dynamic model can be used for the identification phase, as long as they can be rewritten in a linear form with respect to the base parameters. For instance, we can mention the energy (or integral) model [Gautier 1988] that does not require the computation of the joint accelerations or the power model [Gautier 2013a] that avoids large errors for low-frequency varying parameters such as offsets.

In the following, indexes are removed for clearness reasons but developments are applicable to both the rigid and flexible cases. For the identification procedure, the linear form with respect to the base parameters in equation (2.20) (*rigid case*) or (2.21) (*flexible case*) is evaluated without any external disturbance at a sufficient number of points on exciting trajectories. The motor currents and positions (and joint positions if available) are measured, and the velocities and accelerations are computed offline by numerical derivation using a central difference algorithm to avoid any phase shift. This leads to the following system of overdetermined linear equations:

$$\mathbf{W}\boldsymbol{\chi} + \boldsymbol{\rho} = \mathbf{Y} \quad (2.26)$$

where, for r time samples along all the DOF ($r \gg N$), $\mathbf{W} \in \mathbb{R}^{r,N}$ is the observation matrix, $\boldsymbol{\rho} \in \mathbb{R}^r$ is the vector of errors due to noisy measurements and modeling errors and $\mathbf{Y} \in \mathbb{R}^r$ is the vector of torque measurements.

Assuming that $\boldsymbol{\rho}$ is a zero-mean additive independent noise of standard deviation σ_ρ , the covariance matrix of $\boldsymbol{\rho}$ is denoted $\boldsymbol{\Sigma}_\rho \in \mathbb{R}^{r,r}$ and is defined by:

$$\boldsymbol{\Sigma}_\rho := E[\boldsymbol{\rho}\boldsymbol{\rho}^T] = \sigma_\rho^2 \mathbf{I}_r \quad (2.27)$$

where $E[\cdot]$ is the expectation operator and \mathbf{I}_r is the $(r \times r)$ identity matrix.

An unbiased estimation of σ_ρ can be calculated using the following equation:

$$\hat{\sigma}_\rho^2 = \frac{\|\mathbf{Y} - \mathbf{W} \hat{\boldsymbol{\chi}}\|^2}{r - N} \quad (2.28)$$

where $\hat{\boldsymbol{\chi}}$ is the Least-Squares (LS) solution of equation (2.26) which is the most widespread resolution method. Nonetheless, alternative solutions have been proposed, such as maximum-likelihood parameter estimation [Swevers 1997], linear matrix inequalities [Sousa 2014], extended Kalman filtering [Gautier 2001] or machine learning [Tu 2018].

The determination of the optimal trajectories, also called *persistently exciting trajectories*, aims at increasing the parameters excitation to improve the convergence rate and the noise immunity of the estimation. Two procedures can be applied:

- Determining sequential sets of trajectories that stimulate specific dynamic parameters. For instance, the dynamic parameters can be identified link by link by moving some joints while blocking the other ones, starting from the last link to avoid cumulative errors due to the block-triangular form of \mathbf{W} . In a similar approach, when shoulder and wrist contributions can be decoupled, associated parameters can be identified in two stages to address the difference in the order of magnitude. Another technique consists in dividing the base parameters in groups (e. g. inertial, gravity, friction) and defining characteristic trajectories that stimulate only one group of parameters at a time [Vandanjon 1995].
- Calculating exciting trajectories by minimizing a criterion to define. Since the sensitivity of the solution with respect to modeling errors and noise can be measured by the condition number of the observation matrix, a widely used optimization criterion is the minimization of the conditioning of \mathbf{W} [Presse 1993]. Other approaches rely on the minimization of the uncertainties on the parameter estimates as in [Swevers 1997] with a maximum-likelihood estimator.

In order to deal with the problem of heterogeneous measurements between the different axes and experiments, a Weighted Least-Squares (WLS) formulation of the system (2.26) can be used [Gautier 2001]. For this purpose, for each experiment and each joint, we consider the subsystem $\mathbf{W}_s \boldsymbol{\chi} + \boldsymbol{\rho}_s = \mathbf{Y}_s$ composed only of the associated equations, where s refers to the subsystem number. Based on this subsystem, the standard deviation $\hat{\sigma}_{\rho_s}$ of the corresponding error is calculated separately using equation (2.28). Then the r_s equations of the subsystem s are weighted by a factor $1/\hat{\sigma}_{\rho_s}$. The global system of weighted equations is written as follows:

$$\mathbf{W}_w \boldsymbol{\chi} + \boldsymbol{\rho}_w = \mathbf{Y}_w \quad (2.29)$$

where the weighted matrices \mathbf{W}_w , $\boldsymbol{\rho}_w$ and \mathbf{Y}_w are obtained with:

$$\mathbf{W}_w = \mathbf{G} \mathbf{W}, \quad \boldsymbol{\rho}_w = \mathbf{G} \boldsymbol{\rho}, \quad \mathbf{Y}_w = \mathbf{G} \mathbf{Y} \quad \text{and} \quad \mathbf{G} = \text{diag} \left(\frac{1}{\hat{\sigma}_{\rho_1}} \mathbf{I}_{r_1} \quad \dots \quad \frac{1}{\hat{\sigma}_{\rho_{n_s}}} \mathbf{I}_{r_{n_s}} \right) \quad (2.30)$$

with $\mathbf{G} \in \mathbb{R}^{r,r}$ the diagonal matrix containing the weights for each subsystem and n_s the total number of subsystems.

The solution $\boldsymbol{\chi}_\star$ of equation (2.29) is obtained by LS minimization of the 2-norm of the weighted errors vector $\boldsymbol{\rho}_w$. Assuming that \mathbf{W}_w is full column rank, the explicit solution $\boldsymbol{\chi}_\star$ is given by:

$$\boldsymbol{\chi}_\star := \min_{\boldsymbol{\chi}} \|\boldsymbol{\rho}_w\|^2 = \mathbf{W}_w^+ \mathbf{Y}_w \quad (2.31)$$

with $\mathbf{W}_w^+ = (\mathbf{W}_w^T \mathbf{W}_w)^{-1} \mathbf{W}_w^T$ the pseudo-inverse matrix of \mathbf{W}_w .

2.3.1.3 Characterization of associated errors

Let $\boldsymbol{\delta\chi}$ be the vector of estimation errors such as:

$$\boldsymbol{\delta\chi} := \boldsymbol{\chi}_\star - \boldsymbol{\chi} \quad (2.32)$$

For instance, given the definition of $\boldsymbol{\chi}_f$ in equation (2.25) for the single elastic joint example, in this case $\boldsymbol{\delta\chi}_f = \left(\delta M \quad \delta F_{va} \quad \delta F_{sa} \quad \delta K \quad \delta \tau_{k0} \quad \delta J_m \quad \delta F_{vm} \quad \delta F_{sm} \right)^T$. Assuming that \mathbf{W} is deterministic, the covariance matrix $\boldsymbol{\Sigma}_\chi \in \mathbb{R}^{N,N}$ of the estimation error $\boldsymbol{\delta\chi}$ is given by:

$$\boldsymbol{\Sigma}_\chi := E[\boldsymbol{\delta\chi} (\boldsymbol{\delta\chi})^T] = \hat{\sigma}_\rho^2 (\mathbf{W}^T \mathbf{W})^{-1} = (\mathbf{W}_w^T \mathbf{W}_w)^{-1} \quad (2.33)$$

The standard deviation of the i^{th} base parameter is given by $\sigma_{\chi_i} = \sqrt{\Sigma_{\chi_{ii}}}$ where $\Sigma_{\chi_{ii}}$ is the i^{th} diagonal component of $\boldsymbol{\Sigma}_\chi$. The relative standard deviation $\% \sigma_{\chi_i}$ of the i^{th} base parameter is defined by:

$$\% \sigma_{\chi_i} = 100 \frac{\sigma_{\chi_i}}{|\chi_{\star_i}|} \quad (2.34)$$

The relative standard deviation $\% \sigma_{\chi_i}$ is used as a criterion to measure the identification quality of the i^{th} base parameter. According to [Khalil 2004], the identification of a given parameter is considered acceptable if its relative standard deviation is less than ten times the minimum of the relative standard deviations. Thus, the identification procedure can be considered acceptable if the following condition is satisfied: $\frac{\max(\% \sigma_\chi)}{\min(\% \sigma_\chi)} < 10$.

In the following, the error vector $\boldsymbol{\delta\chi}$ on the dynamic model parameters is supposed to follow a normal distribution, of zero mean and standard deviation $\boldsymbol{\sigma}_\chi$. Assuming that the error on each dynamic parameter is not correlated with the others, then the covariance matrix $\boldsymbol{\Sigma}_\chi$ is approximated by:

$$\boldsymbol{\Sigma}_\chi = \text{diag} \left(\sigma_{\chi_1}^2 \quad \dots \quad \sigma_{\chi_N}^2 \right) \quad (2.35)$$

Applicative case

In order to evaluate the impact detection and classification algorithms in simulation and experimentation, the entire identification procedure has been applied to the ISYBOT prototype robot to estimate its dynamic model parameters and the associated uncertainties. The detailed results are presented in [Appendix B – Section B.3](#).

By propagating the errors on the base parameters to each contribution of the dynamic model, we can express the resulting error induced by the parameter errors. For instance, the resulting error on the rigid inertia matrix is denoted $\delta M_r(\mathbf{q})$ and is defined by:

$$\delta M_r(\mathbf{q}) := M_{r_\star}(\mathbf{q}) - M_r(\mathbf{q}) \quad (2.36)$$

with $M_{r_\star}(\mathbf{q})$ and $M_r(\mathbf{q})$ the rigid inertia matrix evaluated with the identified parameters and with the exact parameters respectively. Then, in the rigid case, by subtraction of the RDM rewritten as a linear regression with respect to χ_{r_\star} :

$$M_{r_\star}(\mathbf{q})\ddot{\mathbf{q}} + \mathbf{C}_\star(\mathbf{q}, \dot{\mathbf{q}})\dot{\mathbf{q}} + \mathbf{G}_\star(\mathbf{q}) + \mathbf{F}_{v_\star}\dot{\mathbf{q}} + \mathbf{F}_{s_\star}\text{sign}(\dot{\mathbf{q}}) = \phi_r(\mathbf{q}, \dot{\mathbf{q}}, \ddot{\mathbf{q}})\chi_{r_\star} \quad (2.37)$$

with the same rewriting with respect to the exact parameters χ_r in equation (2.20), it yields:

$$\delta M_r(\mathbf{q})\ddot{\mathbf{q}} + \delta \mathbf{C}(\mathbf{q}, \dot{\mathbf{q}})\dot{\mathbf{q}} + \delta \mathbf{G}(\mathbf{q}) + \delta \mathbf{F}_v\dot{\mathbf{q}} + \delta \mathbf{F}_s\text{sign}(\dot{\mathbf{q}}) = \phi_r(\mathbf{q}, \dot{\mathbf{q}}, \ddot{\mathbf{q}})\delta \chi_r \quad (2.38)$$

An equivalent formulation can be found in the flexible case. These formulations will be used in the subsequent design of impact detection algorithms to characterize the errors induced by uncertainties in the robot dynamic parameters (see [Chapter 3: "Design of impact detection strategies under model uncertainties"](#)).

2.3.2 State calculation

To evaluate the dynamic behavior of the robot, the knowledge of its position, velocity and acceleration is required. Depending on the method used to measure or calculate them, their knowledge will be more or less accurate, hence the resulting errors will be different.

2.3.2.1 Existing approaches

Depending on available instrumentation and computational load, several solutions can be employed to determine the complete state of the robot. Most of the time, a trade-off has to be found between noise reduction, estimate accuracy, reliability and bandwidth.

A first option is to integrate specific sensors on the robot for direct measurements. For instance, tachometer and gyroscope can be used for measuring linear and angular velocities but accelerations are not directly available [Lee 2009]. Accelerometers can measure accelerations, and when integrated in an inertial measurement unit (IMU), positions and velocities can be retrieved by integration [De Luca 2007]. But in addition to cost and integration constraints, these sensors suffer from accumulated errors which, when integrated, result in estimates that drift over time.

When only position measurements are available, existing methods for estimating or approximating the time derivative of the position signal fall into two categories: model-based methods and data processing algorithms.

On the one hand, among model-based methods, deterministic state observers (e.g. Luenberger observers) can be used for velocity estimation [Yang 2000]. When the parameters of the system model and the statistical attributes of the disturbance are known to a certain accuracy, stochastic Kalman filters can be used as optimal state estimators of velocity and acceleration. In [Belanger 1992], joint motions are modeled as the outputs of independent linear Kalman filters driven by white noise, whereas [Brunot 2016] proposes a state-space estimation based on Kalman filtering and fixed interval smoothing. An extended Kalman filter (EKF) taking into account the non-linear dynamics of the robot is also investigated in [Lightcap 2010]. A particular formulation called the kinematic Kalman filter (KKF) relies on the robot kinematic model for velocity and acceleration estimation [Jeon 2010, Kirchoff 2018]. However, since the adjustment of the covariance matrix of process noise can be tedious, the stability and convergence of the Kalman filter is not always guaranteed. Hence, velocity observers with global convergence for non-linear systems such as multi-axis robotic arms are still an open issue. Other techniques rely on the robot dynamic model, such as fuzzy logic [Yusivar 1999] or neural networks-based approaches [Chan 1998, Kim 2001], but these methods are strongly context-dependent. Moreover, their performances significantly rely on the accuracy of the robot dynamic model and on the accurate knowledge of external disturbances, which is precisely the challenge for impact detection.

On the other hand, data processing algorithms provide a predictive estimation based on the past signal with the advantage of being model-free. The most basic approach is the numerical differentiation from Taylor series because the computation load is low [Brown 1992]. Since the differentiation process is noise amplifying, usually low-pass filters are used in addition to derivative filters for noise reduction. To deal with the numerical differentiation limitations (phase distortion, delay, poor accuracy for low velocity at short sampling time), adaptive windowing techniques can be used to adjust the size of the time window such that all position estimation errors within the selected window lie inside a tolerance band [Janabi-Sharifi 2000, Kilic 2010]. To another extent, least-squares methods can be used to fit a low-order polynomial function through a given number of position data as in [Merry 2010]. Therefore the velocity and acceleration are simply deduced by evaluating the derivative of the polynomial function at the most recent data point. However, these smoothing techniques may suffer from tracking errors or amplitude attenuation. To avoid this, it is necessary to use a small window length, which, on the other hand, leads to poor noise attenuation capabilities. In case of periodic signals, the approach proposed by [Swevers 2007] consists in computing the position signal in the frequency domain using the Fourier transform, isolating the spectrum of interest by removing the frequencies related to noise, and then deriving the resulting signal. Nevertheless, this method cannot be applied for any arbitrary trajectory.

In an industrial context, when only position sensors are integrated into the robot, velocities and accelerations are often approximated by finite differences from Taylor series instead of being estimated by observers. Therefore state calculation by numerical differentiation is considered in this study, with the objective of quantifying the induced errors for the velocity and acceleration estimation.

2.3.2.2 Methodology under consideration

When position measurements are provided by a digital sensor, the digitization process involves two main limitations:

- The sensor resolution is finite: the measured output can only take defined values, although the actual current position may lie between two adjacent states.
- The sample time is finite: the information can only be measured at regular time intervals, but the true motion between samples cannot be known.

An example of digital signal can be observed in [Figure 2.3](#). The difference between the digital and the exact signals is referred to as *quantization error*. The smaller the resolution and the sampling time, the higher the accuracy of the position measurement.

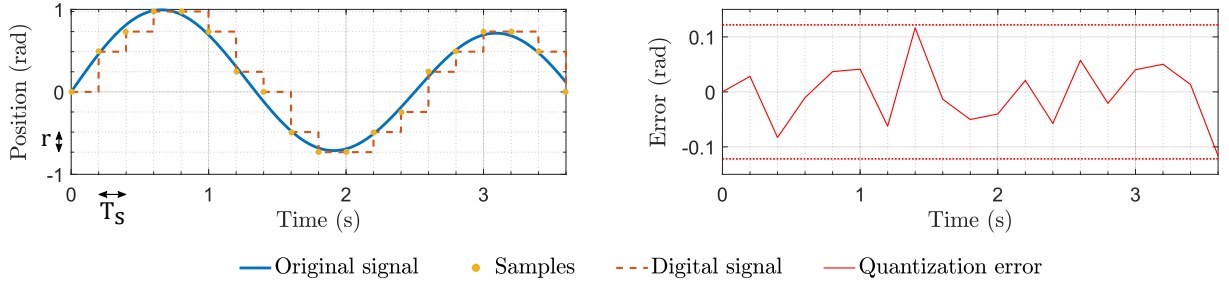


Figure 2.3: Example of a continuous position and corresponding digital signal (sampled and quantified) obtained at a sampling time T_s with a sensor resolution r .

The challenge then consists in retrieving the speed and acceleration information from the digital position measurement. Many methods exist for numerical approximation of the derivation based on finite difference developments from Taylor series [[Puglisi 2015](#)]. The most elementary is the Euler formula of order 1, but it tends to amplify high-frequency noise.

For this thesis, a first-order low-pass filtered derivative is considered for noise attenuation, which continuous-time expression $H_c(s)$ in the Laplace-domain is given by:

$$H_c(s) = \frac{s}{1 + \frac{1}{\omega_c} s} \quad (2.39)$$

where s is the Laplace variable and ω_c the cut-off frequency. The discretization by bilinear transform leads to the discrete filter $H_d(z)$, such as:

$$H_d(z) = a_0 \frac{1 - z^{-1}}{1 - b_1 z^{-1}} \quad (2.40)$$

with z the discrete variable, $a_0 = (d\omega_c)/(1 + d)$, $b_1 = (d - 1)/(d + 1)$ and $d = 2/(\omega_c T_s)$.

Finally, this is equivalent to the following time-domain equation:

$$y_k = a_0 (u_k - u_{k-1}) + b_1 y_{k-1} \quad (2.41)$$

where y is the approximate derivative of u . Filter $H_d(z)$ is part of the class of infinite impulse response (IIR) filters.

Figure 2.4 compares in the frequency domain the low-pass first-order derivative filter for two distinct cut-off frequencies. We note that when the cut-off frequency decreases, the measurement noise is more filtered but the approximate derivative further deviates from the exact derivation (amplitude distortion). It is also observed that the smoother the estimate (smaller cut-off frequency), the longer the time delay that is introduced by the filter (phase lag). Therefore the cut-off frequency must be set accordingly with the trajectory dynamics, the noise level and the sampling time. The following section focuses on quantifying the error induced by the numerical derivation filter approximating the exact derivative.

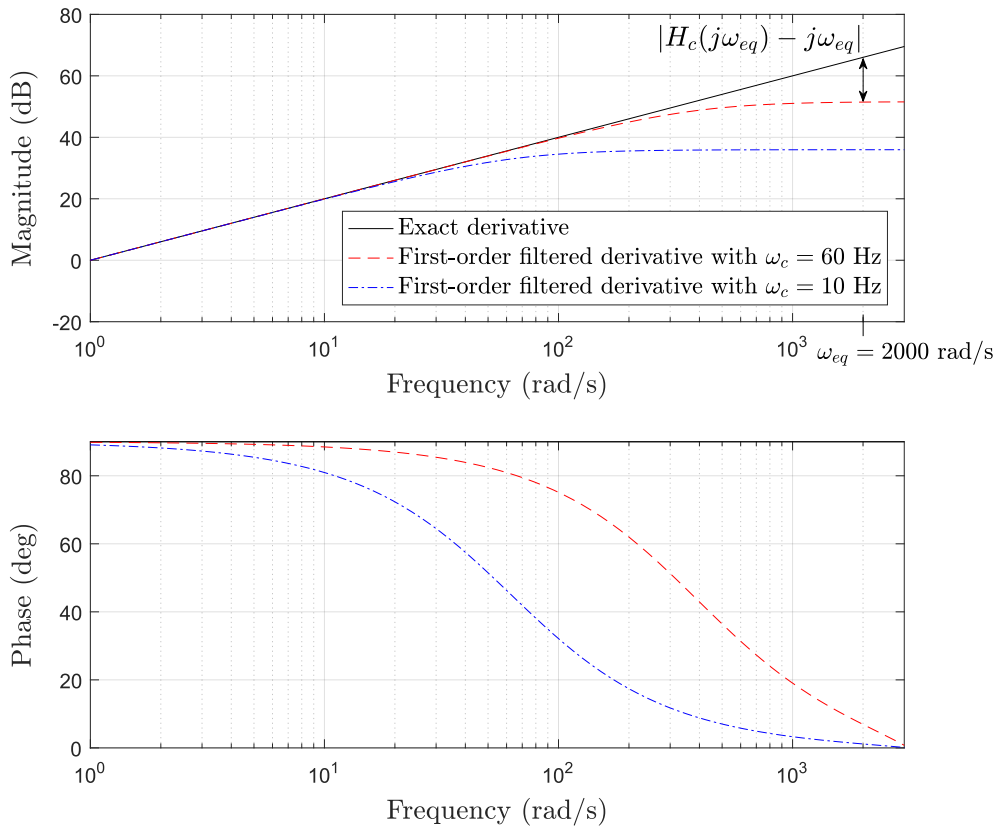


Figure 2.4: Frequency responses of exact derivative and first-order low-pass filtered derivative with $\omega_c = 2\pi 10$ rad/s and $\omega_c = 2\pi 60$ rad/s for a sampling time of $T_s = 1$ ms. The error in magnitude between the exact derivative and the filter output is illustrated for a frequency $\omega_{eq} = 2000$ rad/s.

2.3.2.3 Characterization of associated errors

The upcoming developments are presented for the joint variable \mathbf{q} but apply identically to the motor variable $\boldsymbol{\theta}$. We denote \mathbf{q}_\star the vector of the measured joint positions. Regardless of the selected numerical differentiation filter, we define $\dot{\mathbf{q}}_\star$ and $\ddot{\mathbf{q}}_\star$ respectively the joint velocities and accelerations obtained by numerical differentiation of \mathbf{q}_\star . The vectors of errors on joint velocities $\delta\dot{\mathbf{q}}$ and acceleration $\delta\ddot{\mathbf{q}}$ are given by:

$$\delta\dot{\mathbf{q}} := \dot{\mathbf{q}}_\star - \dot{\mathbf{q}} \quad (2.42)$$

$$\delta\ddot{\mathbf{q}} := \ddot{\mathbf{q}}_\star - \ddot{\mathbf{q}} \quad (2.43)$$

Under experimental conditions, the position measured from the sensor is inevitably noisy, due in particular to quantization but also to other potential sources (electrical, thermal, etc.). Consequently, the measured position is expressed as:

$$\mathbf{q}_\star = \mathbf{q} + \boldsymbol{\xi}_q \quad (2.44)$$

where $\boldsymbol{\xi}_q \in \mathbb{R}^n$ collects the noise on the position measurement. In the absence of additional information, the error $\boldsymbol{\xi}_q$ can be assumed to follow a zero-mean uniform distribution (e. g. in case of pure quantization), such that $-r_j/2 \leq \xi_{q_j} \leq r_j/2$ where r_j is the resolution of the position sensor j (see Figure 2.3). According to the properties on the uniform probability distribution stated in Section 2.2.2, the covariance matrix $\boldsymbol{\Sigma}_{\boldsymbol{\xi}_q} \in \mathbb{R}^{n,n}$ of the measurement noise is given by:

$$\boldsymbol{\Sigma}_{\boldsymbol{\xi}_q} := E[\boldsymbol{\xi}_q (\boldsymbol{\xi}_q)^T] = \text{diag} \left(\frac{r_1^2}{12} \quad \dots \quad \frac{r_n^2}{12} \right) \quad (2.45)$$

The characterization of errors on velocity and acceleration estimates induced by numerical differentiation is addressed in the Laplace domain. For axis j , we define $\xi_{q_j}(s)$, $Q_j(s)$, $\Delta Q_{d_j}(s)$ and $\Delta Q_{dd_j}(s)$, the Laplace transforms of ξ_{q_j} , q_j , $\delta\dot{q}_j$ and $\delta\ddot{q}_j$ respectively. Based on equations (2.42) and (2.44), the Laplace transform $\Delta Q_{d_j}(s)$ is given by:

$$\Delta Q_{d_j}(s) = \underbrace{[H_c(s) - s] Q_j(s)}_{\text{approximated velocity-induced error}} + \underbrace{H_c(s) \xi_{q_j}(s)}_{\text{filtered noise}} \quad (2.46)$$

Similarly, the Laplace transform $\Delta Q_{dd_j}(s)$ is given by:

$$\Delta Q_{dd_j}(s) = \underbrace{[H_c(s)^2 - s^2] Q_j(s)}_{\text{approximated acceleration-induced error}} + \underbrace{H_c(s)^2 \xi_{q_j}(s)}_{\text{filtered noise}} \quad (2.47)$$

For both the velocity and the acceleration, the source of errors due to numerical differentiation is twofold: one part is due to the derivative approximation and the other one is due to the measurement noise filtered by the numerical differentiation scheme, where only the first contribution depends on the robot's trajectory. Below we propose an approach to characterize the induced errors.

We treat separately the two contributions to the resulting errors:

1. We first consider the term due to the derivative approximation in velocity estimates, corresponding to the transfer function $[H_c(s) - s]$ between the exact position input and its filtered derivative error output. For a given trajectory characterized by velocities bounded by \mathbf{v}_{max} and accelerations bounded by \mathbf{a}_{max} , the trajectory for axis j can be approximated for analysis purposes by an equivalent sinusoidal signal of amplitude $A_{eq_j} = v_{max_j}^2/a_{max_j}$ and pulsation $\omega_{eq_j} = a_{max_j}/v_{max_j}$. Therefore, the term due to the derivative approximation in velocity estimates can be bounded by:

$$A_{d_j} = A_{eq_j} \left| H_c(j\omega_{eq_j}) - j\omega_{eq_j} \right| \quad (2.48)$$

In Figure 2.4, the term $\left| H_c(j\omega_{eq_j}) - j\omega_{eq_j} \right|$ is illustrated for $\omega_{eq} = 2000$ rad/s and with a filter cut-off frequency of $\omega_c = 2\pi 60$ rad/s. The term due to the derivative approximation in acceleration estimates is similarly bounded by:

$$A_{dd_j} = A_{eq_j} \left| H_c(j\omega_{eq_j})^2 - (j\omega_{eq_j})^2 \right| \quad (2.49)$$

If the consideration of \mathbf{v}_{max} and \mathbf{a}_{max} is too conservative (e. g. in the case of a triangular trajectory with brief acceleration peaks), then \mathbf{A}_d and \mathbf{A}_{dd} can be evaluated over a sliding time window.

2. Then we consider the term due to the filtered measurement noise in velocity estimates for the j^{th} axis. In discrete time, if the input noise ξ_{q_j} is white of variance $\sigma_{q_j}^2 = \Sigma_{q_{jj}}$ where $\Sigma_{q_{jj}}$ is the j^{th} diagonal component of $\Sigma_{\mathbf{q}}$, the output noise filtered by $H_d(z)$ (of impulse response $h[k]$) is Gaussian of variance $\sigma_{d_j}^2$ such as:

$$\sigma_{d_j}^2 = \sigma_{q_j}^2 \sum_{k=-\infty}^{\infty} h^2[k] = \sigma_{q_j}^2 \int_{-1/2}^{1/2} |H_d(\nu)|^2 d\nu \quad (2.50)$$

For the first-order low-pass filtered derivative, we obtain:

$$\sigma_{d_j}^2 = \sigma_{q_j}^2 \frac{2a_0^2}{1+b_1} \quad (2.51)$$

with a_0 and b_1 defined in (2.40). We proceed similarly for the acceleration estimates to find the output noise variance $\sigma_{dd_j}^2$.

The ultimate objective is to determine the maximum contribution of uncertainties in order to discriminate their effects from an actual contact. For the approximated velocity, we consider that $\delta\dot{\mathbf{q}}$ can be bounded by $\pm(\mathbf{A}_d + 3\sigma_d)$ using the 3σ -confidence interval of the normal distribution of σ_d that covers 99.7% of the values (see Section 2.2.2). Therefore, for analysis purposes and with the objective to ultimately study the 3σ -confidence interval of the overall uncertainties, the boundary on $\delta\dot{\mathbf{q}}$ is related to a standard deviation $\sigma_{\dot{\mathbf{q}}}$ such as $3\sigma_{\dot{\mathbf{q}}} = \mathbf{A}_d + 3\sigma_d$. We proceed similarly for the approximated acceleration to determine the standard deviation $\sigma_{\ddot{\mathbf{q}}}$ such as $3\sigma_{\ddot{\mathbf{q}}} = \mathbf{A}_{dd} + 3\sigma_{dd}$.

In the following, the error vectors $\delta\dot{\mathbf{q}}$ and $\delta\ddot{\mathbf{q}}$ on the joint velocity and acceleration are supposed to follow a normal distribution, of zero mean and standard deviation $\sigma_{\dot{\mathbf{q}}}$ and $\sigma_{\ddot{\mathbf{q}}}$ respectively. Assuming that the error on each joint is not correlated with the others, then the covariance matrices $\Sigma_{\dot{\mathbf{q}}} \in \mathbb{R}^{n,n}$ and $\Sigma_{\ddot{\mathbf{q}}} \in \mathbb{R}^{n,n}$ of the errors on the approximated joint velocity and acceleration are respectively given by:

$$\Sigma_{\dot{\mathbf{q}}} := E[\delta\dot{\mathbf{q}}(\delta\dot{\mathbf{q}})^T] = \text{diag} \left(\left(\frac{A_{d1}}{3} + \sigma_{d1} \right)^2 \quad \dots \quad \left(\frac{A_{dn}}{3} + \sigma_{dn} \right)^2 \right) \quad (2.52)$$

$$\Sigma_{\ddot{\mathbf{q}}} := E[\delta\ddot{\mathbf{q}}(\delta\ddot{\mathbf{q}})^T] = \text{diag} \left(\left(\frac{A_{dd1}}{3} + \sigma_{dd1} \right)^2 \quad \dots \quad \left(\frac{A_{ddn}}{3} + \sigma_{ddn} \right)^2 \right) \quad (2.53)$$

In addition, we note that in practice, the noise $\xi_{\mathbf{q}}$ on the position measurement may have a Gaussian tendency due to a possible prior filtering (see [Appendix B – Section B.4.1](#) for the case of the ISYBOT prototype robot). In this case, the covariance matrix $\Sigma_{\mathbf{q}}$ can be deduced from the standard deviation vector $\sigma_{\mathbf{q}}$ obtained by experimental measurements and assuming that the error on each joint is not correlated with the others:

$$\Sigma_{\mathbf{q}} = \text{diag} \left(\sigma_{q1}^2 \quad \dots \quad \sigma_{qn}^2 \right) \quad (2.54)$$

Applicative case

Errors induced by the approximated velocities and accelerations have been characterized in the case of the ISYBOT prototype robot for the numerical derivation scheme implemented on the controller. The detailed results are presented in [Appendix B – Section B.4](#).

2.3.3 Geometric model parameters estimation

An accurate knowledge of the geometric parameters (essentially the Khalil-Kleininger parameters) is required not only for precisely positioning the end-effector in the Cartesian space, but also because geometric parameters intervene during the identification of the dynamic parameters through the calculation of the observation matrix (see [Section 2.3.1](#)), which thus affects the dynamic parameter estimation. Despite the fact that their nominal values are defined during the robot design stage, their actual values may differ. Possible causes of errors are listed in [[Judd 1990](#)], among which we can mention manufacturing and assembly tolerances, structural deformations due to the robot's own weight together with any carried load, non-ideal gear alignment, etc.

For this purpose, similarly as for the identification of dynamic parameters, the calibration procedure aims at estimating the robot geometric model by minimizing the difference between a function of the real robot variables and its mathematical model using measurements provided by the joint position sensors. The generalized differential model of the robot is used to express

a differential variation of the geometric parameters depending on a differential variation of the location of the end-effector [Khalil 2004]. The latter can be obtained by an external sensor (e. g. vision systems, measuring machines, laser interferometers, laser tracking systems, theodolites) or by imposing constraints on the position, location or motion of the robot end-effector. The interested reader can refer to [Khalil 2000a, Khalil 2002, Khalil 2004] for more details about the identification procedure for geometric parameters.

In this thesis, the contribution of errors due to geometric parameters has not been included in the design of algorithms for detecting and classifying impacts under uncertainties. If their contribution is not negligible compared to the other types of errors identified (dynamic model parameters and state coordinates), a possible extension of this work could include these uncertainties and their consequences on impact detection and classification algorithms.

2.4 Conclusion

This chapter introduced the general terminology of serial robot manipulators. The core models required for impact detection and classification were presented: the force/torque transmission model that determines the repercussion of an external force on the joint torques, and the dynamic model that describes the relation between the torque applied at the joints and the robot motion. The dynamic model was defined for the case of robots with rigid links and infinitely stiff joints and for robots with elastic joints.

For the purpose of impact detection and classification, an accurate knowledge of the robot dynamic model is necessary. Indeed, errors induced by uncertainties will contribute as additional noise with the same effects as an actual external contact, leading to false alarms during the detection phase and then to classification errors during the characterization phase. Consequently, an overview of all the potential sources of errors was established and, for parameters uncertainties identified as the main contribution, a stochastic approach was considered to characterize their distribution. For both the dynamic model parameters and the state coordinates, a methodology to obtain and characterize them was proposed among the various possible methods. This choice is based on the industrial and real-time constraints, that demand a minimum number of sensors and a small computational load. Nevertheless, other approaches would deserve to be verified and compared in terms of induced errors.

Once the errors on the modeling parameters have been determined and characterized, [Chapter 3: "Design of impact detection strategies under model uncertainties"](#) studies their propagation during the design of impact detection algorithms since the sensitivity and reactivity of these strategies depend directly on the amount of errors involved.

Design of impact detection strategies under model uncertainties

Contents

3.1	Related work	52
3.1.1	Impact detection strategies	52
3.1.2	Works explicitly addressing uncertainties	55
3.1.3	Positioning statement	57
3.2	Direct external torque estimation (DETE)	59
3.2.1	Residual generation	59
3.2.2	Residual evaluation	62
3.2.3	Illustration of the uncertainties contribution	66
3.2.3.1	Comparison of the parametric and numerical differentiation contributions	67
3.2.3.2	Validation of approximations	69
3.2.3.3	Interpretation of the error range	70
3.3	Disturbance observers design	71
3.3.1	State-space representations under uncertainties	71
3.3.1.1	Joint position and velocity observer (JPVO)	72
3.3.1.2	Generalized momentum observer (GMO)	74
3.3.2	Discretization and Kalman filter design	76
3.3.2.1	Sampled-time model for Kalman filter design	77
3.3.2.2	Sampled-time model for Kalman filter analysis	78
3.3.3	Evaluation of the estimated external torque	79
3.3.4	Discussion	84
3.4	Extension to robots with rigid links and elastic joints	87
3.4.1	Deficiencies of the rigid model	88
3.4.2	Extension of the direct external torque estimation (DETE)	89
3.4.3	Extension of the disturbance observers design	91
3.4.3.1	Extension of the joint position and velocity observer (JPVO)	91
3.4.3.2	Extension of the generalized momentum observer (GMO)	93
3.5	Qualitative comparison of the developed strategies	95
3.6	Conclusion	96

To comply with robotic safety standards, it is essential to be able to detect any contact of the robot with its environment in a short time and with high sensitivity. When only proprioceptive information from the robot is available, contact detection algorithms have to provide a relevant monitoring signal containing the contact signature to produce the alert signal while being robust to the modeling uncertainties.

This thesis focuses on model-based detection algorithms that rely on the general theory of Fault Detection and Isolation (FDI). In the special case of impact detection, the robotic models described in Chapter 2: "Modeling serial robot manipulators under uncertainties" are used to derive the monitoring signal. However, since the considered model uncertainties affect the monitoring signal in the same way as an external disturbance caused by an impact, they may trigger false alarms that would interfere with the smooth operation of the task. To address this issue, our approach consists in proposing new impact detection strategies based on the explicit contribution of model uncertainties and their stochastic characterization from the previous chapter. The methodology developed to render explicit the uncertainties contribution also provides a qualitative and quantitative evaluation tool to analyze and compare different impact detection methods that are subject to model uncertainties.

After introducing the related work in Section 3.1, the proposed approach is applied to two categories of model-based impact detection methods: detection by direct estimation of the external torque in Section 3.2 or by using linear disturbance observers in Section 3.3. The case of robots with perfectly rigid joints and links is first considered, but this approach is also adapted to the case of robots with rigid links and elastic joints in Section 3.4. Finally, Section 3.5 provides a qualitative summary of the developments obtained. Throughout the chapter, simulation results based on the ISYBOT prototype robot illustrate the methods developed.

3.1 Related work

3.1.1 Impact detection strategies

Fault diagnosis theory, particularly FDI schemes, provides a relevant framework for impact detection since a contact disrupts the normal operation of the robot, causes a sudden change in its state variables and can therefore be related to a faulty behaviour. The fault detection is decomposed into two steps: 1) *generation of a monitoring signal*, also called the *residual* and denoted \mathbf{r} in the following, that contains the fault signature, 2) *evaluation of this signal* by comparison with a threshold (see Figure 3.1). The objective of the first step is to generate a signal that reflects the occurrence of a contact (null without contact, non-zero in case of contact), while the second step triggers the detection alert indicating that an impact has actually occurred. This alert must be given with sufficient sensitivity to avoid any damage, but must avoid false detections. Additional information of interest for further reaction strategies may be provided (e.g. amplitude of the external force, localization of the contact on the robot...).

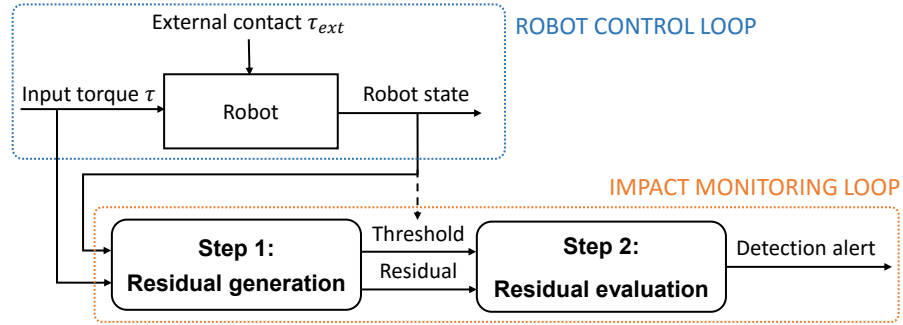


Figure 3.1: Steps of an impact detection algorithm based on fault diagnosis

Residual generation

The various methods for generating the residual can be classified into two categories: non-model-based and model-based methods.

Non-model-based methods rely on a direct evaluation of the characteristics of the signals involved in the control algorithm, such as the amplitude or the instantaneous variation of the position-tracking error or the applied motor torque τ . As an example, [Geravand 2013] proposes to monitor filtered versions of the motor currents on a KUKA KR5 manipulator with a closed control architecture. However, these approaches are directly related to the structure and tuning of the controller used and cannot be designed independently from the system control architecture.

In a different approach, model-based fault diagnostic methods developed in [Venkatasubramanian 2003, Ding 2008, Chen 2012] rely on mathematical models and can be used independently from the system control law. Any possible candidate for the monitoring signal in the specific case of impact detection must reflect the occurrence of an impact by being subject to rapid transients when a contact occurs somewhere on the robot structure and being null otherwise. The survey in [Haddadin 2017] provides an extensive comparison of several impact detection schemes, in terms of main advantages and disadvantages, required measurement quantities and computational effort. Among the proposed methods, some resort to a scalar energetic function, based either on the total energy of the robot or on its kinetic energy [De Luca 2006]. Another intuitive monitoring signal is the external torque τ_{ext} since it gathers the effects of an external wrench applied to the robot (see Chapter 2: "Modeling serial robot manipulators under uncertainties" – Section 2.1.2).

In the absence of dedicated sensors, the external torque τ_{ext} has to be reconstructed using only the proprioceptive information, referring to torque/force estimation techniques. One possibility is obtained by direct estimation of τ_{ext} using the IDM (this method is called Direct External Torque Estimation (DETE) in the following). In the case of robots with perfectly rigid links and joints, the residual generation amounts to comparing the actual motor torque τ with its nominal model-based prediction τ_\star without contact, with any difference being attributed to an external wrench [Haddadin 2008a]:

$$r = \tau_\star - \tau \quad (3.1)$$

The unknown torque τ_{ext} can also be estimated using a Disturbance Observer (DOB) in parallel with the robot control loop, the residual being in this case the estimated state $\hat{\tau}_{ext}$. In this case, the objective of using a DOB is not to attenuate or eliminate the influence of disturbances as for disturbance observer-based control or active disturbance rejection control [Chen 2016], but to monitor the deviations potentially caused by external forces [Frank 1997]. Although non-linear disturbance observers could be used e. g. in [Chen 2000], linear disturbance observers are usually preferred for their stability and reduced implementation cost. However in this case, it requires a linearised model that involves either inverting the inertia matrix $\mathbf{M}(\mathbf{q})$, which may be numerically and computationally demanding, or calculating the acceleration terms $\ddot{\theta}$ or $\ddot{\mathbf{q}}$ by two-times numerical differentiation of the position data, which is known for amplifying noise and introducing delay (see Chapter 2: "Modeling serial robot manipulators under uncertainties" – Section 2.3.2). A preferred approach circumventing these issues was first introduced in [De Luca 2003] under the following integral formulation of the residual:

$$\mathbf{r} = \mathbf{K} \left[\mathbf{p} - \int_0^t \left(\boldsymbol{\tau} + \mathbf{C}(\mathbf{q}, \dot{\mathbf{q}})^T \dot{\mathbf{q}} - \mathbf{G}(\mathbf{q}) + \mathbf{r} \right) ds - \mathbf{p}(0) \right] \quad (3.2)$$

It relies on the generalized momentum \mathbf{p} and a diagonal gain matrix \mathbf{K} , and it has been demonstrated that this is equivalent to a low-pass filtered version of the external torque τ_{ext} . It has been extensively covered since: in particular, a Fault Isolation Observer (FIO) interpretation of this approach is provided in [Wahrburg 2015a], while a state-space representation of the initial integral formulation is derived in [Wahrburg 2015b]. In [Van Damme 2011], this approach is compared to the filtering technique which also avoids the calculation of the acceleration term by filtering the robot dynamic equation with a stable and proper filter, combined with a recursive least-squares estimator.

Residual evaluation

Regardless of the model-based residual generation method, the residual may be affected by modeling uncertainties if the model parameters are not exactly known or are not properly adapted to the various operational conditions (e. g. payload variations). Since model uncertainties have similar effects on the residual as an actual contact, the objective of the residual evaluation is to discriminate faults due to model uncertainties from those due to a real external contact using an appropriate thresholding.

When modeling errors are relatively small in comparison with the expected detection sensitivity, a static threshold can be set above the residual maximum value that has been previously observed experimentally on robot motions for a sufficiently long time interval without any external disturbance [Haddadin 2017]. In a similar perspective, other methods are based on a frequency-domain distinction between the contribution of the real impact and the modeling uncertainties. More precisely, a filter bank that consists of appropriately designed low-pass and high-pass filters, leading to an overall band-pass filter behavior, can be used to eliminate from the residual on the one hand, the low-frequency components due to the robot motion such as the gravity force effect and on the other hand, undesirable high-frequency components due for instance to measurement noise [Song 2013] (see Figure 3.2).

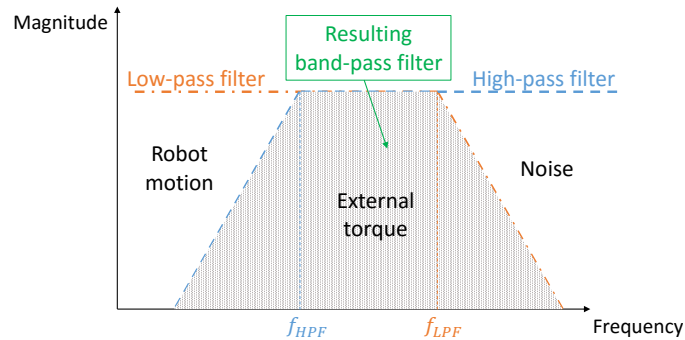


Figure 3.2: Band-pass filter for removing torques due to robot motion and noise [Song 2013]

These approaches involve tuning threshold values (maximum model uncertainties, cut-off frequencies, etc.) that are usually adjusted based on a certain number of measurements in the absence of disturbances. However, since the effects of model uncertainties directly depends on the robot’s trajectory, this approach is not systematic and is highly dependent on the experiments performed. Therefore, there is no guarantee that the obtained thresholds remain valid under new experimental conditions.

3.1.2 Works explicitly addressing uncertainties

If the effects of the uncertainties are significant in comparison with the contact forces involved, or if their dependence on operating conditions is substantial, further refinements of the previously mentioned methods are required. These can be performed either at the residual generation level, with a more precise estimate of the residual exempt from modeling errors, or during the residual evaluation with an uncertainties-dependent threshold.

Residual generation

Advanced estimation methods can be used to improve the contact torque/force estimate in presence of uncertainties. A method based on the minimum variance unbiased estimate of the external force and using prior knowledge on the variance of contact forces and disturbance joint torques is used in [Stolt 2012], where only joint position control errors are required. This approach has been extended in [Linderoth 2013] by characterizing the velocity-dependent uncertainties on the friction torques, which are assumed to be the main source of disturbing torques, in order to solve a complex optimization problem under constraints. In the same vein, [Wahrburg 2014] proposes a calibration procedure for the unknown covariance matrices to solve this type of optimization problem.

In another perspective, an approach based on linear Kalman filtering for estimating the contact force at the end-effector is investigated in [Wahrburg 2015b]. Indeed, the Kalman filter is considered as the optimal observer in presence of noises and, in this case, modeling uncertainties are approximated by Gaussian noises. This method is refined in [Wahrburg 2018] by proposing

an experimental characterization of state and noise covariance matrices. [Hu 2018] complements this approach by a prior semi-parametric identification of the dynamic model and compares the accuracy of the obtained force estimation with that of a non-linear disturbance observer and a generalized momentum-based observer. A method using an extended Kalman filter (EKF) is also proposed in [Jung 2006] based on simulation results.

Another category of approaches relies on online parameter estimation techniques. In [Dixon 2000], the torque filtering technique is augmented with an adaptive law that updates the robot parameters online instead of using constant best-guess parameter estimates. However, this adaptation has to be performed on a contact-free trajectory prior to the detection phase and must therefore be repeated each time the reference trajectory is changed. Simultaneous adaptation and detection phases are achieved in [Morinaga 2003] and [De Luca 2004], using respectively a non-linear adaptive impedance control law and an over-parametrization of the uncertain robot dynamics.

Data-driven approaches using learning techniques are also investigated in the general framework of FDI for robotic tasks. Their main advantage is their ability to model non-linear effects such as friction, elasticities or backlashes only from experimentally collected data. Supervised learning approaches based on neural networks are a first solution, as in [Popov 2017] where the results achieved with a feed-forward artificial neural network detecting contact events are compared with those obtained with a simple static thresholding technique. A Support Vector Machine (SVM) used in combination with a Principal Component Analysis (PCA) is exploited in [Rodriguez 2010] to learn a set of force signature models encoding the correlations between wrench measurements and successful or failed assembly tasks. In [Stolt 2015], several classifiers are compared, namely the least-squares method, SVM and boosting algorithm, with the objective of detecting transients in force/torque data in order to reduce the total assembly time. In another aspect, [Dimeas 2015] proposes to reconstruct the external torque using fuzzy parameters and rules trained on experimental data.

Residual evaluation

Model-based adaptive thresholding is another possibility to deal with uncertainties. For instance, a time-variant threshold is defined in [Sotoudehnejad 2012] that explicitly considers model errors in robot parameters but with a preliminary tuning process to adjust certain parameters on trajectories without contact. In [Wagner 2018], an interval-arithmetic-based approach is proposed to compute an interval within which the actual motor torque τ must lie in absence of contact.

The approaches mentioned above require an a priori knowledge of the uncertainties range. When unstructured disturbances are present, an adaptive fuzzy logic-based threshold can be of interest as in [Sneider 1996], but may require a large number of experiments to formulate the appropriate logic rules (see Figure 3.3). To avoid this limitation, a state-dependent dynamic threshold is considered in [Makarov 2014], based on a simplified linear modeling of the residual and using online estimation of filter coefficients to ensure the adaptation of the algorithm to different operating conditions.

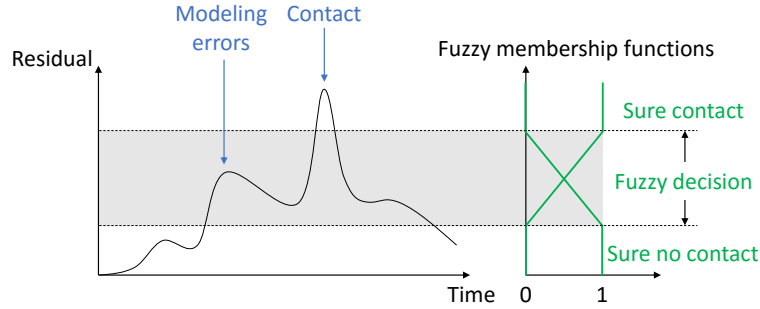


Figure 3.3: Adaptive threshold using fuzzy logic [Sneider 1996]

3.1.3 Positioning statement

In this thesis, a model-based approach is followed, which has the advantage of being independent from the control law architecture. Since only proprioceptive information is considered, the torque τ_{ext} induced by an external force F_{ext} applied to the robot is retrieved from the actual state of the robot and its nominal state in absence of contact. The robot actual state is given by the applied motor torque that can be measured from joint torque sensors or estimated from the motor currents in case of backdrivable actuator transmissions, while its nominal state is obtained from the robot dynamic model.

Nevertheless, this approach is subject to the trade-off between sensitivity of detection and robustness to model uncertainties. Although most works focus on friction uncertainties [Linderoth 2013, Wahrburg 2018], in the following developments all types of modeling inaccuracies are considered, i. e. uncertainties on dynamic model parameters, measurement noise, as well as errors on velocity and acceleration approximations.

The general approach of this work lies in developing a methodology to render explicit the model uncertainties associated with a given impact detection method. Once the specific composition of uncertainties is known, it is then possible to use the stochastic approach developed in the previous chapter to characterize their distribution and their associated error range $[-T, T]$ (see Figure 3.4). The limit T defines at each time step the maximum contribution of uncertainties and depends on the robot trajectory, the parametric uncertainties level, the measurement noise and the numerical approximation method for the derivation. Therefore, as soon as the residual exceeds this range, it means that there is necessarily an additional contribution due to a contact occurrence and, consequently, an alert signal is triggered. When the residual is below this threshold, the detection signal is disabled although it is possible that a contact may occur but with an amplitude too small to cross the threshold.

Finally, the limit T of the error range due to the associated uncertainties constitutes an appropriate detection threshold for the residual evaluation. In addition, this method allows to evaluate a given impact detection algorithm with regard to the uncertainties involved, to predict its performance along the robot's trajectory, and thus to compare it against concurrent detection approaches that involve a different composition of uncertainties.

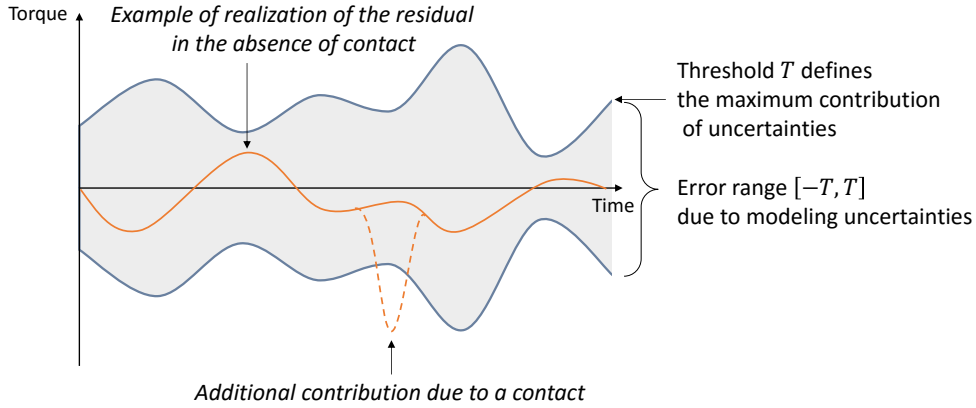


Figure 3.4: Adaptive threshold defined by the maximum contribution of uncertainties

In this respect, the proposed approach is applied to impact detection algorithms that rely either on direct estimation of τ_{ext} or on linear disturbance observers:

- In case of direct estimation of τ_{ext} (DETE-based method), the residual generation in equation (3.1) is extended by explicitly introducing the contribution of uncertainties. Associated confidence intervals are derived at each time step, defining the error margins due to uncertainties with a certain confidence level.
- In case of linear disturbance observers (DOB-based method), a linearised formulation of the IDM is derived and the contribution of the associated uncertainties is rendered explicit. The latter are then treated as noises to design a linear disturbance observer using a Kalman filter that will estimate the external torque τ_{ext} , similarly to [Wahrburg 2018]. Nonetheless, in our case, the covariance matrices of state and measurement noises are not empirically adjusted but stem from the characterization of the uncertainties developed in the previous chapter. Since covariance matrices are state-dependent, it results in a Kalman gain varying along the robot trajectory. The adaptive detection threshold is derived from the covariance matrix of the estimation error in absence of external torque.

For both methods, the approach is developed in the rigid and flexible cases. The proposed approach, as well as the sections corresponding to each case and method, is summarized in Table 3.1.

Method	Residual generation	Residual evaluation	Rigid case	Flexible case
DETE	$\mathbf{r} = \tau_{\star} - \tau$	Confidence intervals associated to the uncertainties contribution	Section 3.2	Section 3.4.2
DOB	$\mathbf{r} = \hat{\tau}_{ext}$	Confidence intervals associated to the estimation error in the absence of external torque	Section 3.3	Section 3.4.3

Table 3.1: Summary of the proposed methods and corresponding sections

3.2 Direct external torque estimation (DETE)

3.2.1 Residual generation

For this method, the residual is generated by the direct comparison between the estimated motor torque denoted $\tau_\star \in \mathbb{R}^n$ and the applied motor torque $\tau \in \mathbb{R}^n$ as defined in equation (3.1). While the applied motor torque τ can be directly measured if joint torque sensors are integrated or estimated from motor currents in case of backdrivable actuators (transmission efficiency close to 1), the estimated motor torque τ_\star has to be computed based on the IDM in absence of external torque (see Figure 3.5).

The RDM for robots with rigid links and joints is recalled below:

$$M_r(q) \ddot{q} + C(q, \dot{q}) \dot{q} + G(q) + F_v \dot{q} + F_s \text{sign}(\dot{q}) = \tau + \tau_{ext} \quad (3.3)$$

Then the estimated motor torque τ_\star is obtained by evaluating the RDM on the actual trajectory in absence of external torque and with the estimated model matrices and coordinates:

$$\tau_\star = M_{r\star}(q_\star) \ddot{q}_\star + C_\star(q_\star, \dot{q}_\star) \dot{q}_\star + G_\star(q_\star) + F_{v\star} \dot{q}_\star + F_{s\star} \text{sign}(\dot{q}_\star) \quad (3.4)$$

Note that the reference trajectory can also be used but with the risk of being affected by trajectory tracking errors depending on the controller performance.

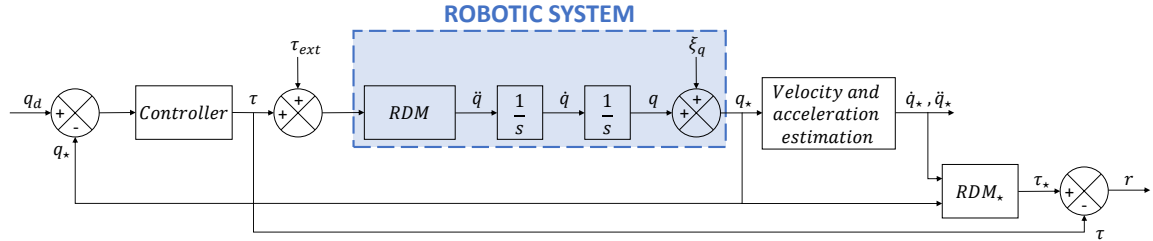


Figure 3.5: Block diagram of the residual generation step with exact and uncertain terms. RDM and RDM_\star refer to the rigid IDM evaluated respectively with the exact (equation (3.3)) and estimated (equation (3.4)) model matrices and coordinates. The reference position is denoted q_d .

Ideal case

If all the model terms and joint coordinates are accurately known, equation (3.4) becomes:

$$\tau_{\star_{ideal}} = M_r(q) \ddot{q} + C(q, \dot{q}) \dot{q} + G(q) + F_v \dot{q} + F_s \text{sign}(\dot{q}) \quad (3.5)$$

Consequently, according to equation (3.3), the residual verifies:

$$r = \tau_\star - \tau_{\star_{ideal}} = \tau_{ext} \quad (3.6)$$

Thus, in the case of a perfectly known model, the residual r is a relevant monitoring signal for impact detection since it is different from zero if there is an impact and always zero otherwise.

Realistic case under uncertainties

In practice, model terms and joint coordinates in equation (3.4) are known with errors. Consequently, the estimated motor torque τ_\star is affected by an error term $\delta\tau$, such as:

$$\tau_\star = M_r(q)\ddot{q} + C(q, \dot{q})\dot{q} + G(q) + F_v\dot{q} + F_s \text{sign}(\dot{q}) + \delta\tau \quad (3.7)$$

Then, the residual becomes:

$$r = \tau_\star - \tau_{\text{realistic}} = \tau_{\text{ext}} + \delta\tau \quad (3.8)$$

Therefore in the general case, even without contact, the residual may be non-zero due to the presence of modeling errors that depend on the robot's state and affect the residual in the same structural way as an actual contact. The term $\delta\tau$, which represents the accumulation of these errors, is now being made explicit. From equations (3.4) and (3.7), it follows:

$$\begin{aligned} \delta\tau = & [M_{r\star}(q_\star)\ddot{q}_\star + C_\star(q_\star, \dot{q}_\star)\dot{q}_\star + G_\star(q_\star) + F_{v\star}\dot{q}_\star + F_{s\star} \text{sign}(\dot{q}_\star)] \\ & - [M_r(q)\ddot{q} + C(q, \dot{q})\dot{q} + G(q) + F_v\dot{q} + F_s \text{sign}(\dot{q})] \end{aligned} \quad (3.9)$$

Let us first consider the errors induced by the uncertainties on the estimated rigid inertia torque $M_{r\star}(q_\star)\ddot{q}_\star$. From the definitions of errors formulated in the previous chapter, and more specifically using $\delta M_r(q) = M_{r\star}(q) - M_r(q)$ and $\delta\ddot{q} = \ddot{q}_\star - \ddot{q}$, it follows:

$$M_{r\star}(q_\star)\ddot{q}_\star - M_r(q)\ddot{q} = M_{r\star}(q_\star)\ddot{q}_\star - [M_{r\star}(q) - \delta M_r(q)][\ddot{q}_\star - \delta\ddot{q}] \quad (3.10)$$

$$= [M_{r\star}(q_\star) - M_{r\star}(q)]\ddot{q}_\star + \delta M_r(q)\ddot{q}_\star + M_{r\star}(q)\delta\ddot{q} - \delta M_r(q)\delta\ddot{q} \quad (3.11)$$

Since q appears only through trigonometric functions in the expression of the inertia matrix, and since small variations of q induce small variations of these functions, we assume that:

$$M_r(q_\star) \approx M_r(q) \quad (3.12)$$

$$M_{r\star}(q_\star) \approx M_{r\star}(q) \quad (3.13)$$

Then, it yields:

$$\delta M_r(q_\star) \approx \delta M_r(q) \quad (3.14)$$

Thus, assuming that the second-order error term $\delta M_r(q)\delta\ddot{q}$ is negligible compared to the other first-order terms, the contribution to the error $\delta\tau$ due to the inertial term is:

$$M_{r\star}(q_\star)\ddot{q}_\star - M_r(q)\ddot{q} = \delta M_r(q_\star)\ddot{q}_\star + M_{r\star}(q_\star)\delta\ddot{q} \quad (3.15)$$

where the first term $\delta M_r(q_\star)\ddot{q}_\star$ is due to the errors on the dynamic parameters involved in the calculation of the rigid inertia matrix, whereas the second term $M_{r\star}(q_\star)\delta\ddot{q}$ explicitly depends on the error on the approximated acceleration.

We proceed similarly for the other torque contributions in equation (3.9), assuming that:

$$\mathbf{C}(\mathbf{q}_\star, \dot{\mathbf{q}}_\star) \approx \mathbf{C}(\mathbf{q}, \dot{\mathbf{q}}) \quad (3.16)$$

$$\mathbf{C}_\star(\mathbf{q}_\star, \dot{\mathbf{q}}_\star) \approx \mathbf{C}_\star(\mathbf{q}, \dot{\mathbf{q}}) \quad (3.17)$$

$$\mathbf{G}(\mathbf{q}_\star) \approx \mathbf{G}(\mathbf{q}) \quad (3.18)$$

$$\mathbf{G}_\star(\mathbf{q}_\star) \approx \mathbf{G}_\star(\mathbf{q}) \quad (3.19)$$

These assumptions are considered for the developments to come. Neglected terms are evaluated in simulation on the applicative case of the ISYBOT prototype robot in Section 3.2.3.

Particular case of dry friction uncertainties

The contribution to the error $\delta\boldsymbol{\tau}$ due to dry friction is given by $\mathbf{F}_{s\star} \text{sign}(\dot{\mathbf{q}}_\star) - \mathbf{F}_s \text{sign}(\dot{\mathbf{q}})$. Hence, two cases stand out:

- when $\dot{\mathbf{q}}_\star$ and $\dot{\mathbf{q}}$ are of different sign, it leads to:

$$\mathbf{F}_{s\star} \text{sign}(\dot{\mathbf{q}}_\star) - \mathbf{F}_s \text{sign}(\dot{\mathbf{q}}) = [-\delta\mathbf{F}_s + 2\mathbf{F}_{s\star}] \text{sign}(\dot{\mathbf{q}}_\star) \quad (3.20)$$

- when $\dot{\mathbf{q}}_\star$ and $\dot{\mathbf{q}}$ are of same sign, it results in:

$$\mathbf{F}_{s\star} \text{sign}(\dot{\mathbf{q}}_\star) - \mathbf{F}_s \text{sign}(\dot{\mathbf{q}}) = \delta\mathbf{F}_s \text{sign}(\dot{\mathbf{q}}_\star) \quad (3.21)$$

Finally, the contribution of the dry friction depends on the sign of the approximated joint velocity with respect to the actual velocity. For sufficiently high joint velocities, the exact derivative $\dot{\mathbf{q}}$ and the approximated derivative $\dot{\mathbf{q}}_\star$ are likely to be of the same sign, but around zero velocity the signs may be different for a few samples due to the time delay induced by the numerical differentiation. In this case, specific uncertainty terms must be taken into account.

Therefore, we can define two vectors $\boldsymbol{\lambda}_P \in \mathbb{R}^n$ and $\boldsymbol{\lambda}_D \in \mathbb{R}^n$, such as:

$$\mathbf{F}_{s\star} \text{sign}(\dot{\mathbf{q}}_\star) - \mathbf{F}_s \text{sign}(\dot{\mathbf{q}}) = [\boldsymbol{\lambda}_P \delta\mathbf{F}_s + \boldsymbol{\lambda}_D \mathbf{F}_{s\star}] \text{sign}(\dot{\mathbf{q}}_\star) \quad (3.22)$$

and a speed threshold $\boldsymbol{\alpha} \in \mathbb{R}^n$ during which, if the approximated joint velocity is lower than this threshold, then $\dot{\mathbf{q}}$ and $\dot{\mathbf{q}}_\star$ would be of different sign. Thus, for each component i , we get:

$$\lambda_{P_i} = \begin{cases} -1 & \text{if } |\dot{q}_{\star_i}| < \alpha_i \\ 1 & \text{otherwise.} \end{cases} \quad \text{and} \quad \lambda_{D_i} = \begin{cases} 2 & \text{if } |\dot{q}_{\star_i}| < \alpha_i \\ 0 & \text{otherwise.} \end{cases} \quad (3.23)$$

The value of $\boldsymbol{\alpha}$ is determined for the current derivation scheme either in simulation or using the reference trajectory. The term $\boldsymbol{\lambda}_P \delta\mathbf{F}_s \text{sign}(\dot{\mathbf{q}}_\star)$ is associated with parametric errors while $\boldsymbol{\lambda}_D \mathbf{F}_{s\star} \text{sign}(\dot{\mathbf{q}}_\star)$ is related to the velocity approximation since it stems from the difference $[\text{sign}(\dot{\mathbf{q}}_\star) - \text{sign}(\dot{\mathbf{q}})]$.

Finally, the sources of errors in $\delta\tau$ can be divided into two parts:

$$\delta\tau = \delta\tau^P + \delta\tau^D \quad (3.24)$$

with $\delta\tau^P$ accounting for the errors on the robot dynamic parameters whereas $\delta\tau^D$ describes the errors on the velocity and acceleration approximations, such as:

$$\delta\tau^P = \delta M_r(q_\star) \ddot{q}_\star + \delta C(q_\star, \dot{q}_\star) \dot{q}_\star + \delta G(q_\star) + \delta F_v \dot{q}_\star + \lambda_P \delta F_s \text{sign}(\dot{q}_\star) \quad (3.25)$$

$$\delta\tau^D = M_{r\star}(q_\star) \delta \ddot{q} + C_\star(q_\star, \dot{q}_\star) \delta \dot{q} + F_{v\star} \delta \dot{q} + \lambda_D F_{s\star} \text{sign}(\dot{q}_\star) \quad (3.26)$$

Although the individual contributions of $\delta\tau^P$ and $\delta\tau^D$ cannot be assessed separately by experiment, these formulations make it possible:

- to give a structural indication of the type of uncertainties involved and contributing to modeling errors,
- to evaluate in simulation the predominant contribution between parameter estimation and numerical differentiation errors while taking into account the dependency on the robot's trajectory (see the case of the ISYBOT prototype robot illustrated in [Section 3.2.3](#)),
- to provide insights into possible options for reducing errors induced by model uncertainties (improving the identification of the dynamic parameters, reconsidering the tuning of the numerical derivation scheme with respect to the trajectory dynamics and measurement noise, modifying the trajectory in order to limit error peaks such as acceleration peaks, etc.).

3.2.2 Residual evaluation

In this section, we aim to determine the uncertainty-dependent threshold for the residual evaluation using a stochastic approach. Since the contribution of the error term $\delta\tau$ is not structurally separable from τ_{ext} within the residual, the objective is to determine the maximum envelope in which $\delta\tau$ could lie in order to isolate any additional contribution due to an external contact. For this purpose, the error range due to uncertainties is investigated by estimating the standard deviation $\sigma_{\delta\tau} \in \mathbb{R}^n$ of $\delta\tau$.

First the covariance matrix of $\delta\tau$, denoted $\Sigma_{\delta\tau} \in \mathbb{R}^{n,n}$, is computed by assuming that $\delta\tau^P$ and $\delta\tau^D$ are uncorrelated (errors on the dynamic model parameters being a priori uncorrelated with the errors on the robot state) and zero mean (which means that there is no bias in the estimation of model terms and joint coordinates):

$$\Sigma_{\delta\tau} := E \left[\delta\tau (\delta\tau)^T \right] \quad (3.27)$$

$$= E \left[\delta\tau^P (\delta\tau^P)^T \right] + E \left[\delta\tau^D (\delta\tau^D)^T \right] \quad (3.28)$$

$$= \Sigma_{\delta\tau^P} + \Sigma_{\delta\tau^D} \quad (3.29)$$

with $\Sigma_{\delta\tau^P} \in \mathbb{R}^{n,n}$ and $\Sigma_{\delta\tau^D} \in \mathbb{R}^{n,n}$ the covariance matrices of $\delta\tau^P$ and $\delta\tau^D$ respectively.

Remark 3.1 *In practice, a bias in the identification of dynamic parameters may be committed, especially because of errors in gravitational terms. In this case, the residual should be evaluated on a trajectory without contact in order to estimate the bias and subtract it in a second step. In the following, we assume that the estimation of the bias is processed by other techniques and we focus on the dynamic effects of the impact, so that these assumptions can be considered as valid.*

Let us express the covariance matrices of $\delta\tau^P$ and $\delta\tau^D$:

- **Covariance matrix of $\delta\tau^P$**

First, we define the rigid regression matrix $\varphi_r(\mathbf{q}, \dot{\mathbf{q}}, \ddot{\mathbf{q}}) \in \mathbb{R}^{n, N_r}$, such as:

$$\mathbf{M}_r(\mathbf{q})\ddot{\mathbf{q}} + \mathbf{C}(\mathbf{q}, \dot{\mathbf{q}})\dot{\mathbf{q}} + \mathbf{G}(\mathbf{q}) + \mathbf{F}_v \dot{\mathbf{q}} + \lambda_P \mathbf{F}_s \text{sign}(\dot{\mathbf{q}}) = \varphi_r(\mathbf{q}, \dot{\mathbf{q}}, \ddot{\mathbf{q}}) \chi_r \quad (3.30)$$

where the left-hand side has been rewritten in a linear form with respect to the rigid base parameters χ_r (in the same respect as [Property 2.3](#)). In a similar way as for equation (2.38), we examine the difference between the equation (3.30) evaluated in the estimated dynamic parameters (e.g. $\mathbf{M}_{r\star}(\mathbf{q})\ddot{\mathbf{q}}$ for the inertial term) and the same expression evaluated in the exact dynamic parameters (e.g. $\mathbf{M}_r(\mathbf{q})\ddot{\mathbf{q}}$). When computed in the robot estimated states \mathbf{q}_\star , $\dot{\mathbf{q}}_\star$ and $\ddot{\mathbf{q}}_\star$, we recognize that equation (3.25) can be rewritten as:

$$\delta\tau^P = \varphi_r(\mathbf{q}_\star, \dot{\mathbf{q}}_\star, \ddot{\mathbf{q}}_\star) \delta\chi_r \quad (3.31)$$

where $\delta\chi_r$ is the vector of errors on the rigid base parameters. Therefore, assuming that $\varphi_r(\mathbf{q}_\star, \dot{\mathbf{q}}_\star, \ddot{\mathbf{q}}_\star)$ is deterministic, the covariance matrix of $\delta\tau^P$ is given by:

$$\Sigma_{\delta\tau^P} := E \left[\delta\tau^P (\delta\tau^P)^T \right] \quad (3.32)$$

$$= \varphi_r(\mathbf{q}_\star, \dot{\mathbf{q}}_\star, \ddot{\mathbf{q}}_\star) E \left[\delta\chi_r (\delta\chi_r)^T \right] \varphi_r(\mathbf{q}_\star, \dot{\mathbf{q}}_\star, \ddot{\mathbf{q}}_\star)^T \quad (3.33)$$

$$= \varphi_r(\mathbf{q}_\star, \dot{\mathbf{q}}_\star, \ddot{\mathbf{q}}_\star) \Sigma_{\chi_r} \varphi_r(\mathbf{q}_\star, \dot{\mathbf{q}}_\star, \ddot{\mathbf{q}}_\star)^T \quad (3.34)$$

with $\Sigma_{\chi_r} \in \mathbb{R}^{N_r, N_r}$ the diagonal covariance matrix of $\delta\chi_r$ where standard deviations result from the identification of the rigid dynamic model parameters (see equation (2.35)).

- **Covariance matrix of $\delta\tau^D$**

From equation (3.26), the covariance matrix of $\delta\tau^D$ is given by:

$$\Sigma_{\delta\tau^D} := E \left[\delta\tau^D (\delta\tau^D)^T \right] \quad (3.35)$$

$$= E \left[\left(\mathbf{M}_{r\star}(\mathbf{q}_\star) \delta\ddot{\mathbf{q}} + (\mathbf{C}_\star(\mathbf{q}_\star, \dot{\mathbf{q}}_\star) + \mathbf{F}_{v\star}) \delta\dot{\mathbf{q}} + \lambda_D \mathbf{F}_{s\star} \text{sign}(\dot{\mathbf{q}}_\star) \right) \left(\mathbf{M}_{r\star}(\mathbf{q}_\star) \delta\ddot{\mathbf{q}} + (\mathbf{C}_\star(\mathbf{q}_\star, \dot{\mathbf{q}}_\star) + \mathbf{F}_{v\star}) \delta\dot{\mathbf{q}} + \lambda_D \mathbf{F}_{s\star} \text{sign}(\dot{\mathbf{q}}_\star) \right)^T \right] \quad (3.36)$$

Assuming that the correlation between $\delta\dot{\mathbf{q}}$, $\delta\ddot{\mathbf{q}}$ and $\text{sign}(\dot{\mathbf{q}}_\star)$ is negligible in comparison with their own variance, and that matrices $\mathbf{M}_{r\star}(\mathbf{q}_\star)$, $\mathbf{C}_\star(\mathbf{q}_\star, \dot{\mathbf{q}}_\star)$, $\mathbf{F}_{v\star}$ and $\lambda_D \mathbf{F}_{s\star}$ are deterministic,

equation (3.36) becomes:

$$\begin{aligned} \Sigma_{\delta\tau^D} = & M_{r\star}(\mathbf{q}_\star) \Sigma_{\dot{\mathbf{q}}} M_{r\star}(\mathbf{q}_\star)^T + \left[\mathbf{C}_\star(\mathbf{q}_\star, \dot{\mathbf{q}}_\star) + \mathbf{F}_{v\star} \right] \Sigma_{\dot{\mathbf{q}}} \left[\mathbf{C}_\star(\mathbf{q}_\star, \dot{\mathbf{q}}_\star) + \mathbf{F}_{v\star} \right]^T \\ & + \lambda_D^2 \mathbf{F}_{s\star} \mathbf{F}_{s\star}^T \end{aligned} \quad (3.37)$$

with $\Sigma_{\dot{\mathbf{q}}}$, $\Sigma_{\ddot{\mathbf{q}}} \in \mathbb{R}^{n,n}$ the diagonal covariance matrices of $\delta\dot{\mathbf{q}}$ and $\delta\ddot{\mathbf{q}}$, defined in equations (2.52) and (2.53) respectively.

In the following, dependencies in joint coordinates are removed in the notations for the sake of simplicity. Then the covariance matrix of $\delta\tau$ is given by:

$$\Sigma_{\delta\tau} = \varphi_r \Sigma_{\chi_r} \varphi_r^T + M_{r\star} \Sigma_{\dot{\mathbf{q}}} M_{r\star}^T + (\mathbf{C}_\star + \mathbf{F}_{v\star}) \Sigma_{\dot{\mathbf{q}}} (\mathbf{C}_\star + \mathbf{F}_{v\star})^T + \lambda_D^2 \mathbf{F}_{s\star} \mathbf{F}_{s\star}^T \quad (3.38)$$

Finally, the standard deviation vector $\sigma_{\delta\tau}$ is obtained by assuming that the non-diagonal elements within $\Sigma_{\delta\tau}$, which refer to correlated errors between the axes, are negligible with respect to the variance of the error for each axis, which can be verified experimentally (see Remark 3.2). Then it yields:

$$\text{for any axis } i \in \llbracket 1, n \rrbracket, \quad \sigma_{\delta\tau_i} = \sqrt{\Sigma_{\delta\tau_{ii}}} \quad (3.39)$$

Remark 3.2 *The assumption made about negligible non-diagonal elements within the covariance matrix $\Sigma_{\delta\tau}$ is questionable and may lead to false alarms or undetected impact because the influence of the other axes has not been taken into account (especially in case of coupled axes). In this case, it would be interesting to consider a n -dimensional representation of the distribution of errors $\delta\tau$, and to search for a confidence ellipsoid using a Chi-Square distribution, which is the n -dimensional generalization of the confidence interval. The interested reader can refer to [Press 2007] for more information.*

In equation (3.38), matrices φ_r , $M_{r\star}$ and \mathbf{C}_\star have to be evaluated on the actual trajectory of the robot. Consequently, $\sigma_{\delta\tau}$ is computed online at each time step. If the reference trajectory is known in advance (or at least for few samples) and provided that the trajectory tracking errors are sufficiently small, $\sigma_{\delta\tau}$ can be pre-evaluated on the reference trajectory.

According to equations (3.24)-(3.26), $\delta\tau$ results from a linear combination of the error terms $\delta\chi_r$, $\delta\dot{\mathbf{q}}$ and $\delta\ddot{\mathbf{q}}$ that we have assumed to follow a normal distribution in Chapter 2: "Modeling serial robot manipulators under uncertainties". Under these assumptions, $\delta\tau$ also follows a normal distribution by linearity. Moreover, since $\delta\tau^P$ and $\delta\tau^D$ are assumed to be zero mean, $\delta\tau$ is also zero mean. Then, according to the 3σ -confidence interval of $\delta\tau$, in 99.7% of the cases we get:

$$\delta\tau \underset{99.7\%}{\in} [-3\sigma_{\delta\tau}, 3\sigma_{\delta\tau}] \quad (3.40)$$

In other words, $[-3\sigma_{\delta\tau}, 3\sigma_{\delta\tau}]$ represents at each time step the range in which the contribution of the model errors is supposed to lie in 99.7% of the cases. Note that other confidence intervals could be considered, such as the 2σ -interval with 95% of confidence level, which would result in improved detection performance with a slightly higher risk of false alarms.

Since $\mathbf{r} = \boldsymbol{\tau}_{ext} + \boldsymbol{\delta\tau}$, the rule for evaluating the residual and detecting an impact is given by:

If $\exists i \in \llbracket 1, n \rrbracket$ **s.t.** $r_i \notin [-3\sigma_{\delta\tau_i}, 3\sigma_{\delta\tau_i}]$
Then $\tau_{ext_i} \neq 0$: impact occurrence with 99.7% of confidence

Consequently, the adaptive detection threshold considered is defined by $\mathbf{T} = \pm 3\boldsymbol{\sigma}_{\delta\tau}$. However, when $\mathbf{r} \in [-3\boldsymbol{\sigma}_{\delta\tau}, 3\boldsymbol{\sigma}_{\delta\tau}]$, we cannot conclude that there is no impact since $\boldsymbol{\tau}_{ext}$ may be small enough to remain within the error envelope. In this case, it is not possible to distinguish between the two contributions $\boldsymbol{\tau}_{ext}$ and $\boldsymbol{\delta\tau}$ within \mathbf{r} .

Thus the logical detection signal that indicates the occurrence of an impact is given at each time step by:

$$d(k) = \begin{cases} 1 & \text{if } \exists i \in \llbracket 1, n \rrbracket \text{ s.t. } |r_i| > |3\sigma_{\delta\tau_i}| \\ 0 & \text{otherwise.} \end{cases}$$

Hence, the envelope created by the range $[-3\boldsymbol{\sigma}_{\delta\tau}, 3\boldsymbol{\sigma}_{\delta\tau}]$ represents the minimum level of detection sensitivity that can be expected in presence of model errors. Therefore, it is of great interest for impact detection to minimize the model errors in order to reduce the size of the envelope and improve the detection sensitivity.

**Summary of the methodology:
Direct external torque estimation (DETE)**

Known a priori: $\Sigma_{\chi_r}, \Sigma_{\dot{q}}, \Sigma_{\ddot{q}}$

1. Measure $\tau, q_*, \dot{q}_*, \ddot{q}_*$
2. Compute the residual with

$$\mathbf{r} = [M_{r*}(q_*)\ddot{q}_* + C_*(q_*, \dot{q}_*)\dot{q}_* + G_*(q_*) + F_{v*}\dot{q}_* + F_{s*} \text{sign}(\dot{q}_*)] - \tau$$

3. Determine the threshold T with

$$\Sigma_{\delta\tau^P} = \boldsymbol{\varphi}_r(q_*, \dot{q}_*, \ddot{q}_*) \Sigma_{\chi_r} \boldsymbol{\varphi}_r(q_*, \dot{q}_*, \ddot{q}_*)^T$$

$$\Sigma_{\delta\tau^D} = M_{r*}(q_*) \Sigma_{\ddot{q}} M_{r*}(q_*)^T + [C_*(q_*, \dot{q}_*) + F_{v*}] \Sigma_{\dot{q}} [C_*(q_*, \dot{q}_*) + F_{v*}]^T + \lambda_D^2 F_{s*} F_{s*}^T$$

$$\Sigma_{\delta\tau} = \Sigma_{\delta\tau^P} + \Sigma_{\delta\tau^D}$$

$$T_i = \pm 3 \sqrt{\Sigma_{\delta\tau_{ii}}} \text{ for the 99.7\%-confidence interval}$$

4. Compute the alert signal indicating the detection of an impact with

$$d = \begin{cases} 1 & \text{if } \exists i \in \llbracket 1, n \rrbracket \text{ s.t. } |r_i| > T_i \\ 0 & \text{otherwise.} \end{cases}$$

3.2.3 Illustration of the uncertainties contribution

The contribution of the uncertainties coming from the DETE method is examined on the application case of the ISYBOT prototype robot described in Appendix B. In this respect, a Matlab/Simulink simulator of the robot is used to simulate a certain amount of errors induced by uncertainties on the parameters of the dynamic model and on the state coordinates. The objectives are:

- to compare the contributions of $\delta\tau^P$ and $\delta\tau^D$ to the total error torque $\delta\tau$ and their associated error range,
- to assess the validity of the approximations in equations (3.12) to (3.19),
- to interpret the resulting error range in the case of the DETE method.

Simulations are carried out with the robot controlled in position in the joint space with a decentralized proportional-derivative (PD) control law at a sampling time $T_s = 0.001s$. For the study, the simulated reference trajectory is a sinusoidal trajectory of magnitude \mathbf{A}_0 and frequency \mathbf{f}_0 around the configuration $\mathbf{q} = (0 \ 0.6 \ -1 \ 0 \ 0 \ 0)^T$, such as:

$$\mathbf{A}_0 = \begin{pmatrix} 0.2 & 0.2 & 0.2 & 0.2 & 0.2 & 0.2 \end{pmatrix} \text{ rad} \quad (3.41)$$

$$\mathbf{f}_0 = \begin{pmatrix} 0.7 & 0.6 & 0.5 & 0.4 & 0.3 & 0.2 \end{pmatrix} \text{ Hz} \quad (3.42)$$

Each axis is actuated simultaneously with movements of different frequencies to stimulate the couplings between the axes. No external torque is applied during the simulation. The following results are shown for axis 3 as an example, whose trajectory in absence of uncertainties is illustrated in Figure 3.6.

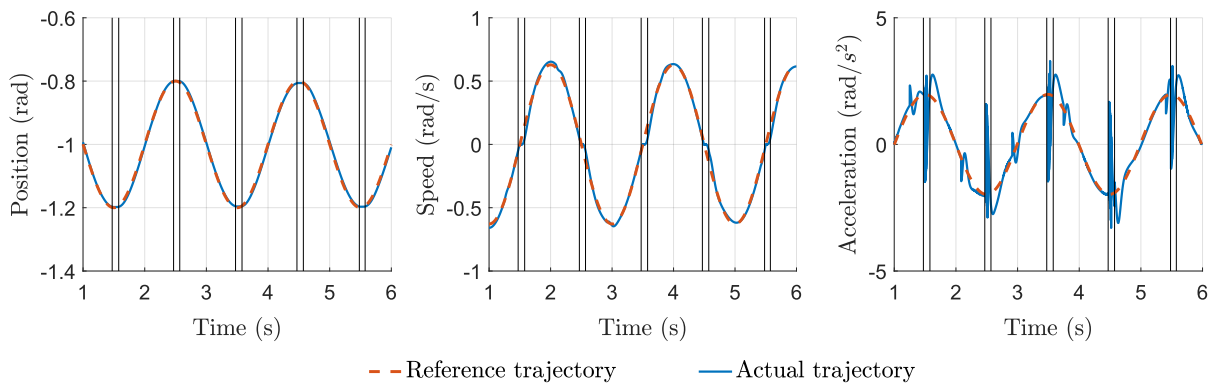


Figure 3.6: Displacement of robot axis 3. Vertical lines indicate the range during which $|\dot{q}_{\star 3}| < \alpha_3$ with $\alpha_3 = 0.05 \text{ rad/s}$ and that the contribution $\lambda_D^2 \mathbf{F}_{s\star} \mathbf{F}_{s\star}^T$ within $\Sigma_{\delta\tau}$ is non-zero.

3.2.3.1 Comparison of the parametric and numerical differentiation contributions

First, we study the contribution of the parametric uncertainties $\delta\tau^P$. The parameters chosen for the simulation are described below. Results are presented for axis 3 in Figure 3.7.

Parametric errors (Figure 3.7)

Favorable (**P1**) and unfavorable (**P2**) identification results are studied:

- **P1** – Proper quality identification: for each parameter i , $\% \sigma_{\chi_i} \in [0\%, 5\%]$,
- **P2** – Poor quality identification: for each parameter i , $\% \sigma_{\chi_i} \in [0\%, 20\%]$.

For this purpose, each $\% \sigma_{\chi_i}$ is fixed randomly and independently within these ranges, prior to the simulation and with the same random distribution between **P1** and **P2**. Simulations are based on a given random realization of the uncertain parameters χ_{r^*} according to a normal distribution, centered around the exact values χ_r and of standard deviation deduced from $\% \sigma_{\chi}$ (see equation (2.34)). To study only the effect of parametric uncertainties, the estimation of the joint coordinates is considered as perfect ($\mathbf{q}_* = \mathbf{q}$, $\dot{\mathbf{q}}_* = \dot{\mathbf{q}}$ and $\ddot{\mathbf{q}}_* = \ddot{\mathbf{q}}$ thus $\delta\tau^D = \mathbf{0}$).

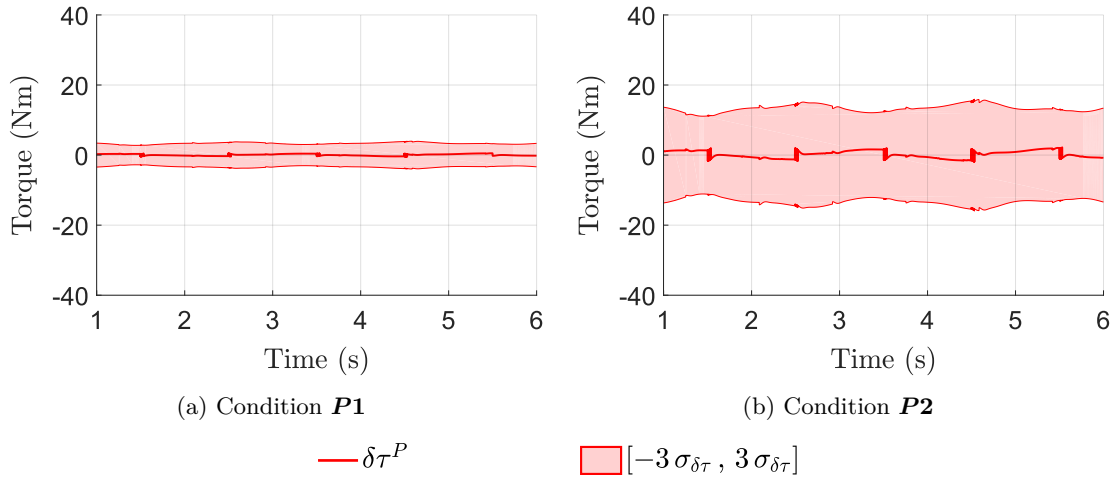


Figure 3.7: Uncertainties $\delta\tau^P$ and their associated error envelope under **P1** and **P2** conditions

We observe that the envelope generated by $[-3\sigma_{\delta\tau}, 3\sigma_{\delta\tau}]$ increases in accordance with $\% \sigma_{\chi(\cdot)}$ from **P1** to **P2** conditions. In this way, the error $\delta\tau^P$ remain bounded by $[-3\sigma_{\delta\tau}, 3\sigma_{\delta\tau}]$ in both cases. We also note the dependency on the robot's trajectory, which causes $\delta\tau^P$ and $\sigma_{\delta\tau}$ to vary over time.

The shape of $\delta\tau^P$ may vary from one random distribution of χ_{r^*} to another. However, in any situation, $\delta\tau^P$ remains bounded by its associated error range $[-3\sigma_{\delta\tau}, 3\sigma_{\delta\tau}]$.

applied, thus triggering a false alarm. Although the **D2** scheme seems better at first sight, it is important to remember that the error induced by the derivative approximation term depends on the trajectory and that the approximate derivative is more delayed than with the **D1** scheme. Finally, a compromise has to be found on the cut-off frequency tuning between the amount of noise (causing false alarms) and delay (causing detection delay). In addition, for both **D1** and **D2** schemes, the envelopes increase correctly at low speed, i. e. when the term $\lambda_D \mathbf{F}_{s\star} \text{sign}(\dot{\mathbf{q}}_\star)$ is activated within $\delta\tau^D$, thus avoiding false alarms that would otherwise have occurred.

Regarding the relative contribution of $\delta\tau^P$ and $\delta\tau^D$, the latter is often neglected [Dixon 2000, Jung 2014]. However, when they are compared under **P1** and **D2** conditions for instance (see Figure 3.9), we observe that the two contributions can be of the same order of magnitude (except during low speed phases where the numerical differentiation error $\delta\tau^D$ is predominant).

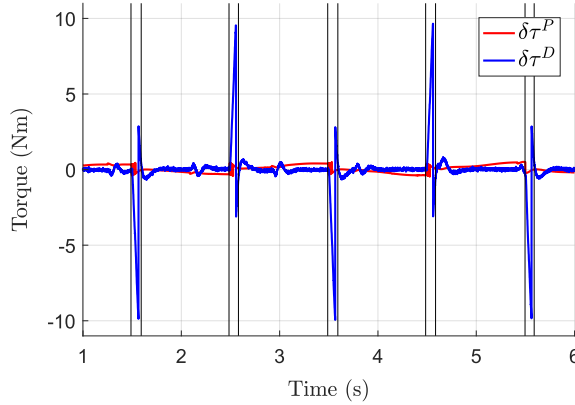


Figure 3.9: Comparison of $\delta\tau^P$ (under condition **P1**) and $\delta\tau^D$ (under condition **D2**). Vertical lines indicate the range during which $|\dot{q}_{\star 3}| < \alpha_3$ with $\alpha_3 = 0.05$ rad/s.

3.2.3.2 Validation of approximations

The decomposition of $\delta\tau$ into $\delta\tau^P + \delta\tau^D$ is an approximation where second-order terms have been neglected (see equation (3.11) for the exact error on the inertial term). In Figure 3.10, the difference $\delta\tau - (\delta\tau^P + \delta\tau^D)$ is illustrated, where $\delta\tau$ has been calculated with the exact formulation from equation (3.9). Both parametric errors and numerical differentiation errors are considered for the simulation: more precisely, the conditions **P1** and **D2** described above are simulated simultaneously.

The robot actual speed is also plotted for comparison purposes. We observe that the approximation may not be entirely valid during the low speed phases, which also correspond to trajectory changes. During these periods and for these simulation conditions, the maximum relative error reported is 6.72%, while apart from these phases it is 0.57%. The approximations made can therefore be considered as acceptable under these conditions, and we assume that this remains the case for the rest of the simulation or experimental conditions.

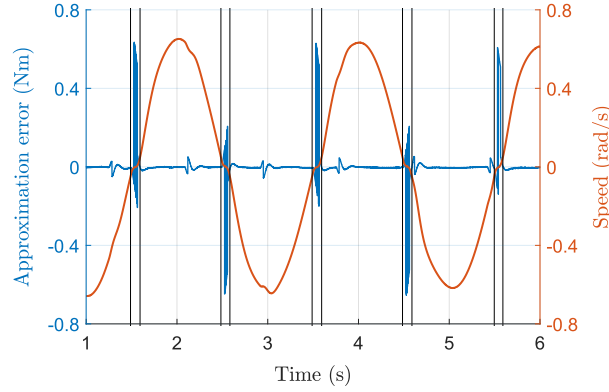
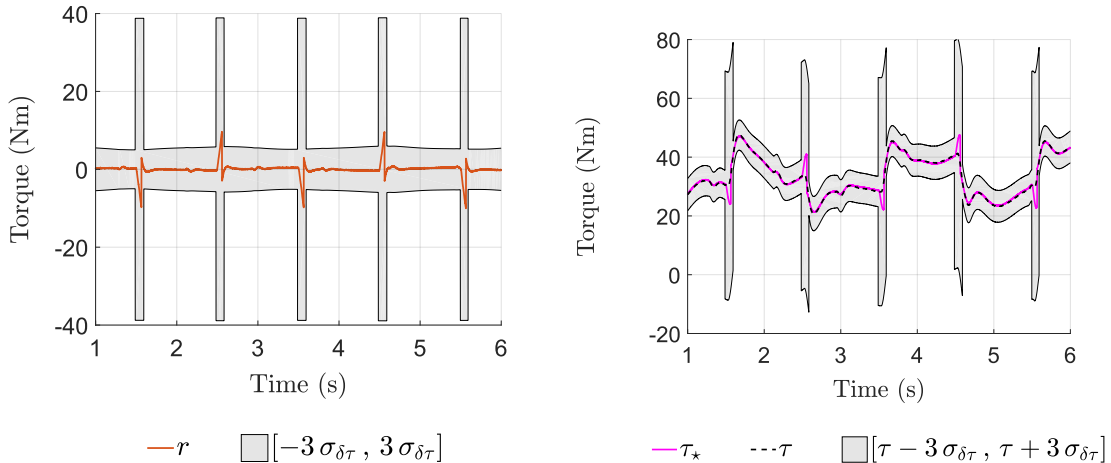


Figure 3.10: Approximation error on $\delta\tau$ under $(P1, D2)$ conditions. Vertical lines indicate the range during which $|\dot{q}_{*3}| < \alpha_3$ with $\alpha_3 = 0.05$ rad/s.

3.2.3.3 Interpretation of the error range

In this section, the residual resulting from the simultaneous simulation conditions $P1$ and $D2$ is evaluated by the detection threshold $T = \pm 3\sigma_{\delta\tau}$ in Figure 3.11a. Given the envelope’s boundaries, we note that if an impact of less than 6 Nm is applied to the robot, then it is not possible to distinguish it from the contribution of modeling errors. Therefore, the error range associated with the uncertainties involved allows to quantify the sensitivity of the impact detection algorithm.

Since $r = \tau_* - \tau = \tau_{ext} + \delta\tau$, the error range can also be seen as a tunnel of uncertainties around τ (see Figure 3.11b). Then, an impact is detected as soon as τ_* gets out of this tunnel. The width of the tunnel is directly related to the amount of uncertainties involved.



(a) Evaluation of the residual r by the detection threshold $[-3\sigma_{\delta\tau}, 3\sigma_{\delta\tau}]$ (b) Evaluation of the estimated motor torque τ_* by the detection threshold $[\tau - 3\sigma_{\delta\tau}, \tau + 3\sigma_{\delta\tau}]$

Figure 3.11: Two interpretations of the residual evaluation step with the DETE method

3.3 Disturbance observers design

In this section, the external torque $\boldsymbol{\tau}_{ext}$ is estimated using linear disturbance observers for impact detection. First, the general approach is detailed in [Section 3.3.1](#) before being applied to two different observer-based methods. The discretization step associated with the observer design is presented in [Section 3.3.2](#), then [Section 3.3.3](#) is dedicated to the evaluation step in the specific case of disturbance observers. Finally, [Section 3.3.4](#) compares the different methods developed and highlights the effect of uncertainties in each case, from a theoretical point of view and based on simulation examples.

3.3.1 State-space representations under uncertainties

First, an approximate model of the external disturbance is required which attempts to reflect the dynamics of the impact, although its actual temporal behaviour is unknown a priori (especially in the case of an unexpected collision). We propose a unitary first-order disturbance model such as:

$$\dot{\boldsymbol{\tau}}_{ext} = -\mathbf{A}_{ext} \boldsymbol{\tau}_{ext} + \mathbf{B}_{ext} \boldsymbol{w}_{ext} \quad (3.43)$$

where

$$\mathbf{B}_{ext} = \begin{cases} \mathbf{A}_{ext} & \text{if } \mathbf{A}_{ext} \neq \mathbf{0}_{n,n} \\ \mathbf{I}_{n,n} & \text{if } \mathbf{A}_{ext} = \mathbf{0}_{n,n} \end{cases}$$

$\mathbf{A}_{ext} \in \mathbb{R}^{n,n}$ is a diagonal matrix of positive or null terms and $\boldsymbol{w}_{ext} \in \mathbb{R}^n$ is a noise such that $\boldsymbol{w}_{ext} \sim \mathcal{N}(\mathbf{0}, \boldsymbol{\Sigma}_{w_{ext}})$ with $\boldsymbol{\Sigma}_{w_{ext}} \in \mathbb{R}^{n,n}$. The variance of the global noise contribution is denoted $\boldsymbol{\Sigma}_{ext} \in \mathbb{R}^{n,n}$ and verifies $\boldsymbol{\Sigma}_{ext} = \mathbf{B}_{ext} \boldsymbol{\Sigma}_{w_{ext}} \mathbf{B}_{ext}^T$. In this disturbance model, the matrix \mathbf{A}_{ext} parametrizes the impact dynamics, while the matrix $\boldsymbol{\Sigma}_{ext}$ refers to the uncertainties not only on the external impact model but also on all other effects not considered. They are both treated as design parameters. The covariance matrix $\boldsymbol{\Sigma}_{w_{ext}}$ is deduced from $\boldsymbol{\Sigma}_{ext}$ with $\boldsymbol{\Sigma}_{w_{ext}} = \mathbf{B}_{ext}^{-1} \boldsymbol{\Sigma}_{ext} \mathbf{B}_{ext}^{-T}$.

In the following, two different approaches are developed: one is based on the classical form of the RDM recalled in [equation \(3.3\)](#), while the other one exploits its rewriting according to the generalized momentum, which is recalled below in the rigid case:

$$\dot{\boldsymbol{p}}(\boldsymbol{q}, \dot{\boldsymbol{q}}, \ddot{\boldsymbol{q}}) - \mathbf{C}(\boldsymbol{q}, \dot{\boldsymbol{q}})^T \dot{\boldsymbol{q}} + \mathbf{G}(\boldsymbol{q}) + \mathbf{F}_v \dot{\boldsymbol{q}} + \mathbf{F}_s \text{sign}(\dot{\boldsymbol{q}}) = \boldsymbol{\tau} + \boldsymbol{\tau}_{ext} \quad (3.44)$$

In the first case, it leads to a Joint Position and Velocity Observer (JPVO) where the state vector to observe is $\mathbf{X}_r = [\boldsymbol{q}^T \ \dot{\boldsymbol{q}}^T]^T$ (approach developed in [Section 3.3.1.1](#)), whereas in the second case it amounts to a Generalized Momentum Observer (GMO) with $\mathbf{X}_r = \boldsymbol{p}(\boldsymbol{q}, \dot{\boldsymbol{q}})$ (approach developed in [Section 3.3.1.2](#)). For both approaches, the objective is to rewrite the IDM into a linear expression in order to derive a state-space representation of the form:

$$\begin{cases} \dot{\mathbf{X}}_r &= \mathbf{A}_r \mathbf{X}_r + \mathbf{B}_r \tilde{\boldsymbol{\tau}} + \mathbf{G}_{\delta\tau} \delta\boldsymbol{\tau} + \mathbf{G}_{ext} \boldsymbol{\tau}_{ext} \\ \mathbf{Y} &= \mathbf{C}_r \mathbf{X}_r + \boldsymbol{v} \end{cases} \quad (3.45)$$

To achieve this, a virtual input torque $\tilde{\tau} \in \mathbb{R}^n$ (to be defined for each method) is computed based on estimated terms of the IDM which, due to model uncertainties, generates errors gathered in the term $\delta\tau$. \mathbf{A}_r , \mathbf{B}_r , \mathbf{C}_r , $\mathbf{G}_{\delta\tau}$ and \mathbf{G}_{ext} are matrices to be determined for each method. Finally, $\mathbf{v} \in \mathbb{R}^n$ collects the error on the output vector, which is the joint position \mathbf{q}_\star for the JPVO and the generalized momentum $\mathbf{p}_\star(\mathbf{q}_\star, \dot{\mathbf{q}}_\star)$ for the GMO.

The state-space representation (3.45) can then be augmented with the disturbance model defined in equation (3.43), the new state vector becoming $\mathbf{X} = [\mathbf{X}_r^T \quad \tau_{ext}^T]^T$:

$$\begin{cases} \dot{\mathbf{X}} = \mathbf{A} \mathbf{X} + \mathbf{B} \tilde{\tau} + \mathbf{G} \mathbf{w} \\ \mathbf{Y} = \mathbf{C} \mathbf{X} + \mathbf{v} \end{cases} \quad (3.46)$$

with $\mathbf{w} = [\delta\tau^T \quad \mathbf{w}_{ext}^T]^T \in \mathbb{R}^{2n}$ containing all modeling errors, including those on the disturbance model. Matrices \mathbf{A} , \mathbf{B} , \mathbf{C} and \mathbf{G} are deduced from matrices \mathbf{A}_r , \mathbf{B}_r , \mathbf{C}_r , $\mathbf{G}_{\delta\tau}$, \mathbf{G}_{ext} , \mathbf{A}_{ext} and \mathbf{B}_{ext} .

For the purpose of designing an observer using a Kalman filter, the state error \mathbf{w} and the measurement error \mathbf{v} will be approximated by white and uncorrelated noises of Power Spectral Density (PSD) denoted respectively $\Sigma_w \in \mathbb{R}^{2n, 2n}$ and $\Sigma_v \in \mathbb{R}^{n, n}$. In addition, $\delta\tau$ and \mathbf{w}_{ext} are assumed to be uncorrelated, such that:

$$\Sigma_w = \begin{pmatrix} \Sigma_{\delta\tau} & \mathbf{0} \\ \mathbf{0} & \Sigma_{\mathbf{w}_{ext}} \end{pmatrix} \quad (3.47)$$

where $\Sigma_{\delta\tau} \in \mathbb{R}^{n, n}$ and $\Sigma_{\mathbf{w}_{ext}}$ are the PSD of $\delta\tau$ and \mathbf{w}_{ext} respectively. Note that the non-correlation assumption is introduced for clarity reasons but is not required in the general formulation of the Kalman filter: the interested reader can refer to [Labarrère 1993] for the general formulation taking into account a correlation between state and measurement noises. The following sections deal with the determination of the state-space model (3.46) and of the PSD $\Sigma_{\delta\tau}$ and Σ_v for each approach.

3.3.1.1 Joint position and velocity observer (JPVO)

For impact monitoring purposes, a virtual input torque $\tilde{\tau}$ is computed in parallel with the robot control loop, such as:

$$\tilde{\tau} = \tau - [\mathbf{M}_\star(\mathbf{q}_\star) \ddot{\mathbf{q}}_\star + \mathbf{C}_\star(\mathbf{q}_\star, \dot{\mathbf{q}}_\star) \dot{\mathbf{q}}_\star + \mathbf{G}_\star(\mathbf{q}_\star) + \mathbf{F}_{s\star} \text{sign}(\dot{\mathbf{q}}_\star)] \quad (3.48)$$

The RDM in equation (3.3) is rearranged with $\tilde{\tau}$, by decomposing the rigid inertia matrix $\mathbf{M}_r(\mathbf{q})$ into $\mathbf{M}(\mathbf{q}) + \mathbf{J}_m$ where \mathbf{J}_m is the diagonal matrix of the actuators inertia after the reduction stage. Since estimated dynamic parameters and state coordinates may be affected by model uncertainties, introducing $\tilde{\tau}$ in the RDM yields:

$$\mathbf{J}_m \ddot{\mathbf{q}} + \mathbf{F}_v \dot{\mathbf{q}} = \tilde{\tau} + \tau_{ext} + \delta\tau' \quad (3.49)$$

where $\delta\tau'$ collects the uncertainties-induced errors, such that:

$$\begin{aligned} \delta\tau' = & [M_\star(q_\star)\ddot{q}_\star + C_\star(q_\star, \dot{q}_\star)\dot{q}_\star + G_\star(q_\star) + F_{s\star}\text{sign}(\dot{q}_\star)] \\ & - [M(q)\ddot{q} + C(q, \dot{q})\dot{q} + G(q) + F_s\text{sign}(\dot{q})] \end{aligned} \quad (3.50)$$

Given that $\delta J_m = J_{m\star} - J_m$ and $\delta F_v = F_{v\star} - F_v$ and assuming that second-order errors are negligible compared to first-order errors, it follows:

$$J_{m\star}\ddot{q} + F_{v\star}\dot{q} = \tilde{\tau} + \tau_{ext} + \underbrace{(\delta\tau' + \delta J_m\ddot{q}_\star + \delta F_v\dot{q}_\star)}_{\delta\tau} \quad (3.51)$$

With the same assumptions as for the approach based on DETE and similar developments (see Section 3.2.1), the error term $\delta\tau$ is rewritten as the sum of a contribution $\delta\tau^P$ due to parametric errors and a contribution $\delta\tau^D$ due to numerical differentiation errors, such as:

$$\delta\tau^P = \delta M_r(q_\star)\ddot{q}_\star + \delta C(q_\star, \dot{q}_\star)\dot{q}_\star + \delta G(q_\star) + \delta F_v\dot{q}_\star + \lambda_P \delta F_s \text{sign}(\dot{q}_\star) \quad (3.52)$$

$$\delta\tau^D = M_\star(q_\star)\delta\ddot{q} + C_\star(q_\star, \dot{q}_\star)\delta\dot{q} + \lambda_D F_{s\star}\text{sign}(\dot{q}_\star) \quad (3.53)$$

Remark 3.3 We note that in the expression of $\tilde{\tau}$ (equation (3.48)), the terms $J_{m\star}\ddot{q}_\star$ and $F_{v\star}\dot{q}_\star$ could also have been included. However, in this case, additional errors $J_{m\star}\delta\ddot{q}$ and $F_{v\star}\delta\dot{q}$ would have been present within $\delta\tau^D$. Therefore, the advantage of the observer-based approach lies in the fact that, since the joint position and velocity are estimated as part of the state vector, the terms that linearly depend on them (or their derivative) do not generate any numerical differentiation error if they are kept in the linear formulation of the RDM (equation (3.51)).

Remark 3.4 We also note that the term $\delta\tau^P$ for the JPVO (equation (3.52)) is identical to that for the DETE (equation (3.25)), therefore these two methods are affected by the same parametric errors. However, the terms $J_{m\star}\delta\ddot{q}$ and $F_{v\star}\delta\dot{q}$ do not appear in $\delta\tau^D$ for the JPVO (equation (3.53)) unlike the DETE (equation (3.26)), thus fewer numerical differentiation errors are expected in the JPVO compared to the DETE.

From equation (3.51), the following reduced state-space representation is derived:

$$\left\{ \begin{array}{l} \begin{bmatrix} \dot{q} \\ \ddot{q} \end{bmatrix} = \underbrace{\begin{pmatrix} \mathbf{0} & I \\ \mathbf{0} & -J_{m\star}^{-1}F_{v\star} \end{pmatrix}}_{A_r} \begin{bmatrix} q \\ \dot{q} \end{bmatrix} + \underbrace{\begin{pmatrix} \mathbf{0} \\ J_{m\star}^{-1} \end{pmatrix}}_{B_r} \tilde{\tau} + \underbrace{\begin{pmatrix} \mathbf{0} \\ J_{m\star}^{-1} \end{pmatrix}}_{G_{\delta\tau}} \delta\tau + \underbrace{\begin{pmatrix} \mathbf{0} \\ J_{m\star}^{-1} \end{pmatrix}}_{G_{ext}} \tau_{ext} \\ q_\star = \underbrace{\begin{pmatrix} I & \mathbf{0} \end{pmatrix}}_{C_r} \begin{bmatrix} q \\ \dot{q} \end{bmatrix} + \underbrace{\xi_q}_v \end{array} \right. \quad (3.54)$$

Using the disturbance model (3.43), the augmented state-space representation is given by:

$$\begin{cases} \begin{bmatrix} \dot{q} \\ \ddot{q} \\ \dot{\tau}_{ext} \end{bmatrix} = \underbrace{\begin{pmatrix} A_r & G_{ext} \\ 0 & -A_{ext} \end{pmatrix}}_A \begin{bmatrix} q \\ \dot{q} \\ \tau_{ext} \end{bmatrix} + \underbrace{\begin{pmatrix} B_r \\ 0 \end{pmatrix}}_B \tilde{\tau} + \underbrace{\begin{pmatrix} G_{\delta\tau} & 0 \\ 0 & B_{ext} \end{pmatrix}}_G \begin{bmatrix} \delta\tau \\ w_{ext} \end{bmatrix} \\ q_\star = \underbrace{\begin{pmatrix} C_r & 0 \end{pmatrix}}_C \begin{bmatrix} q \\ \dot{q} \\ \tau_{ext} \end{bmatrix} + \underbrace{\xi_q}_v \end{cases} \quad (3.55)$$

In this case, matrices A , B , G and C are constant but other approaches with time-varying matrices are also possible when Cartesian contact forces F_{ext} are estimated instead of external torques τ_{ext} , provided that the Jacobian matrix at the contact point is known [Wahrburg 2018].

Derivation of the PSD

Matrices $\Sigma_{\delta\tau}$ and Σ_v are derived using the same developments as for the DETE in Section 3.2.2, which leads to:

$$\Sigma_{\delta\tau} = \varphi_r \Sigma_{\chi_r} \varphi_r^T + M_\star \Sigma_{\ddot{q}} M_\star^T + C_\star \Sigma_{\dot{q}} C_\star^T + \lambda_D^2 F_{s\star} F_{s\star}^T \quad (3.56)$$

$$\Sigma_v = \Sigma_q \quad (3.57)$$

where dependencies in joint coordinates have been removed for the sake of simplicity but φ_r , M_\star and C_\star depend on the actual robot trajectory. In this case, $\Sigma_{\delta\tau}$ varies along the robot trajectory, whereas Σ_v is constant.

Following Remark 3.4, the contributions of $J_{m\star} \Sigma_{\ddot{q}} J_{m\star}^T$ and $F_{v\star} \Sigma_{\dot{q}} F_{v\star}$ are not present in $\Sigma_{\delta\tau}$, unlike the PSD obtained with the DETE method in equation (3.38). Therefore, not only the estimation of τ_{ext} will not be affected by these terms, but also the error range should also be exempt from the associated errors.

3.3.1.2 Generalized momentum observer (GMO)

For this approach, the virtual input torque $\tilde{\tau}$ is computed as follows:

$$\tilde{\tau} = \tau - \left[-C_\star(q_\star, \dot{q}_\star)^T \dot{q}_\star + G_\star(q_\star) + F_{v\star} \dot{q}_\star + F_{s\star} \text{sign}(\dot{q}_\star) \right] \quad (3.58)$$

The RDM that has been rewritten using the generalized momentum in equation (3.44) can be expressed in an equivalent way using $\tilde{\tau}$ defined previously. Due to model uncertainties, equation (3.44) yields:

$$\dot{p} = \tilde{\tau} + \tau_{ext} + \delta\tau \quad (3.59)$$

In this case, the error $\delta\tau$ is defined by:

$$\begin{aligned} \delta\tau = & \left[-C_\star(q_\star, \dot{q}_\star)^T \dot{q}_\star + G_\star(q_\star) + F_{v\star} \dot{q}_\star + F_{s\star} \text{sign}(\dot{q}_\star) \right] \\ & - \left[-C(q, \dot{q})^T \dot{q} + G(q) + F_v \dot{q} + F_s \text{sign}(\dot{q}) \right] \end{aligned} \quad (3.60)$$

With the same assumptions as for the approach based on DETE and similar developments (see Section 3.2.1), the error term $\delta\tau$ is rewritten as the sum of a contribution $\delta\tau^P$ due to parametric errors and a contribution $\delta\tau^D$ due to numerical differentiation errors, such as:

$$\delta\tau^P = -\delta C(q_\star, \dot{q}_\star)^T \dot{q}_\star + \delta G(q_\star) + \delta F_v \dot{q}_\star + \lambda_P \delta F_s \text{sign}(\dot{q}_\star) \quad (3.61)$$

$$\delta\tau^D = -C_\star(q_\star, \dot{q}_\star)^T \delta\dot{q} + F_{v\star} \delta\dot{q} + \lambda_D F_{s\star} \text{sign}(\dot{q}_\star) \quad (3.62)$$

Although the generalized momentum $p_\star(q_\star, \dot{q}_\star)$ is used as the output of the state-space representation, it is not directly measured but computed with errors due to model uncertainties as detailed below:

$$p_\star(q_\star, \dot{q}_\star) = M_{r\star}(q_\star) \dot{q}_\star \quad (3.63)$$

$$= p(q, \dot{q}) + \underbrace{\delta M_r(q_\star) \dot{q}_\star + M_{r\star}(q_\star) \delta\dot{q}}_{\delta p} \quad (3.64)$$

In the same way as $\delta\tau$, δp is also divided into a contribution δp^P due to parametric uncertainties and a contribution δp^D due to numerical differentiation errors, such that:

$$\delta p^P = \delta M_r(q_\star) \dot{q}_\star \quad (3.65)$$

$$\delta p^D = M_{r\star}(q_\star) \delta\dot{q} \quad (3.66)$$

Remark 3.5 *It is worth noting that, whether in $\delta\tau$ or δp , acceleration terms do not need to be calculated and therefore do not generate any error for the GMO method. It is precisely the advantage of this method that makes it widely used.*

From equation (3.59) and using the disturbance model (3.43), the augmented state-space representation is obtained:

$$\left\{ \begin{array}{l} \begin{bmatrix} \dot{p} \\ \dot{\tau}_{ext} \end{bmatrix} = \underbrace{\begin{pmatrix} A_r & G_{ext} \\ \mathbf{0} & -A_{ext} \end{pmatrix}}_A \begin{bmatrix} p \\ \tau_{ext} \end{bmatrix} + \underbrace{\begin{pmatrix} B_r \\ \mathbf{0} \end{pmatrix}}_B \tilde{\tau} + \underbrace{\begin{pmatrix} G_{\delta\tau} & \mathbf{0} \\ \mathbf{0} & B_{ext} \end{pmatrix}}_G \begin{bmatrix} \delta\tau \\ w_{ext} \end{bmatrix} \\ p_\star = \underbrace{\begin{pmatrix} C_r & \mathbf{0} \end{pmatrix}}_C \begin{bmatrix} p \\ \tau_{ext} \end{bmatrix} + \underbrace{\delta p}_v \end{array} \right. \quad (3.67)$$

with $A_r = \mathbf{0}$, $B_r = G_{\delta\tau} = G_{ext} = I$ and $C_r = I$. Contrary to the JPVO described above, for the GMO the measurement noise v is not due only to the measurement error on the position but depends on the uncertainties on the rigid inertia matrix and on the approximated velocity.

Derivation of the PSD

First, we define the rigid regression matrices $\Phi_r \in \mathbb{R}^{n, N_r}$ and $\Omega_r \in \mathbb{R}^{n, N_r}$, such as:

$$-C(q, \dot{q})^T \dot{q} + G(q) + F_v \dot{q} + \lambda_P F_s \text{sign}(\dot{q}) = \Phi_r(q, \dot{q}) \chi_r \quad (3.68)$$

$$M_r(q) \dot{q} = \Omega_r(q, \dot{q}) \chi_r \quad (3.69)$$

where the left-hand sides have been rewritten in a linear form with respect to the rigid base parameters χ_r (in the same respect as [Property 2.3](#)). In a similar way as for equation (2.38), we examine the difference between the equation (3.68) (resp. (3.69)) evaluated in the estimated dynamic parameters and the same expression evaluated in the exact dynamic parameters. When computed in the robot estimated states q_\star and \dot{q}_\star , we recognize that equation (3.61) (resp. (3.65)) can be rewritten as:

$$\delta \tau^P = \Phi_r(q_\star, \dot{q}_\star) \delta \chi_r \quad (3.70)$$

$$\delta p^P = \Omega_r(q_\star, \dot{q}_\star) \delta \chi_r \quad (3.71)$$

where $\delta \chi_r$ is the vector of errors on the rigid base parameters. Therefore the PSD of $\delta \tau$ and δp are respectively given by:

$$\Sigma_{\delta \tau} = \Phi_r \Sigma_{\chi_r} \Phi_r^T + (-C_\star^T + F_{v\star}) \Sigma_{\dot{q}} (-C_\star^T + F_{v\star})^T + \lambda_D^2 F_{s\star} F_{s\star}^T \quad (3.72)$$

$$\Sigma_v = \Omega_r \Sigma_{\chi_r} \Omega_r^T + M_{r\star} \Sigma_{\dot{q}} M_{r\star}^T \quad (3.73)$$

where dependencies in joint coordinates have been removed for the sake of simplicity but Φ_r , Ω_r , C_\star and $M_{r\star}$ depend on the actual robot trajectory. In this case, both $\Sigma_{\delta \tau}$ and Σ_v vary along the robot trajectory.

Following [Remark 3.5](#), the contributions of $M_\star \Sigma_{\dot{q}} M_\star^T$ and $J_{m\star} \Sigma_{\dot{q}} J_{m\star}^T$ have disappeared within $\Sigma_{\delta \tau}$ when compared to the DETE method (equation (3.38)) or the JPVO method (equation (3.56)). However Σ_v is more complex than for the JPVO method (equation (3.57)). Therefore, the behavior of the estimate resulting from the Kalman filter can be expected to depend on the error ratio between $\Sigma_{\delta \tau}$ and Σ_v .

3.3.2 Discretization and Kalman filter design

The continuous-time model in equation (3.45) is sampled at T_s for observer design and analysis. For the design of the Kalman filter, τ_{ext} intervenes by its disturbance model (see [Figure 3.12a](#)). Assuming a zero-order hold for the deterministic input $\tilde{\tau}$, the augmented state-space representation (3.46) is integrated between $t_0 = kT_s$ and $t = (k+1)T_s$ as described in [Section 3.3.2.1](#). However, this model does not correspond to a physical reality, since τ_{ext} is actually a deterministic unknown input (see [Figure 3.12b](#)). Thus equation (3.45) has to be discretized differently for the subsequent filter analysis as detailed in [Section 3.3.2.2](#). This analysis is necessary for the evaluation step of the external torque estimate.

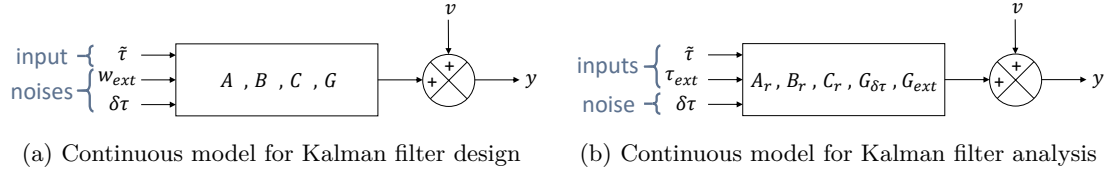


Figure 3.12: Continuous models used for the Kalman filter design and analysis

3.3.2.1 Sampled-time model for Kalman filter design

After approximating the state error \mathbf{w} and the measurement error \mathbf{v} by white and uncorrelated noises of PSD Σ_w (as defined in equation (3.47)) and Σ_v respectively, the augmented state-space representation (3.46) is discretized as follows [Alazard 2005]:

$$\begin{cases} \mathbf{X}(k+1) = \mathbf{A}_d \mathbf{X}(k) + \mathbf{B}_d \tilde{\tau}(k) + \mathbf{G}_d \mathbf{w}(k) \\ \mathbf{Y}(k) = \mathbf{C}_d \mathbf{X}(k) + \mathbf{v}(k) \end{cases} \quad (3.74)$$

where $\mathbf{X}(k)$ denotes the sampled signal of \mathbf{X} and similarly for the other signals involved. The discrete state-space matrices are given by:

$$\mathbf{A}_d = e^{\mathbf{A}T_s} \quad ; \quad \mathbf{B}_d = \int_0^{T_s} e^{\mathbf{A}\nu} \mathbf{B} d\nu \quad ; \quad \mathbf{C}_d = \mathbf{C} \quad (3.75)$$

For the particular case of \mathbf{G}_d , we get:

- for JPVO:

$$\mathbf{G} = \begin{pmatrix} \mathbf{0} & \mathbf{0} \\ \mathbf{J}_{m^*}^{-1} & \mathbf{0} \\ \mathbf{0} & \mathbf{B}_{ext} \end{pmatrix} \Rightarrow \mathbf{G}_d = \begin{pmatrix} \mathbf{0} & \mathbf{0} \\ \mathbf{I} & \mathbf{0} \\ \mathbf{0} & \mathbf{I} \end{pmatrix} \quad (3.76)$$

- for GMO:

$$\mathbf{G} = \begin{pmatrix} \mathbf{I} & \mathbf{0} \\ \mathbf{0} & \mathbf{B}_{ext} \end{pmatrix} \Rightarrow \mathbf{G}_d = \begin{pmatrix} \mathbf{I} & \mathbf{0} \\ \mathbf{0} & \mathbf{I} \end{pmatrix} \quad (3.77)$$

We can define the matrices \mathbf{A}_{d_r} , \mathbf{B}_{d_r} , \mathbf{C}_{d_r} , $\mathbf{G}_{d_{\delta\tau}}$ and $\mathbf{G}_{d_{ext}}$ as the discrete-time equivalents of \mathbf{A}_r , \mathbf{B}_r , \mathbf{C}_r , $\mathbf{G}_{\delta\tau}$ and \mathbf{G}_{ext} , such as:

$$\mathbf{A}_d = \begin{pmatrix} \mathbf{A}_{d_r} & \mathbf{G}_{d_{ext}} \\ \mathbf{0} & \mathbf{A}_{d_{ext}} \end{pmatrix} ; \quad \mathbf{B}_d = \begin{pmatrix} \mathbf{B}_{d_r} \\ \mathbf{0} \end{pmatrix} ; \quad \mathbf{C}_d = \begin{pmatrix} \mathbf{C}_{d_r} \\ \mathbf{0} \end{pmatrix}^T ; \quad \mathbf{G}_d = \begin{pmatrix} \mathbf{G}_{d_{\delta\tau}} & \mathbf{0} \\ \mathbf{0} & \mathbf{I} \end{pmatrix} \quad (3.78)$$

Assuming that T_s is small with respect to the response time of the system, the covariances matrices $\Sigma_w(k)$ and $\Sigma_v(k)$ of respectively $\mathbf{w}(k)$ and $\mathbf{v}(k)$ verify:

$$\Sigma_w(k) \approx T_s (\mathbf{G}_d^T \mathbf{G}) \Sigma_w (\mathbf{G}^T \mathbf{G}_d) \quad (3.79)$$

$$\Sigma_v(k) = \frac{1}{T_s} \Sigma_v \quad (3.80)$$

We can then extract from $\Sigma_w(k)$ the covariance matrices $\Sigma_{\delta\tau}(k)$ and $\Sigma_{w_{ext}}(k)$ of respectively $\delta\tau(k)$ and $w_{ext}(k)$, given that:

$$\Sigma_w(k) = \begin{pmatrix} \Sigma_{\delta\tau}(k) & \mathbf{0} \\ \mathbf{0} & \Sigma_{w_{ext}}(k) \end{pmatrix} \quad (3.81)$$

The asymptotic discrete Kalman gain $K_f(k)$ is computed at each time step k based on the discrete state-space representation (3.74) and the covariances matrices $\Sigma_w(k)$ and $\Sigma_v(k)$. The equations of the discrete Kalman filter are given by (see Figure 3.13):

$$\begin{cases} \hat{X}(k+1) = A_d \hat{X}(k) + B_d \tilde{\tau}(k) + K_f(k) [Y(k+1) - C_d (A_d \hat{X}(k) + B_d \tilde{\tau}(k))] \\ \hat{Y}(k) = C_d \hat{X}(k) \end{cases} \quad (3.82)$$

The estimation $\hat{\tau}_{ext}(k)$ of $\tau_{ext}(k)$ is extracted from $\hat{X}(k)$ with:

$$\hat{\tau}_{ext}(k) = \begin{pmatrix} \mathbf{0} & I \end{pmatrix} \hat{X}(k) \quad (3.83)$$

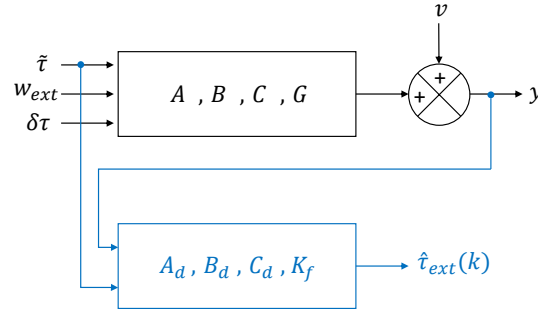


Figure 3.13: Estimation of $\tau_{ext}(k)$ resulting from the Kalman filter design

3.3.2.2 Sampled-time model for Kalman filter analysis

In this case, τ_{ext} is considered as a deterministic unknown input and therefore the sampled-time model is different from the one used in the Kalman filter design. The reduced state-space representation (3.45) is first rewritten as:

$$\begin{cases} \dot{X}_r = A_r X_r + B_u u + G_{\delta\tau} \delta\tau \\ Y = C_r X_r + v \end{cases} \quad (3.84)$$

where $B_u = [G_{ext} \ B_r]$ and $u = [\tau_{ext}^T \ \tilde{\tau}^T]^T$ contains the input vectors. Then the resulting discrete state-space representation is:

$$\begin{cases} X_r(k+1) = A_{a_r} X_r(k) + B_{a_u} u(k) + G_{a_{\delta\tau}} \delta\tau(k) \\ Y_r(k) = C_{a_r} X_r(k) + v(k) \end{cases} \quad (3.85)$$

The discrete state-space matrices are given by:

$$\mathbf{A}_{a_r} = e^{\mathbf{A}_r T_s} \quad ; \quad \mathbf{B}_{a_u} = \int_0^{T_s} e^{\mathbf{A}_r \nu} \mathbf{B}_u d\nu \quad ; \quad \mathbf{C}_{a_r} = \mathbf{C}_r \quad ; \quad \mathbf{G}_{a_{\delta\tau}} = \begin{cases} \begin{bmatrix} \mathbf{0} & \mathbf{I} \end{bmatrix}^T & \text{if JPVO} \\ \mathbf{I} & \text{if GMO} \end{cases} \quad (3.86)$$

Denoting $\mathbf{B}_{a_u} = \begin{bmatrix} \mathbf{G}_{a_{ext}} & \mathbf{B}_{a_r} \end{bmatrix}$ with $\mathbf{G}_{a_{ext}}$ and \mathbf{B}_{a_r} the discrete-time equivalents of \mathbf{G}_{ext} and \mathbf{B}_r respectively, we can notice by using properties on matrix exponentials and structures of matrices \mathbf{A} and \mathbf{B} that:

$$\mathbf{A}_{a_r} = \mathbf{A}_{d_r} \quad ; \quad \mathbf{B}_{a_r} = \mathbf{B}_{d_r} \quad ; \quad \mathbf{C}_{a_r} = \mathbf{C}_{d_r} \quad ; \quad \mathbf{G}_{a_{\delta\tau}} = \mathbf{G}_{d_{\delta\tau}} \quad (3.87)$$

Then the state-space representation (3.85) is rewritten as:

$$\begin{cases} \mathbf{X}_r(k+1) &= \mathbf{A}_{d_r} \mathbf{X}_r(k) + \mathbf{G}_{a_{ext}} \boldsymbol{\tau}_{ext}(k) + \mathbf{B}_{d_r} \tilde{\boldsymbol{\tau}}(k) + \mathbf{G}_{d_{\delta\tau}} \boldsymbol{\delta\tau}(k) \\ \mathbf{Y}_r(k) &= \mathbf{C}_{d_r} \mathbf{X}_r(k) + \mathbf{v}(k) \end{cases} \quad (3.88)$$

Finally, we observe that state-space representation (3.88) (of the analysis model) differs from that of $\mathbf{X}_r(k)$ extracted from state-space representation (3.74) (of the design model) only by $\mathbf{G}_{a_{ext}}$ instead of $\mathbf{G}_{d_{ext}}$, which results from the different treatment of $\boldsymbol{\tau}_{ext}$ in the discretization step. The analysis model in equation (3.88) is used in the next section for the evaluation phase of the impact detection algorithm in order to examine the estimation error on $\hat{\boldsymbol{\tau}}_{ext}(k)$.

3.3.3 Evaluation of the estimated external torque

Similarly to the DETE in Section 3.2.2, the proposed approach for deriving an adaptive detection threshold with disturbance observers is based on stochastic methods. Since the estimated state $\hat{\boldsymbol{\tau}}_{ext}(k)$ reconstructs all external disturbances, i. e. not only the external torque due to a contact but also all modeling errors, and considering that they are not separately distinguishable, the objective is to determine an interval within which the estimate would lie in the absence of external contact, i. e. if it was due solely to model errors. This interval is inferred from the variance of the estimation error on $\boldsymbol{\tau}_{ext}(k)$ in the absence of external contact. In this way, any additional contribution within $\hat{\boldsymbol{\tau}}_{ext}(k)$ above this threshold could only be due to an impact.

In the following, we are interested in the variance of the estimation error $\boldsymbol{\tau}_{ext}(k) - \hat{\boldsymbol{\tau}}_{ext}(k)$ in the absence of external torque $\boldsymbol{\tau}_{ext}(k)$, which amounts to studying the variance of $\hat{\boldsymbol{\tau}}_{ext}(k)$ when the latter results only from the model errors $\boldsymbol{\delta\tau}(k)$ and $\mathbf{v}(k)$. To achieve this, an input-output formulation of the complete system (Kalman filter design model and real system analysis model) is sought to obtain $\hat{\boldsymbol{\tau}}_{ext}(k)$ as a function of the inputs $\boldsymbol{\tau}_{ext}(k)$, $\boldsymbol{\delta\tau}(k)$ and $\mathbf{v}(k)$ (see Figure 3.14 where \mathbf{A}_t^k , \mathbf{B}_t^k and \mathbf{C}_t are matrices to be determined). For this purpose, the approach consists in evaluating $\hat{\boldsymbol{\tau}}_{ext}(k)$ resulting from the Kalman filter obtained with the design model (3.74) using the analysis system (3.88).

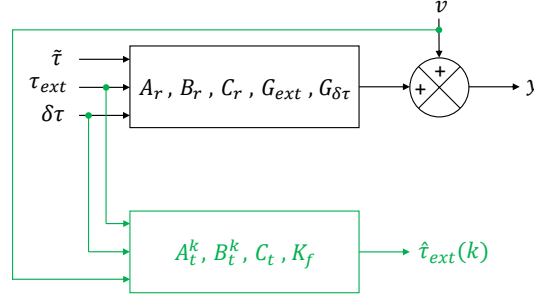


Figure 3.14: Input-output formulation of $\hat{\tau}_{ext}(k)$ according to $\tau_{ext}(k)$, $\delta\tau(k)$ and $v(k)$

First, the estimated state $\hat{\tau}_{ext}(k+1)$ is isolated from the Kalman filter equation (3.82):

$$\hat{\tau}_{ext}(k+1) = \mathbf{A}_{d_{ext}} \hat{\tau}_{ext}(k) + \mathbf{K}_2(k) \left[\mathbf{Y}(k+1) - \mathbf{C}_d \left(\mathbf{A}_d \hat{\mathbf{X}}(k) + \mathbf{B}_d \tilde{\tau}(k) \right) \right] \quad (3.89)$$

with $\mathbf{K}_f(k) = \begin{bmatrix} \mathbf{K}_1(k)^T & \mathbf{K}_2(k)^T \end{bmatrix}^T$ such as $\mathbf{K}_1(k)$ and $\mathbf{K}_2(k)$ correspond to states $\mathbf{X}_r(k)$ and $\tau_{ext}(k)$ respectively. The two terms $\mathbf{Y}(k+1)$ and $\mathbf{C}_d \left(\mathbf{A}_d \hat{\mathbf{X}}(k) + \mathbf{B}_d \tilde{\tau}(k) \right)$ in equation (3.89) are now detailed based on the analysis model. Using equation (3.88), $\mathbf{Y}(k+1)$ becomes:

$$\mathbf{Y}(k+1) = \mathbf{C}_{d_r} \left(\mathbf{A}_{d_r} \mathbf{X}_r(k) + \mathbf{G}_{a_{ext}} \tau_{ext}(k) + \mathbf{B}_{d_r} \tilde{\tau}(k) + \mathbf{G}_{d_{\delta\tau}} \delta\tau(k) \right) + \mathbf{v}(k+1) \quad (3.90)$$

Then $\mathbf{C}_d \left(\mathbf{A}_d \hat{\mathbf{X}}(k) + \mathbf{B}_d \tilde{\tau}(k) \right)$ is made explicit by decomposing \mathbf{A}_d and \mathbf{B}_d using equations (3.78):

$$\mathbf{C}_d \left(\mathbf{A}_d \hat{\mathbf{X}}(k) + \mathbf{B}_d \tilde{\tau}(k) \right) = \mathbf{C}_{d_r} \left(\mathbf{A}_{d_r} \hat{\mathbf{X}}_r(k) + \mathbf{G}_{d_{ext}} \hat{\tau}_{ext}(k) + \mathbf{B}_{d_r} \tilde{\tau}(k) \right) \quad (3.91)$$

Therefore equation (3.89) leads to:

$$\begin{aligned} \hat{\tau}_{ext}(k+1) &= \mathbf{K}_2(k) \mathbf{C}_{d_r} \mathbf{A}_{d_r} \tilde{\mathbf{X}}_r(k) + [\mathbf{A}_{d_{ext}} - \mathbf{K}_2(k) \mathbf{C}_{d_r} \mathbf{G}_{d_{ext}}] \hat{\tau}_{ext}(k) \\ &\quad + \mathbf{K}_2(k) \mathbf{C}_{d_r} \mathbf{G}_{a_{ext}} \tau_{ext}(k) + \mathbf{K}_2(k) \mathbf{C}_{d_r} \mathbf{G}_{d_{\delta\tau}} \delta\tau(k) + \mathbf{K}_2(k) \mathbf{v}(k+1) \end{aligned} \quad (3.92)$$

with $\tilde{\mathbf{X}}_r(k) = \mathbf{X}_r(k) - \hat{\mathbf{X}}_r(k)$ the estimation error on $\mathbf{X}_r(k)$. Finally, $\tilde{\mathbf{X}}_r(k+1)$ is made explicit, using on the one hand, the analysis model in equation (3.88) for $\mathbf{X}_r(k+1)$, and on the other hand, the Kalman filter equation (3.82) for $\hat{\mathbf{X}}_r(k+1)$. It yields:

$$\begin{aligned} \tilde{\mathbf{X}}_r(k+1) &= [\mathbf{A}_{d_r} - \mathbf{K}_1(k) \mathbf{C}_{d_r} \mathbf{A}_{d_r}] \tilde{\mathbf{X}}_r(k) - [\mathbf{G}_{d_{ext}} - \mathbf{K}_1(k) \mathbf{C}_{d_r} \mathbf{G}_{d_{ext}}] \hat{\tau}_{ext}(k) \\ &\quad + [\mathbf{G}_{a_{ext}} - \mathbf{K}_1(k) \mathbf{C}_{d_r} \mathbf{G}_{a_{ext}}] \tau_{ext}(k) + [\mathbf{G}_{d_{\delta\tau}} - \mathbf{K}_1(k) \mathbf{C}_{d_r} \mathbf{G}_{d_{\delta\tau}}] \delta\tau(k) \\ &\quad - \mathbf{K}_1(k) \mathbf{v}(k+1) \end{aligned} \quad (3.93)$$

Using equations (3.92) and (3.93), the following discrete state-space representation is derived at each time step k :

$$\begin{cases} \mathbf{X}_t(k+1) &= \mathbf{A}_t^k \mathbf{X}_t(k) + \mathbf{B}_t^k \mathbf{U}_t(k) \\ \mathbf{Y}_t(k) &= \mathbf{C}_t \mathbf{X}_t(k) \end{cases} \quad (3.94)$$

with

$$\mathbf{X}_t(k) = \begin{pmatrix} \tilde{\mathbf{X}}_r(k) \\ \hat{\boldsymbol{\tau}}_{ext}(k) \end{pmatrix} ; \quad \mathbf{Y}_t(k) = \hat{\boldsymbol{\tau}}_{ext}(k) ; \quad \mathbf{U}_t(k) = \begin{pmatrix} \boldsymbol{\tau}_{ext}(k) \\ \boldsymbol{\delta}\boldsymbol{\tau}(k) \\ \mathbf{v}(k+1) \end{pmatrix} \quad (3.95)$$

and

$$\mathbf{A}_t^k = \begin{pmatrix} \mathbf{A}_{d_r} - \mathbf{K}_1(k) \mathbf{C}_{d_r} \mathbf{A}_{d_r} & -\mathbf{G}_{d_{ext}} + \mathbf{K}_1(k) \mathbf{C}_{d_r} \mathbf{G}_{d_{ext}} \\ \mathbf{K}_2(k) \mathbf{C}_{d_r} \mathbf{A}_{d_r} & \mathbf{A}_{d_{ext}} - \mathbf{K}_2(k) \mathbf{C}_{d_r} \mathbf{G}_{d_{ext}} \end{pmatrix} \quad (3.96)$$

$$\mathbf{B}_t^k = \begin{pmatrix} \mathbf{G}_{a_{ext}} - \mathbf{K}_1(k) \mathbf{C}_{d_r} \mathbf{G}_{a_{ext}} & \mathbf{G}_{d_{\delta\tau}} - \mathbf{K}_1(k) \mathbf{C}_{d_r} \mathbf{G}_{d_{\delta\tau}} & -\mathbf{K}_1(k) \\ \mathbf{K}_2(k) \mathbf{C}_{d_r} \mathbf{G}_{a_{ext}} & \mathbf{K}_2(k) \mathbf{C}_{d_r} \mathbf{G}_{d_{\delta\tau}} & \mathbf{K}_2(k) \end{pmatrix} \quad (3.97)$$

$$\mathbf{C}_t = \begin{pmatrix} \mathbf{0} & \mathbf{I} \end{pmatrix} \quad (3.98)$$

Based on the state-space representation (3.94), we can now derive another state-space representation in the absence of external torque $\boldsymbol{\tau}_{ext}(k)$. Denoting $\tilde{\mathbf{X}}_r^e(k)$ and $\hat{\boldsymbol{\tau}}_{ext}^e(k)$ the states $\tilde{\mathbf{X}}_r(k)$ and $\hat{\boldsymbol{\tau}}_{ext}(k)$ under these circumstances, the following state-space representation is deduced:

$$\begin{cases} \mathbf{X}_e(k+1) = \mathbf{A}_e^k \mathbf{X}_e(k) + \mathbf{B}_e^k \mathbf{U}_e(k) \\ \mathbf{Y}_e(k) = \mathbf{C}_e \mathbf{X}_e(k) \end{cases} \quad (3.99)$$

with

$$\mathbf{X}_e(k) = \begin{pmatrix} \tilde{\mathbf{X}}_r^e(k) \\ \hat{\boldsymbol{\tau}}_{ext}^e(k) \end{pmatrix} ; \quad \mathbf{Y}_e(k) = \hat{\boldsymbol{\tau}}_{ext}^e(k) ; \quad \mathbf{U}_e(k) = \begin{pmatrix} \boldsymbol{\delta}\boldsymbol{\tau}(k) \\ \mathbf{v}(k+1) \end{pmatrix} \quad (3.100)$$

and

$$\mathbf{A}_e^k = \mathbf{A}_t^k ; \quad \mathbf{B}_e^k = \begin{pmatrix} \mathbf{G}_{d_{\delta\tau}} - \mathbf{K}_1(k) \mathbf{C}_{d_r} \mathbf{G}_{d_{\delta\tau}} & -\mathbf{K}_1(k) \\ \mathbf{K}_2(k) \mathbf{C}_{d_r} \mathbf{G}_{d_{\delta\tau}} & \mathbf{K}_2(k) \end{pmatrix} ; \quad \mathbf{C}_e = \mathbf{C}_t \quad (3.101)$$

We denote $\boldsymbol{\Sigma}_{\mathbf{X}_e}(k)$ the state covariance matrix of $\mathbf{X}_e(k)$ defined by:

$$\boldsymbol{\Sigma}_{\mathbf{X}_e}(k) := E \left[\mathbf{X}_e(k) \mathbf{X}_e(k)^T \right] \quad (3.102)$$

In the following, we assume that $\mathbf{X}_e(k)$ and $\mathbf{U}_e(k)$ are not correlated, which is an approximation because, in particular, the estimation error $\tilde{\mathbf{X}}_r^e(k)$ and the model errors $\boldsymbol{\delta}\boldsymbol{\tau}(k)$ are not independent and may be correlated. We also consider that $\boldsymbol{\delta}\boldsymbol{\tau}(k)$ and $\mathbf{v}(k+1)$ are not correlated. Thus the state covariance matrix $\boldsymbol{\Sigma}_{\mathbf{X}_e}(k)$ verifies:

$$\boldsymbol{\Sigma}_{\mathbf{X}_e}(k+1) = \mathbf{A}_e^k \boldsymbol{\Sigma}_{\mathbf{X}_e}(k) \left(\mathbf{A}_e^k \right)^T + \mathbf{B}_e^k \begin{pmatrix} \boldsymbol{\Sigma}_{\boldsymbol{\delta}\boldsymbol{\tau}}(k) & \mathbf{0} \\ \mathbf{0} & \boldsymbol{\Sigma}_{\mathbf{v}}(k+1) \end{pmatrix} \left(\mathbf{B}_e^k \right)^T \quad (3.103)$$

By considering that the dynamics of $\boldsymbol{\Sigma}_{\mathbf{X}_e}(k)$ is sufficiently slow in comparison with the variation of the model and of the covariance matrices $\boldsymbol{\Sigma}_{\boldsymbol{\delta}\boldsymbol{\tau}}(k)$ and $\boldsymbol{\Sigma}_{\mathbf{v}}(k+1)$ so that $\boldsymbol{\Sigma}_{\mathbf{X}_e}(k+1) \approx \boldsymbol{\Sigma}_{\mathbf{X}_e}(k)$, then at each time step k , the covariance matrix $\boldsymbol{\Sigma}_{\mathbf{X}_e}(k)$ is the positive solution of the algebraic equation of Riccati (3.103).

Finally, the covariance matrix of $\hat{\boldsymbol{\tau}}_{ext}^e(k)$ is given by:

$$\boldsymbol{\Sigma}_e(k) := E \left[\hat{\boldsymbol{\tau}}_{ext}^e(k) \left(\hat{\boldsymbol{\tau}}_{ext}^e(k) \right)^T \right] = \mathbf{C}_e \boldsymbol{\Sigma}_{\mathbf{X}_e}(k) \mathbf{C}_e^T \quad (3.104)$$

The standard deviation vector $\boldsymbol{\sigma}_e(k)$ of $\hat{\boldsymbol{\tau}}_{ext}^e(k)$ is obtained by assuming that the non-diagonal elements within $\boldsymbol{\Sigma}_e(k)$, which refer to correlated errors between the axes, are negligible with respect to the variance of the error for each axis, which can be verified experimentally (see Remark 3.2). Then it yields:

$$\text{for any axis } i \in \llbracket 1, n \rrbracket, \quad \sigma_{e_i}(k) = \sqrt{\Sigma_{e_{ii}}(k)} \quad (3.105)$$

Note that $\boldsymbol{\sigma}_e(k)$ is computed at each time step along the robot trajectory since the system (3.99) is time-varying.

Remark 3.6 *If the reference trajectory (or a trajectory without contact) is known in advance, or at least for few time steps, then the covariance matrices $\boldsymbol{\Sigma}_w(k)$ and $\boldsymbol{\Sigma}_v(k)$, hence the Kalman gain $\mathbf{K}_f(k)$ and the standard deviation vector $\boldsymbol{\sigma}_e(k)$, can be computed in advance or even offline. This trajectory has the advantage of not being affected by the impact but may be subject to trajectory tracking errors. In addition, it reduces the constraint of calculating the Kalman gain online and in real time.*

According to equation (3.99), $\hat{\boldsymbol{\tau}}_{ext}^e(k)$ results from a linear combination of the error terms $\boldsymbol{\delta}\mathbf{X}_r$, $\boldsymbol{\delta}\dot{\mathbf{q}}$ and $\boldsymbol{\delta}\ddot{\mathbf{q}}$ that we have assumed to follow a normal distribution in Chapter 2: "Modeling serial robot manipulators under uncertainties". Under these assumptions, $\hat{\boldsymbol{\tau}}_{ext}^e(k)$ also follows a normal distribution by linearity. Moreover, $\boldsymbol{\delta}\boldsymbol{\tau}$ and \mathbf{v} are assumed to be zero mean, thus $\hat{\boldsymbol{\tau}}_{ext}^e(k)$ is also zero mean. Then, according to the 3σ -confidence interval of $\hat{\boldsymbol{\tau}}_{ext}^e(k)$, in 99.7% of the cases we get:

$$\hat{\boldsymbol{\tau}}_{ext}^e(k) \underset{99.7\%}{\in} [-3\boldsymbol{\sigma}_e(k), 3\boldsymbol{\sigma}_e(k)] \quad (3.106)$$

In other words, $[-3\boldsymbol{\sigma}_e(k), 3\boldsymbol{\sigma}_e(k)]$ represents at each time step the envelope in which $\hat{\boldsymbol{\tau}}_{ext}^e(k)$ would lie in 99.7% of the cases if it was only due to the model errors $\boldsymbol{\delta}\boldsymbol{\tau}(k)$ and $\mathbf{v}(k)$. This leads to the following rule for evaluating $\hat{\boldsymbol{\tau}}_{ext}^e(k)$ and detecting an impact:

If $\exists i \in \llbracket 1, n \rrbracket$ **s.t.** $\hat{\tau}_{ext_i} \notin [-3\sigma_{e_i}(k), 3\sigma_{e_i}(k)]$

Then $\tau_{ext_i} \neq 0$: impact occurrence with 99.7% of confidence

Consequently, the adaptive detection threshold considered is defined by $\mathbf{T}^k = \pm 3\boldsymbol{\sigma}_e(k)$. Thus the logical detection signal that indicates the occurrence of an impact is given at each time step by:

$$d(k) = \begin{cases} 1 & \text{if } \exists i \in \llbracket 1, n \rrbracket \text{ s.t. } |\hat{\tau}_{ext_i}(k)| > |3\sigma_{e_i}(k)| \\ 0 & \text{otherwise.} \end{cases}$$

**Summary of the methodology:
Disturbance observers design (JPVO and GMO)**

Known a priori: $\Sigma_{\chi_r}, \Sigma_{\dot{q}}, \Sigma_{\ddot{q}}$ (JPVO and GMO), $\Sigma_{\ddot{q}}$ (JPVO only) **To tune:** A_{ext}, Σ_{ext}

1. Measure τ, q_*, \dot{q}_* (JPVO and GMO), \ddot{q}_* (JPVO only)
2. Calculate $\tilde{\tau}$ with

$$\text{JPVO} \quad \tilde{\tau} = \tau - [M_*(q_*)\ddot{q}_* + C_*(q_*, \dot{q}_*)\dot{q}_* + G_*(q_*) + F_{S^*} \text{sign}(\dot{q}_*)]$$

$$\text{GMO} \quad \tilde{\tau} = \tau - [-C_*(q_*, \dot{q}_*)^T \dot{q}_* + G_*(q_*) + F_{v^*}\dot{q}_* + F_{S^*} \text{sign}(\dot{q}_*)]$$

3. Compute the matrices A, B, C and G and the power spectral densities Σ_w and Σ_v of state and measurement noises with

$$\text{JPVO} \quad \begin{aligned} \Sigma_{\delta\tau^P} &= \varphi_r(q_*, \dot{q}_*, \ddot{q}_*) \Sigma_{\chi_r} \varphi_r(q_*, \dot{q}_*, \ddot{q}_*)^T \\ \Sigma_{\delta\tau^D} &= M_*(q_*) \Sigma_{\ddot{q}} M_*(q_*)^T + C_*(q_*, \dot{q}_*) \Sigma_{\dot{q}} C_*(q_*, \dot{q}_*)^T + \lambda_D^2 F_{S^*} F_{S^*}^T \end{aligned}$$

$$\text{GMO} \quad \begin{aligned} \Sigma_{\delta\tau^P} &= \Phi_r(q_*, \dot{q}_*) \Sigma_{\chi_r} \Phi_r(q_*, \dot{q}_*)^T \\ \Sigma_{\delta\tau^D} &= [-C_*(q_*, \dot{q}_*)^T + F_{v^*}] \Sigma_{\dot{q}} [-C_*(q_*, \dot{q}_*)^T + F_{v^*}]^T + \lambda_D^2 F_{S^*} F_{S^*}^T \end{aligned}$$

$$\Sigma_{\delta\tau} = \Sigma_{\delta\tau^P} + \Sigma_{\delta\tau^D}$$

$$\Sigma_w = \begin{pmatrix} \Sigma_{\delta\tau} & 0 \\ 0 & \Sigma_{ext} \end{pmatrix}$$

$$\text{JPVO} \quad \Sigma_v = \Sigma_q$$

$$\text{GMO} \quad \Sigma_v = \Omega(q_*, \dot{q}_*) \Sigma_{\chi_r} \Omega(q_*, \dot{q}_*)^T + M_{r^*}(q_*) \Sigma_{\dot{q}} M_{r^*}(q_*)^T$$

4. Compute the discrete matrices A_d, B_d, C_d, G_d and the covariance matrices $\Sigma_w(k)$ and $\Sigma_v(k)$
5. Calculate the Kalman gain $K_f(k)$
6. Compute the matrices A_e^k, B_e^k, C_e and determine the threshold T with

Steady-state solution $\Sigma_{x_e}(k)$ of the Riccati equation: $\Sigma_{x_e}(k) = A_e^k \Sigma_{x_e}(k) (A_e^k)^T + B_e^k \begin{pmatrix} \Sigma_{\delta\tau}(k) & 0 \\ 0 & \Sigma_v(k+1) \end{pmatrix} (B_e^k)^T$

$$\Sigma_e(k) = C_e \Sigma_{x_e}(k) C_e^T$$

$$T_i^k = \pm 3 \sqrt{\Sigma_{e_{ii}}(k)} \text{ for the 99.7\%-confidence interval}$$

7. Calculate the estimated state $\hat{t}_{ext}(k)$
8. Compute the alert signal indicating the detection of an impact with

$$d(k) = \begin{cases} 1 & \text{if } \exists i \in \llbracket 1, n \rrbracket \text{ s.t. } |\hat{t}_{ext_i}(k)| > T_i(k) \\ 0 & \text{otherwise.} \end{cases}$$

NB: Steps 1 to 6 can be processed offline if Σ_w and Σ_v are evaluated on the reference trajectory known in advance.

3.3.4 Discussion

In this section, the impact detection strategies developed previously are compared: first the two types of approaches (DETE and disturbance observers), then the two types of disturbance observers (JPVO and GMO). Simulations results are used to support the conclusions drawn.

Direct external torque estimation and disturbance observers

The main difference between the DETE method and the disturbance observers is the filtering nature of the latter. This implies that the method based on DETE can be interesting for its rapid response compared to disturbance observers. When there is an acceptable amount of noise (i. e. of uncertainties), the detection threshold is also low, which ensures a good detection of the impact in terms of rapidity and sensitivity (see Figure 3.15). It also requires a lower cost of implementation and real-time resources compared to the use of a Kalman filter. However, as soon as there is a significant amount of uncertainties, the DETE response is likely to be noisy with more false alarms, making it difficult to exploit for subsequent use (e. g. reconstruction of the applied force), and less sensitive due to the increase in the error range (see Figure 3.16). On the other hand, the observer-based approach offers additional adjustment parameters with \mathbf{A}_{ext} and $\Sigma_{w_{ext}}$ from the disturbance model (see Figure 3.17). In the next chapter, the specific influence of these parameters on the detection characteristics are studied.

Joint position and velocity observer and generalized momentum observer

The distinction in these two methods lies on the different distribution between state and measurement noises. For the JPVO, the measurement noise is only the noise on the measured joint position. Then in this case, the ratio Σ_w / Σ_v is likely to be very large due, on the one hand, to the presence of significant error terms within Σ_w (e. g. inertial and acceleration terms, among others) and, on the other hand, to the resolution of position sensors that is usually low. This implies that the filter will rely more on the measurement than on the model, leading to a rapid estimation but with the risk of being noisy. For the GMO, the analysis of the ratio Σ_w / Σ_v is less straightforward since it is related to the relative proportion of errors between those on the generalized momentum and those on the other dynamic parameters involved. In addition, the trend may vary from one axis to another due in particular to the different orders of magnitude of the inertia between the axes. Another notable difference between the two observers is the presence of acceleration terms for the JPVO: for a high dynamic trajectory, the JPVO is likely to be less sensitive than the GMO, while for a trajectory where the acceleration terms contribute slightly, the JPVO will have the advantage of being faster than the GMO (see Figure 3.15 and Figure 3.17).

Given that the estimated state $\hat{\tau}_{ext}(k)$ results not only from inputs in the external torque $\tau_{ext}(k)$ but also in the disturbances $\delta\tau(k)$ and $\mathbf{v}(k)$ (see Section 3.3.3), a detailed frequency-domain study of the filtering effect is carried out in the next chapter.

Simulation examples

Below are simulations carried out on the application case of the ISYBOT prototype robot. They aim to illustrate these different situations in the rigid case, according to the amount of uncertainties and the adjustment of the parameters \mathbf{A}_{ext} and Σ_{ext} for the disturbance observers.

Simulation parameters

Parametric and numerical differentiation errors are both simulated, in a favorable case with few errors (**U1**) and in an unfavorable case with a large amount of errors (**U2**):

- **U1**:
 - for each parameter i , $\% \sigma_{\chi_i} \in [0\%, 5\%]$,
 - first-order low-pass filtered derivative of cut-off frequency $\omega_c = 2\pi 10$ rad/s.
- **U2**:
 - for each parameter i , $\% \sigma_{\chi_i} \in [0\%, 20\%]$,
 - first-order low-pass filtered derivative of cut-off frequency $\omega_c = 2\pi 60$ rad/s.

Each $\% \sigma_{\chi_i}$ is fixed randomly and independently within these ranges, prior to the simulation and with the same random distribution between **U1** and **U2**. Simulations are based on a given random realization of the uncertain parameters $\mathbf{X}_{r\star}$ according to a normal distribution, centered around the exact values \mathbf{X}_r and of standard deviation deduced from $\% \sigma_{\chi}$. The evolution of the estimates and the detection thresholds may slightly differ from one random distribution to another, but the overall trend remains similar. The terms \mathbf{A}_d and \mathbf{A}_{dd} within $\Sigma_{\dot{q}}$ and $\Sigma_{\ddot{q}}$ are computed based on a previously simulated trajectory without contact. The speed threshold α related to the errors on dry friction at low speed is set equal to $\alpha = 0.05 \mathbf{I}_n$ rad/s. Parameters \mathbf{A}_{ext} and Σ_{ext} are identical for both disturbance observers and are indicated in the figure caption.

Simulations are carried out on the sinusoidal trajectory defined in [Section 3.2.3](#). An external torque modeled by a step of 8 Nm is applied on axis 3 at 5s. The responses obtained for the residual (DETE) and the estimation of the external disturbance (JPVO and GMO), as well as their respective detection threshold corresponding to the 3σ -confidence interval, are illustrated below for axis 3 in three different situations of uncertainties or tuning. The delay between the beginning of the impact and the impact detection is indicated for each method, with the 2σ - and the 3σ -confidence intervals for comparison purposes. The detection times are given as an indication for comparison between the different methods. As a reference, the speed of the robot's end-effector at the beginning of the impact is 1.05 m/s.

Through these simulation examples, we can see that the residual must not only be rapid, but the detection threshold must also be low enough for the impact to be detected in a short time. In addition, the static error must be reasonable if the external torque is to be accurately reconstructed (e.g. to deduce the applied force if the contact point on the robot is known). There is therefore a need for defined criteria to characterize the impact detection, which will be explored in the next chapter based on experimental data.

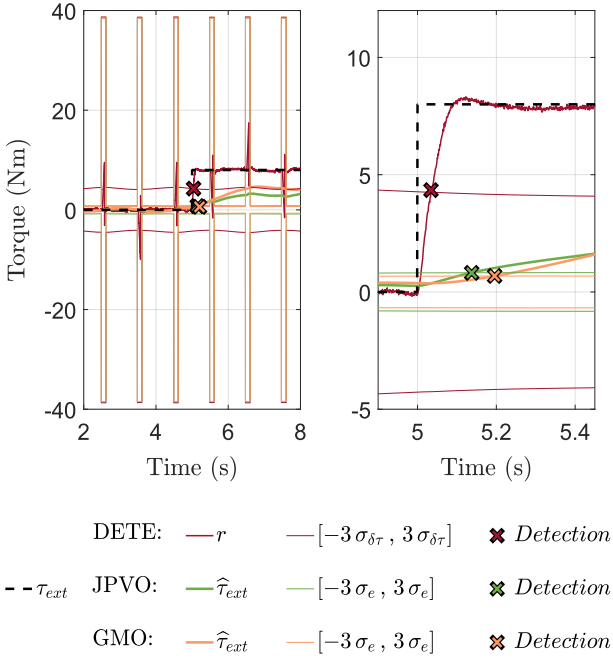


Figure 3.15: Case $U1$ — $A_{ext} = I, \Sigma_{ext} = I$

Method	Detection time at 2σ (ms)	Detection time at 3σ (ms)
DETE	22	35
JPVO	73	137
GMO	105	196

In this favorable situation in terms of uncertainties, the DETE method allows an impact detection in a short time, while the responses of disturbance observers are slower, resulting in longer detection times. The residual obtained by DETE effectively reconstructs the external torque, making it properly usable for further analyses. The detection thresholds are almost identical between JPVO and GMO but the estimate with the JPVO is slightly faster. Both estimations show a significant static error compared to the external torque actually applied.

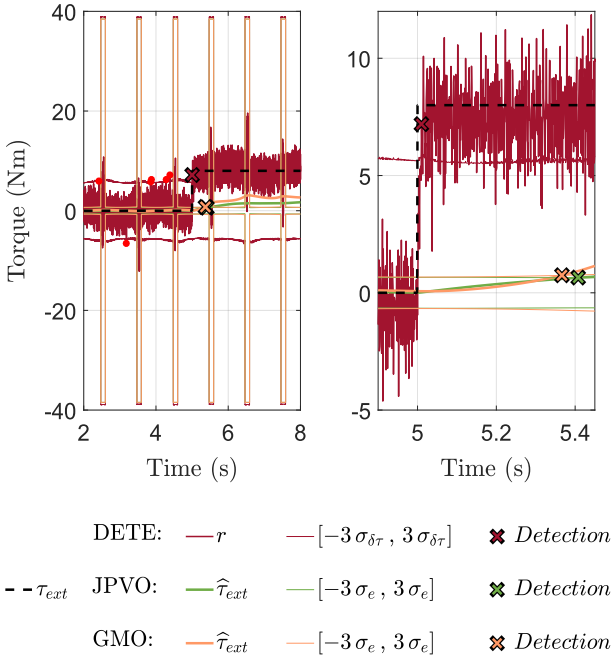
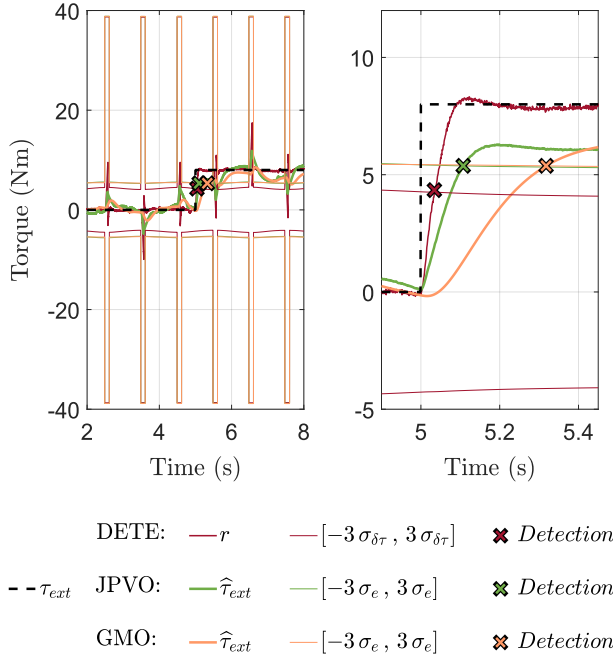


Figure 3.16: Case $U2$ — $A_{ext} = I, \Sigma_{ext} = I$

Method	Detection time at 2σ (ms)	Detection time at 3σ (ms)
DETE	4	10
JPVO	245	408
GMO	289	367

Despite an almost immediate detection of the impact, the residual obtained by DETE is extremely noisy, hence unusable without prior filtering. On the contrary, the JPVO and GMO responses being filtered by the Kalman filter, the estimates of the external torque are smoother. In addition, the DETE method generates several false alarms due to the noisy residual (at 2σ , 2.84% of the residual is above the detection threshold in the absence of impact, against 0.15% at 3σ), where the JPVO and the GMO do not generate any. The results obtained with the JPVO and the GMO are comparable.


 Figure 3.17: Case $U1$ — $A_{ext} = I$, $\Sigma_{ext} = 100I$

Method	Detection time at 2σ (ms)	Detection time at 3σ (ms)
DETE	22	35
JPVO	63	108
GMO	202	318

Uncertainties on the disturbance model are increased compared to Figure 3.15, thus we can expect higher detection thresholds for the JPVO and GMO methods. This new adjustment also modifies the observers' response, which are faster and closer to the external torque actually applied. For the JPVO, the response is fast enough for the impact to be detected rapidly, while for the GMO, the response is not sufficiently rapid with respect to the increase in the detection threshold, resulting in an increased detection time compared to Figure 3.15.

3.4 Extension to robots with rigid links and elastic joints

Few studies deal with impact detection algorithms for the case of robots with rigid links and elastic joints using proprioceptive sensing only. In [De Luca 2006], the integral formulation of the GMO in equation (3.2) is adapted to the flexible case by considering the elastic torque τ_k as the torque input in the link equations of the FDM. Then τ is replaced by τ_k during the residual generation step, which gives:

$$r = K \left[p - \int_0^t (\tau_k + C(q, \dot{q})^T \dot{q} - G(q) + r) ds - p(0) \right] \quad (3.107)$$

Additionally, [Haddadin 2017] compares different impact monitoring schemes for elastic-joint robots and, for each of them, indicates the required measurement quantities. However, none of these approaches takes explicitly into account uncertainties on the elastic-joint model that may affect the detection.

In the following, first the errors induced by a rigid model applied to an elastic-joint robot are highlighted in Section 3.4.1 for the DETE. Therefore the latter is specifically derived for the case of robots with rigid links and elastic joints in Section 3.4.2. The case of disturbance observers is finally treated in Section 3.4.3. Only the elements necessary to derive the specific models are presented, since the subsequent steps are performed in the same way as in the rigid case.

3.4.1 Deficiencies of the rigid model

When algorithms derived in the rigid case are used on a robot with rigid links and elastic joints, additional modeling errors are generated from this approximation. They are made explicit below for the method based on DETE. The ideal case without uncertainties is considered for simplification reasons (i. e. considering that $\mathcal{X}_\star = \mathcal{X}$, $\mathbf{q}_\star = \mathbf{q}$, $\dot{\mathbf{q}}_\star = \dot{\mathbf{q}}$ and $\ddot{\mathbf{q}}_\star = \ddot{\mathbf{q}}$).

As previously detailed, the residual is generated by the direct comparison between the estimated motor torque τ_\star and the actual motor torque τ . However, in this case, while the estimated torque τ_\star is still obtained by evaluating the RDM on the actual trajectory in absence of external torque:

$$\tau_\star \underset{ideal}{=} \mathbf{M}_r(\mathbf{q}) \ddot{\mathbf{q}} + \mathbf{C}(\mathbf{q}, \dot{\mathbf{q}}) \dot{\mathbf{q}} + \mathbf{G}(\mathbf{q}) + \mathbf{F}_v \dot{\mathbf{q}} + \mathbf{F}_s \text{sign}(\dot{\mathbf{q}}) \quad (3.108)$$

the actual motor torque τ comes from the FDM recalled below:

$$\mathbf{M}(\mathbf{q}) \ddot{\mathbf{q}} + \mathbf{C}(\mathbf{q}, \dot{\mathbf{q}}) \dot{\mathbf{q}} + \mathbf{G}(\mathbf{q}) + \mathbf{F}_{va} \dot{\mathbf{q}} + \mathbf{F}_{sa} \text{sign}(\dot{\mathbf{q}}) + \mathbf{K}(\mathbf{q} - \boldsymbol{\theta}) - \boldsymbol{\tau}_{k0} = \boldsymbol{\tau}_{ext} \quad (3.109a)$$

$$\mathbf{J}_m \ddot{\boldsymbol{\theta}} + \mathbf{F}_{vm} \dot{\boldsymbol{\theta}} + \mathbf{F}_{sm} \text{sign}(\dot{\boldsymbol{\theta}}) - \mathbf{K}(\mathbf{q} - \boldsymbol{\theta}) + \boldsymbol{\tau}_{k0} = \boldsymbol{\tau} \quad (3.109b)$$

The actual motor torque can also be expressed by summing the two previous equations:

$$\mathbf{M}(\mathbf{q}) \ddot{\mathbf{q}} + \mathbf{C}(\mathbf{q}, \dot{\mathbf{q}}) \dot{\mathbf{q}} + \mathbf{G}(\mathbf{q}) + \mathbf{F}_{va} \dot{\mathbf{q}} + \mathbf{F}_{sa} \text{sign}(\dot{\mathbf{q}}) + \mathbf{J}_m \ddot{\boldsymbol{\theta}} + \mathbf{F}_{vm} \dot{\boldsymbol{\theta}} + \mathbf{F}_{sm} \text{sign}(\dot{\boldsymbol{\theta}}) = \boldsymbol{\tau} + \boldsymbol{\tau}_{ext} \quad (3.110)$$

Hence, using equation (3.110), the residual calculation leads to:

$$\mathbf{r} = \tau_\star - \tau \underset{ideal}{=} \boldsymbol{\tau}_{ext} + \boldsymbol{\delta\tau} \quad (3.111)$$

where $\boldsymbol{\delta\tau}$ contains the errors due to the use of the rigid model on a robot with elastic joints:

$$\boldsymbol{\delta\tau} = \mathbf{J}_m [\ddot{\mathbf{q}} - \ddot{\boldsymbol{\theta}}] + [\mathbf{F}_v \dot{\mathbf{q}} - \mathbf{F}_{va} \dot{\mathbf{q}} - \mathbf{F}_{vm} \dot{\boldsymbol{\theta}}] + [\mathbf{F}_s \text{sign}(\dot{\mathbf{q}}) - \mathbf{F}_{sa} \text{sign}(\dot{\mathbf{q}}) - \mathbf{F}_{sm} \text{sign}(\dot{\boldsymbol{\theta}})] \quad (3.112)$$

Therefore, even in an ideal situation without model uncertainties, the residual does not only reflect the occurrence of a contact. Indeed, model errors resulting from the mismatch between the joint and motor variables arise in the residual. It should be noted that the error term $\boldsymbol{\delta\tau}$ is all the more significant as elasticities are highly stimulated along the trajectory.

For a possible usage despite this, we must know the range of this contribution during the residual evaluation as it is done with model errors. If the model terms involved are not available, then this contribution must be determined experimentally by first computing the residual on a trajectory without contact and by evaluating the deviation to zero. Note that this approach can be adopted for any non-modeled term within the estimated motor torque τ_\star .

Furthermore, if the mechanical structure of the robot under consideration is close to that of a robot with rigid links and elastic joints, then its dynamic behavior should be better identified using the FDM and by distinguishing between motor and joint measurements. To this end, the previous impact detection algorithms are extended to the flexible case in the following.

3.4.2 Extension of the direct external torque estimation (DETE)

In case of robots with rigid links and elastic joints, the residual can be obtained from the FDM using two different methods: either with the equation (3.110) resulting from the sum of the joint and motor equations (called *method F₁*) or by using only the link equation (3.109a) (called *method F₂*). Indeed, in both cases the external torque τ_{ext} appears and can be deduced by direct estimation. These two approaches are developed below for the realistic case under uncertainties.

– Method F_1 :

In this case, the residual is given by:

$$\mathbf{r} = \boldsymbol{\tau}_\star - \boldsymbol{\tau} = \boldsymbol{\tau}_{ext} + \boldsymbol{\delta\tau} \quad (3.113)$$

and the estimated motor torque $\boldsymbol{\tau}_\star$ in absence of external torque is deduced from equation (3.110):

$$\begin{aligned} \boldsymbol{\tau}_\star = & \mathbf{M}_\star(\mathbf{q}_\star) \ddot{\mathbf{q}}_\star + \mathbf{C}_\star(\mathbf{q}_\star, \dot{\mathbf{q}}_\star) \dot{\mathbf{q}}_\star + \mathbf{G}_\star(\mathbf{q}_\star) + \mathbf{F}_{va\star} \dot{\mathbf{q}}_\star + \mathbf{F}_{sa\star} \text{sign}(\dot{\mathbf{q}}_\star) \\ & + \mathbf{J}_{m\star} \ddot{\boldsymbol{\theta}}_\star + \mathbf{F}_{vm\star} \dot{\boldsymbol{\theta}}_\star + \mathbf{F}_{sm\star} \text{sign}(\dot{\boldsymbol{\theta}}_\star) \end{aligned} \quad (3.114)$$

The uncertainties-induced error term $\boldsymbol{\delta\tau}$ is expressed as $\boldsymbol{\delta\tau} = \boldsymbol{\delta\tau}^P + \boldsymbol{\delta\tau}^D$ with:

$$\begin{aligned} \boldsymbol{\delta\tau}^P = & \delta\mathbf{M}(\mathbf{q}_\star) \ddot{\mathbf{q}}_\star + \delta\mathbf{C}(\mathbf{q}_\star, \dot{\mathbf{q}}_\star) \dot{\mathbf{q}}_\star + \delta\mathbf{G}(\mathbf{q}_\star) + \delta\mathbf{F}_{va} \dot{\mathbf{q}}_\star + \lambda_{P_q} \delta\mathbf{F}_{sa} \text{sign}(\dot{\mathbf{q}}_\star) \\ & + \delta\mathbf{J}_m \ddot{\boldsymbol{\theta}}_\star + \delta\mathbf{F}_{vm} \dot{\boldsymbol{\theta}}_\star + \lambda_{P_\theta} \delta\mathbf{F}_{sm} \text{sign}(\dot{\boldsymbol{\theta}}_\star) \end{aligned} \quad (3.115)$$

$$\begin{aligned} \boldsymbol{\delta\tau}^D = & \mathbf{M}_\star(\mathbf{q}_\star) \delta\ddot{\mathbf{q}} + \mathbf{C}_\star(\mathbf{q}_\star, \dot{\mathbf{q}}_\star) \delta\dot{\mathbf{q}} + \mathbf{F}_{va\star} \delta\dot{\mathbf{q}} + \lambda_{D_q} \mathbf{F}_{sa\star} \text{sign}(\dot{\mathbf{q}}_\star) \\ & + \mathbf{J}_{m\star} \delta\ddot{\boldsymbol{\theta}} + \mathbf{F}_{vm\star} \delta\dot{\boldsymbol{\theta}} + \lambda_{D_\theta} \mathbf{F}_{sm\star} \text{sign}(\dot{\boldsymbol{\theta}}_\star) \end{aligned} \quad (3.116)$$

Particular case of dry friction uncertainties

Similarly as in the rigid case, we can define the vectors $\boldsymbol{\lambda}_{P_q}, \boldsymbol{\lambda}_{D_q}, \boldsymbol{\lambda}_{P_\theta}, \boldsymbol{\lambda}_{D_\theta} \in \mathbb{R}^n$, such as:

$$\mathbf{F}_{sa\star} \text{sign}(\dot{\mathbf{q}}_\star) - \mathbf{F}_{sa} \text{sign}(\dot{\mathbf{q}}) = [\boldsymbol{\lambda}_{P_q} \delta\mathbf{F}_{sa} + \boldsymbol{\lambda}_{D_q} \mathbf{F}_{sa\star}] \text{sign}(\dot{\mathbf{q}}_\star) \quad (3.117)$$

$$\mathbf{F}_{sm\star} \text{sign}(\dot{\boldsymbol{\theta}}_\star) - \mathbf{F}_{sm} \text{sign}(\dot{\boldsymbol{\theta}}) = [\boldsymbol{\lambda}_{P_\theta} \delta\mathbf{F}_{sm} + \boldsymbol{\lambda}_{D_\theta} \mathbf{F}_{sm\star}] \text{sign}(\dot{\boldsymbol{\theta}}_\star) \quad (3.118)$$

and speed thresholds $\boldsymbol{\alpha}_q \in \mathbb{R}^n$ and $\boldsymbol{\alpha}_\theta \in \mathbb{R}^n$ during which, if the approximated joint (resp. motor) velocity is lower than $\boldsymbol{\alpha}_q$ (resp. $\boldsymbol{\alpha}_\theta$), then $\dot{\mathbf{q}}$ (resp. $\dot{\boldsymbol{\theta}}$) and $\dot{\mathbf{q}}_\star$ (resp. $\dot{\boldsymbol{\theta}}_\star$) would be of different sign. Thus, for each component i , we get:

$$\lambda_{P_{q_i}} = \begin{cases} -1 & \text{if } |\dot{q}_{\star_i}| < \alpha_{q_i} \\ 1 & \text{otherwise.} \end{cases}, \quad \lambda_{D_{q_i}} = \begin{cases} 2 & \text{if } |\dot{q}_{\star_i}| < \alpha_{q_i} \\ 0 & \text{otherwise.} \end{cases} \quad (3.119)$$

$$\lambda_{P_{\theta_i}} = \begin{cases} -1 & \text{if } |\dot{\theta}_{\star_i}| < \alpha_{\theta_i} \\ 1 & \text{otherwise.} \end{cases}, \quad \lambda_{D_{\theta_i}} = \begin{cases} 2 & \text{if } |\dot{\theta}_{\star_i}| < \alpha_{\theta_i} \\ 0 & \text{otherwise.} \end{cases} \quad (3.120)$$

With the same developments as in the rigid case, and assuming that $\delta\chi_f$, $\delta\dot{q}$, $\delta\ddot{q}$, $\delta\dot{\theta}$ and $\delta\ddot{\theta}$ are uncorrelated two by two, the covariance matrix calculation leads to:

$$\Sigma_{\delta\tau} = \varphi_{f1} \Sigma_{\chi_f} \varphi_{f1}^T + M_{\star} \Sigma_{\ddot{q}} M_{\star}^T + (C_{\star} + F_{va\star}) \Sigma_{\dot{q}} (C_{\star} + F_{va\star})^T + \lambda_{D_q}^2 F_{sa\star} F_{sa\star}^T + J_{m\star} \Sigma_{\ddot{\theta}} J_{m\star}^T + F_{vm\star} \Sigma_{\dot{\theta}} F_{vm\star}^T + \lambda_{D_{\theta}}^2 F_{sm\star} F_{sm\star}^T \quad (3.121)$$

with $\Sigma_{\chi_f} \in \mathbb{R}^{N_f, N_f}$ the diagonal covariance matrix of $\delta\chi_f$ where standard deviations result from the identification of the flexible dynamic model parameters (see equation (2.35)) and $\varphi_{f1} \in \mathbb{R}^{n, N_f}$ the regression matrix defined by:

$$\varphi_{f1}(q, \dot{q}, \ddot{q}, \dot{\theta}, \ddot{\theta}) \chi_f = M(q) \ddot{q} + C(q, \dot{q}) \dot{q} + G(q) + F_{va} \dot{q} + \lambda_{P_q} F_{sa} \text{sign}(\dot{q}) + J_m \ddot{\theta} + F_{vm} \dot{\theta} + \lambda_{P_{\theta}} F_{sm} \text{sign}(\dot{\theta}) \quad (3.122)$$

– Method F_2 :

For this approach, the residual is directly obtained by estimating the external torque using the link equation (3.109a), that is:

$$r = \tau_{ext\star} = \tau_{ext} + \delta\tau \quad (3.123)$$

and the estimated external torque $\tau_{ext\star}$ is calculated with:

$$\tau_{ext\star} = M_{\star}(q_{\star}) \ddot{q}_{\star} + C_{\star}(q_{\star}, \dot{q}_{\star}) \dot{q}_{\star} + G_{\star}(q_{\star}) + F_{va\star} \dot{q}_{\star} + F_{sa\star} \text{sign}(\dot{q}_{\star}) + K_{\star}(q_{\star} - \theta_{\star}) - \tau_{k0\star} \quad (3.124)$$

The uncertainties-induced error term $\delta\tau$ is expressed as $\delta\tau = \delta\tau^P + \delta\tau^D$ with:

$$\delta\tau^P = \delta M(q_{\star}) \ddot{q}_{\star} + \delta C(q_{\star}, \dot{q}_{\star}) \dot{q}_{\star} + \delta G(q_{\star}) + \delta F_{va} \dot{q}_{\star} + \lambda_{P_q} \delta F_{sa} \text{sign}(\dot{q}_{\star}) + \delta K(q_{\star} - \theta_{\star}) - \delta\tau_{k0} \quad (3.125)$$

$$\delta\tau^D = M_{\star}(q_{\star}) \delta\ddot{q} + C_{\star}(q_{\star}, \dot{q}_{\star}) \delta\dot{q} + F_{va\star} \delta\dot{q} + \lambda_{D_q} F_{sa\star} \text{sign}(\dot{q}_{\star}) + K_{\star}(\xi_q - \xi_{\theta}) \quad (3.126)$$

Assuming that $\delta\chi_f$, ξ_q , $\delta\dot{q}$, $\delta\ddot{q}$, and ξ_{θ} are uncorrelated two by two, the covariance matrix calculation leads to:

$$\Sigma_{\delta\tau} = \varphi_{f2} \Sigma_{\chi_f} \varphi_{f2}^T + M_{\star} \Sigma_{\ddot{q}} M_{\star}^T + (C_{\star} + F_{va\star}) \Sigma_{\dot{q}} (C_{\star} + F_{va\star})^T + \lambda_{D_q}^2 F_{sa\star} F_{sa\star}^T + K_{\star} (\Sigma_q + \Sigma_{\theta}) K_{\star}^T \quad (3.127)$$

where $\varphi_{f2} \in \mathbb{R}^{n, N_f}$ is the regression matrix defined by:

$$\varphi_{f2}(q, \dot{q}, \ddot{q}, \theta) \chi_f = M(q) \ddot{q} + C(q, \dot{q}) \dot{q} + G(q) + F_{va} \dot{q} + \lambda_{P_q} F_{sa} \text{sign}(\dot{q}) + K(q - \theta) - \tau_{k0} \quad (3.128)$$

Dependencies in joint and motor state coordinates have been removed in equations (3.121) and (3.127) for the sake of clarity, but both covariance matrices are evaluated at each time step on the robot trajectory. The residual evaluation and impact detection phases are then carried out in the same way as in the rigid case.

Remark 3.7 *The difference between equations (3.115)-(3.116) and (3.125)-(3.126) is related to the presence of errors on the terms $\mathbf{J}_m \ddot{\boldsymbol{\theta}}$, $\mathbf{F}_{vm} \dot{\boldsymbol{\theta}}$, and $\lambda_{P_\theta} \mathbf{F}_{sm} \text{sign}(\dot{\boldsymbol{\theta}})$ in method F_1 , while the errors on the terms $\mathbf{K}(\mathbf{q} - \boldsymbol{\theta})$ and $\boldsymbol{\tau}_{k0}$ appear in method F_2 . The choice of one or the other method can therefore be guided according to the parameters that generate the smallest errors in order to minimize the effects of uncertainties.*

3.4.3 Extension of the disturbance observers design

In this section, the two previously designed disturbance observers JPVO and GMO are extended to the case of robots with rigid links and elastic joints. The methods F_1 and F_2 pointed out previously with the DETE method are transposed to the case of disturbance observers.

3.4.3.1 Extension of the joint position and velocity observer (JPVO)

– Method F_1 :

When the summed equation (3.110) is used, we define $\tilde{\boldsymbol{\tau}}$ such as:

$$\tilde{\boldsymbol{\tau}} = \boldsymbol{\tau} - \left[\mathbf{M}_*(\mathbf{q}_*) \ddot{\mathbf{q}}_* + \mathbf{C}_*(\mathbf{q}_*, \dot{\mathbf{q}}_*) \dot{\mathbf{q}}_* + \mathbf{G}_*(\mathbf{q}_*) + \mathbf{F}_{va*} \dot{\mathbf{q}}_* + \mathbf{F}_{sa*} \text{sign}(\dot{\mathbf{q}}_*) + \mathbf{F}_{sm*} \text{sign}(\dot{\boldsymbol{\theta}}_*) \right] \quad (3.129)$$

The summed equation is rearranged using $\tilde{\boldsymbol{\tau}}$ as follows:

$$\mathbf{J}_{m*} \ddot{\boldsymbol{\theta}} + \mathbf{F}_{vm*} \dot{\boldsymbol{\theta}} = \tilde{\boldsymbol{\tau}} + \boldsymbol{\tau}_{ext} + \boldsymbol{\delta\tau} \quad (3.130)$$

The uncertainties-induced error term $\boldsymbol{\delta\tau}$ is expressed as $\boldsymbol{\delta\tau} = \boldsymbol{\delta\tau}^P + \boldsymbol{\delta\tau}^D$ with:

$$\boxed{\begin{aligned} \boldsymbol{\delta\tau}^P &= \boldsymbol{\delta M}(\mathbf{q}_*) \ddot{\mathbf{q}}_* + \boldsymbol{\delta C}(\mathbf{q}_*, \dot{\mathbf{q}}_*) \dot{\mathbf{q}}_* + \boldsymbol{\delta G}(\mathbf{q}_*) + \boldsymbol{\delta F}_{va} \dot{\mathbf{q}}_* + \lambda_{P_q} \boldsymbol{\delta F}_{sa} \text{sign}(\dot{\mathbf{q}}_*) \\ &\quad + \boldsymbol{\delta J}_m \ddot{\boldsymbol{\theta}}_* + \boldsymbol{\delta F}_{vm} \dot{\boldsymbol{\theta}}_* + \lambda_{P_\theta} \boldsymbol{\delta F}_{sm} \text{sign}(\dot{\boldsymbol{\theta}}_*) \end{aligned}} \quad (3.131)$$

$$\boxed{\boldsymbol{\delta\tau}^D = \mathbf{M}_*(\mathbf{q}_*) \boldsymbol{\delta\ddot{q}} + \mathbf{C}_*(\mathbf{q}_*, \dot{\mathbf{q}}_*) \boldsymbol{\delta\dot{q}} + \mathbf{F}_{va*} \boldsymbol{\delta\dot{q}} + \lambda_{D_q} \mathbf{F}_{sa*} \text{sign}(\dot{\mathbf{q}}_*) + \lambda_{D_\theta} \mathbf{F}_{sm*} \text{sign}(\dot{\boldsymbol{\theta}}_*)} \quad (3.132)$$

From equation (3.130), the following reduced state-space representation is derived:

$$\left\{ \begin{aligned} \begin{bmatrix} \dot{\boldsymbol{\theta}} \\ \ddot{\boldsymbol{\theta}} \end{bmatrix} &= \underbrace{\begin{pmatrix} \mathbf{0} & \mathbf{I} \\ \mathbf{0} & -\mathbf{J}_{m*}^{-1} \mathbf{F}_{vm*} \end{pmatrix}}_{\mathbf{A}_r} \begin{bmatrix} \boldsymbol{\theta} \\ \dot{\boldsymbol{\theta}} \end{bmatrix} + \underbrace{\begin{pmatrix} \mathbf{0} \\ \mathbf{J}_{m*}^{-1} \end{pmatrix}}_{\mathbf{B}_r} \tilde{\boldsymbol{\tau}} + \underbrace{\begin{pmatrix} \mathbf{0} \\ \mathbf{J}_{m*}^{-1} \end{pmatrix}}_{\mathbf{G}_{\delta\tau}} \boldsymbol{\delta\tau} + \underbrace{\begin{pmatrix} \mathbf{0} \\ \mathbf{J}_{m*}^{-1} \end{pmatrix}}_{\mathbf{G}_{ext}} \boldsymbol{\tau}_{ext} \\ \boldsymbol{\theta}_* &= \underbrace{(\mathbf{I} \quad \mathbf{0})}_{\mathbf{C}_r} \begin{bmatrix} \boldsymbol{\theta} \\ \dot{\boldsymbol{\theta}} \end{bmatrix} + \underbrace{\boldsymbol{\xi}_\theta}_{\mathbf{v}} \end{aligned} \right. \quad (3.133)$$

We note that in this case, the JPVO is actually a motor position and velocity observer since $\mathbf{X}_r = [\boldsymbol{\theta}^T \quad \dot{\boldsymbol{\theta}}^T]^T$.

Using the disturbance model (3.43), the augmented state-space representation is obtained:

$$\left\{ \begin{array}{l} \begin{bmatrix} \dot{\theta} \\ \ddot{\theta} \\ \dot{\tau}_{ext} \end{bmatrix} = \underbrace{\begin{pmatrix} \mathbf{A}_r & \mathbf{G}_{ext} \\ \mathbf{0} & -\mathbf{A}_{ext} \end{pmatrix}}_A \begin{bmatrix} \theta \\ \dot{\theta} \\ \tau_{ext} \end{bmatrix} + \underbrace{\begin{pmatrix} \mathbf{B}_r \\ \mathbf{0} \end{pmatrix}}_B \tilde{\tau} + \underbrace{\begin{pmatrix} \mathbf{G}_{\delta\tau} & \mathbf{0} \\ \mathbf{0} & \mathbf{B}_{ext} \end{pmatrix}}_G \begin{bmatrix} \delta\tau \\ \mathbf{w}_{ext} \end{bmatrix} \\ \theta_\star = \underbrace{\begin{pmatrix} \mathbf{C}_r & \mathbf{0} \end{pmatrix}}_C \begin{bmatrix} \theta \\ \dot{\theta} \\ \tau_{ext} \end{bmatrix} + \underbrace{\begin{bmatrix} \xi_\theta \\ \mathbf{0} \\ \mathbf{0} \end{bmatrix}}_v \end{array} \right. \quad (3.134)$$

Assuming that $\delta\mathbf{X}_f$, $\delta\dot{\mathbf{q}}$ and $\delta\ddot{\mathbf{q}}$ are uncorrelated two by two, and using the definition of φ_{f1} in equation (3.122), the covariance matrices calculation leads to:

$$\begin{array}{l} \Sigma_{\delta\tau} = \varphi_{f1} \Sigma_{\mathbf{X}_f} \varphi_{f1}^T + \mathbf{M}_\star \Sigma_{\ddot{\mathbf{q}}} \mathbf{M}_\star^T + (\mathbf{C}_\star + \mathbf{F}_{va\star}) \Sigma_{\dot{\mathbf{q}}} (\mathbf{C}_\star + \mathbf{F}_{va\star})^T + \lambda_{D_q}^2 \mathbf{F}_{sa\star} \mathbf{F}_{sa\star}^T \\ \quad + \lambda_{D_\theta}^2 \mathbf{F}_{sm\star} \mathbf{F}_{sm\star}^T \\ \Sigma_v = \Sigma_\theta \end{array} \quad (3.135)$$

– Method F_2 :

When only the link equation (3.109a) is used, $\tilde{\tau}$ is defined as:

$$\tilde{\tau} = - \left[\mathbf{M}_\star(\mathbf{q}_\star) \ddot{\mathbf{q}}_\star + \mathbf{C}_\star(\mathbf{q}_\star, \dot{\mathbf{q}}_\star) \dot{\mathbf{q}}_\star + \mathbf{G}_\star(\mathbf{q}_\star) + \mathbf{F}_{sa\star} \text{sign}(\dot{\mathbf{q}}_\star) + \mathbf{K}_\star(\mathbf{q}_\star - \theta_\star) - \tau_{k0\star} \right] \quad (3.137)$$

The link equation is rearranged using $\tilde{\tau}$, which gives:

$$\mathbf{F}_{va\star} \dot{\mathbf{q}} = \tilde{\tau} + \tau_{ext} + \delta\tau \quad (3.138)$$

The uncertainties-induced error term $\delta\tau$ is expressed as $\delta\tau = \delta\tau^P + \delta\tau^D$ with:

$$\begin{array}{l} \delta\tau^P = \delta\mathbf{M}(\mathbf{q}_\star) \ddot{\mathbf{q}}_\star + \delta\mathbf{C}(\mathbf{q}_\star, \dot{\mathbf{q}}_\star) \dot{\mathbf{q}}_\star + \delta\mathbf{G}(\mathbf{q}_\star) + \delta\mathbf{F}_{va} \dot{\mathbf{q}}_\star + \lambda_{P_q} \delta\mathbf{F}_{sa} \text{sign}(\dot{\mathbf{q}}_\star) \\ \quad + \delta\mathbf{K}(\mathbf{q}_\star - \theta_\star) - \delta\tau_{k0} \end{array} \quad (3.139)$$

$$\delta\tau^D = \mathbf{M}_\star(\mathbf{q}_\star) \delta\ddot{\mathbf{q}} + \mathbf{C}_\star(\mathbf{q}_\star, \dot{\mathbf{q}}_\star) \delta\dot{\mathbf{q}} + \lambda_{D_q} \mathbf{F}_{sa\star} \text{sign}(\dot{\mathbf{q}}_\star) + \mathbf{K}_\star(\xi_q - \xi_\theta) \quad (3.140)$$

From equation (3.138) and using the disturbance model (3.43), the augmented state-space representation is obtained:

$$\left\{ \begin{array}{l} \begin{bmatrix} \dot{\mathbf{q}} \\ \dot{\tau}_{ext} \end{bmatrix} = \underbrace{\begin{pmatrix} \mathbf{A}_r & \mathbf{G}_{ext} \\ \mathbf{0} & -\mathbf{A}_{ext} \end{pmatrix}}_A \begin{bmatrix} \mathbf{q} \\ \tau_{ext} \end{bmatrix} + \underbrace{\begin{pmatrix} \mathbf{B}_r \\ \mathbf{0} \end{pmatrix}}_B \tilde{\tau} + \underbrace{\begin{pmatrix} \mathbf{G}_{\delta\tau} & \mathbf{0} \\ \mathbf{0} & \mathbf{B}_{ext} \end{pmatrix}}_G \begin{bmatrix} \delta\tau \\ \mathbf{w}_{ext} \end{bmatrix} \\ \mathbf{q}_\star = \underbrace{\begin{pmatrix} \mathbf{C}_r & \mathbf{0} \end{pmatrix}}_C \begin{bmatrix} \mathbf{q} \\ \tau_{ext} \end{bmatrix} + \underbrace{\begin{bmatrix} \xi_q \\ \mathbf{0} \\ \mathbf{0} \end{bmatrix}}_v \end{array} \right. \quad (3.141)$$

with $\mathbf{A}_r = \mathbf{0}$, $\mathbf{B}_r = \mathbf{G}_{\delta\tau} = \mathbf{G}_{ext} = \mathbf{F}_{va\star}^{-1}$ and $\mathbf{C}_r = \mathbf{I}$. In this case, the JPVO is reduced to a joint position observer since $\mathbf{X}_r = \mathbf{q}$.

Assuming that $\delta\chi_f$, ξ_q , $\delta\dot{q}$, $\delta\ddot{q}$, and ξ_θ are uncorrelated two by two, and using the definition of φ_{f2} in equation (3.128), the covariance matrices calculation leads to:

$$\Sigma_{\delta\tau} = \varphi_{f2} \Sigma_{\chi_f} \varphi_{f2}^T + M_\star \Sigma_{\ddot{q}} M_\star^T + C_\star \Sigma_{\dot{q}} C_\star^T + \lambda_{D_q}^2 F_{sa\star} F_{sa\star}^T + K_\star (\Sigma_q + \Sigma_\theta) K_\star^T \quad (3.142)$$

$$\Sigma_v = \Sigma_q \quad (3.143)$$

3.4.3.2 Extension of the generalized momentum observer (GMO)

– Method F_1 :

When the summed equation (3.110) is used, we define $\tilde{\tau}$ such as:

$$\tilde{\tau} = \tau - \left[-C_\star(q_\star, \dot{q}_\star)^T \dot{q}_\star + G_\star(q_\star) + F_{va\star} \dot{q}_\star + F_{sa\star} \text{sign}(\dot{q}_\star) + F_{vm\star} \dot{\theta}_\star + F_{sm\star} \text{sign}(\dot{\theta}_\star) \right] \quad (3.144)$$

The summed equation is rearranged using $\tilde{\tau}$ as follows:

$$\dot{p} = \tilde{\tau} + \tau_{ext} + \delta\tau \quad (3.145)$$

The uncertainties-induced error term $\delta\tau$ is expressed as $\delta\tau = \delta\tau^P + \delta\tau^D$ with:

$$\delta\tau^P = -\delta C(q_\star, \dot{q}_\star)^T \dot{q}_\star + \delta G(q_\star) + \delta F_{va} \dot{q}_\star + \lambda_{P_q} \delta F_{sa} \text{sign}(\dot{q}_\star) + \delta F_{vm} \dot{\theta}_\star + \lambda_{P_\theta} \delta F_{sm} \text{sign}(\dot{\theta}_\star) \quad (3.146)$$

$$\delta\tau^D = -C_\star(q_\star, \dot{q}_\star)^T \delta\dot{q} + F_{va\star} \delta\dot{q} + \lambda_{D_q} F_{sa\star} \text{sign}(\dot{q}_\star) + F_{vm\star} \delta\dot{\theta} + \lambda_{D_\theta} F_{sm\star} \text{sign}(\dot{\theta}_\star) \quad (3.147)$$

Similarly to the rigid case, the generalized momentum defined in the flexible case as $p_\star = M_\star(q_\star) \dot{q}_\star + J_{m\star} \dot{\theta}_\star$ is not directly measured but computed with errors. The associated error δp is decomposed into $\delta p = \delta p^P + \delta p^D$ with:

$$\delta p^P = \delta M(q_\star) \dot{q}_\star + \delta J_{m\star} \dot{\theta}_\star \quad (3.148)$$

$$\delta p^D = M_\star(q_\star) \delta\dot{q} + J_{m\star} \delta\dot{\theta} \quad (3.149)$$

From equation (3.145) and using the disturbance model (3.43), the augmented state-space representation is obtained:

$$\begin{cases} \begin{bmatrix} \dot{p} \\ \dot{\tau}_{ext} \end{bmatrix} = \underbrace{\begin{pmatrix} A_r & G_{ext} \\ 0 & -A_{ext} \end{pmatrix}}_A \begin{bmatrix} p \\ \tau_{ext} \end{bmatrix} + \underbrace{\begin{pmatrix} B_r \\ 0 \end{pmatrix}}_B \tilde{\tau} + \underbrace{\begin{pmatrix} G_{\delta\tau} & 0 \\ 0 & B_{ext} \end{pmatrix}}_G \begin{bmatrix} \delta\tau \\ w_{ext} \end{bmatrix} \\ p_\star = \underbrace{\begin{pmatrix} C_r & 0 \end{pmatrix}}_C \begin{bmatrix} p \\ \tau_{ext} \end{bmatrix} + \underbrace{\begin{bmatrix} \delta p \\ v \end{bmatrix}}_v \end{cases} \quad (3.150)$$

with $A_r = 0$, $B_r = G_{\delta\tau} = G_{ext} = I$ and $C_r = I$.

Assuming that $\delta\chi_f$, $\delta\dot{q}$ and $\delta\dot{\theta}$ are uncorrelated two by two, the covariance matrices calculation leads to:

$$\Sigma_{\delta\tau} = \Phi_{f1} \Sigma_{\chi_f} \Phi_{f1}^T + (-C_\star^T + F_{va\star}) \Sigma_{\dot{q}} (-C_\star^T + F_{va\star})^T + \lambda_{D^2} F_{sa\star} F_{sa\star}^T + F_{vm\star} \Sigma_{\dot{\theta}} F_{vm\star}^T + \lambda_{D\theta^2} F_{sm\star} F_{sm\star}^T \quad (3.151)$$

$$\Sigma_v = \Omega_{f1} \Sigma_{\chi_f} \Omega_{f1}^T + M_\star \Sigma_{\dot{q}} M_\star^T + J_{m\star} \Sigma_{\dot{\theta}} J_{m\star}^T \quad (3.152)$$

where the regression matrices $\Phi_{f1} \in \mathbb{R}^{n, N_f}$ and $\Omega_{f1} \in \mathbb{R}^{n, N_f}$ are defined by:

$$\Phi_{f1}(q, \dot{q}, \dot{\theta}) \chi_f = -C(q, \dot{q})^T \dot{q} + G(q) + F_{va} \dot{q} + \lambda_{P_q} F_{sa} \text{sign}(\dot{q}) + F_{vm} \dot{\theta} + \lambda_{P_\theta} F_{sm} \text{sign}(\dot{\theta}) \quad (3.153)$$

$$\Omega_{f1}(q, \dot{q}, \dot{\theta}) \chi_f = M(q) \dot{q} + J_m \dot{\theta} \quad (3.154)$$

– Method F_2 :

Given that $p = M(q) \dot{q} + J_m \dot{\theta}$ in the flexible case, rewriting the link equation (3.109a) using the generalized momentum yields:

$$\dot{p} - J_m \ddot{\theta} - C(q, \dot{q})^T \dot{q} + G(q) + F_{va} \dot{q} + F_{sa} \text{sign}(\dot{q}) + K(q - \theta) - \tau_{k0} = \tau_{ext} \quad (3.155)$$

It is therefore not possible to derive a linear state representation without having to calculate the motor acceleration $\ddot{\theta}$, whereas this is precisely the interest of the method based on the generalized momentum.

Nevertheless, the reduced generalized momentum defined as $p_r = M(q) \dot{q}$ can be used, and then the link equation (3.109a) of the FDM is rewritten as:

$$\dot{p}_r - C(q, \dot{q})^T \dot{q} + G(q) + F_{va} \dot{q} + F_{sa} \text{sign}(\dot{q}) + K(q - \theta) - \tau_{k0} = \tau_{ext} \quad (3.156)$$

In this case, $\tilde{\tau}$ is defined as:

$$\tilde{\tau} = - \left[-C_\star(q_\star, \dot{q}_\star)^T \dot{q}_\star + G_\star(q_\star) + F_{va\star} \dot{q}_\star + F_{sa\star} \text{sign}(\dot{q}_\star) + K_\star(q_\star - \theta_\star) - \tau_{k0\star} \right] \quad (3.157)$$

The link equation is rearranged using $\tilde{\tau}$, which gives:

$$\dot{p}_r = \tilde{\tau} + \tau_{ext} + \delta\tau \quad (3.158)$$

The uncertainties-induced error term $\delta\tau$ is expressed as $\delta\tau = \delta\tau^P + \delta\tau^D$ with:

$$\delta\tau^P = -\delta C(q_\star, \dot{q}_\star)^T \dot{q}_\star + \delta G(q_\star) + \delta F_{va} \dot{q}_\star + \lambda_{P_q} \delta F_{sa} \text{sign}(\dot{q}_\star) + \delta K(q_\star - \theta_\star) - \delta\tau_{k0} \quad (3.159)$$

$$\delta\tau^D = -C_\star(q_\star, \dot{q}_\star)^T \delta\dot{q}_\star + F_{va\star} \delta\dot{q}_\star + \lambda_{D_q} F_{sa\star} \text{sign}(\dot{q}_\star) + K_\star(\xi_q - \xi_\theta) \quad (3.160)$$

As for the generalized momentum, the reduced formulation $p_{r\star} = M_\star(q_\star)$ is not directly mea-

sured but computed with errors, such as $\delta p_r = \delta p_r^P + \delta p_r^D$ with:

$$\delta p_r^P = \delta M(q_*) \dot{q}_* \quad (3.161)$$

$$\delta p_r^D = M_*(q_*) \delta \dot{q} \quad (3.162)$$

From equation (3.158) and using the disturbance model (3.43), the augmented state-space representation is obtained:

$$\begin{cases} \begin{bmatrix} \dot{p}_r \\ \dot{\tau}_{ext} \end{bmatrix} = \underbrace{\begin{pmatrix} A_r & G_{ext} \\ \mathbf{0} & -A_{ext} \end{pmatrix}}_A \begin{bmatrix} p_r \\ \tau_{ext} \end{bmatrix} + \underbrace{\begin{pmatrix} B_r \\ \mathbf{0} \end{pmatrix}}_B \tilde{\tau} + \underbrace{\begin{pmatrix} G_{\delta\tau} & \mathbf{0} \\ \mathbf{0} & B_{ext} \end{pmatrix}}_G \begin{bmatrix} \delta\tau \\ w_{ext} \end{bmatrix} \\ p_{r*} = \underbrace{\begin{pmatrix} C_r & \mathbf{0} \end{pmatrix}}_C \begin{bmatrix} p_r \\ \tau_{ext} \end{bmatrix} + \underbrace{\delta p_r}_v \end{cases} \quad (3.163)$$

with $A_r = \mathbf{0}$, $B_r = G_{\delta\tau} = G_{ext} = I$ and $C_r = I$. Assuming that $\delta\chi_f$, ξ_q , $\delta\dot{q}$ and ξ_θ are uncorrelated two by two, the covariance matrices calculation leads to:

$$\Sigma_{\delta\tau} = \Phi_{f2} \Sigma_{\chi_f} \Phi_{f2}^T + (-C_*^T + F_{va*}) \Sigma_{\dot{q}} (-C_*^T + F_{va*})^T + \lambda_{D_q}^2 F_{sa*} F_{sa*}^T + K_*(\Sigma_q + \Sigma_\theta) K_*^T \quad (3.164)$$

$$\Sigma_v = \Omega_{f2} \Sigma_{\chi_f} \Omega_{f2}^T + M_* \Sigma_{\dot{q}} M_*^T \quad (3.165)$$

where the regression matrices $\Phi_{f2} \in \mathbb{R}^{n, N_f}$ and $\Omega_{f2} \in \mathbb{R}^{n, N_f}$ are defined by:

$$\Phi_{f2}(q, \dot{q}, \theta) \chi_f = -C(q, \dot{q})^T \dot{q} + G(q) + F_{va} \dot{q} + \lambda_{P_q} F_{sa} \text{sign}(\dot{q}) + K(q - \theta) - \tau_{k0} \quad (3.166)$$

$$\Omega_{f2}(q, \dot{q}) \chi_f = M(q) \dot{q} \quad (3.167)$$

3.5 Qualitative comparison of the developed strategies

The methodology consisting in rendering explicit the contribution of uncertainties has made it possible to highlight the type and the structure of errors involved in a given impact detection algorithm. Depending on the method and the type of parameters which are the most uncertain, the modeling errors may have more or less effect on the impact detection. For instance, the effects of the errors on the inertial terms in the DETE and JPVO methods are more direct than those in the GMO.

These differences are interpreted in terms of advantages (+) and drawbacks (-) of each method and are presented in Table 3.2 for the rigid case and in Table 3.3 for the flexible case. The symbol +/− means that the evaluation of the criterion is not direct and may depend on different factors (e. g. the robot trajectory or the amount of uncertainties).

Method	Type of errors involved	Structure of the estimation method
DETE	– Affected by errors on the inertial terms	+/- Direct estimation without filtering
JPVO	+ Not affected by error on terms that linearly depend on the joint velocity and acceleration errors – Affected by errors on the inertial terms	+/- Estimation by Kalman filtering + Measurement noise reduced to noise on the measured joint position
GMO	+ Not affected by error on the inertial terms	+/- Estimation by Kalman filtering +/- Measurement noise corresponding to errors on the generalized momentum

Table 3.2: Comparison of the impact detection strategies developed *in the rigid case*

3.6 Conclusion

This chapter was dedicated to the design of impact detection algorithms in presence of uncertainties. In a context of reduced measurements, we were particularly interested in model-based fault diagnosis methods. The constraint, in this case, is the presence of modeling uncertainties that affect the detection with the same effects as an actual external contact. Therefore, existing impact detection strategies were reconsidered to analyse the model errors involved and their propagation during the generation and evaluation of the impact monitoring signal.

First, the direct external torque estimation (DETE) that merely uses the robot IDM by isolating the external torque contribution was studied. Our approach highlighted the two main sources of errors: inaccuracies in the robot dynamic parameters and numerical differentiation errors. Both are propagated through the IDM, can lead to equivalent effects in the external torque estimation and depend on the robot's trajectory. With the stochastic characterization of uncertainties from the previous chapter, it is possible to know the range in which these uncertainties may lie. Since any additional contribution within the monitoring signal can only be due to an impact occurring on the robot, this envelope constitutes an appropriate adaptive detection threshold that explicitly takes into account the contribution of uncertainties.

In a second step, disturbance observers using Kalman filters were investigated to reconstruct the external torque contribution. By using a first-order model for the disturbance, this approach benefits from additional adjustment parameters. Two methods were derived in the rigid case: one based on a joint position and velocity observer (JPVO), the other based on the generalized momentum observer (GMO). These two observers present a different distribution of uncertainties

Method	Type of errors involved	Structure of the estimation method
DETE – F1	+ Not affected by error on elastic stiffness terms	+/- Direct estimation without filtering
	– Affected by errors on motor friction terms	
	– Affected by errors on inertial terms	
DETE – F2	+ Not affected by error on motor friction terms	+/- Direct estimation without filtering
	– Affected by errors on elastic stiffness terms	
	– Affected by errors on inertial terms	
JPVO – F1	+ Not affected by error on elastic stiffness terms	+/- Estimation by Kalman filtering
	+ Not affected by error on terms that linearly depend on the motor velocity and acceleration errors	+ Measurement noise reduced to noise on the measured motor position
	– Affected by errors on motor friction terms	
	– Affected by errors on inertial terms	
JPVO – F2	+ Not affected by error on motor friction terms	+/- Estimation by Kalman filtering
	+ Not affected by error on terms that linearly depend on the joint velocity errors	+ Measurement noise reduced to noise on the measured joint position
	– Affected by errors on elastic stiffness terms	
	– Affected by errors on inertial terms	
GMO – F1	+ Not affected by error on elastic stiffness terms	+/- Estimation by Kalman filtering
	+ Not affected by error on inertial terms	+/- Measurement noise consisting of errors on the generalized momentum
	– Affected by errors on motor friction terms	
GMO – F2	+ Not affected by error on motor friction terms	+/- Estimation by Kalman filtering
	+ Not affected by error on inertial terms	+/- Measurement noise consisting of errors on the reduced generalized momentum
	– Affected by errors on elastic stiffness terms	

Table 3.3: Comparison of the impact detection strategies developed *in the elastic-joint case*

among state and measurement noises. Since the output estimate of the Kalman filter is based on this distribution, they will have different responses regarding the external torque estimation and the modeling errors. In this case, the covariance matrix of the estimation error in the absence of external torque is used to generate the adaptive detection threshold.

These impact detection strategies are generally considered in the rigid case. We proposed to extend our methodology to the flexible case in order to deduce new impact detection algorithms to be applied on robots with rigid links and elastic joints. In particular, whether for direct estimation of the external torque or for observer-based methods, two strategies have been developed with different model errors involved, which can thus guide the user's choice.

While these strategies have so far been applied in simulation to access uncertainties that are not available on a real robot, [Chapter 4: "Experimental validation of impact detection strategies"](#) compares their impact detection performance using experimental measurements.

Experimental validation of impact detection strategies

Contents

4.1	Validation and characterization of detection performance	100
4.1.1	Description of the experiment	100
4.1.2	Preliminary analysis of disturbance observer settings	102
4.1.2.1	Analytical criteria for detection	105
4.1.2.2	Influence of the robot's modeling parameters	107
4.1.2.3	Influence of the disturbance model parameters	109
4.1.3	Experimental validation	114
4.1.3.1	Protocols and settings	114
4.1.3.2	Experimental results	116
4.2	Validation with regard to the energy transferred	120
4.2.1	Description of the experimental set-up	120
4.2.2	Evaluation of the results	121
4.3	Conclusion	125

This chapter aims to experimentally validate the impact detection algorithms derived in [Chapter 3: "Design of impact detection strategies under model uncertainties"](#). To be successful, they must guarantee that a contact with the robot is correctly detected, but also that the detection characteristics comply with the robotics safety standards to ensure a safe pHRI. Quantitative criteria are therefore to be defined in this chapter to evaluate the detection results obtained.

For this purpose, a human-robot contact recorded with the ISYBOT prototype robot is used as illustrative experiment for the validation in [Section 4.1](#). In the particular case of disturbance observers, the estimated disturbance torque depends not only on the actual external torque but also on the disturbances produced by modeling uncertainties. In order to analyze and compare the filtering action on these inputs depending on the setting parameters, a frequency-domain study is carried out for the two observers designed in the rigid case (JPVO and GMO) and applied to the illustrative example. An analytical approach to quantify the detection sensitivity and the response time of the estimate is proposed for these strategies.

In [Section 4.2](#), the detection results are interpreted in terms of energy transferred to the collided system in order to be related to robotic standards. A dedicated experimental system has been set up to collect additional measurements required for the computation of the energy transferred and compare these results with the recommended safety values. This experiment is conducted for several robot speeds and environmental stiffness.

4.1 Validation and characterization of detection performance

4.1.1 Description of the experiment

In order to highlight the effects of an impact, two successive experiments are performed on the ISYBOT prototype robot presented in [Appendix B](#). During the first experiment, the second joint of the robot follows a filtered triangular trajectory around the “extended arm”-configuration $\mathbf{q}_0 = (0\ 0\ 0\ 0\ 0\ 0)^T$ while the other motors have the brakes locked. In the second experiment, the robot performs the same trajectory while a human subject comes to its contact, without any impact detection strategy being active (see [Figure 4.1](#)). A resistive force is applied locally on the third axis by the operator and opposite to the robot motion, before he removes his arm. Four successive contacts at the same contact point but of different amplitude are recorded during the second experiment. A 6-axis force/torque sensor is placed at the contact location, which measures the force during the impacts (see [Figure 4.2](#)). For the experiments, the robot is controlled in position in the joint space with a decentralized proportional-derivative (PD) control law. [Figure 4.3](#) illustrates the signals measured for axis 2 with and without contact. The impact effects can be observed by comparing the trajectory tracking error and the actual motor torque between the two experiments. The residual obtained with the DETE by computing $\mathbf{r} = \boldsymbol{\tau}_* - \boldsymbol{\tau}$ is also calculated in both situations.

If an impact detection strategy with a fixed threshold on the trajectory tracking error or the actual motor torque was implemented, it may be difficult to detect some of these contacts since the trajectory without contact exhibits peaks of amplitude that can be as high as those due to the contacts (e.g. impact 3). Furthermore, the variations induced by impacts 2 and 3 on the residual are of the same order of magnitude as the peaks due to modeling errors, also visible on the trajectory without contact. Thus a static threshold on the residual that would be tuned higher than the modeling errors to avoid false alarms would not be sufficient to detect impact 3 for example or forces of lower amplitude. Consequently, adaptive impact detection strategies are required to adjust to any operating conditions and state of the robot on a given trajectory.

Before evaluating the detection algorithms derived in the previous chapter on this experiment, the estimation by the two disturbance observers requires first to compute the covariance matrices of state and measurement noises. These matrices are then involved in the calculation of the estimated disturbance torque and the detection threshold and depend on the robot modeling parameters on the one hand, and on the tuning of the external disturbance model on the other hand. In the following, the influence of these parameters on the expected characteristics of the detection is studied in more detail based on the previous experiment.

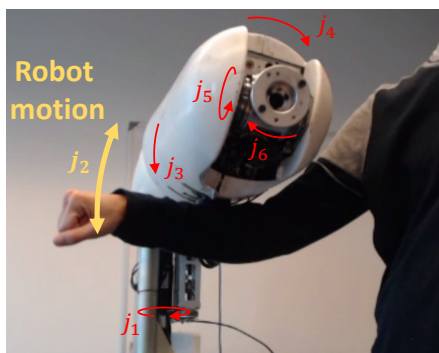


Figure 4.1: Picture of a recorded contact with the axis 2 in motion (in yellow) and the other axes locked (in red).

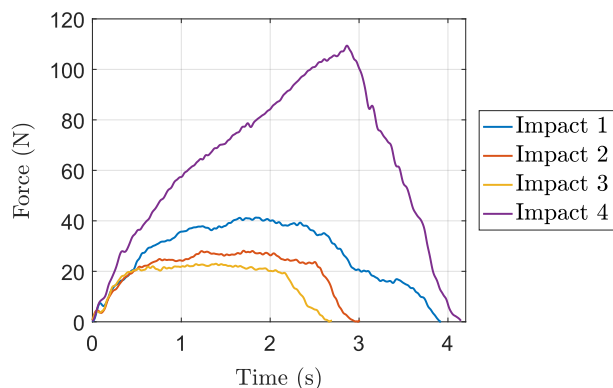


Figure 4.2: Force measured by the force/torque sensor in the direction perpendicular to the movement.

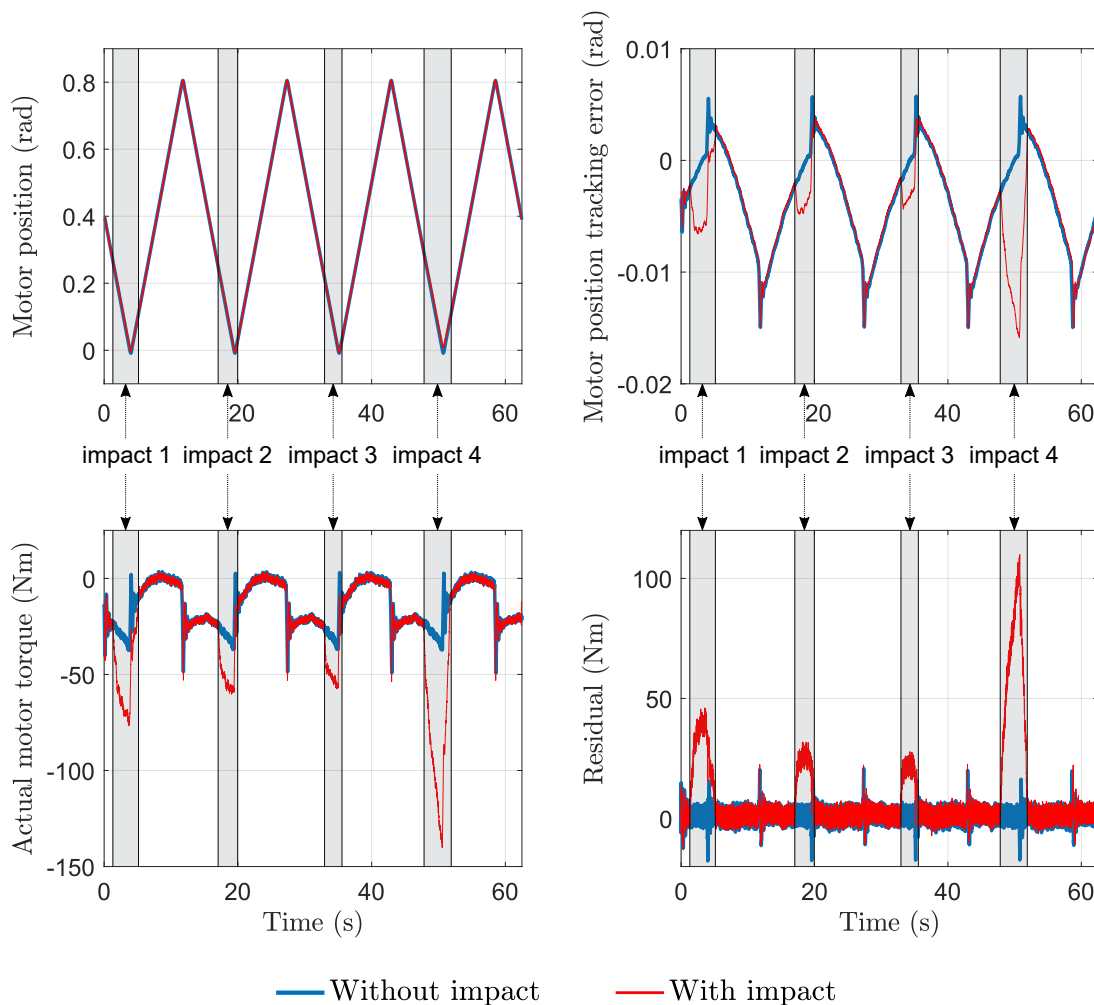


Figure 4.3: Illustration of the effects of an impact on several signals measured during two identical tests performed without and with contact.

4.1.2 Preliminary analysis of disturbance observer settings

The behavior of the estimated external torque $\hat{\tau}_{ext}$ depends not only on the external torque input τ_{ext} but also on the disturbances $\delta\tau$ and \mathbf{v} . In this section, we study the effect of the filtering on these different inputs, and in particular how it evolves with the setting parameters. For this purpose, a frequency-domain analysis is conducted to identify trends for each observer and each contribution influencing $\hat{\tau}_{ext}$ in order to ultimately provide several tuning guidelines. Only impact detection observers designed in the rigid case are examined (JPVO and GMO), but a similar study could be conducted for those designed in the elastic-joint case. The previous experiment is used as an applicative framework for the following analysis.

We recall below the input-output formulation expressing $\hat{\tau}_{ext}(k)$ as a function of the inputs $\tau_{ext}(k)$, $\delta\tau(k)$ and $\mathbf{v}(k)$ that was derived for the evaluation of the estimated external torque (see Chapter 3: "Design of impact detection strategies under model uncertainties" – Section 3.3.3):

$$\begin{cases} \mathbf{X}_t(k+1) &= \mathbf{A}_t^k \mathbf{X}_t(k) + \mathbf{B}_t^k \mathbf{U}_t(k) \\ \mathbf{Y}_t(k) &= \mathbf{C}_t \mathbf{X}_t(k) \end{cases} \quad (4.1)$$

with

$$\mathbf{X}_t(k) = \begin{pmatrix} \tilde{\mathbf{X}}_r(k) \\ \hat{\tau}_{ext}(k) \end{pmatrix} ; \quad \mathbf{Y}_t(k) = \hat{\tau}_{ext}(k) ; \quad \mathbf{U}_t(k) = \begin{pmatrix} \tau_{ext}(k) \\ \delta\tau(k) \\ \mathbf{v}(k+1) \end{pmatrix} \quad (4.2)$$

and

$$\mathbf{A}_t^k = \begin{pmatrix} \mathbf{A}_{d_r} - \mathbf{K}_1(k) \mathbf{C}_{d_r} \mathbf{A}_{d_r} & -\mathbf{G}_{d_{ext}} + \mathbf{K}_1(k) \mathbf{C}_{d_r} \mathbf{G}_{d_{ext}} \\ \mathbf{K}_2(k) \mathbf{C}_{d_r} \mathbf{A}_{d_r} & \mathbf{A}_{d_{ext}} - \mathbf{K}_2(k) \mathbf{C}_{d_r} \mathbf{G}_{d_{ext}} \end{pmatrix} \quad (4.3)$$

$$\mathbf{B}_t^k = \begin{pmatrix} \mathbf{G}_{a_{ext}} - \mathbf{K}_1(k) \mathbf{C}_{d_r} \mathbf{G}_{a_{ext}} & \mathbf{G}_{d_{\delta\tau}} - \mathbf{K}_1(k) \mathbf{C}_{d_r} \mathbf{G}_{d_{\delta\tau}} & -\mathbf{K}_1(k) \\ \mathbf{K}_2(k) \mathbf{C}_{d_r} \mathbf{G}_{a_{ext}} & \mathbf{K}_2(k) \mathbf{C}_{d_r} \mathbf{G}_{d_{\delta\tau}} & \mathbf{K}_2(k) \end{pmatrix} \quad (4.4)$$

$$\mathbf{C}_t = \begin{pmatrix} \mathbf{0} & \mathbf{I} \end{pmatrix} \quad (4.5)$$

First, for normalization purposes, we define the matrices $\underline{\mathbf{G}}_{\delta\tau}(k)$ and $\underline{\mathbf{G}}_v(k)$ such as:

$$\underline{\mathbf{G}}_{\delta\tau}(k) \left(\underline{\mathbf{G}}_{\delta\tau}(k) \right)^T = \underline{\Sigma}_{\delta\tau}(k) \quad (4.6)$$

$$\underline{\mathbf{G}}_v(k) \left(\underline{\mathbf{G}}_v(k) \right)^T = \underline{\Sigma}_v(k) \quad (4.7)$$

where $\underline{\mathbf{G}}_{\delta\tau}(k)$ and $\underline{\mathbf{G}}_v(k)$ can be obtained by Cholesky decomposition and the covariance matrices $\underline{\Sigma}_{\delta\tau}(k)$ and $\underline{\Sigma}_v(k)$ of $\delta\tau(k)$ and $\mathbf{v}(k)$ respectively were defined in equations (3.80) and (3.81). We also define the vector of inputs $\underline{\mathbf{U}}_t(k) = \left[\tau_{ext}(k) \quad \delta\tau(k) \quad \mathbf{v}(k+1) \right]^T$ so that $\delta\tau(k)$ and $\mathbf{v}(k+1)$ are of unitary covariance matrices and we denote \mathbf{G}_t^k the matrix that verifies:

$$\mathbf{U}_t(k) = \underbrace{\begin{pmatrix} \mathbf{I} & \mathbf{0} & \mathbf{0} \\ \mathbf{0} & \underline{\mathbf{G}}_{\delta\tau}(k) & \mathbf{0} \\ \mathbf{0} & \mathbf{0} & \underline{\mathbf{G}}_v(k) \end{pmatrix}}_{\mathbf{G}_t^k} \underline{\mathbf{U}}_t(k) \quad (4.8)$$

Given that the system in equation (4.1) is non-stationary, a local analysis around different operating points is undertaken. Denoting $\hat{\tau}_{ext}(z)$ the Z -transform of the discrete-time signal $\hat{\tau}_{ext}(k)$ and similarly for the other signals involved, the system (4.1) transformed in the Z -domain yields:

$$\hat{\tau}_{ext}(z) = \underbrace{C_t [zI - A_t^k]^{-1} B_t^k G_t^k}_{H^k(z)} U_t(z) \quad (4.9)$$

Then the following transfer functions matrices can be calculated at each time step k :

$$H_1^k(z) = \frac{\hat{\tau}_{ext}(z)}{\tau_{ext}(z)} = H^k(z) \begin{pmatrix} I & \mathbf{0} & \mathbf{0} \end{pmatrix}^T \quad (4.10)$$

$$H_2^k(z) = \frac{\hat{\tau}_{ext}(z)}{\delta\tau(z)} = H^k(z) \begin{pmatrix} \mathbf{0} & I & \mathbf{0} \end{pmatrix}^T \quad (4.11)$$

$$H_3^k(z) = \frac{\hat{\tau}_{ext}(z)}{v(z)} = H^k(z) \begin{pmatrix} \mathbf{0} & \mathbf{0} & zI \end{pmatrix}^T \quad (4.12)$$

Note that these transfer functions depend on the Kalman gain. By considering that the covariance matrices of the state and measurement noises are calculated beforehand on the reference trajectory (see Remark 3.6), then the Kalman gain and these transfer functions can be known in advance. Consequently, we can already predict the behavior of $\hat{\tau}_{ext}$ in response to online inputs in τ_{ext} , $\delta\tau$ and v .

Since an analytical analysis is hardly feasible because of the multivariate and non-linear nature of the problem, general trends are extracted based on the experiment described in Section 4.1.1. As these transfer functions matrices vary with time, a set of responses is computed at 78 different time instants along the reference triangular trajectory (see Figure 4.4). A first analysis illustrating the nature of the transfer functions $H_1^k(z)$, $H_2^k(z)$ and $H_3^k(z)$ is carried out with the parameters considered below.

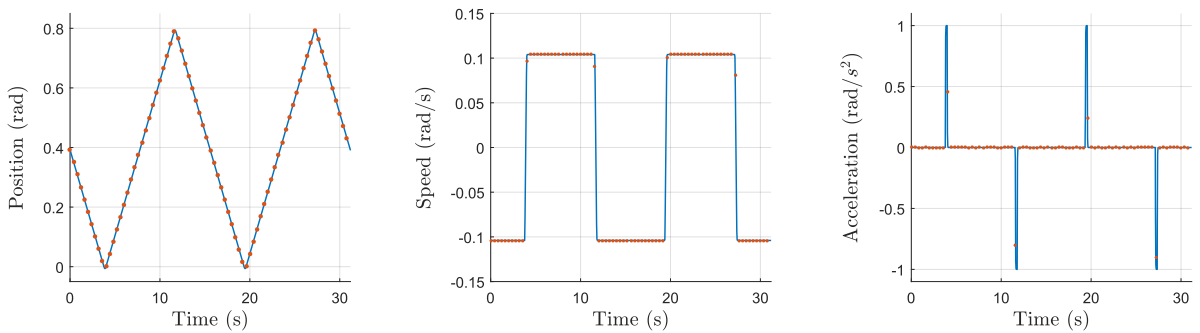


Figure 4.4: Reference trajectory of robot axis 2 (*blue lines*) with the calculation time steps of the transfer functions matrices (*orange markers*).

Simulation parameters (Figure 4.5)

- Parametric errors: for each parameter i , $\% \sigma_{\chi_i}$ is fixed randomly and independently within $[0\%, 5\%]$. Simulations are based on a given random realization of the uncertain parameters \mathcal{X}_{r^*} according to a normal distribution, centered around the exact values \mathcal{X}_r and of standard deviation deduced from $\% \sigma_{\chi}$.
- Numerical differentiation errors: the first order low-pass filtered derivative is set with $\omega_c = 2\pi 10$ rad/s. The terms \mathbf{A}_d and \mathbf{A}_{dd} within $\Sigma_{\dot{q}}$ and $\Sigma_{\ddot{q}}$ are computed based on a trajectory without contact.
- The disturbance model is set with $\mathbf{A}_{ext} = \mathbf{I}$ and $\Sigma_{ext} = 10\mathbf{I}$.

Results are illustrated for axis 2 (second diagonal term of the transfer functions matrices computed at the 78 time instants) in Figure 4.5 for the two disturbance observers JPVO and GMO. The similarity between the diagrams at the different calculation points suggests that an invariant system could be sufficient in this case. This is due to the constant speed and acceleration over a large part of the reference trajectory (see Figure 4.4). However, for a trajectory with more variable speeds and accelerations (e. g. a sinusoidal trajectory), this approximation is less obvious.

From Figure 4.5, we observe that for both methods JPVO and GMO, $\mathbf{H}_1^k(z)$ and $\mathbf{H}_2^k(z)$ have a low-pass filter tendency, whereas $\mathbf{H}_3^k(z)$ is more akin to a high-pass filter (for JPVO) or a band-pass filter (for GMO). We also notice that $\mathbf{H}_1^k(z)$ and $\mathbf{H}_2^k(z)$ have similar behaviors (at least for frequencies up to 200 rad/s) but differ only by a gain factor in magnitude, which is consistent with the fact that modeling uncertainties affect the estimate in the same structural way as an external contact. In addition, both methods tend to filter the contribution of τ_{ext} in the estimate output but to amplify that of uncertainties $\delta\tau$. We also note that on this trajectory, the two contributions τ_{ext} and $\delta\tau$ are more filtered in the low frequencies for the JPVO than for the GMO, while it is the opposite in the high frequencies.

Nevertheless, differences between methods JPVO and GMO can be pointed out. For instance for JPVO, $\mathbf{H}_1^k(z)$ and $\mathbf{H}_2^k(z)$ exhibit a slope of -20 dB/dec and a phase between 0 and -90 degrees (at least for frequencies up to 30 rad/s), whereas for GMO the slope is of -40 dB/dec and the phase is between 0 and -180 degrees. Furthermore, according to the Bode diagrams of $\mathbf{H}_3^k(z)$, the noise contribution \underline{v} is more filtered for JPVO than for GMO.

In the following, we focus on $\mathbf{H}_1^k(z)$ since we are interested in the observer performances for detecting the external torque input τ_{ext} in a fast and sensitive way. For this purpose, we first propose analytical criteria in Section 4.1.2.1 to evaluate and compare the detection rapidity and sensitivity of disturbance observers along the robot trajectory. Then we study the influence of the tuning parameters on these criteria. In particular, we distinguish two types of setting parameters: those that are fixed outside the scope of impact detection (robot dynamic parameters and associated uncertainties, adjustment of the numerical differentiation scheme) in Section 4.1.2.2, and those that are specific to the algorithm and configurable (disturbance model parameters) in Section 4.1.2.3.

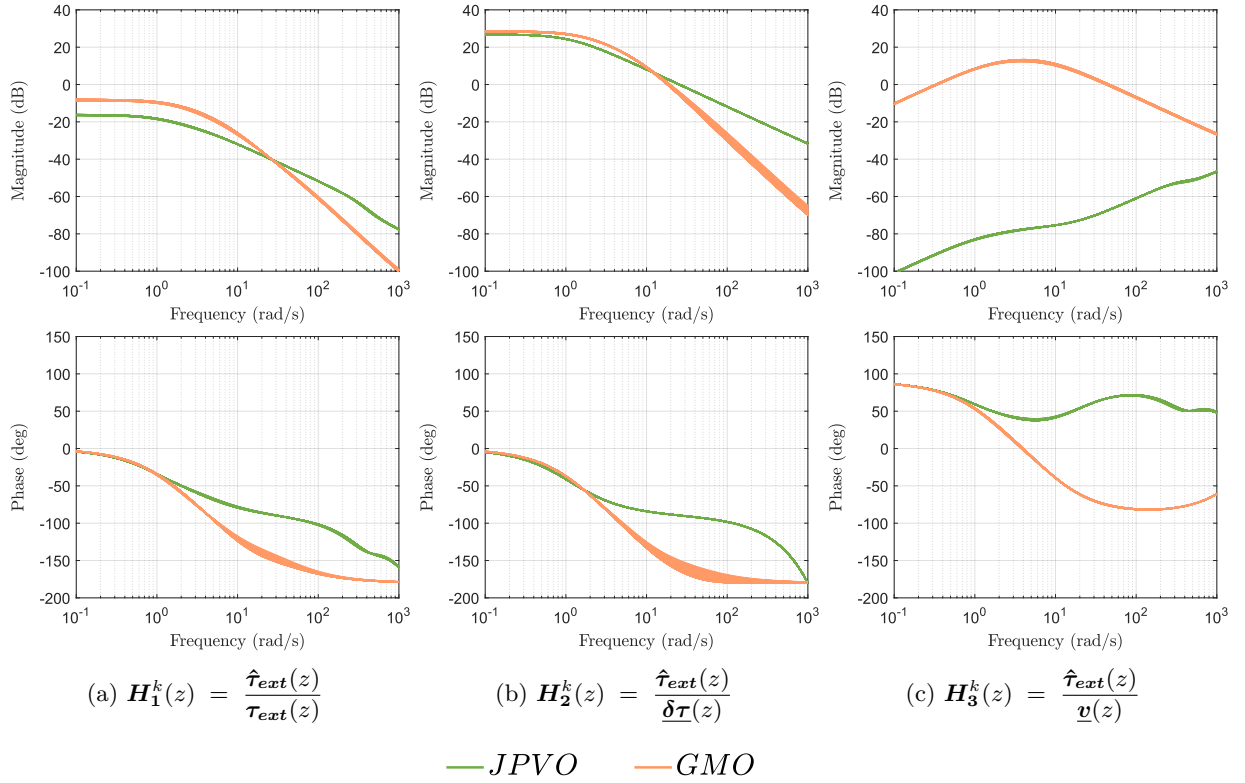


Figure 4.5: Bode diagrams of $\mathbf{H}_1^k(z)$, $\mathbf{H}_2^k(z)$ and $\mathbf{H}_3^k(z)$ for JPVO and GMO methods (computed at the 78 time instants represented in Figure 4.4).

4.1.2.1 Analytical criteria for detection

An impact detection algorithm is generally evaluated based on its ability to detect an impact quickly and sensitively. For the DETE, detection is likely to be very fast since there is no filtering step, and the sensitivity of the algorithm is directly given by the detection threshold. In contrast, for methods based on disturbance observers, the evaluation is less direct since the external torque is estimated by Kalman filtering. Therefore, an analytical characterization of the rapidity and sensitivity of detection is proposed in the following for disturbance observers.

Through the analysis of $\mathbf{H}_1^k(z)$, we are only interested in the contribution that reconstructs the external torque $\boldsymbol{\tau}_{ext}$ within $\hat{\boldsymbol{\tau}}_{ext}$, the other inputs $\underline{\boldsymbol{\delta\tau}}$ and $\underline{\mathbf{v}}$ being considered as null for the study. For the derivation of the analytical criteria, we consider the case where the external torque $\boldsymbol{\tau}_{ext}$ follows a step input of amplitude $\boldsymbol{\Gamma}$. The upcoming study is conducted for a given axis j to simplify the notations.

Impact detection rapidity The rapidity of detection of an impact is directly related to the response time of the filter: the faster the estimate $\hat{\boldsymbol{\tau}}_{ext}$ reaches its final value, the faster it may exceed the detection threshold provided that the latter is sufficiently low.

The 5%-criterion for settling time, denoted $t_{r5\%}^k$, is a good indicator to compare the response times of $\hat{\tau}_{ext}$ between several impact detection algorithms. Note that it is different from the detection time since the latter also depends on the level of the detection threshold. This criterion can be obtained either by approximating $\mathbf{H}_1^k(z)$ at each time step by a diagonal matrix of first-order filters for JPVO (at least for frequencies up to 30 rad/s) and second-order filters for GMO, or using numerical algorithms such as the `stepinfo` procedure in Matlab.

Impact detection sensitivity By denoting G^k the static gain of the transfer function $\mathbf{H}_1^k(z)$ at each time step k , which can be obtained using numerical algorithms such as the `dcgain` procedure in Matlab, the final value V^k of the estimated external torque $\hat{\tau}_{ext}(k)$ verifies:

$$V^k = G^k \Gamma \quad (4.13)$$

Denoting T^k the detection threshold at time step k defined by $T^k = 3\sigma_e(k)$, an impact can be detected if the following condition is verified (see Figure 4.6):

$$V^k > T^k \iff \Gamma > \Gamma_{min}^k \quad (4.14)$$

with $\Gamma_{min}^k = \frac{T^k}{G^k}$ the minimum amplitude of a detectable impact defined at each time step: the smaller Γ_{min}^k , the more sensitive the algorithm. Indeed, not only the detection threshold must be low for the impact to be detected, but it is also necessary that the static error is low enough so that the external torque estimate can exceed the detection threshold. This is the reason why the consideration of the detection threshold alone is not sufficient to describe the sensitivity of the algorithm in the specific case of disturbance observers, contrary to the DETE.

For the subsequent analyses, the influence of the various tuning parameters on the detection is studied through the settling time and the expected sensitivity¹, both being computed along the robot trajectory for the case of a step input in the external torque.

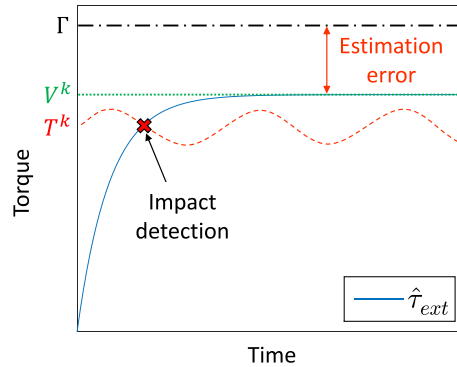


Figure 4.6: Schematic response of $\mathbf{H}_1^k(z)$ to a step input of amplitude Γ in the external torque $\tau_{ext}(k)$ (example of a first-order response).

¹Note that the term $\lambda_D^2 \mathbf{F}_{s*} \mathbf{F}_{s*}^T$ due to the error on dry friction that arises within $\Sigma_{\delta\tau}$ at low speeds (see the note on *Particular case of dry friction uncertainties* in Chapter 3: "Design of impact detection strategies under model uncertainties" – Section 3.2.1) will not be taken into account for readability reasons. Indeed, when considered, it results in a significant increase in the detection threshold during low speed phases.

4.1.2.2 Influence of the robot's modeling parameters

In this section, the influence of modeling parameters on the robot-side are investigated. In particular, the quality of the identification of the robot's dynamic parameters and the tuning of the numerical differentiation scheme are studied. For both analyses, the parameters considered are first specified, then the Bode diagrams of $\mathbf{H}_1^k(z)$ are illustrated. The resulting settling times and sensitivity thresholds are extracted according to the approach previously described.

Identification of the robot's dynamic parameters (Figure 4.7)

The influence of parametric errors is studied through several values of $\% \sigma_{\chi_i}$, which corresponds to different quality of identification:

- **P0** – Each parameter is perfectly identified: for each parameter i , $\% \sigma_{\chi_i} = 0$,
- **P1** – Proper quality of identification: for each parameter i , $\% \sigma_{\chi_i} \in [0\%, 5\%]$,
- **P2** – Poor quality of identification: for each parameter i , $\% \sigma_{\chi_i} \in [0\%, 20\%]$.

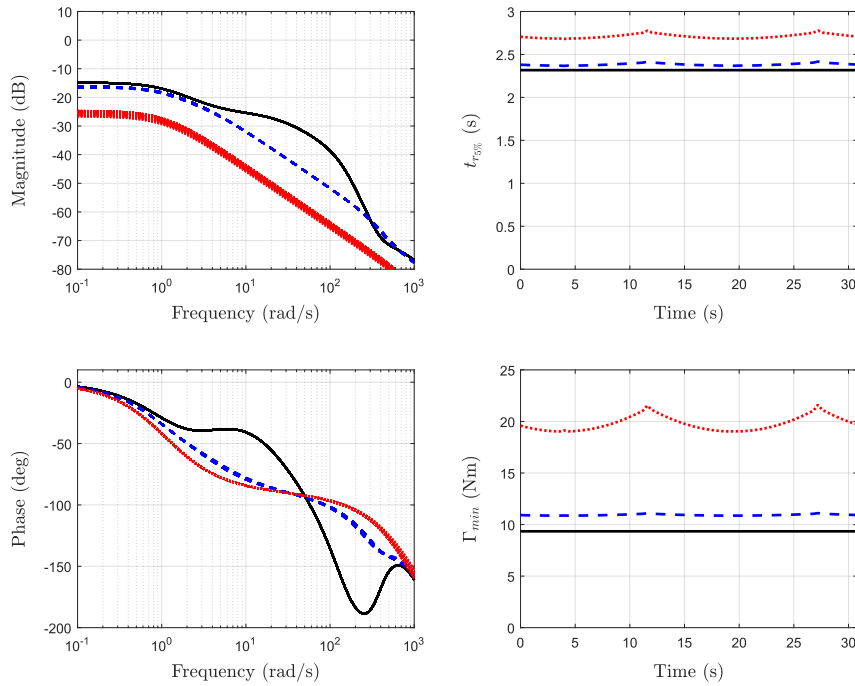
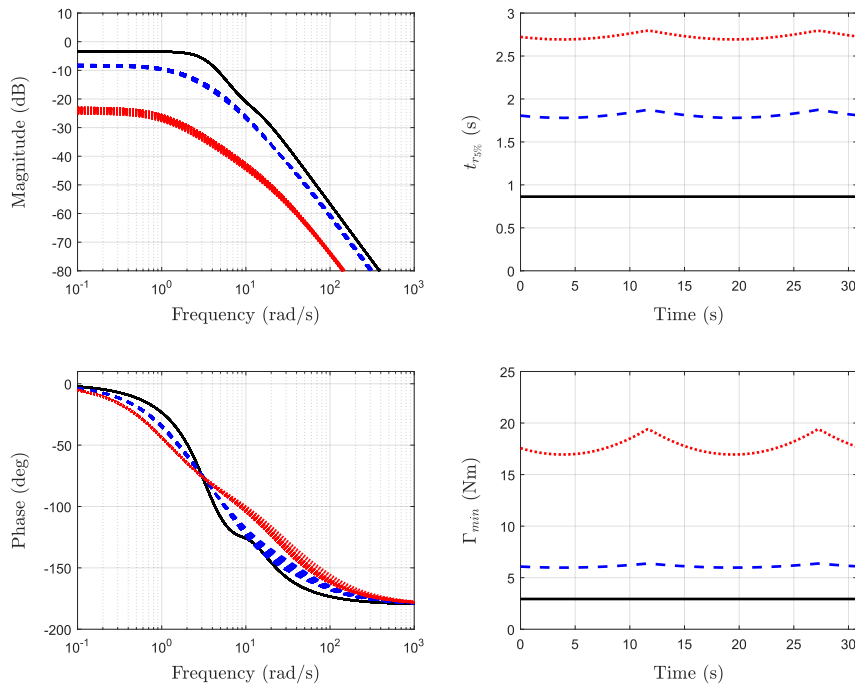
For this purpose, each $\% \sigma_{\chi_i}$ is fixed randomly and independently within these ranges with the same random distribution between **P1** and **P2**. Simulations are based on a given random realization of the uncertain parameters χ_{r^*} according to a normal distribution, centered around the exact values χ_r and of standard deviation deduced from $\% \sigma_{\chi}$.

Concerning numerical differentiation errors, the first order low-pass filtered derivative is set with $\omega_c = 2\pi 10$ rad/s. The terms \mathbf{A}_d and \mathbf{A}_{dd} within $\Sigma_{\dot{q}}$ and $\Sigma_{\ddot{q}}$ are computed based on a trajectory without contact. The disturbance model is set with $\mathbf{A}_{ext} = \mathbf{I}$ and $\Sigma_{ext} = 10\mathbf{I}$.

As observed in Figure 4.7, for both methods JPVO and GMO, when parametric uncertainties increase, the general trend is a decrease in the cut-off frequency and in the static gain of $\mathbf{H}_1^k(z)$. Therefore the estimate response will be slower and more filtered when the quality of the identification decreases. This results in a longer settling time and a worse detection sensitivity. The amplitude of the settling times may seem significant, but we recall that this criterion provides information on the response time of $\hat{\tau}_{ext}$ and is different from the detection time.

By comparing these two methods, we can note that for a reasonable quality of identification (**P1** condition), the GMO is likely to be faster and more sensitive than the JPVO. Nevertheless, we observe that the JPVO shows less variability to parametric errors in the estimation response time and the detection sensitivity than the GMO, which is significantly affected by this type of errors. In case of poor quality of identification (**P2** condition), the two methods would therefore be equivalent.

Note that the amplitude of the settling time and the minimum detectable torque may differ from one random distribution of parameters to another, but the estimate response will always be longer and the detection sensitivity lower when the quality of the identification decreases.

(a) Method based on JPVO under $P0$, $P1$ and $P2$ conditions(b) Method based on GMO under $P0$, $P1$ and $P2$ conditions

— $P0$ - - - $P1$ ····· $P2$

Figure 4.7: Bode diagrams of $H_1^k(z)$ (left) and resulting settling time $t_{r_{5\%}}$ and minimum detectable torque Γ_{min} (right) under $P0$, $P1$ and $P2$ conditions for JPVO and GMO methods (computed at the time instants represented in Figure 4.4).

Settings of the robot's numerical differentiation scheme (Figure 4.8)

The influence of the cut-off frequency tuning for the first-order low-pass filtered derivative is studied through several values of ω_c :

- **D0** – The numerical differentiation of joint coordinates is deemed perfect,
- **D1** – First-order low-pass filtered derivative of cut-off frequency $\omega_c = 2\pi 60$ rad/s,
- **D2** – First-order low-pass filtered derivative of cut-off frequency $\omega_c = 2\pi 10$ rad/s.

In the last two cases, the terms \mathbf{A}_d and \mathbf{A}_{dd} within $\Sigma_{\dot{q}}$ and $\Sigma_{\ddot{q}}$ are computed based on a trajectory without contact.

Concerning parametric errors, for each parameter i , $\% \sigma_{\chi_i}$ is fixed randomly and independently within $[0\%, 5\%]$. Simulations are based on a given random realization of the uncertain parameters $\mathbf{X}_{r\star}$ according to a normal distribution, centered around the exact values \mathbf{X}_r and of standard deviation deduced from $\% \sigma_{\chi}$. The disturbance model is set with $\mathbf{A}_{ext} = \mathbf{I}$ and $\Sigma_{ext} = 10\mathbf{I}$.

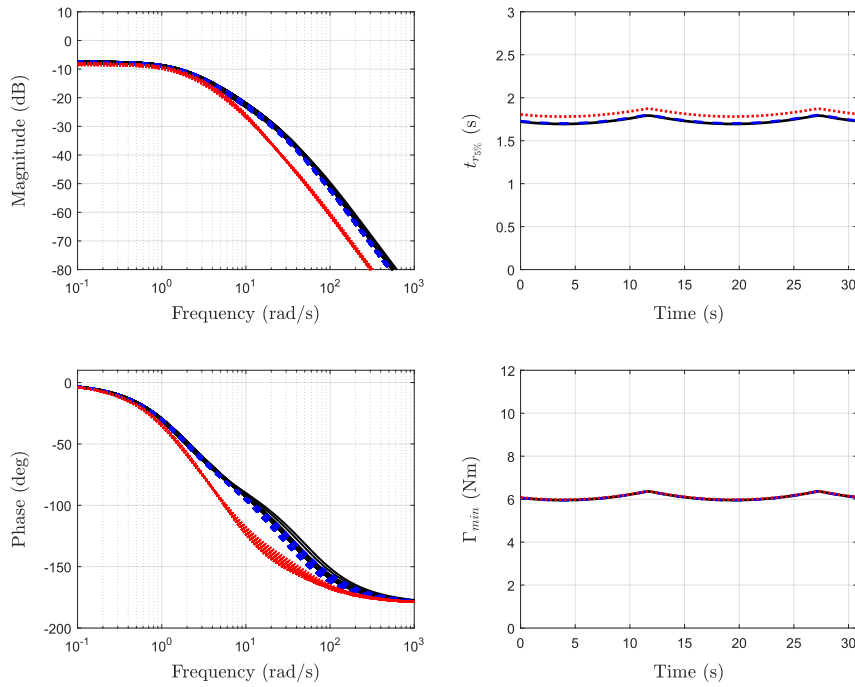
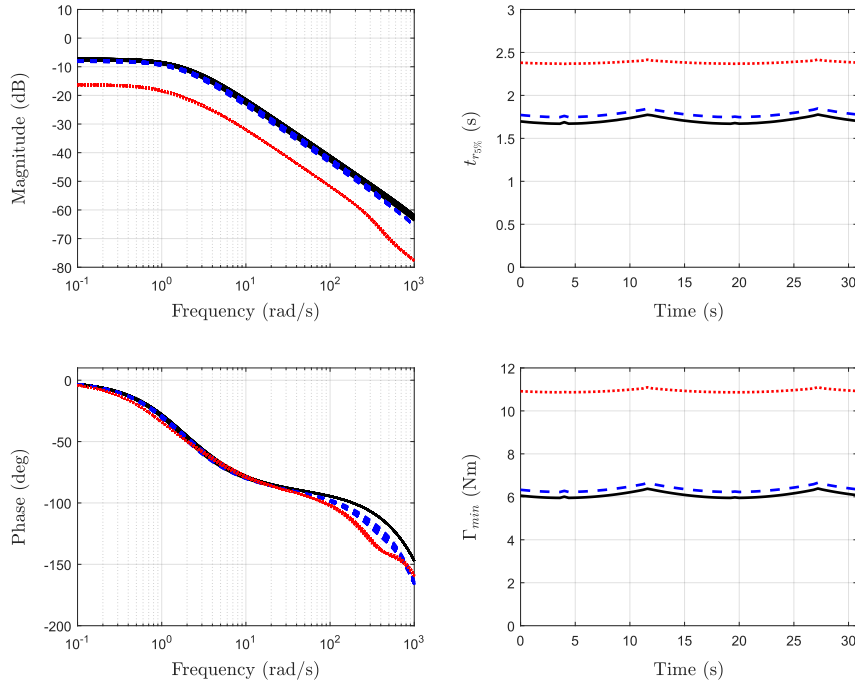
For both methods JPVO and GMO, we notice in Figure 4.8 that when the cut-off frequency ω_c of the derivative filter decreases, it leads to a slower response and a lower sensitivity. This is particularly true for the JPVO due to the presence of acceleration terms. For the GMO, the influence of the derivation filter cut-off frequency is reduced since it only affects velocity terms.

In the case of the JPVO, an alternative way to limit the influence of the filter cut-off frequency when the trajectory exhibits brief acceleration peaks (e.g. for the triangular trajectory under consideration) would be to evaluate the trajectory-dependent term \mathbf{A}_{dd} within $\Sigma_{\ddot{q}}$ over a sliding time window. Indeed, in this case, the variance induced by the derivative approximation error in acceleration estimates would be calculated based on the maximum acceleration over a few time steps of the trajectory without contact, which would lead to a smaller variance when the robot velocity is constant (see Figure 4.4).

It should be noted that these trends are valid for the trajectory under consideration during which significant acceleration peaks are present. For another trajectory with lower accelerations, the comparison of the two methods may lead to different conclusions: in particular, the JPVO-based method would not necessarily be the most disadvantageous one in terms of detection rapidity and sensitivity (see Section 4.2.2).

4.1.2.3 Influence of the disturbance model parameters

In this section, the influence of the disturbance model parameters \mathbf{A}_{ext} and Σ_{ext} on the transfer functions matrix $\mathbf{H}_1^k(z)$ is studied. The parameters considered are detailed below. Results of this analysis are presented for axis 2 on Bode diagrams, resulting settling times and sensitivity thresholds in Figures 4.9, 4.10 and 4.11 respectively.



— $D0$ - - - $D1$ ···· $D2$

Figure 4.8: Bode diagrams of $H_1^k(z)$ (left) and resulting settling time $t_{r5\%}$ and minimum detectable torque Γ_{min} (right) under $D0$, $D1$ and $D2$ conditions for JPVO and GMO methods (computed at the time instants represented in Figure 4.4).

Adjustment of the disturbance model parameters (Figures 4.9, 4.10, 4.11)

The influence of the settings of the disturbance model is studied through several values of \mathbf{A}_{ext} and $\mathbf{\Sigma}_{ext}$:

- \mathbf{A}_{ext} – first-order disturbance model dynamics: the higher \mathbf{A}_{ext} , the faster the assumed disturbance model. The parameters considered are:
 - $\mathbf{A1} - \mathbf{A}_{ext} = \mathbf{0}$,
 - $\mathbf{A2} - \mathbf{A}_{ext} = \mathbf{I}$,
 - $\mathbf{A3} - \mathbf{A}_{ext} = 5\mathbf{I}$.
- $\mathbf{\Sigma}_{ext}$ – uncertainty on the disturbance model: the higher $\mathbf{\Sigma}_{ext}$, the less reliable the assumed disturbance model. The parameters considered are:
 - $\mathbf{\Sigma1} - \mathbf{\Sigma}_{ext} = \mathbf{I}$,
 - $\mathbf{\Sigma2} - \mathbf{\Sigma}_{ext} = 10\mathbf{I}$,
 - $\mathbf{\Sigma3} - \mathbf{\Sigma}_{ext} = 100\mathbf{I}$.

Concerning parametric errors, for each parameter i , $\% \sigma_{\chi_i}$ is fixed randomly and independently within $[0\%, 5\%]$. Simulations are based on a given random realization of the uncertain parameters χ_{r^*} according to a normal distribution, centered around the exact values χ_r and of standard deviation deduced from $\% \sigma_{\chi}$. Concerning numerical differentiation errors, the first order low-pass filtered derivative is set with $\omega_c = 2\pi 10$ rad/s. The terms \mathbf{A}_d and \mathbf{A}_{dd} within $\mathbf{\Sigma}_{\dot{q}}$ and $\mathbf{\Sigma}_{\ddot{q}}$ are computed based on a trajectory without contact.

From Figures 4.9, 4.10, 4.11, it can be observed that the larger \mathbf{A}_{ext} and $\mathbf{\Sigma}_{ext}$, the higher the cut-off frequency and the faster the response, but at the same time the smaller the static gain and the worse the sensitivity of the detection. Therefore, if \mathbf{A}_{ext} and $\mathbf{\Sigma}_{ext}$ are set very large to ensure a rapid detection, there is a risk that the impact will not be detected. On the contrary, when \mathbf{A}_{ext} and $\mathbf{\Sigma}_{ext}$ are set relatively small, the impact detection will be sensitive but slow. Furthermore, when the two observers are compared, it seems that in most situations the GMO is more sensitive and faster than the JPVO for these parametric uncertainties, this setting of the numerical differentiation scheme and this robot trajectory.

The \mathbf{A}_{ext} and $\mathbf{\Sigma}_{ext}$ parameters can therefore be adapted according to the desired objective:

- a fast estimation of τ_{ext} for a rapid detection: \mathbf{A}_{ext} and $\mathbf{\Sigma}_{ext}$ should be both set large,
- a sensitive detection: \mathbf{A}_{ext} and $\mathbf{\Sigma}_{ext}$ should be both set small.

In order to meet safety requirements, these two criteria are both essential. Thus a trade-off on \mathbf{A}_{ext} and $\mathbf{\Sigma}_{ext}$ has to be found, which is directly related to the trade-off between rapidity and sensitivity of detection. To overcome this problem, a bank of Kalman filters can be implemented with different adjustments of \mathbf{A}_{ext} and $\mathbf{\Sigma}_{ext}$.

The final trends observed in this section are summarized in Table 4.1. While certain trends could have been predicted, quantitative criteria characterizing the detection were also determined through this analysis in order to compare the performance of the two disturbance observers.

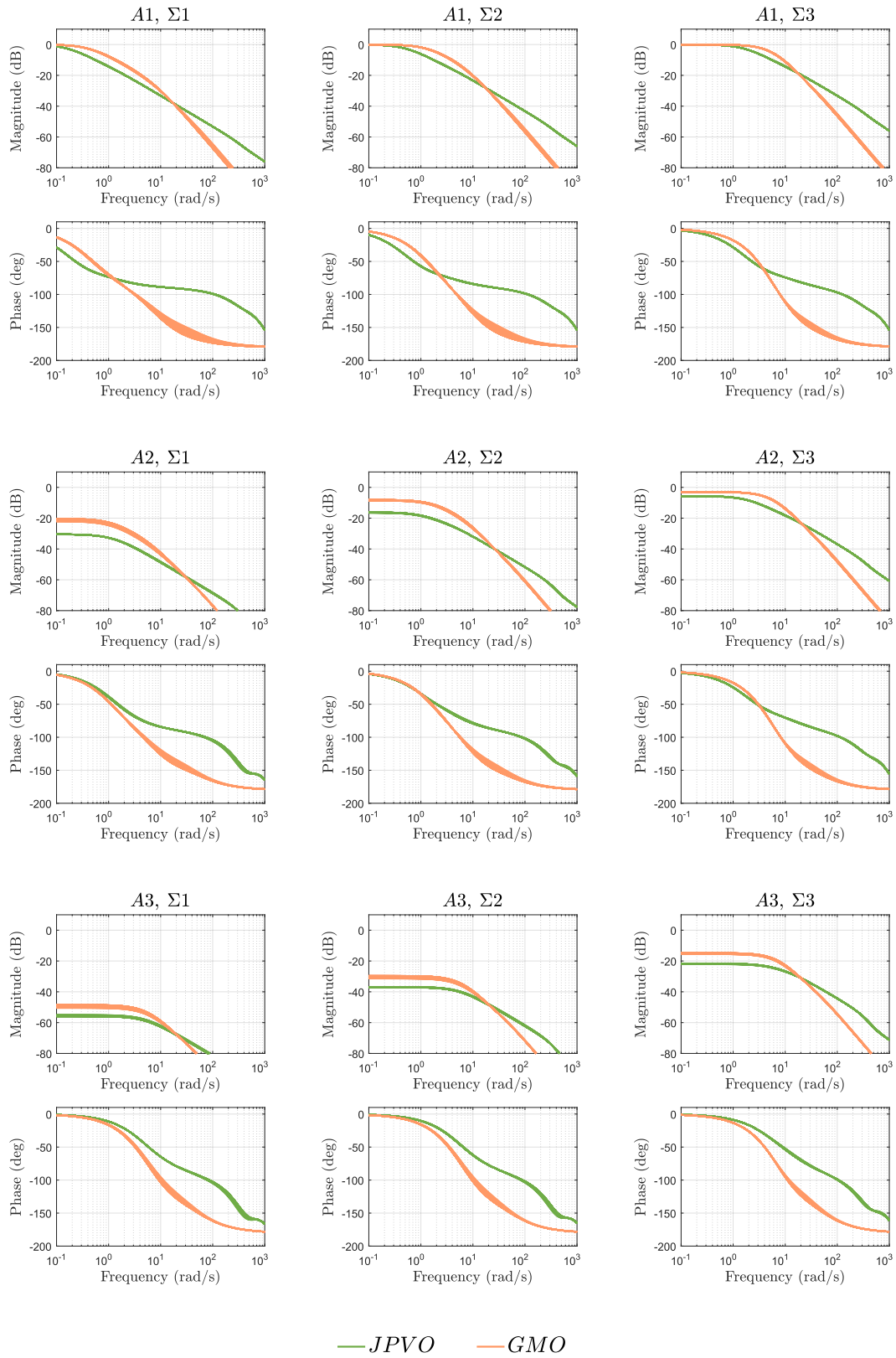


Figure 4.9: Bode diagrams of $H_1^k(z)$ for JPVO and GMO methods under conditions A1 to A3 and $\Sigma 1$ to $\Sigma 3$ (computed at the time instants represented in Figure 4.4).

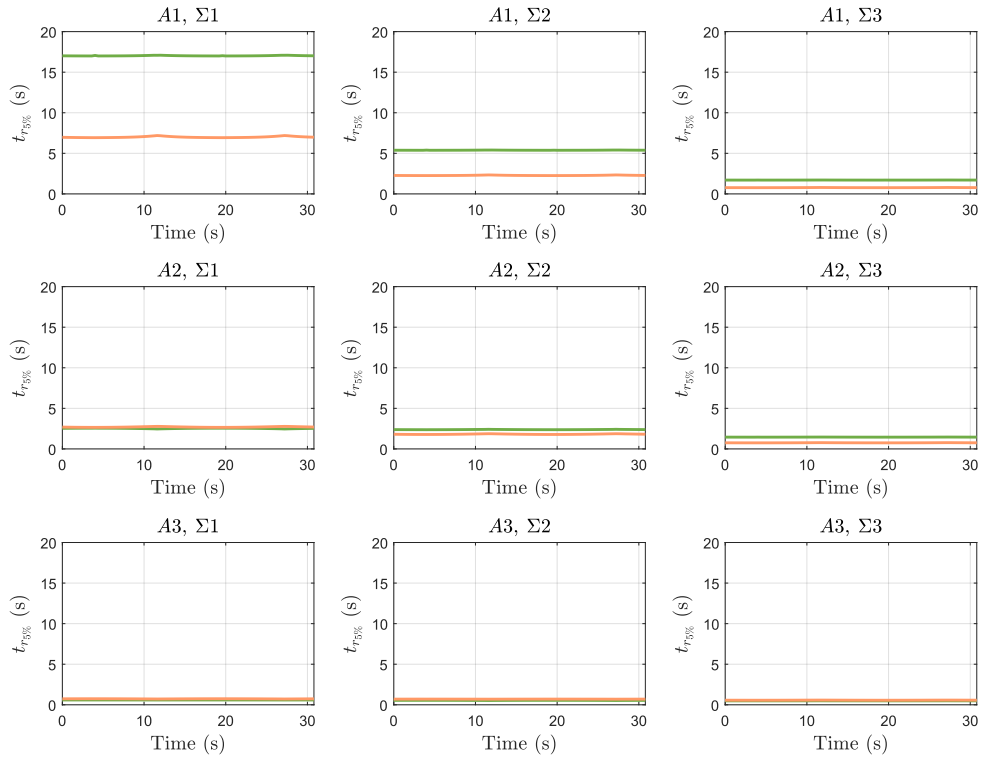


Figure 4.10: Settling time $t_{r_{5\%}}$ for JPVO and GMO methods under conditions A1 to A3 and $\Sigma 1$ to $\Sigma 3$ (computed at the time instants represented in Figure 4.4).

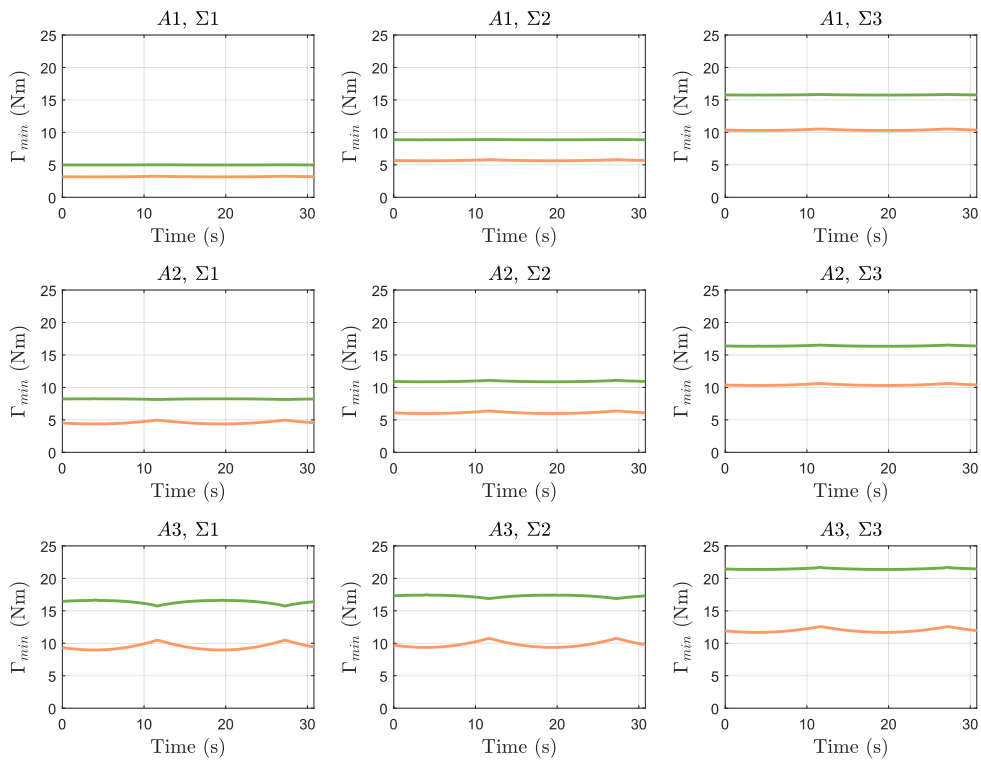


Figure 4.11: Minimum detectable torque Γ_{min} for JPVO and GMO methods under conditions A1 to A3 and $\Sigma 1$ to $\Sigma 3$ (computed at the time instants represented in Figure 4.4).

	$\% \sigma_{\chi^*}$ increases	ω_c increases	A_{ext} increases	Σ_{ext} increases
Rapidity	↘	↗	↗	↗
Sensitivity	↘	↗	↘	↘

Table 4.1: Resulting trends (↗ increasing or ↘ decreasing) for the observer-based strategies according to the various influential parameters.

4.1.3 Experimental validation

The three algorithms for impact detection (DETE, JPVO and GMO) derived in [Chapter 3: "Design of impact detection strategies under model uncertainties"](#) are evaluated in the rigid case on the experiment described in [Section 4.1.1](#). The evaluation is processed offline in order to compare the detection results. First, preliminary settings are presented in [Section 4.1.3.1](#), then [Section 4.1.3.2](#) reports the detection results obtained.

4.1.3.1 Protocols and settings

As seen in the previous section, the detection of external impacts is influenced by the quality of the identification of dynamic parameters, the numerical differentiation scheme and the settings of the disturbance model (in the case of disturbance observers). The specific choices associated with these parameters and the approaches adopted to obtain them are detailed below.

Identification of the dynamic model parameters

The identification of the robot dynamic model parameters of the ISYBOT prototype robot was carried out in two steps:

- Step 1: Sequential sets of non-contact trajectories were performed to stimulate specific dynamic model parameters. Experimental values were obtained by post-processing the recorded data.
- Step 2: Since some parameters can vary locally (e.g. friction parameters), local non-contact trajectories around the one under consideration for the detection were performed to identify these specific parameters. During post-processing, the other parameters that are assumed to be constant over the entire robot workspace (e.g. inertial parameters) were set to the values obtained in Step 1.

This second step also provides the relative standard deviation vector $\% \sigma_{\chi}$ and the covariance matrix Σ_{χ} of the estimation error on the dynamic model parameters specifically for the detection trajectory under study. Indeed, if the identification was limited to Step 1, there would be a risk of increasing the false alarm rate because the operating conditions might be under-represented in the set of identification trajectories (e.g. identification of a friction model at relatively high speeds although the detection is carried out on a trajectory at a lower speed). The identified dynamic model parameters after Step 1 can be found in [Appendix B – Section B.3](#).

Numerical differentiation scheme and associated parameters

First, the distribution of the measurement noise on the joints position is verified by experimental measurement at different robot configurations (see [Appendix B – Section B.4.1](#)). The associated covariance matrix Σ_q can either be calculated analytically as proposed in equation (2.45) for a uniform noise distribution or numerically using the values collected experimentally.

To compute the robot speeds and accelerations, the cut-off frequency of the first-order low-pass filtered derivative is set to $\omega_c = 2\pi 10$ rad/s. Although this setting is relatively low compared to those generally used (around $2\pi 50$ rad/s), this choice guarantees an estimation of the external torque with a low level of noise but it leads to rather unfavorable conditions in terms of rapidity and sensitivity of detection (see [Table 4.1](#)). The terms A_d and A_{dd} within $\Sigma_{\dot{q}}$ and $\Sigma_{\ddot{q}}$ are computed based on a trajectory without contact. Finally, the speed threshold α_q related to errors due to dry friction at low speed is set equal to $\alpha_q = 0.07 I_n$ rad/s.

Disturbance observers settings

For the design of the Kalman filter, the covariance matrices of the model errors $\Sigma_{\delta\tau}$ and the measurement noise Σ_v are predetermined based on the reference trajectory (see [Remark 3.6](#)). In order to maximize the chances of detection, a bank of Kalman filters is used for each of the two observers as illustrated in [Figure 4.12](#). For this purpose, the 9 possible combinations of the following settings of the external disturbance model are tested:

- A1: $A_{ext} = 0$,
- A2: $A_{ext} = I$,
- A3: $A_{ext} = 5I$.
- $\Sigma 1$: $\Sigma_{ext} = I$,
- $\Sigma 2$: $\Sigma_{ext} = 10I$,
- $\Sigma 3$: $\Sigma_{ext} = 100I$.

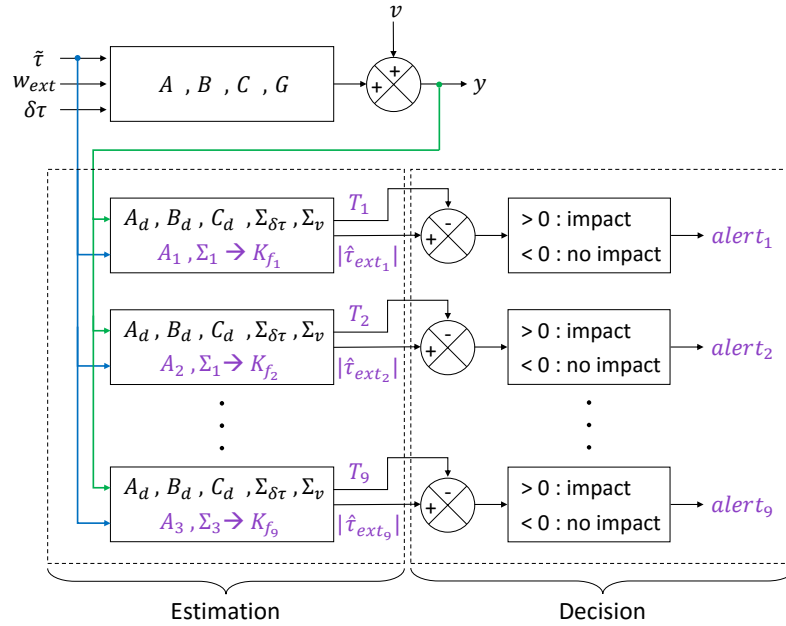


Figure 4.12: Evaluation by the bank of Kalman filters

4.1.3.2 Experimental results

The offline evaluation of the detection algorithms is described below, based on the previous preliminary settings. As a reminder, the experiment in Section 4.1.1 involves four impacts of different amplitude, which effects on the residual may be of the same order of magnitude as the peaks due to modeling uncertainties. The objective in the following is to compare the results obtained with the different impact detection algorithms in order to highlight the advantages and disadvantages of each method.

The estimated external torque $\hat{\tau}_{ext}$ and its associated detection thresholds are illustrated for axis 2 in Figure 4.13 for the DETE-based method and the JPVO and GMO, all being computed in the rigid case because the robot elasticities were not “strongly” stimulated along the trajectory. As described in Chapter 3: "Design of impact detection strategies under model uncertainties", the envelope formed by the positive and negative detection thresholds $T^k = \pm 3\sigma_e(k)$ represents at each time step the maximum contribution of the uncertainties in absence of external contact. Consequently, when one of these thresholds is exceeded, it necessarily implies that there is an additional contribution due to an external contact (in 99.7% of the cases for the 3σ -confidence interval). The induced alarm signal, which is triggered as soon as one of the components of $\hat{\tau}_{ext}$ exceeds its thresholds, is displayed for each method in relation with the applied force as measured by the force/torque sensor in Figure 4.14. The corresponding detection times are reported in the associated tables. For disturbance observers, the results are given for the Kalman filter that provides the earliest detection, which parameters are specified in the associated tables.

The peaks on the detection thresholds that can be observed in Figure 4.13 correspond to low-speed transitions below α_q (e. g. change in the trajectory direction) during which the sign of the measured velocity may be different from the sign of the robot’s actual velocity. This generates a peak of error on the residual, which is noticeable for the DETE, but for disturbance observers, the transition being fast, it is not visible on the estimate output. Nonetheless, to account for this error, the detection thresholds increase accordingly during that period of time, which makes the detection of an impact occurring at this moment less sensitive.

We observe that the strongest impacts (impacts 1 and 4) are correctly detected by all three methods. However, when the impact is of lower amplitude (impacts 2 and 3), the three detection methods barely detect it. In particular, impact 3 is only detected by the GMO, which makes it the most sensitive algorithm in this situation. In addition, the residual provided by the DETE is quite noisy and would probably be unusable as it stands for further developments (e. g. location of the contact point, reconstruction of the applied force) without prior filtering. Conversely, the Kalman filtering estimates are more filtered and reusable.

Regarding the Kalman filters bank adjusted with different disturbance models, the combination ($A_{ext} = \mathbf{0}$, $\Sigma_{ext} = \mathbf{I}$) is the one that actually gives the longest detection times (e. g. for impact 4, we get 1.519s for the JPVO and 1.288s for the GMO), while for ($A_{ext} = 5\mathbf{I}$, $\Sigma_{ext} = 100\mathbf{I}$), corresponding to the least sensitive adjustment, only impact 4 is detected for both observers since this is the strongest impact. Finally, the combination ($A_{ext} = \mathbf{0}$, $\Sigma_{ext} = 100\mathbf{I}$) provides the best trade-off between sensitivity and rapidity of detection in most of these contact situations.

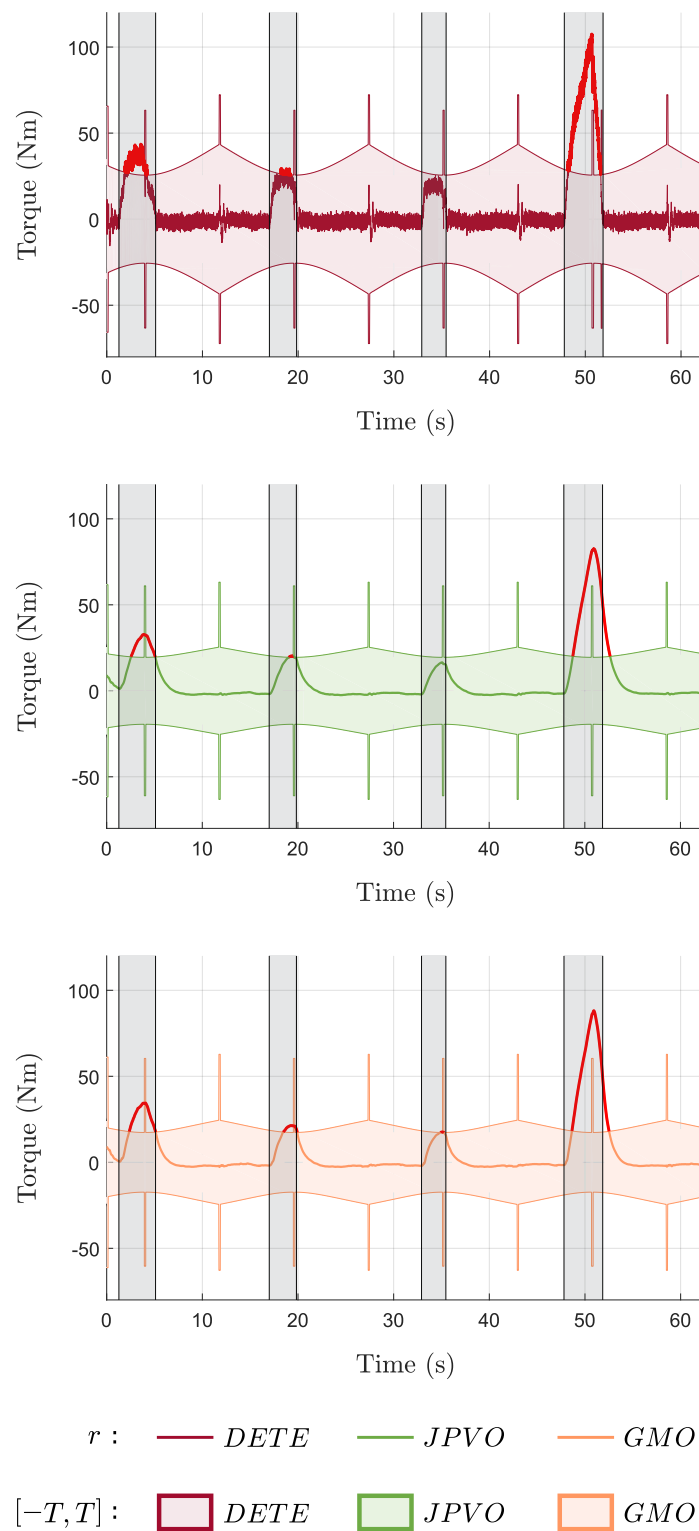
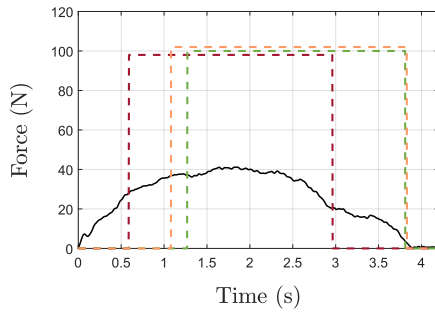
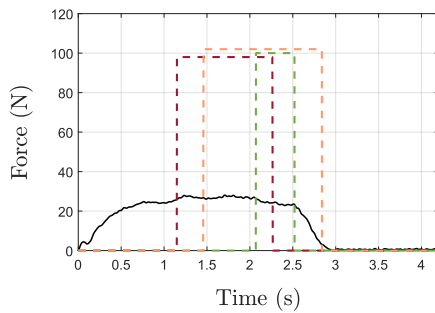


Figure 4.13: Residual (estimation $\hat{\tau}_{ext}$ of the external torque) obtained in the rigid case with the DETE, the JPVO and the GMO (with disturbance model $A1, \Sigma3$) and its associated detection thresholds. Impact times are indicated by the shaded areas. In red are indicated the points above the thresholds that trigger a detection alert.



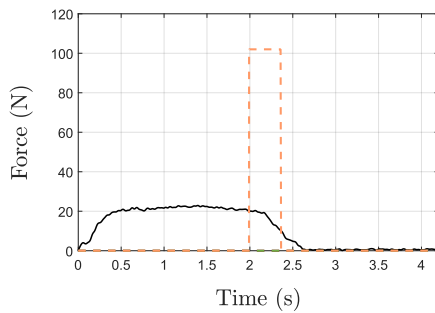
(a) Results for impact 1

Method	Detection time	Disturbance model
DETE	0.591 s	–
JPVO	1.272 s	$A1, \Sigma3$
GMO	1.081 s	$A1, \Sigma3$



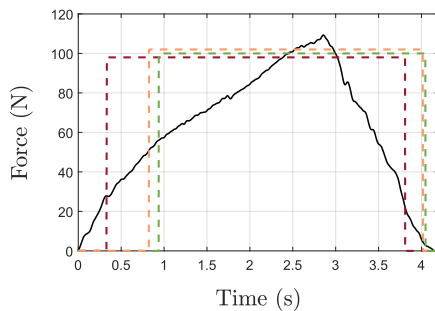
(b) Results for impact 2

Method	Detection time	Disturbance model
DETE	1.150 s	–
JPVO	2.071 s	$A1, \Sigma3$
GMO	1.460 s	$A1, \Sigma3$



(c) Results for impact 3

Method	Detection time	Disturbance model
DETE	–	–
JPVO	–	–
GMO	1.991 s	$A1, \Sigma3$



(d) Results for impact 4

Method	Detection time	Disturbance model
DETE	0.333 s	–
JPVO	0.938 s	$A1, \Sigma3$
GMO	0.825 s	$A2, \Sigma3$

— F_{ext} Alert signals: - - - *DETE* - - - *JPVO* - - - *GMO*

Figure 4.14: Alert signals (*dashed lines*) indicating the impact detection (*impact if > 0*) in relation with the applied force measured by the force/torque sensor (*solid black line*). The corresponding detection times are reported in the associated tables.

The analytical criteria of settling time and expected sensitivity threshold are derived for this experiment for axis 2 in Figure 4.15. Note that the settling time for the DETE is not illustrated but given the absence of filtering, the rise time is very fast, making this method the fastest regardless of the disturbance observers adjustment. The actual external torque τ_{ext} , induced by the wrench measured by the force/torque sensor and transmitted at the joint-level with equation (2.1), is also reported for comparison with the algorithms sensitivity. The frequency-domain analysis confirms that the response time of $\hat{\tau}_{ext}$ with the GMO is faster than with the JPVO, the latter being probably affected by a penalizing delay on the acceleration estimates due to the pessimistic settings of $\omega_c = 2\pi 10$ rad/s. The sensitivity analysis of these algorithms shows that for some adjustments of the disturbance model parameters, the two observers can provide a better detection sensitivity than the DETE. However, this sensitivity is achieved at the cost of a relatively long detection time. Indeed, in the case of impact 3, the input torque τ_{ext} starts to decrease before the JPVO estimate has reached the detection threshold (see Figure 4.13), which is why this impact is not detected by the JPVO as it should be according to Figure 4.15b.

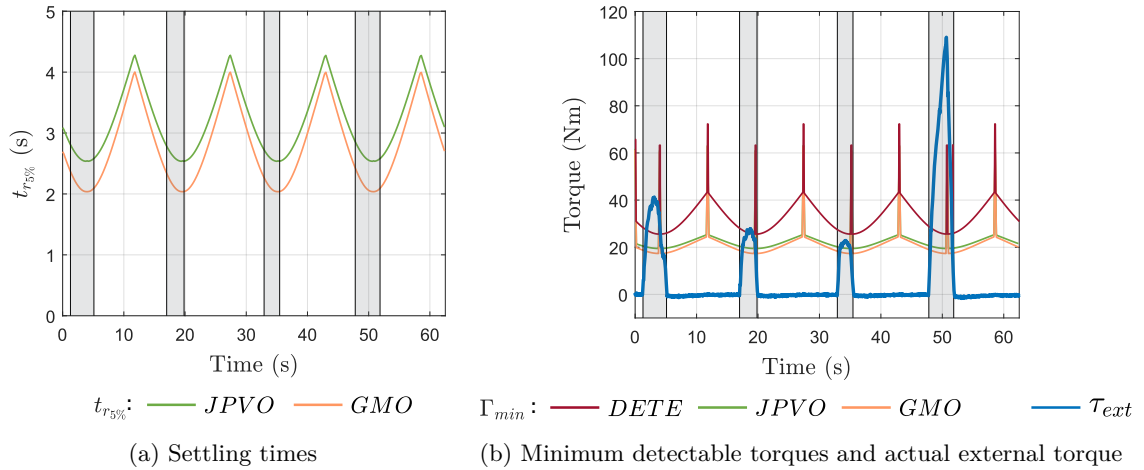


Figure 4.15: Analytical criteria for the DETE, the JPVO and the GMO (with disturbance model A1, $\Sigma 3$). Impact times are indicated by the shaded areas.

Finally, from the previous frequency-domain analysis and these experimental results, we can consider that the DETE is advantageous for its detection rapidity, while disturbance observers JPVO and GMO are interesting to achieve a sensitive detection. The comparison between these two observers depends on the levels of acceleration involved during the robot's trajectory. Besides, the output of the observers being filtered, it is more directly reusable for further developments than the residual computed with the DETE.

However, the comparison of detection times gives an idea of the algorithms reactivity but does not provide information about the contact dangerousness. Indeed, a severe impact that is rapidly detected may be as dangerous as an impact of low amplitude but detected late. In addition, at identical detection times, an impact will not produce the same effects depending on the robot speed or the type of environment collided. Therefore, the next section proposes to investigate the energy dissipated by the robot and the environment during the contact and to determine the amount of energy absorbed by the collided object.

4.2 Validation with regard to the energy transferred

In this section, the results obtained with the impact detection algorithms are evaluated in terms of energy as it is the case for robotic safety standards. In order to measure the energy absorbed by the human operator during a contact with a robot, it would be necessary to know the penetration depth of the robot into the body area. To overcome this constraint, an experimental protocol reproducing this type of contact has been considered based on the analogy with the two-mass system connected by a spring described in Chapter 1: "Context and objectives".

4.2.1 Description of the experimental set-up

An experimental set-up composed of a sliding carriage mounted on a rail has been designed (see Figure 4.16). The sliding carriage is connected to the rail by a linear spring. At its top is a 6-axis force/torque sensor where the robot end-effector will come into contact. A position sensor is fixed on the rail on the one hand and attached to the sliding carriage on the other hand in order to measure its displacement during the contact with the robot. The rail is rigidly positioned on a table in front of the robot.

The purpose of this experiment is to reproduce a human-robot contact, where the linear spring models the effective stiffness of the body area. Two different springs are used such that the linear stiffness of the overall system is equal to $k_1 = 1.3 \text{ N/mm}$ and $k_2 = 18 \text{ N/mm}$. According to the stiffness of the different regions of the human body given in Appendix A, the value of k_2 is between the minimum stiffness of the human body corresponding to the abdomen region (10 N/mm) and the chest and pelvis regions (25 N/mm). The stiffness k_1 is used for comparison purposes.

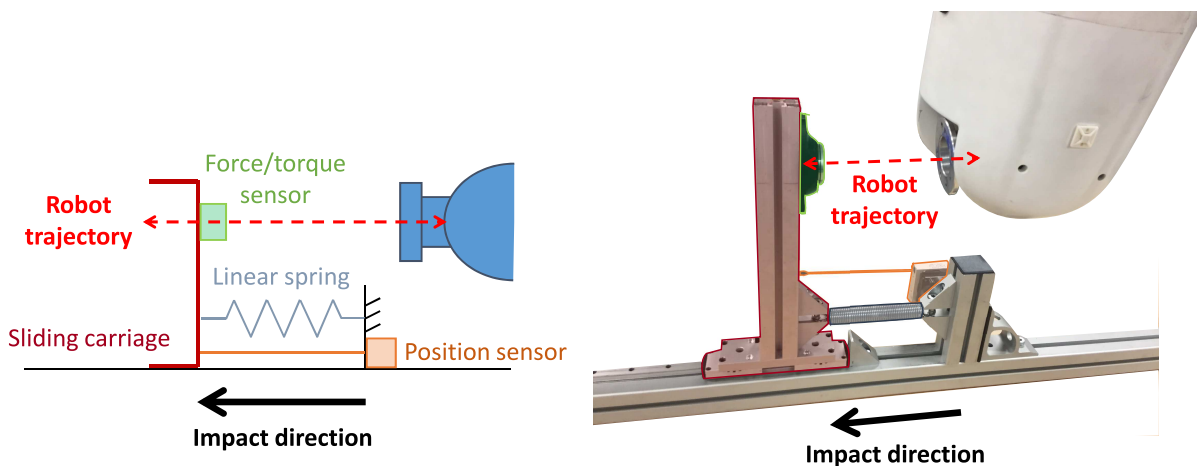


Figure 4.16: Experimental set-up to reproduce human-robot impacts

During the experiment, the robot end-effector moves back and forth in a straight line along the rail (see Figure 4.17a). The robot is controlled in position in the Cartesian space with a proportional-derivative (PD) control law to follow a filtered triangular trajectory illustrated in Figure 4.17b. This trajectory is programmed so that the robot comes into contact with the carriage at the force/torque sensor location, pushes it, then returns to its initial position. Two Cartesian velocities ($v_1 = 115$ mm/s and $v_2 = 269$ mm/s) are tested to vary the force applied on the force/torque sensor at the time of impact.

Figure 4.18 shows the force measured in the direction perpendicular to that of the applied force during a contact occurrence for the different end-effector speeds and spring stiffnesses. It can be noted that the rise time of the measured force increases with the stiffness of the spring and slightly with the speed of the robot. In addition, some oscillations can be observed at the beginning that may be due to a recoil after the contact of the two rigid surfaces.

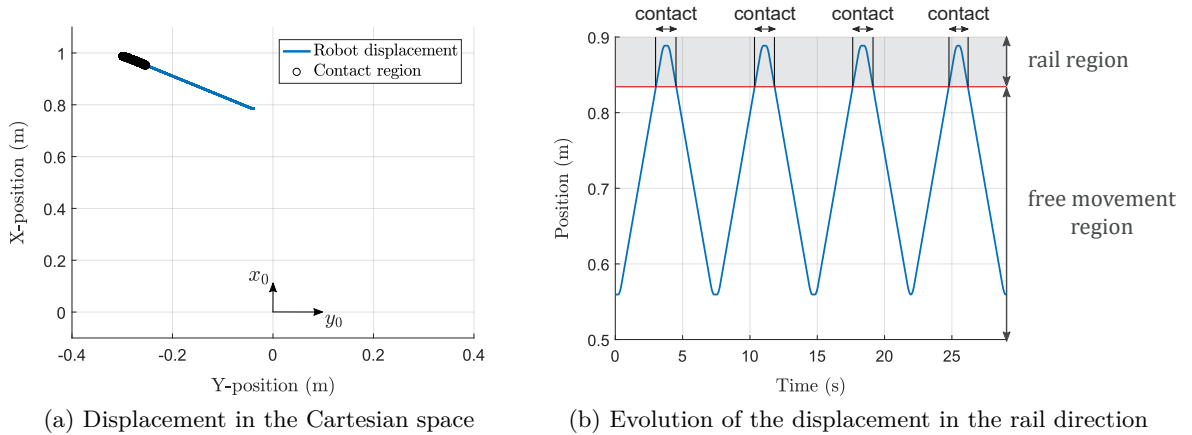
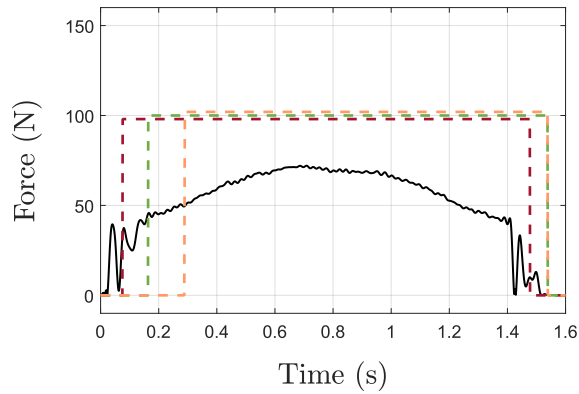


Figure 4.17: Reference trajectory of the robot's end-effector (speed v_1)

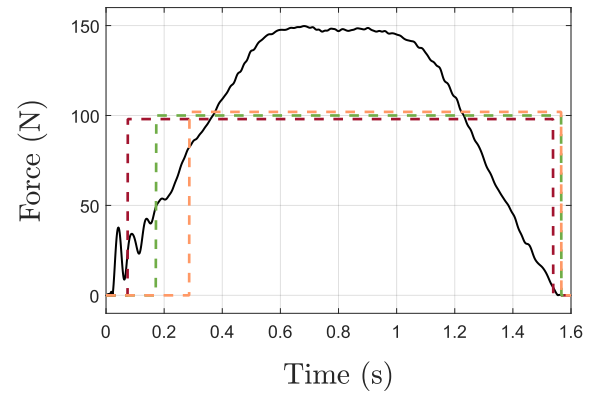
4.2.2 Evaluation of the results

The three detection methods seen previously in the rigid case (DETE, JPVO and GMO) are applied offline to evaluate and compare the characteristics of the contact detection. For this purpose, the same preliminary configuration procedure as in Section 4.1.3.1 is followed. Nevertheless, in this case only one Kalman filter is designed for each disturbance observer-based method and its external disturbance model is configured with $\mathbf{A}_{ext} = 5\mathbf{I}$ and $\Sigma_{ext} = 100\mathbf{I}$.

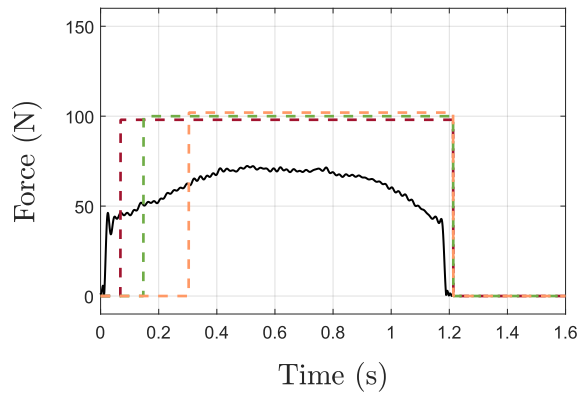
Axes 1 and 3 are mainly affected by the impact and the corresponding alert signals are illustrated in Figure 4.18 for the three methods. The detection times and forces at that instant are reported in the associated tables. It can be noticed that, whatever the method considered, when the robot's impact speed increases, the contact is generally detected earlier but the force at that moment is also higher. This is also the case when the stiffness increases, although it is less generalizable to the three methods with respect to the detection time.



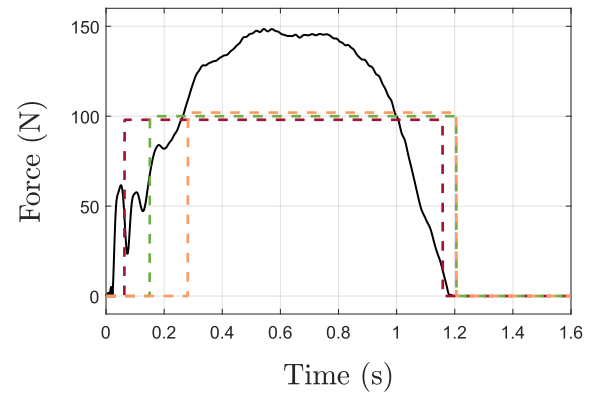
Detection	time (ms)	force (N)
DETE	76	33
JPVO	164	44
GMO	290	49

(a) Speed v_1 , stiffness k_1 

Detection	time (ms)	force (N)
DETE	75	24
JPVO	173	49
GMO	287	82

(b) Speed v_1 , stiffness k_2 

Detection	time (ms)	force (N)
DETE	69	46
JPVO	148	50
GMO	304	62

(c) Speed v_2 , stiffness k_1 

Detection	time (ms)	force (N)
DETE	64	42
JPVO	151	68
GMO	282	109

(d) Speed v_2 , stiffness k_2

— F_{ext} Alert signals: - - - *DETE* - - - *JPVO* - - - *GMO*

Figure 4.18: Evolution of the force applied to the sliding carriage as measured by the force/torque sensor (*solid black lines*) and alert signals (*dashed lines*) indicating the detection of the impact for each method (*impact if > 0*). The corresponding detection times and forces at that instant are reported in the associated tables.

For this reason, the consideration of the energy dissipated during the contact and absorbed by the collided system is more relevant. Figure 4.19 depicts the evolution of the contact force (as measured by the force/torque sensor) as a function of the carriage displacement (as measured by the position sensor). The corresponding contact detection instant for each method is marked with a cross. Among the total energy dissipated during the contact, the amount absorbed by the collided system during the impact detection phase, denoted E , corresponds to the mechanical work provided by the external force to move the carriage, that is:

$$E = \int_{x_0}^{x_d} F_{ext} dx \quad (4.15)$$

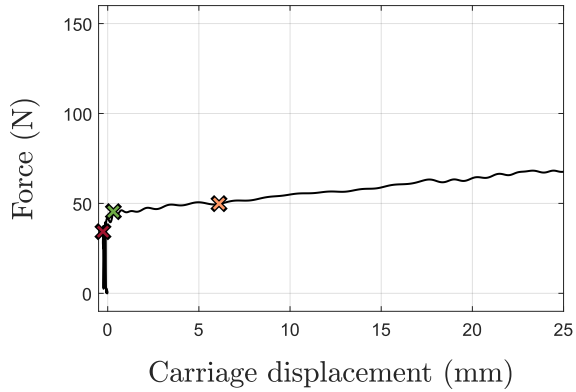
where F_{ext} is the force measured by the force/torque sensor in the perpendicular direction of contact, x_0 is the carriage position at the beginning of the contact and x_d is its position at the time of the detection. The energy absorbed by the collided system is reported in the associated tables for the three methods.

We observe that, regardless of the speed and stiffness conditions, the GMO-based method is the one that causes the greatest absorbed energy due to its late detection time compared to the two other impact detection methods. In addition, with the DETE and at velocity v_1 , the total energy absorbed by the system is nearly zero because the detection occurs within the first few milliseconds of contact during which the carriage undergoes a recoil effect (negative displacement) before being pushed by the robot (positive displacement).

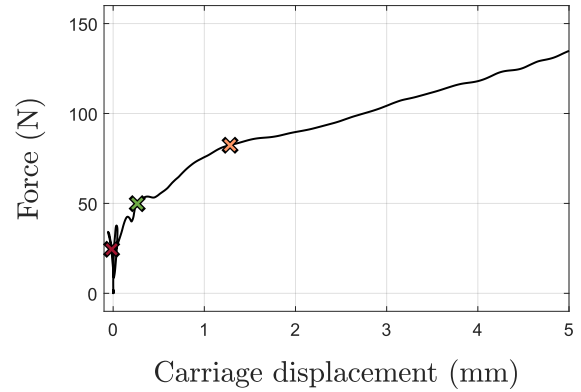
Finally, regardless of the detection method considered, the energy absorbed by the carriage is the highest for the lowest stiffness k_1 and the highest speed v_2 (see Figure 4.19c). As a guideline for comparison, the values obtained can be related to the limits defined by the technical specification [ISO/TS 15066: 2016] (see Appendix A). In particular, the maximum transferred energy allowed for transient contact forces applied at the abdomen, the chest or the pelvis regions, whose stiffness is close to stiffness k_2 , are 2.4, 1.6 and 2.6 J respectively.

Several improvements to this evaluation procedure could be proposed for future work:

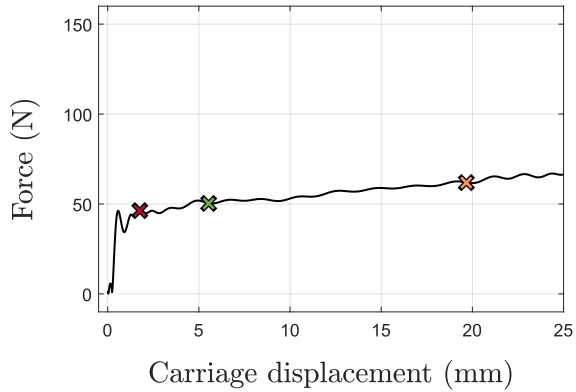
- First, it would be necessary to integrate a variable mass attached to the sliding carriage to be in the same circumstances of equivalent mass for each body region as the robotic standard ISO/TS 15066.
- Then, by implementing these algorithms online, it would be possible to initiate a strategy after detection (e. g. switching to gravity compensation mode, reversing the trajectory to escape from the contact, ...). Thus, the total energy absorbed by the collided system during the contact could be calculated, that is, by including the additional energy induced during the post-reaction phase of the robot.
- Finally, further experiments could be carried out by increasing the robot speed to determine the maximum permissible speed before exceeding the limit of the technical specification. In an industrial context, this test could be performed for a stiffness and an equivalent mass corresponding to the minimum permissible transferred energy among the human body areas exposed to a contact with the robot. This would ensure that the robot equipped with the detection algorithm under consideration is safe for these operating conditions.



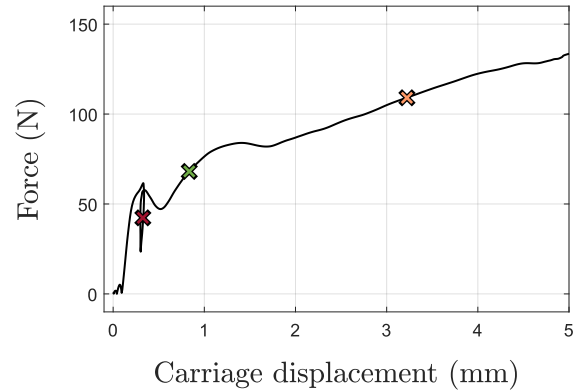
Absorbed energy (J)	
DETE	0.00
JPVO	0.02
GMO	0.30

(a) Speed v_1 , stiffness k_1 

Absorbed energy (J)	
DETE	0.00
JPVO	0.01
GMO	0.08

(b) Speed v_1 , stiffness k_2 

Absorbed energy (J)	
DETE	0.06
JPVO	0.24
GMO	1.03

(c) Speed v_2 , stiffness k_1 

Absorbed energy (J)	
DETE	0.01
JPVO	0.04
GMO	0.25

(d) Speed v_2 , stiffness k_2

— F_{ext} Detection moments: ✕ *DETE* ✕ *JPVO* ✕ *GMO*

Figure 4.19: Evolution of the force applied to the sliding carriage as a function of its displacement (*solid black lines*) and impact detection moments (*color crosses*) for each method. Only the forward phase (the robot pushes the carriage) is shown. The corresponding absorbed energy during the impact detection phase is reported in the associated tables.

4.3 Conclusion

The impact detection methods developed previously were verified and compared experimentally in this chapter. To this end, some of the most essential aspects for a safe interaction between the human operator and a manipulator robot were examined.

An in-depth frequency-domain analysis was carried out for disturbance observer-based methods to describe the specific effect of filtering on the three inputs influencing the estimation of the external disturbance, i. e. the actual disturbance but also the uncertainties involved as measurement or state noises. This study also made it possible to examine the influence of the tuning parameters on the detection characteristics (rapidity, sensitivity). The advantages and disadvantages of the different impact detection methods proposed were highlighted according to the characteristics of the robot's trajectory, the knowledge of its dynamic model, its numerical differentiation scheme and the additional settings available. For an industrial application, the same approach could be conducted to guide the integrator or the end-user to know what detection sensitivity to expect and what parameter to improve in order to operate under safer conditions.

The three impact detection algorithms proved that a human-robot contact could be correctly detected within a reasonable time. However, the dual requirement of rapidity and sensitivity of detection may be more effectively addressed if the energy absorbed by the collided system is considered. Experimental tests were therefore carried out using a dedicated set-up that simulates a human-robot contact and whose instrumentation allows the computation of the transferred energy. The results obtained were related to the indications given by the robotics standards and guarantee safe human-robot contacts. For future research, the study of a global optimization taking into account the 3 criteria – transferred energy, rapidity and sensitivity of detection – could be worthwhile. In addition, since the robot's speed criterion is essential to ensure fast production cycles, it would be relevant to investigate its influence on the detection performance obtained with these algorithms. Thus the maximum permissible speed while respecting the energy criterion of the robotic standards could be determined.

The integration of these detection methods allows a quicker reaction when an impact occurs to avoid more serious injury and damage. However, before initiating a robot reaction strategy, it is essential to extract all the information necessary to identify the contact so that an appropriate reaction is triggered. This characterization step is investigated in [Chapter 5: "Characterizing Human-Robot contact situations"](#) to locate the impact on the robot arm and to determine if the contact is intended or unintended in case of human-robot contact.

Characterizing Human-Robot contact situations

Contents

5.1	Approaches for characterizing contact situations	128
5.1.1	Related work	128
5.1.2	Positioning statement	131
5.1.3	Case studies	133
5.2	Neural network approach	133
5.2.1	Input data	134
5.2.2	Neural network architecture	134
5.2.3	Training algorithm	136
5.2.4	Performance metrics	139
5.3	Case study 1: contact localization and user adaptability in contact intent classification	140
5.3.1	Data collection	140
5.3.2	Experiment A: results on the training candidate	142
5.3.3	Experiment B: results on test candidates	142
5.3.4	Discussion	144
5.4	Case study 2: generalization of contact intent classification	144
5.4.1	Data collection	145
5.4.2	Experiment A: results on the training candidates	148
5.4.3	Experiment B: results on test candidates from the same trajectory	149
5.4.4	Experiment C: results on test candidates from a new trajectory	153
5.4.5	Discussion	156
5.5	Conclusion	159

Once the contact has been detected, a characterization phase is necessary so that an appropriate reaction of the robot can be initiated. This can be achieved not only by determining the directional information and the intensity involved during the contact but also its location on the robotic arm, the type of environment collided or the underlying intent of the contact. Such information is essential to ensure a reliable hand-to-hand cooperation and an efficient and seamless production process.

The approach proposed in this chapter is limited to human-robot contact situations. The focus is on locating the impact on the robot arm and identifying the user's intent at the time of contact. Indeed, in a pHRI context, contact situations can be either intended (the operator may intentionally interact with the robot for instance to modify its trajectory) or undesired (a human accidentally runs into the robot). To this end, this chapter proposes an approach to distinguish between an intentional contact situation (named *interaction*) and an unintended one (named *collision*), and to estimate the contact location on the robot arm (*upper* or *lower* arm) using supervised learning techniques. In particular, the question of interpersonal variability regarding the intention of contact is investigated.

The proposed approach and the surrounding challenges are first presented in [Section 5.1](#) in relation to the existing methods from the literature. [Section 5.2](#) provides a brief overview of the broad theory on neural networks, but also describes the choices made for the training of the neural networks and the evaluation of the results. Then, two case studies are conducted to evaluate the feasibility and generalizability of this approach ([Sections 5.3](#) and [5.4](#)).

5.1 Approaches for characterizing contact situations

5.1.1 Related work

Although several robot reaction strategies are proposed in the literature [[De Luca 2006](#), [Haddadin 2008a](#), [Mikhel 2018](#)], the choice of a reaction strategy depends on multiple factors that characterize the impact within its context. In particular, locating the contact on the robot arm allows specific reactions to be initiated axis by axis. Furthermore, although only contacts that are not dangerous for the operator should be permitted, it is worthwhile to distinguish between contacts desired as part of the task from unexpected and undesired impacts, in order to avoid triggering a systematic reaction strategy even when it is not appropriate or efficient (e.g. stopping the robot in the simplest case).

The distinction of contact type (intended or unexpected) usually relies on a general observation [[Cho 2012](#), [Kouris 2016](#)]: in the case of an intentional contact, the human attempts to anticipate the robot trajectory and can consciously adapt its own motion to make the contact smooth and gentle. Therefore, the shock at the time of impact, and hence the part of the dissipated energy received by the human subject, tend to be reduced. Conversely, for an unexpected and undesired contact, no adaptation by the human subject is possible which is why the impact is likely to be more severe. As a consequence, the rate of change of the applied force and of the resulting external torque on the robot will be noticeably higher in case of an undesired contact compared to an intended contact situation (see [Figure 5.1](#)).

Based on this intuitive assumption, two types of approaches are proposed. In a first case, filtering methods are used to distinguish between these two situations based on frequency-domain considerations. In a second case, supervised learning methods are investigated. The existing solutions for these two strategies are detailed below.

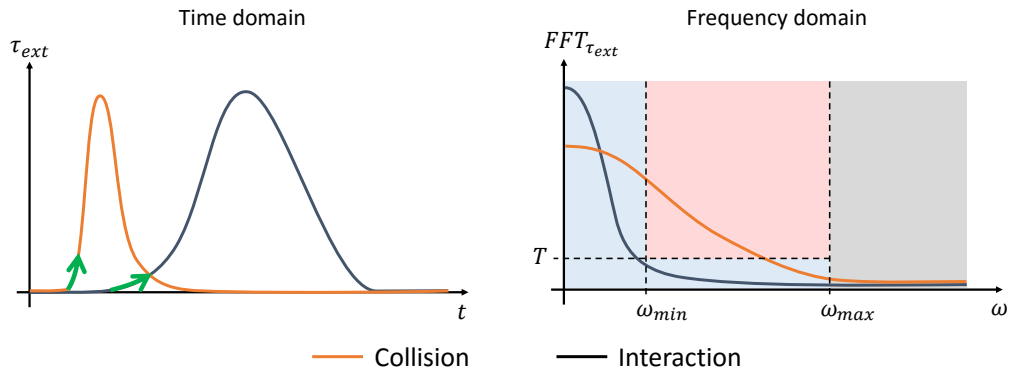


Figure 5.1: Typical profiles of the external torque for collision and interaction in the time and frequency domains [Kouris 2016]. Parameters ω_{min} , ω_{max} and T have to be tuned based on experimental data.

Filtering-based approaches

Intuitively, filtering techniques appear to be quite appropriate to address this challenge. Indeed, when the applied force or resulting external torque is transformed in the frequency domain, those with a higher rate of variation correspond to higher frequency content. As a result, collisions are likely to have higher frequency components than interactions as illustrated in Figure 5.1, while they can be of the same order of magnitude in the time domain.

For this purpose, the GMO introduced in [De Luca 2006] is complemented in [Cho 2012] by a high-pass filter on the estimated external torque in order to filter the low-frequency components induced by interactions. The methodology then detects and reacts only to high-frequency collisions using a fixed threshold determined experimentally. Another approach developed in [Gervand 2013] proposes to detect both interactions and collisions by low-pass and high-pass filtering the motor currents and applying adaptive thresholds tuned on experimental data. A rule of thumb is proposed: when only the low-pass filter threshold is crossed for at least one of the joint, an interaction is detected, while when both thresholds are exceeded, the contact is identified as a collision.

In [Kouris 2016], the distinction is conducted in the frequency domain by calculating the Fast Fourier Transform (FFT) of the external torque on a sliding time window. The derivative of the FFT with respect to time is also investigated in [Kouris 2018] to account for the temporal evolution of the high frequency components of the external torque, in particular in the case of a collision as illustrated in Figure 5.2. For both approaches, parameters such as ω_{min} , ω_{max} and fixed thresholds have to be determined experimentally in order to discriminate high-frequency collisions from low-frequency interactions on the one hand, and from noise under normal conditions on the other hand.

However, all of these methods based on a frequency-domain distinction require considerable parameters adjustment efforts. This tuning depends on the experimental data collected and can significantly affect the success of these methods. As a result, several approaches involving supervised learning techniques have been investigated recently.

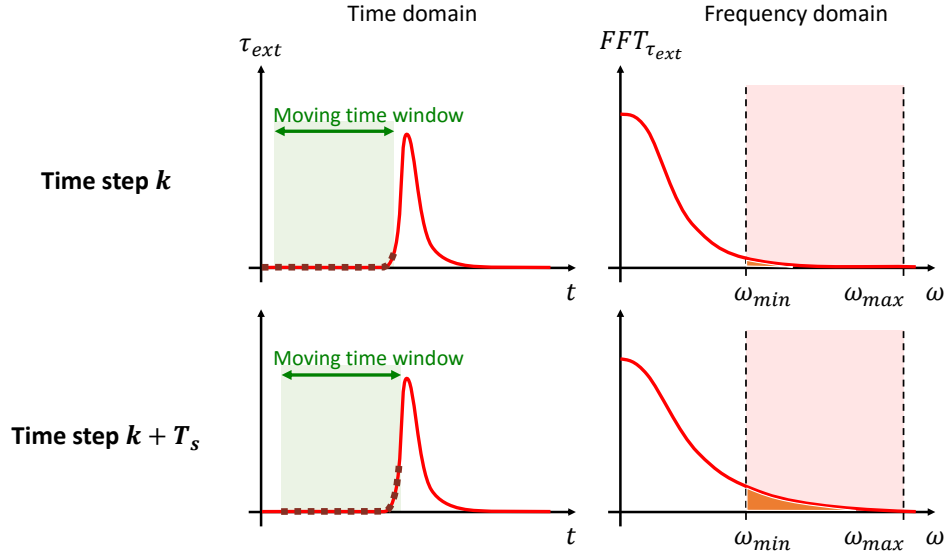


Figure 5.2: Evolution of the external torque in case of collision in the time and frequency domains at two consecutive time steps [Kouris 2018].

Supervised learning-based approaches

Despite the time-consuming phase of data labeling, supervised learning techniques remain advantageous to avoid the determination of a discriminatory rule between collisions and interactions and the manual tuning of adjustment parameters. While this inevitably comes with a loss of transparency of the decision-making algorithm, discriminatory criteria are intrinsically inferred by providing relevant input data and a sufficiently representative set of training data. An analogy might be drawn to advancements in image recognition in recent years, which are no longer based on handcrafted features but rather rely on Convolutional Neural Networks (CNNs) to essentially learn useful features on their own [Krizhevsky 2012].

To this end, in [Golz 2015], a set of 14 linear and non-linear features extracted from the estimated external torque is proposed as input for a SVM-based algorithm, such as the signal mean or duration but also the FFT or the autocorrelation. However, in addition to the limited compatibility with a real-time evaluation of contacts, this approach still requires the manual design of many features to serve as inputs to the classifier.

In a different approach, the benefit of multi-layer neural networks to extract increasingly complex features by themselves and their simple extendability to an increased number of classification outputs by only re-labeling the training data (and possibly reconfiguring the network) render them a versatile tool for contact situations classification. In this respect, [Popov 2017] proposes to compare classical analytical approaches and learning techniques implemented with neural networks for impact detection, localization and characterization of the stiffness of the collided environment. In a similar approach, the methodology developed in [Karlsson 2018] proposes to use the external joint torque estimate as input of a Recurrent Neural Network (RNN), but in this case to detect contact force transients and snap-fit situations.

In this case, the challenge lies in the fact that all configurations, trajectories and speeds of the robot can not be included in the training data due to the extensive size of the input domain. Therefore the capability to generalize beyond training data is an important criterion for the validation of such approaches. This aspect is all the more important when dealing with the classification of contact intent, since the latter may depend on several subject-specific factors (apprehension, sensitivity, anticipation, etc.). This specific issue is addressed hereafter.

5.1.2 Positioning statement

Our approach aims to develop algorithms based on neural network techniques that allow classifying a human-robot contact situation as intended (*interaction*) or unintended (*collision*) and localizing the contact on the robot arm (*upper* or *lower* arm) using a set of labeled data collected experimentally. Unlike filtering or to some extent SVM techniques, the approach followed for this study is to minimize the roboticist’s effort for parameter tuning, by providing raw input signals (or directly available without specific prior processing) and interpreting a neural network as an architecture capable of extracting its own features deemed relevant from the input data. Our specific contribution consists in evaluating the generalizability beyond the training data for the determination of both the intention and location of the contact, i. e. beyond the human subject, the robot trajectory and even the choice of robot used, while using simple neural network structures (elementary and of reduced size). Indeed, among the previously mentioned works addressing the distinction between collisions and interactions, only the study conducted in [Kouris 2018] in the case of filtering-based methods is explicitly validated on several human subjects but is limited to a single robot trajectory.

There is a priori no means to ensure that the trained network would remain “more” valid under new operating conditions than filtering methods. However, when dealing with neural networks, one can simply consider the robot’s state as additional network inputs in order to intrinsically take this dependency into account rather than adjust it by hand as it can be the case for filtering methods (e. g. thresholds depending on the robot speed and acceleration proposed in [Geravand 2013]). Nevertheless, data labeling and design of the neural network structure remain two steps that require engineering input.

One aspect of the characterization of human-robot contact situations deserves particular attention. Conceptually, the detection and localization of a contact are impartial facts that can be attested by external objective indicators. In contrast, the underlying intention when a person comes into contact with the robot may depend on several subject-specific factors (apprehension, sensitivity, expectations, etc.) and can only be attested by subjective personal indicators. This raises the question of the “human factor” when attempting to classify the contact intent: different users can have very subjective judgments on which contacts to classify as *interaction* and which ones as *collision*. In other words, person *A* might be very careful and cautious in interacting with the robot and consider the slightest touch as a collision. In contrast to that, person *B* might touch the robot very harshly and still consider the event as an intended interaction (see the examples of recorded contact situations in Table 5.1).

For such differing expectations, the potential output classes may not be disjoint, thereby making the task of classification much more difficult when dealing with different subjects. Nevertheless, through this study we want to examine the ability of neural networks to extract deep characteristics from the inputs data, potentially more complex than the frequency-domain considerations of filtering-based methods, in order to distinguish between *interactions* and *collisions* regardless of the human subject considered. In the following, we propose three possible outcomes to address this issue, in decreasing order of convenience:

- Outcome 1** By extracting sufficiently high-level features from the input signals of the contact situation, and provided that there are enough people contributing to the training data, a universal classifier could be generated and would remain valid for any new person and robot's trajectory.
- Outcome 2** The neural network classifier could be made easy to adapt and re-train for new users. Each user could then tailor the classifier to his or her personal taste. For such an approach, training has to be possible in a short time.
- Outcome 3** New users are required to adapt to a classifier that has already been trained. Essentially, users have to learn what the people generating the training data considered as *interaction* and *collision*.

Furthermore, the localization of the contact along the robot arm is also considered, although successful applications using neural networks have already been demonstrated, e. g. in [Lu 2005, Popov 2017, Zwiener 2018].

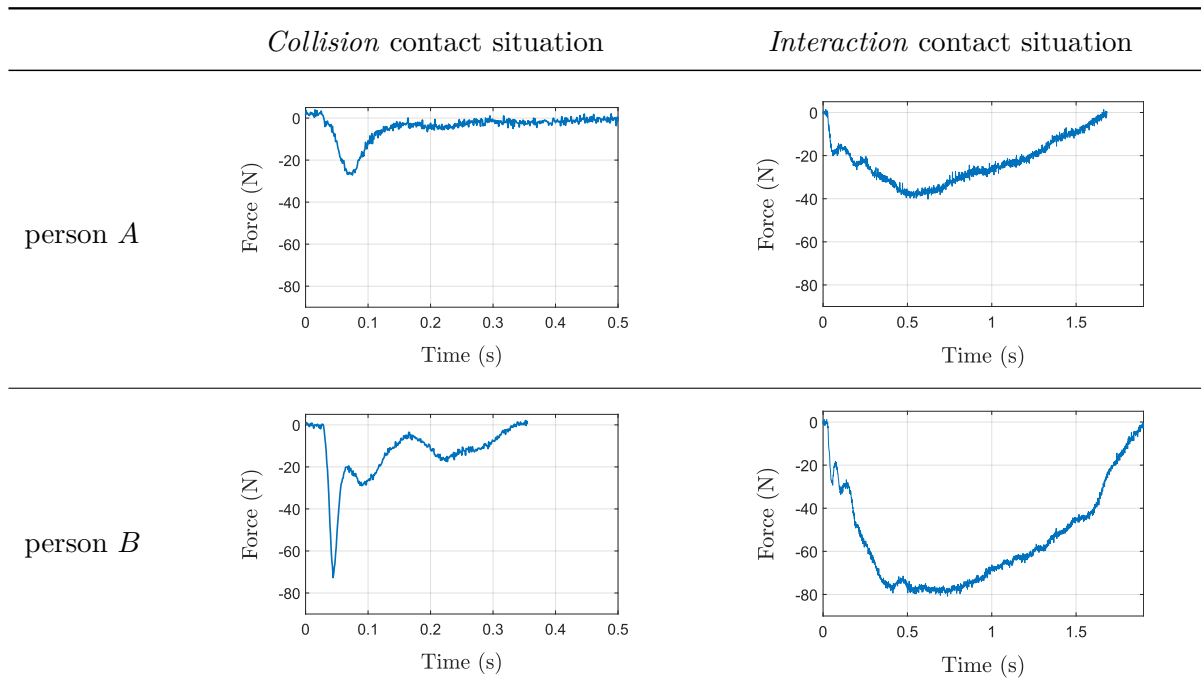


Table 5.1: Examples of force profiles recorded in *collision* and *interaction* contact situations with two different human subjects during *case study 2* (see Section 5.4).

5.1.3 Case studies

Two case studies were conducted to assess the approaches proposed previously about the interpersonal dependency in classifying contact intent. For *case study 1*, only one human subject collected data from different contact situations. After training the neural network on these data, the proposed method is then evaluated online on the robot on contact situations performed both by the person who trained the network (**Outcome 2**) and by new human individuals, before and after an adaptation phase to the classifier (**Outcome 3**). In *case study 2*, a data acquisition campaign was carried out on 16 human individuals in order to build a large database of intentional and undesired contact situations. Then, several neural networks are trained on different subgroups of candidates and results are compared on new human individuals without any prior adaptation to the classifier (**Outcome 1**).

Note that *case study 1* was conducted on an ABB YuMi robot during a 3-month collaboration with the Robotics & Automation group of the global company ABB, while experiments for *case study 2* were carried out on the ISYBOT prototype robot presented in [Appendix B](#). The differences between the two case studies are summarized in [Table 5.2](#).

	<i>Case study 1</i>	<i>Case study 2</i>
Experimental platform	ABB YuMi	ISYBOT prototype
Intention	✓	✓
Localization	✓	✗
Data collection	1 human subject	16 human subjects
Test candidates	New candidates before and after adaptation	New candidates without adaptation
Validation	Online	Offline

Table 5.2: Comparison of the two case studies conducted

5.2 Neural network approach

After detailing the input signals chosen for the neural network in [Section 5.2.1](#), the general principles of the neural networks theory are recalled, along with the specific choices made for the neural network architecture ([Section 5.2.2](#)) and the training step ([Section 5.2.3](#)). Finally, the performance metrics used to evaluate the results of the neural network are presented in [Section 5.2.4](#). More details on the broad theory on neural networks can be found e. g. in [[Lippmann 1987](#), [Kröse 1993](#), [Bishop 2007](#), [Schmidhuber 2015](#)].

5.2.1 Input data

As described in [Section 5.1.1](#), the classification of contact situations is intuitively mainly related to the temporal evolution of the applied external force, and therefore of the external torque induced at the joints. In the absence of dedicated sensors to measure the external forces/torques, the latter have to be retrieved from the motor currents and the robot model, as explained extensively in the previous chapters. Among the different impact detection strategies introduced previously, the method based on DETE is chosen to estimate the external torque in the following because of its ease of calculation and implementation. Nevertheless, a preliminary low-pass filtering of the estimated external torque is applied in order to reduce the noise induced by this method.

As friction modeling is especially challenging at very low speeds (close to standstill), the quality of external torque estimation is in particular highly speed-dependent. In order to enable the neural network classifier to implicitly learn this dependency without triggering false alarms at low speeds, the input of the network consists of both the computed joint speed $\dot{\mathbf{q}}_*$ and the residual \mathbf{r} for each joint.

To provide the classifier with information on the evolution of external torque and speed over time, the network is not only fed with instantaneous quantities but with all data recorded in a moving time window. The width of the moving window corresponds to a duration of 160ms, since experiments showed that 160ms contain a sufficient amount of information to discriminate *collisions* from *interactions*.

Once the data has been collected, the training data set is then generated with the inputs defined above. For this purpose, measurements are flagged sample by sample with the label of the class to which they belong. The label of each time window must be determined according to the individual labels of the samples it contains. It has been decided that the oldest sample gives its label to the time window, as illustrated in [Figure 5.3](#). Although this may generate a delay in the classification equal to the time window duration, it also provides enough information within the time window to correctly classify the contact situation. For future work, a trade-off should be found between the tolerated delay and an acceptable success rate.

5.2.2 Neural network architecture

A neural network is a structure where elements called *neurons* or *nodes* are organized in several layers from the inputs to the outputs of the network. For feedforward neural networks, the information moves always in one direction, from the input layer, potentially through one or more hidden layers, to the output layer. Conversely, RNNs include additional loop connections used as memory through several time steps, making them particularly suitable for processing time sequences of inputs. Although the latter could be particularly well adapted to our problem and interesting to investigate in a future research, for this study we used feedforward networks as a first approach and introduced a temporal aspect with the sliding time window.

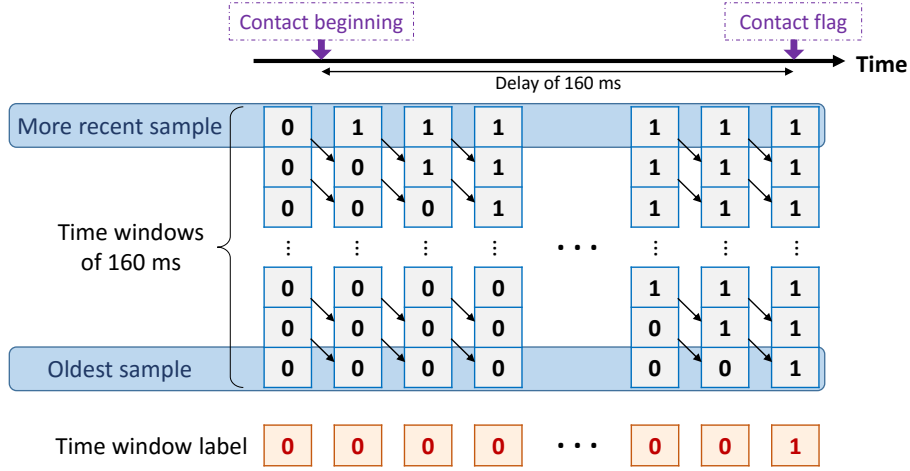


Figure 5.3: Illustration of the time window label and the resulting delay

In a fully connected network, each neuron of each layer is connected to each neuron of the previous and next layers, as shown in Figure 5.4. For the particular case of classification and localization of the contact type, a specific architecture was considered where the inputs are grouped joint-by-joint and for each joint, a sub-network is computed with 1 hidden layer of p neurons (in the following case studies, all networks are designed with $p = 10$ neurons on their hidden layer). Then all the sub-networks are gathered on the output layer with as many neurons on it as the number of output categories (5 for *case study 1*, 3 for *case study 2*). This type of architecture is illustrated in Figure 5.5. The outputs are the likelihood for each category, thus the resulting contact situation corresponds to the maximum output. This architecture can be interpreted as if each sub-network intends to extract p joint-dependent features from the inputs. This choice of architecture is motivated by several reasons:

- For contact type classification: in the filtering-based approaches, features (low- and high-pass external torques, FFT, thresholds,...) are first determined joint by joint, then rules are proposed to figure out the contact type depending on the output for each joint [Geravand 2013]. In a similar way, with this architecture features are first generated joint by joint then gathered together to deduce the contact type.
- For contact localization: an external force \mathbf{F}_{ext} induces at the joint level an external torque vector $\boldsymbol{\tau}_{ext} = \mathbf{J}_C(\mathbf{q})^T \mathbf{F}_{ext}$ where $\mathbf{J}_C(\mathbf{q})^T$ holds for the transposed Jacobian matrix at the contact point C (see equation (2.1)). From Remark 2.2, for a contact on link j , the first j columns of $\boldsymbol{\tau}_{ext}$ will be different from zero as long as the force \mathbf{F}_{ext} does not belong to the kernel of $\mathbf{J}^T(\mathbf{q})$, whereas the last $n - j$ columns of $\boldsymbol{\tau}_{ext}$ will be identically zero. Although this is less straightforward for $\hat{\boldsymbol{\tau}}_{ext}$ because of possible modeling errors, the location of the robot part in contact may be determined by analyzing $\hat{\boldsymbol{\tau}}_{ext}$ component by component.
- Finally, this architecture has a reduced number of weights compared to a fully connected network, which is non-negligible for a real-time online evaluation of the neural network and increases the data efficiency (i. e. a smaller data set is needed to achieve the same level of classification quality).

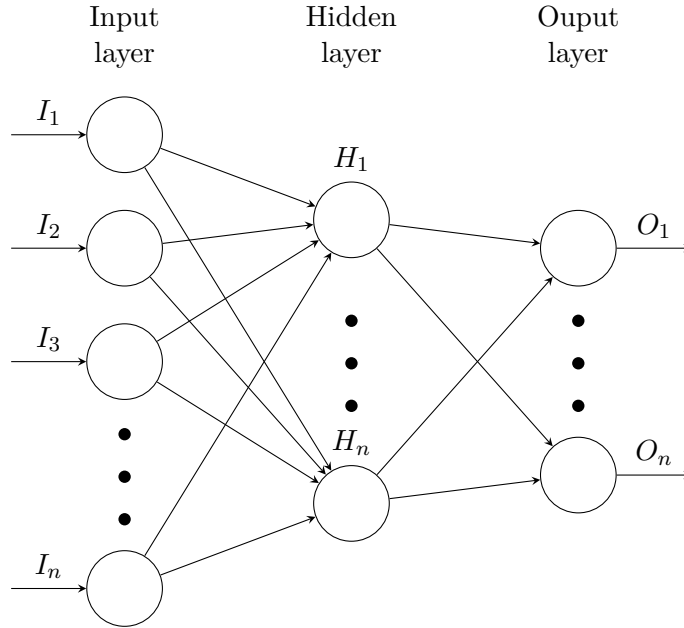


Figure 5.4: Scheme of a basic feedforward neural network with one hidden layer

Changing hyper-parameters such as the number of neurons on each layer or of hidden layers influences the number of features extracted from the inputs and their abstraction level. Alternative structures could also be considered for future work, such as adding a hidden layer to make the contact decision at the joint level before gathering all the decisions on the output layer to decide the final contact situation.

5.2.3 Training algorithm

In a neural network, each neuron is characterized by weights associated with the components of its input vector and a bias. It provides an output value called *activation* which, combined with the other neural activations in its layer, becomes the input of the next layer neurons. In the particular case of the input layer, the input vector corresponds to the neural network input described in Section 5.2.1. For a given neuron j , its activation computation follows the equation:

$$a_j = f \left(b_j + \sum_{i=1}^N w_{i,j} a_i \right) \quad (5.1)$$

where N stands for the total number of neurons on the previous layer, $w_{i,j}$ represents the weight of neuron i from the previous layer to neuron j , a_i designates the activation of neuron i from the previous layer, b_j is the bias associated with neuron j and f denotes the activation function. Inspired by the biological neural networks, the neuron therefore accumulates potential (modeled by the weighted sum $\sum_{i=1}^N w_{i,j} a_i$) which, if it exceeds a certain threshold (modeled by the bias b_j),

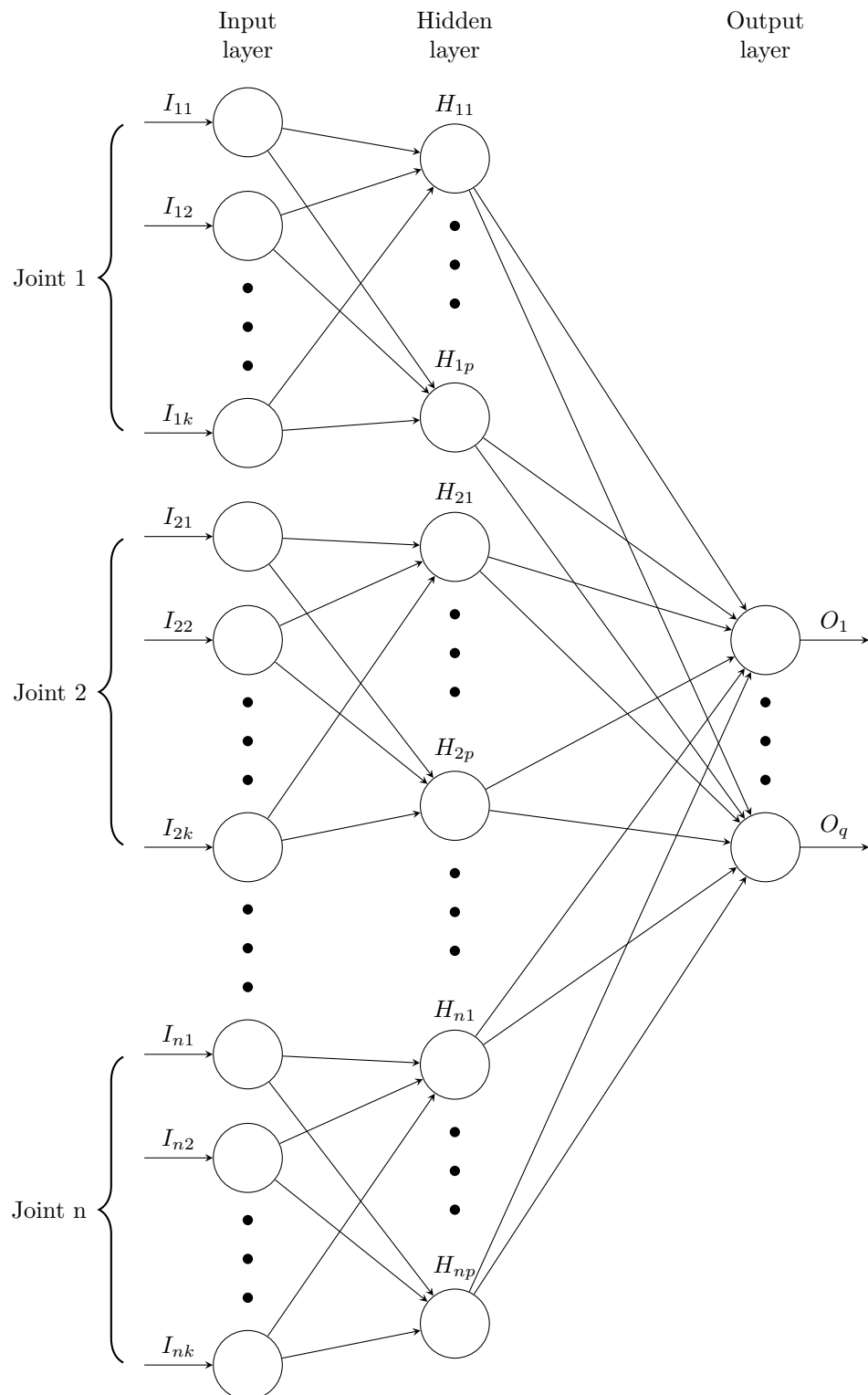


Figure 5.5: Designed neural network architecture (*Case study 1*: $n = 7$, $k = 80$, $p = 10$, $q = 5$ – *Case study 2*: $n = 6$, $k = 320$, $p = 10$, $q = 3$).

can render the neuron activated through the activation function. The important aspect of the activation function is that it can account for the non-linearities of a problem if it is itself non-linear, while ensuring a smooth variation of the output when there is a small change in the input. In this study, the activation functions are the *hyperbolic tangent function* for neurons of the hidden layer (equation (5.2)) and the *softmax function* for neurons of the output layer (equation (5.3)):

$$f_{\tanh}(x_j) = \frac{1 - e^{-x_j}}{1 + e^{-x_j}} \quad (5.2)$$

$$f_{\text{softmax}}(x_j) = \frac{e^{x_j}}{\sum_{c=1}^C e^{x_c}} \quad (5.3)$$

where e stands for the exponential function and C is the number of output neurons and categories ($C = 5$ for *case study 1* and $C = 3$ for *case study 2*).

The neural network training consists in identifying the weights that will minimize the cross-entropy cost function E :

$$E = \frac{1}{SC} \sum_{s=1}^S \sum_{c=1}^C -t_c^s \log(a_c^s) \quad (5.4)$$

with S the total number of training samples and t_c^s and a_c^s respectively the target output for category c and the activation of neuron c on the output layer for training sample s . In order to force the network response to be smoother and less likely to overfit on the training data, the cost function can be modified by adding a weight penalty as follows:

$$\tilde{E} = E + \lambda \sum_{k=1}^K w_k^2 \quad (5.5)$$

where K is the total number of weights in the neural network, w_k represents any of these weights and λ is a regularization parameter that tunes the priority of avoiding overfitting over the network accuracy. In this study, the generalization parameter has been set to $\lambda = 0.05$.

The scaled conjugate gradient backpropagation algorithm detailed in [Møller 1990, Leonard 1990] is used for the training steps that have been performed using the Neural Network Toolbox 9.0 of Matlab. The maximum number of epochs (number of full passes of the training algorithm over the entire training data set) is set at 5000, while the number of validation checks (number of iterations during which the validation error may increase before the algorithm stops) is tuned to 100. Note that the values of the training data set are previously normalized to $[-1, 1]$.

Finally, the training is stopped if:

- the performance of the cost function stops decreasing,
- the maximal number of epochs is reached,
- the maximum number of validation checks is reached.

5.2.4 Performance metrics

To evaluate the performances of a classifier, the common tool is the confusion matrix. It is a square matrix which dimensions correspond to the number of classes. In rows are displayed the actual classes and in columns the predicted classes by the classifier (see Table 5.3).

Percentage		Predicted class	
		Non-contact situation	Contact situation
Actual class	Non-contact situation	$\begin{aligned} & \textit{True negative rate} \\ & = \frac{\sum \textit{True negative}}{\sum \textit{Actual non - contact labels}} \end{aligned}$	$\begin{aligned} & \textit{False positive rate} \\ & \textit{(probability of false alarms)} \\ & = \frac{\sum \textit{False positive}}{\sum \textit{Actual non - contact labels}} \end{aligned}$
	Contact situation	$\begin{aligned} & \textit{False negative rate} \\ & \textit{(undetected contact situation)} \\ & = \frac{\sum \textit{False negative}}{\sum \textit{Actual contact labels}} \end{aligned}$	$\begin{aligned} & \textit{True positive rate} \\ & = \frac{\sum \textit{True positive}}{\sum \textit{Actual contact labels}} \end{aligned}$

Table 5.3: Confusion matrix with performance metrics

Training and testing phases are performed on a sample-by-sample basis without reaction strategy, therefore confusion matrices can be given in terms of percentages of correctly classified samples. Although this has the advantage of providing an overall assessment and taking into account detection times, this may lead to misinterpretations of the results. Indeed, in the absence of reaction strategy, very often *collisions* are initially correctly detected as *collisions* and then after a few samples the output of the network switches to an *interaction*, which worsens the success rate of *collisions*. For instance in Figure 5.6, in a sample-by-sample evaluation without reaction strategies, misclassified samples would be counted from 4.6s. Nonetheless, when tested online, a reaction strategy would have been triggered as soon as a first contact situation is detected, in this case a collision, and everything recorded from 4.6s to 4.75s would not have happened.

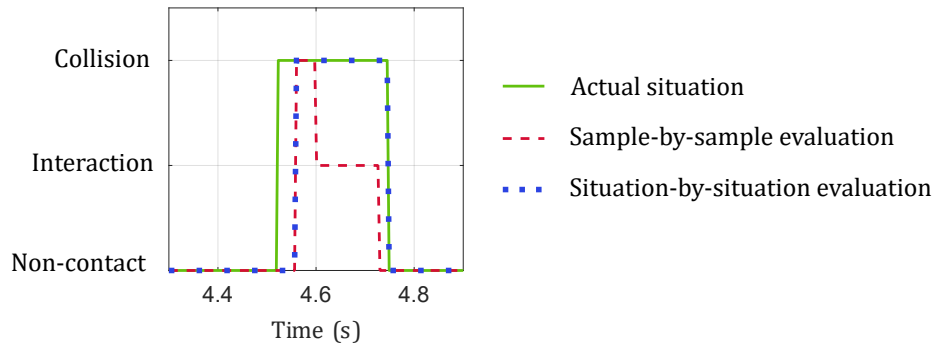


Figure 5.6: Illustration of the sample-by-sample and situation-by-situation evaluations

For this reason, an evaluation of the classification results on a situation-by-situation basis reflects more realistic operational conditions. For instance, in Figure 5.6 the expected classification result is "1 collision situation correctly classified" and not "samples from 4.55 to 4.6s correctly classified and samples from 4.6 to 4.75s wrongly classified". To do this, a contact situation is detected as soon as the neural network output is different from *non-contact* and this first output sample assigns the type of situation detected. The following outputs are not analyzed until the actual situation returns to a *non-contact* situation. In Figure 5.6, the output situation would be a *collision*, leading to a correct classification of the situation for the entire contact duration.

5.3 Case study 1: contact localization and user adaptability in contact intent classification

5.3.1 Data collection

Training data is acquired from contacts between one human subject and the right arm of an ABB YuMi robot (see Figure 5.7). Contact situations occurred while the robot arm was in motion performing a certain number of trajectories. Different Cartesian speeds of the robot end-effector were used in the experiments but overall, its maximum speed was limited to 0.2 m/s for interactions and to 0.5 m/s for collisions (the distinction being attributed to the low likelihood of interacting with the robot at higher speed). Due to the inherent safety features of the robot, all kinds of human-robot contacts are non-hazardous for the human operator.

Data is recorded in both *interaction* (Int.) and *collision* (Coll.) situations, equally distributed between *upper* (Upp.) and *lower* (Low.) arms contacts. All links and joints from the shoulder to (including) the elbow are considered as the upper arm, while links and joints downstream of the elbow to the wrist and tool are termed lower arm (see Figure 5.7). Non-contact (NC) situations

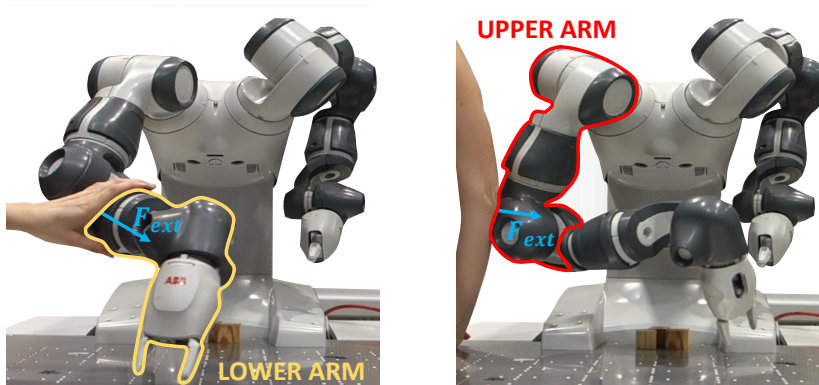


Figure 5.7: ABB YuMi, a dual-arm collaborative manipulator with 7-DOF on each arm (see Table 1.2) used for collecting data to characterize the contact situation: contact type (intended *interaction* on the left, undesired *collision* on the right) and contact localization (*lower arm* on the left, *upper arm* on the right).

were also recorded. Collisions were performed with the whole arm or hand of the operator, while interactions were carried out only with the operator’s hand. Measurements are recorded with a sampling rate of 4ms and then manually flagged sample by sample as *interaction*, *collision*, both associated with the location of the contact (*upper* or *lower arm*), or *non-contact* situations.

The number of collected samples for each class is summarized in Table 5.4. Without dedicated techniques to handle training data imbalance, the classification success rate of a specific category is likely to be higher if more samples of the corresponding category are contained in the training data set. Moreover, normal operation without human contact is by far the most common situation also for collaborative robots. From a practical perspective, it is therefore crucial to achieve a very low rate of false alarms in order to avoid unnecessary stops or other reactions, that is why the number of non-contact samples is significantly higher. Then, there are more collision situations than interactions to compensate the fact that they are relatively short and hence fewer in terms of samples. An approach to handle training data imbalance could be to apply weighting to data that is less represented in the training data set as e. g. reported in [Karlsson 2018].

For this case study, the neural network presented in Section 5.2 is trained once based on the previously recorded contact situations. In order to assess the resulting performances of the classification extended to the whole robot workspace, new robot trajectories that are not included in the training data set and different speeds are used for the validation. Following studies are carried out online:

- Experiment A: validation on the person who gathered the training data (Section 5.3.2),
- Experiment B: validation on two new candidates who did not record any training data (Section 5.3.3). For these two subjects, results are first collected without any prior experience with the classifier, then after about a hundred trials to learn what the classifier rates an *interaction* and what it categorizes a *collision*.

Contact location	Contact type	Number of situations	Number of samples	Percentage of samples
	Non-contact	254	285,789	91.91 %
Lower	Interaction	40	10,348	3.33 %
Lower	Collision	72	1,267	0.41 %
Upper	Interaction	40	10,786	3.47 %
Upper	Collision	72	2,748	0.88 %
TOTAL		478	310,938	100 %

Table 5.4: Number of recorded samples of each category for *case study 1*

5.3.2 Experiment A: results on the training candidate

Online results for the human individual who gathered the training data set are presented in Table 5.5. Over 158 different situations (25 without contact, 29 lower arm interactions, 32 lower arm collisions, 30 upper arm interactions, 42 upper arm collisions), 93.04% of the contact situations are classified correctly.

More precisely, a 100% success rate for actual non-contact situations is achieved, ensuring smooth operation without false alarms. Incorrect classifications arise when the intention is misclassified (e.g. a strong interaction may be interpreted as a collision by the network, or on the contrary, a collision that is too weak is classified as an interaction) or when the contact is not detected (e.g. due to a soft contact). Collisions are slightly less well detected than interactions, potentially due to the fact that they are less represented in the training set (see Table 5.4). In addition, unless the contact has not been detected, otherwise the localization of the robot part in contact is always correct.

Percentage		Situation classified as					Total
		NC	Low. Int.	Low. Coll.	Upp. Int.	Upp. Coll.	
Actual situation	NC	100.00	0.00	0.00	0.00	0.00	100.00
	Low. Int.	3.45	93.10	3.45	0.00	0.00	100.00
	Low. Coll.	6.25	3.13	90.63	0.00	0.00	100.00
	Upp. Int.	0.00	0.00	0.00	93.33	6.67	100.00
	Upp. Coll.	2.38	0.00	0.00	7.14	90.48	100.00
Overall success rate							93.04

Table 5.5: Classification results for the subject that contributed to training data generation

5.3.3 Experiment B: results on test candidates

Classification is then evaluated on two other human subjects that did not participate in the training data collection in order to assess the applicability of the classifier to new candidates. The evaluation is carried out in two stages: first, the results are collected on the spot without prior testing, then users have about a hundred tests to get used to the classifier before re-evaluating the results. The results of each candidate's two steps are presented in Tables 5.6 and 5.7 respectively (over 120 and 77 contact situations for candidates 1 and 2 respectively).

As the classifier is not trained on the personal evaluation of the test candidates, the first tests show a significant number of incorrect classifications. In particular, a poor classification of the upper arm interactions and collisions is achieved for both candidates. Nevertheless, after a few attempts, the new results demonstrate that the candidates have learned very quickly to get used to the classification sensitivity: overall success rates improved from 72.27% to 85.83% for candidate 1 and from 71.43% to 87.01% for candidate 2. More specifically, interactions and collisions are better categorized although localization errors are not always reduced.

Percentage		Situation classified as					Total
		NC	Low. Int.	Low. Coll.	Upp. Int.	Upp. Coll.	
Actual situation	NC	100.00	0.00	0.00	0.00	0.00	100.00
	Low. Int.	5.00	85.00	10.00	0.00	0.00	100.00
	Low. Coll.	0.00	13.64	81.82	0.00	4.55	100.00
	Upp. Int.	0.00	19.35	0.00	41.94	38.71	100.00
	Upp. Coll.	23.81	9.52	0.00	4.76	61.90	100.00
Overall success rate							72.27

Percentage		Situation classified as					Total
		NC	Low. Int.	Low. Coll.	Upp. Int.	Upp. Coll.	
Actual situation	NC	100.00	0.00	0.00	0.00	0.00	100.00
	Low. Int.	5.26	89.47	5.26	0.00	0.00	100.00
	Low. Coll.	0.00	5.56	88.89	0.00	5.56	100.00
	Upp. Int.	5.56	8.33	0.00	77.78	8.33	100.00
	Upp. Coll.	4.55	9.09	0.00	9.09	77.27	100.00
Overall success rate							85.83

Table 5.6: Classification results for test candidate 1: without prior experience with the classifier (*top*) and after adaptation to the classifier (*bottom*).

Percentage		Situation classified as					Total
		NC	Low. Int.	Low. Coll.	Upp. Int.	Upp. Coll.	
Actual situation	NC	100.00	0.00	0.00	0.00	0.00	100.00
	Low. Int.	0.00	68.42	31.58	0.00	0.00	100.00
	Low. Coll.	0.00	20.00	70.00	10.00	0.00	100.00
	Upp. Int.	0.00	0.00	0.00	27.27	72.73	100.00
	Upp. Coll.	0.00	0.00	0.00	41.67	58.33	100.00
Overall success rate							71.43

Percentage		Situation classified as					Total
		NC	Low. Int.	Low. Coll.	Upp. Int.	Upp. Coll.	
Actual situation	NC	100.00	0.00	0.00	0.00	0.00	100.00
	Low. Int.	0.00	81.82	18.18	0.00	0.00	100.00
	Low. Coll.	0.00	0.00	83.33	0.00	16.67	100.00
	Upp. Int.	6.67	6.67	0.00	73.33	13.33	100.00
	Upp. Coll.	0.00	0.00	0.00	14.29	85.71	100.00
Overall success rate							87.01

Table 5.7: Classification results for test candidate 2: without prior experience with the classifier (*top*) and after adaptation to the classifier (*bottom*).

5.3.4 Discussion

This case study dealt with the feasibility of classifying the intention and location of contact between a human subject and a robot, occurring at any time during arbitrary trajectories. Results show that overall, intention is more difficult to classify than location. More specifically for the contact intent, the relevance of **Outcome 2** and **Outcome 3** defined in [Section 5.1.2](#) was examined.

When the same person who generated the training data subsequently evaluates the classifier (**Outcome 2**), results are encouraging and may constitute a plausible solution for a future application. In this case, data collection and training must be done in a short period of time so that they can be easily rescheduled for each new user (compared to about 10 minutes for the current training phase without including the prior data collection phase). In this perspective, future work directions would be twofold: first, simplifying data collection and labeling by a semi-automatic procedure that does not require manual effort or additional sensor, and then determining the minimum set of training data to obtain satisfactory results, i. e. extracting as much information as possible from a small number of training contact situations.

Concerning **Outcome 3**, results demonstrate that humans are very capable in adapting: after just about 100 contact situations, the classification success rates for the two subjects who did not contribute to the training data are already significantly improved. However, this necessary adaptation may induce unnatural user behaviors in working conditions. For example, if an expert user who is familiar with robot handling has to adapt to a classifier trained on a rather “soft” user profile, when he or she wants to interact with the robot, he or she will have to manipulate it more carefully in order to avoid erroneous collision detections, at the risk of being less efficient. On the other hand, a more cautious person may feel insecure if he or she has to interact firmly with the robot to avoid missed detections. Thus this approach seems applicable if the profile of the training candidate and the end users are quite similar to each other, particularly in terms of experience in robot handling. In the other cases, the question of a possible sensitivity adjustment without additional data would be worth investigating.

In the next case study, a data acquisition campaign has been carried out in order to obtain a large database of contact situations produced by various user profiles. In this way, it is possible to evaluate whether a classifier trained on several people has a better chance of guaranteeing universality on any new user without prior adaptation (**Outcome 1**).

5.4 Case study 2: generalization of contact intent classification

Contact localization having been previously validated with *case study 1*, this study is strictly limited to the interpersonal classification of intention. In particular, the feasibility of a classifier sufficiently general to be valid for several people is assessed (**Outcome 1**). To this end, a “median” user profile should be determined by integrating multiple people into the training phase. In order to minimize other existing biases except that of interpersonal variation (e. g. due

to different contact points on the robot or the human subject, different time instants during the robot's trajectory, etc.), interactions and collisions are required to be carried out under the most similar conditions possible, not only between these two types of contacts but also between human subjects. Therefore, data collection must meet a set of specifications and constraints that are detailed below.

5.4.1 Data collection

In this case, training data is acquired from contacts between several human subjects and the 6-DOF ISYBOT prototype robot presented in [Appendix B](#). The contact situations recorded have to meet the following requirements:

- (a) For each human subject, interactions and collisions have to be performed under similar circumstances in order to avoid any other bias due, for example, to the contact direction or the configuration of the robot at the moment of contact,
- (b) In order to specifically study the interpersonal variability when classifying the intention of contact, reproducible contact situations are required from one candidate to the other,
- (c) Given the cumbersome nature of the data labeling process, which usually tends to limit the size of the training data set, an instantaneous and reliable detection of the actual moment of impact is sought. In this way, post-processing time would be significantly reduced by automated data labeling.

Test bench design

To comply with these specifications, a test bench has been set up. It is composed of a sliding carriage mounted on a rail, where the participant's hand is attached as shown in [Figure 5.8](#). The participant is able to move freely on the rail and, for safety reasons, could exit the rail at one end. In this way, the conditions of contact with the robot are repeatable between interactions and collisions and between participants. Also, in this case it has been decided to perform contacts only with the operator's hand for comparable interactions and collisions, as it is usually the body part involved when interacting with the robot although it does not stand as a very representative situation of unexpected and undesired contact.

The rail is equipped with a position sensor that measures the sliding carriage displacement for information purposes only, while on the robot side, a 6-axis force/torque sensor is mounted on the robot tool (design similar to a steering wheel, used to facilitate robot handling), both sensors being synchronized with the robot controller. Using the force/torque sensor measurements, it is therefore possible to know precisely the moment of impact in relation with the robot's state, and hence to label the data in a quasi-automatic way. The choice of positioning the force/torque sensor on the robot, and not attached to the participant's hand, allows a measurement directly at the interface of the human-robot contact without altering the contact profile considerably, but constrains the contacts to take place only at this point on the robotic arm.

Data acquisition campaign

For the experiments, the test bench is placed on a table in front of the robot and in various positions (see [Figure 5.9](#)). Four straight trajectories aligned with the rail are planned, with only one trajectory tested per participant. The robot makes round trips along this line under 3 Cartesian speeds (0.1, 0.2 and 0.3 m/s) and 3 different proportional and derivative control gains to test several robot operating conditions. These $3 \times 3 = 9$ test combinations are presented in a randomized order to avoid biasing the results towards the last one tested due to human learning effects. Each of the 9 combinations are repeated 8 times to ensure sufficient representativeness. In total, $3 \times 3 \times 8 = 72$ (*speeds* \times *gains* \times *repetitions*) collisions, and similarly 72 interactions, are recorded per participant.

In order to record realistic but reproducible contact situations among the different subjects, identical instructions are given to the participants (the detailed experimental protocol can be found in [Appendix C – Section C.1](#)). The acquisition session involved 16 participants (aged from 19 to 54 years old including 2 females and 2 people who had never been in physical contact with a robot, all right-handed except one left-handed person). The participants were distributed over the 4 trajectories, which resulted in $4 \times 72 = 288$ (*number of persons per trajectory* \times *number of contact types per person*) collisions and interactions respectively per trajectory, and $4 \times 288 = 1152$ (*number of trajectories* \times *number of contact types per trajectory*) collisions and interactions respectively in total. The number of collected samples for each contact situation and trajectory is summarized in [Table 5.8](#). Note that the number of collisions recorded for each trajectory is different from 288 due to several missed collisions. We can also notice that collisions are much more represented for *case study 2* than for *case study 1* (see [Table 5.4](#) for comparison). This is due to the fact that the ABB YuMi robot stopped quickly after a collision due to the active impact detection strategy, unlike the ISYBOT prototype robot for which no detection strategy was applied, which made it possible to record the entire contact profile. Measurements were recorded with a sampling rate of 1ms and then flagged sample by sample as *interaction*, *collision* or *non-contact* situations using the force/torque sensor information.

In order to assess the performances of the classification extended to any new human subject, several studies are undertaken, associated with validation steps of increasing complexity:

- Experiment A: for each individual, a classifier is trained on one part of his or her own contact situations and tested on the other part ([Section 5.4.2](#)),
- Experiment B: for each trajectory, a classifier is trained on some of the candidates that generated contact situations on this trajectory and tested on the other participants from the same trajectory, which are therefore new candidates for the classifier ([Section 5.4.3](#)),
- Experiment C: a classifier is trained on contact situations generated on certain trajectories and tested on the others, which are therefore new candidates and trajectories for the classifier ([Section 5.4.4](#)).

For the last two experiments, we investigate the evolution of the success rate when the size of the training data set increases, i. e. the number of people the network is trained on.



Figure 5.8: Pictures of the test bench: hand of a participant attached to the sliding carriage of the rail (*left*), force/torque sensor located on the steering wheel of the robot (*middle*), human-robot contact with the force/torque sensor at the interface (*right*).

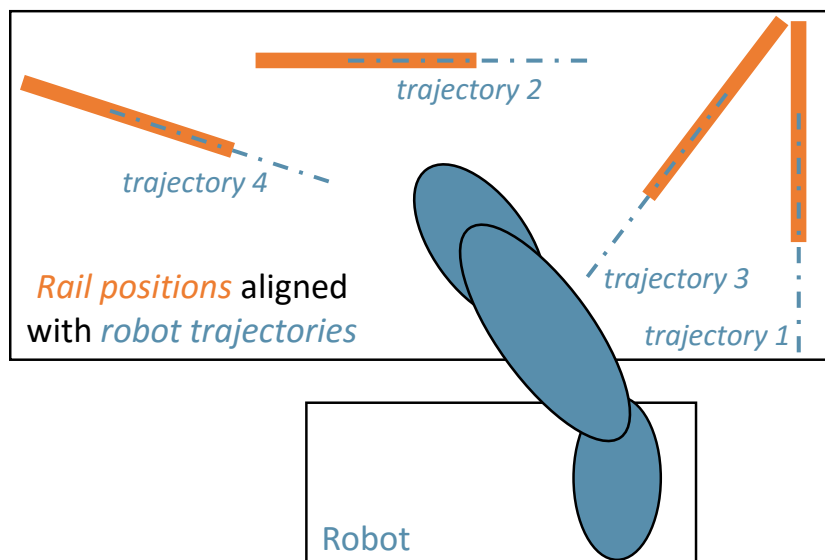


Figure 5.9: Four rectilinear trajectories planned for the robot coming into contact with the participant's hand attached to the sliding carriage of the rail.

Trajectory	Contact situation	Number of situations	Number of samples	Percentage of samples
Trajectory 1	Non-contact	568	4,401,846	85.29 %
	Interaction	288	485,928	9.41 %
	Collision	280	273,528	5.30 %
Trajectory 2	Non-contact	568	4,659,129	84.91 %
	Interaction	288	479,858	8.74 %
	Collision	280	348,171	6.35 %
Trajectory 3	Non-contact	574	4,441,942	84.90 %
	Interaction	288	449,159	8.58 %
	Collision	286	341,112	6.52 %
Trajectory 4	Non-contact	568	4,344,138	84.05 %
	Interaction	288	428,725	8.30 %
	Collision	280	395,617	7.65 %
SUBTOTAL	Non-contact	2,278	17,847,055	84.79 %
	Interaction	1,152	1,843,670	8.76 %
	Collision	1,126	1,358,428	6.45 %
TOTAL		4,556	21,049,153	100 %

Table 5.8: Number of recorded samples of each category for *case study 2*

5.4.2 Experiment A: results on the training candidates

In this study, we verify on another robot the ability of a neural network to correctly classify the contact intention of a human subject after having been trained on some of his or her own contacts (**Outcome 2**). To this end, for each human subject, among his or her own recorded contact situations, half of the interaction and collision situations are used for the training stage, while the remaining contacts are kept for the testing phase. This study can be compared with Experiment A from *case study 1* (Section 5.3.2), except that in the previous case the test was performed on trajectories not included in the training set. In this case, the contacts used for training and testing are performed on the same trajectory, therefore we expect better results.

Thus one neural network is trained per human subject and individual results for each candidate can be found in Appendix C – Section C.2. As a synthesis, the results are combined for the 16 candidates and presented in Table 5.9. Over 576 interactions and 550 collisions tested in total, 98.13% of the contact situations are correctly classified. This validates the fact that when the classifier is trained on the user’s own perception, very good performances can be achieved, regardless of the robot and operating conditions considered.

It can also be noted that some false alarms occur, whereas there were none in *case study 1*. This may be due to a lower accuracy of the dynamic model for this robot, which leads to errors in the estimation of the external torque that are interpreted as contact situations by the network.

Percentage		Situation classified as			Total
		Non-contact	Interaction	Collision	
Actual situation	Non-contact	99.02	0.36	0.62	100.00
	Interaction	0.00	98.78	1.22	100.00
	Collision	0.18	4.18	95.64	100.00
Overall success rate					98.13

Table 5.9: Classification results for the 16 candidates combined when the neural network has been trained on their own recorded contacts.

5.4.3 Experiment B: results on test candidates from the same trajectory

The purpose of **Outcome 1** is to propose a universal classifier that will remain valid to any new human subject who tests the classifier. In a first step, we consider that the robot executes the same trajectory as the one on which the neural network was trained, while new human subjects come to its contact.

For this purpose, for each trajectory, some of the candidates who generated contact situations on that specific trajectory are considered for training the network, while the other participants from the same trajectory whose data have not been used in the training are used as test candidates. Since there are 4 participants who have recorded contacts on the same trajectory, each of them can be used, one after the other, as test candidate of a classifier trained:

- on only 1 other candidate (1/3 of the remaining candidates = 3 possible choices),
- on 2 candidates (2/3 of the remaining candidates = 3 possible combinations),
- on the 3 candidates (3/3 of the remaining candidates = 1 possible combination).

Finally, each candidate is tested on 7 neural networks trained on increasingly diversified data sets.

Due to the large number of cases tested (7 confusion matrices per participant), a graphical representation of the results is given in [Figures 5.10](#) and [5.11](#) for interactions and collisions respectively. For each candidate and each combination, the percentages of correct classifications (*true positive rate* in [Table 5.3](#)), misclassifications (*interactions* detected as *collisions* or vice versa), undetected contact situations (*false negative rate*) and false alarms (*false positive rate*) are compared. The average results by number of candidates included in the training (from 1 to 3) is also plotted.

Whether for collisions or interactions, the general trend from these figures is that classification results are improved and less spread out when the number of candidates included in the training increases: this supports the idea that the more candidates integrated in the training data set, the more universal the profile resulting from the training.

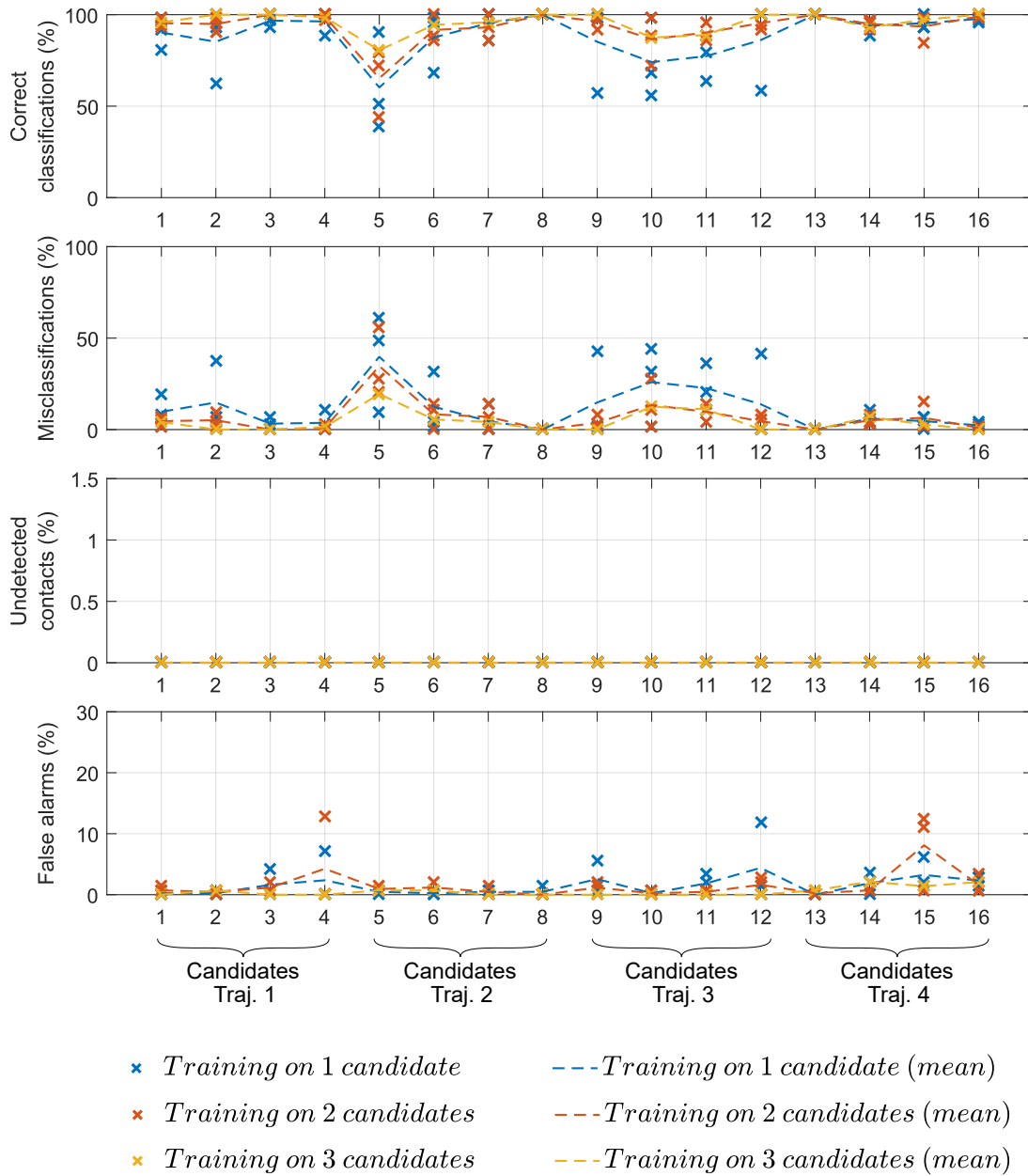


Figure 5.10: Interaction classification results when the test is carried out on the same trajectory as the one the network has been trained on: illustration of the influence of the training data set size on the results.

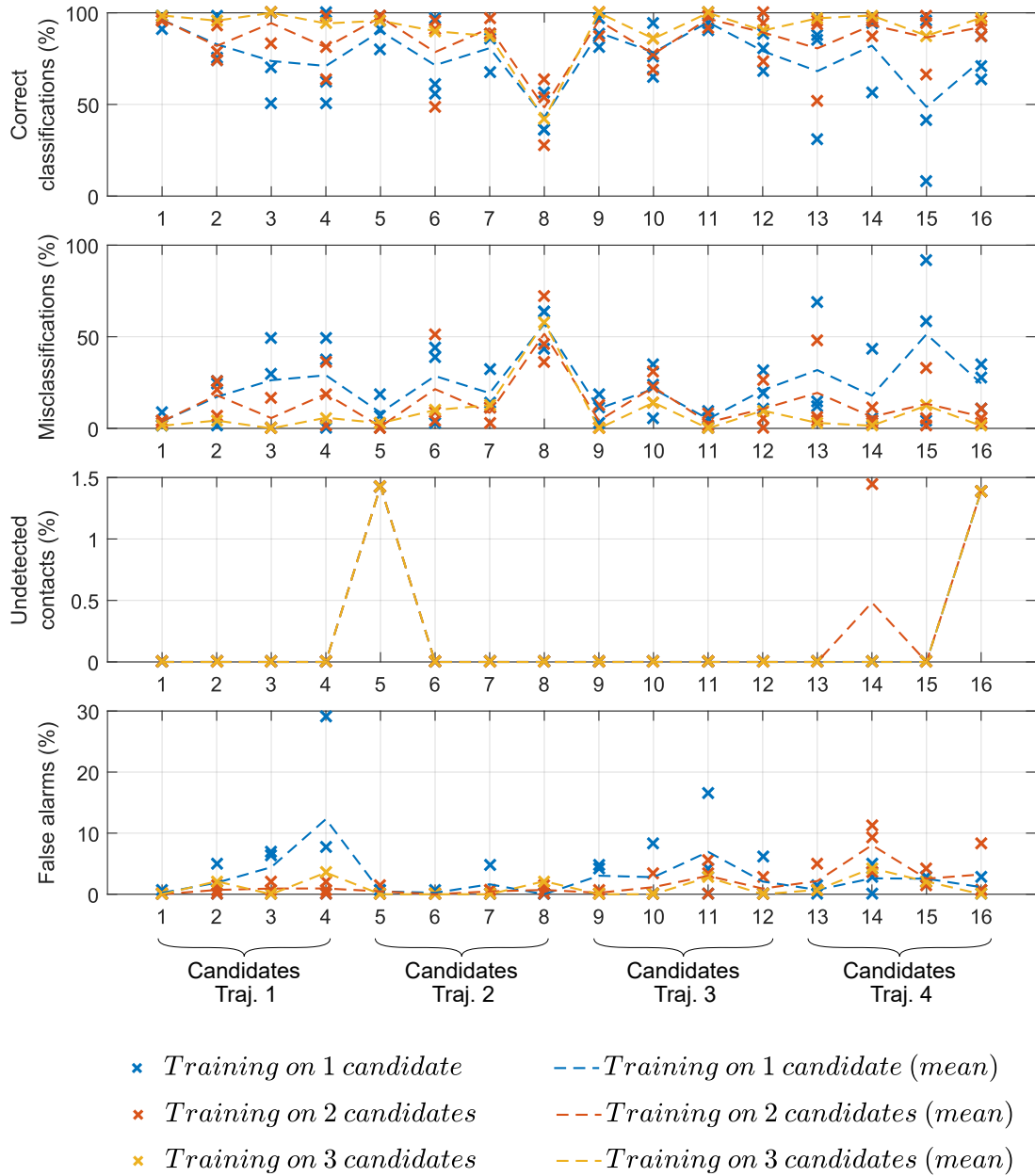


Figure 5.11: Collision classification results when the test is carried out on the same trajectory as the one the network has been trained on: illustration of the influence of the training data set size on the results.

We can notice some candidates who “stand out from the crowd”:

- candidate n°5: many of his or her interactions are misclassified as collisions. This may mean that he or she is used to interact more firmly with the robot than the average candidate, thus the classifier interpret the interactions as collisions.
- candidate n°8: many of his or her collisions are misclassified as interactions. This may be due to smoother collisions than the average candidate, thus the classifier confuses them with interactions.
- candidates n°5, 14 and 16: some of their collisions are non-detected by the classifier. This may be due to smoother or shorter collisions than the average candidate, thus the classifier doesn’t even detect that there is a contact.

To confirm these interpretations, it would be interesting for future research to correlate these observations with a criterion reflecting the contact severity, such as the energy dissipated during the contact, derived from the measured force/torque profiles and carriage displacement. This could be used to sort out atypical contact situations, at least for the training phase, in order to achieve a more universal profile.

For each possible number of candidates included in the training (from 1 to 3), results are combined for the 16 candidates and presented in Tables 5.10 to 5.12 (individual results for each candidate when the 3 other candidates from the same trajectory have been included in the training can be found in Appendix C – Section C.3). Of all interactions and collisions used one after the other as test contact situations, 95.96% are correctly classified without a prior adaptation phase as soon as 3 candidates are included in the training data set.

Percentage		Situation classified as			Total
		Non-contact	Interaction	Collision	
Actual situation	Non-contact	95.89	1.42	2.69	100.00
	Interaction	0.00	88.83	11.17	100.00
	Collision	0.18	23.30	76.52	100.00
Overall success rate					89.32

Table 5.10: Classification results for the 16 candidates combined when the neural network has been trained on 1 other candidate from the same trajectory as the test candidate.

Percentage		Situation classified as			Total
		Non-contact	Interaction	Collision	
Actual situation	Non-contact	96.94	1.46	1.60	100.00
	Interaction	0.00	93.46	6.54	100.00
	Collision	0.21	13.35	86.44	100.00
Overall success rate					93.47

Table 5.11: Classification results for the 16 candidates combined when the neural network has been trained on 2 other candidates from the same trajectory as the test candidate.

Percentage		Situation classified as			Total
		Non-contact	Interaction	Collision	
Actual situation	Non-contact	98.37	0.53	1.10	100.00
	Interaction	0.00	95.75	4.25	100.00
	Collision	0.18	8.52	91.30	100.00
Overall success rate					95.96

Table 5.12: Classification results for the 16 candidates combined when the neural network has been trained on 3 other candidates from the same trajectory as the test candidate.

5.4.4 Experiment C: results on test candidates from a new trajectory

We now consider the case where the robot executes a new trajectory that is not included in the training data set, while human subjects not known to the classifier come to its contact.

For this purpose, the four candidates who generated contact situations on some of the trajectories are considered for training the network, while the candidates from other trajectories that have not been included in the training are used for validation. Since there are 4 trajectories in total, each of them can be used, one after the other, as a test trajectory of a classifier trained on 1, 2 or 3 other trajectories (3, 3 and 1 possible combinations respectively). In other words, each trajectory (i. e. each candidate who has recorded contact situations on that specific trajectory) can be tested on 7 neural networks trained on increasingly diversified data sets.

As in the previous section, results are presented in graphical form in [Figures 5.12](#) and [5.13](#) for interactions and collisions respectively. The average results by number of trajectories included in the training (from 1 to 3) is also displayed. Regardless of the candidate considered, we notice that the results are much more spread out than when the classifier was trained and tested on contact situations from the same trajectory (Experiment B). When only one trajectory is included in the training (in *blue*), the results can range from very poor (less than 10% of success rate) to very good (more than 90% of success rate) depending on the choice of the training trajectory. More specifically, when [Figures 5.12](#) and [5.13](#) are compared, we can observe that one category of contact situation is often correctly classified at the expense of the other contact situation: for example, interactions are generally well detected for candidates from trajectory 1, but the classification gives poor results for collisions.

For each possible number of trajectories included in the training (from 1 to 3), results are combined for the 16 candidates and presented in [Tables 5.13](#) to [5.15](#) (individual results for each candidate when the 3 other trajectories have been included in the training can be found in [Appendix C – Section C.4](#)). Of all interactions and collisions used one after the other as test contact situations, 80.11% are correctly classified without a prior adaptation phase as soon as 3 trajectories are included in the training data set. Although this result is much lower than the 95.96% success rate obtained when the same trajectory is considered for both training and testing, the results are improving as the number of trajectories included in the training increases.

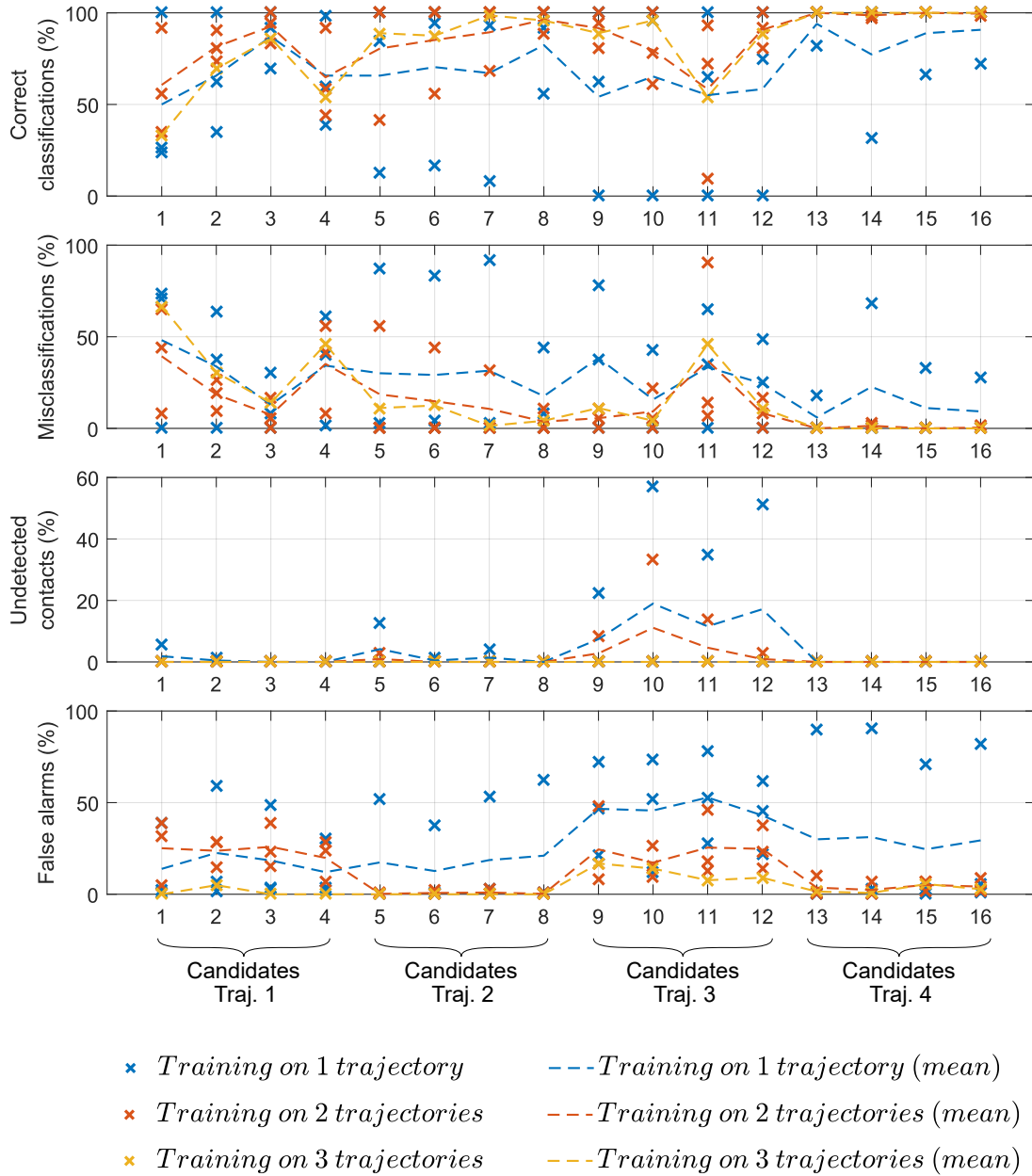


Figure 5.12: Interaction classification results when the test is carried out on a different trajectory from the one(s) the network has been trained on: illustration of the influence of the training data set size on the results.

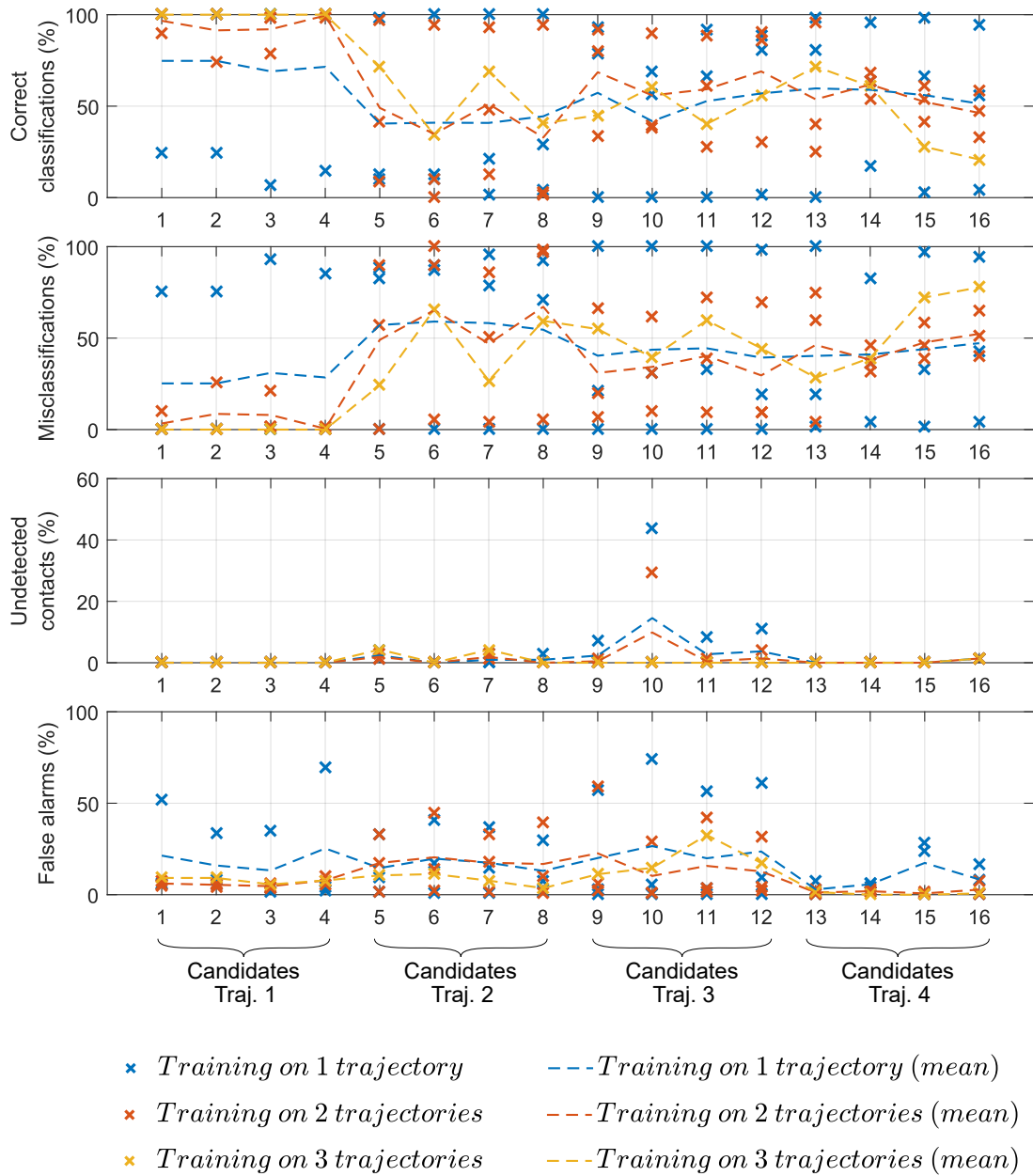


Figure 5.13: Collision classification results when the test is carried out on a different trajectory from the one(s) the network has been trained on: illustration of the influence of the training data set size on the results.

Percentage		Situation classified as			Total
		Non-contact	Interaction	Collision	
Actual situation	Non-contact	55.87	27.54	16.59	100.00
	Interaction	3.97	71.12	24.91	100.00
	Collision	1.84	42.48	55.68	100.00
Overall success rate					59.68

Table 5.13: Classification results for the 16 candidates combined when the neural network has been trained on candidates from 1 other trajectory.

Percentage		Situation classified as			Total
		Non-contact	Interaction	Collision	
Actual situation	Non-contact	76.97	12.77	10.26	100.00
	Interaction	1.27	85.59	13.14	100.00
	Collision	1.10	35.52	63.38	100.00
Overall success rate					75.79

Table 5.14: Classification results for the 16 candidates combined when the neural network has been trained on candidates from 2 other trajectories.

Percentage		Situation classified as			Total
		Non-contact	Interaction	Collision	
Actual situation	Non-contact	87.09	3.95	8.96	100.00
	Interaction	0.00	83.85	16.15	100.00
	Collision	0.62	37.21	62.17	100.00
Overall success rate					80.11

Table 5.15: Classification results for the 16 candidates combined when the neural network has been trained on candidates from 3 other trajectories.

5.4.5 Discussion

This case study examined the feasibility of a universal classifier capable of detecting the contact intent of any human subject on any robot trajectory.

First, the favorable results obtained in *case study 1* when the same person who generated the contact situations for the training subsequently evaluates the classifier (**Outcome 2**) were confirmed in *case study 2*, despite the fact that a different robot and operating conditions were considered.

In a second step, contact situations performed by multiple candidates were integrated in the training data sets (**Outcome 1**). Through different combinations of the 16 participants, the validation step showed that generalization to several individuals gives promising results when limited to a single trajectory. However, the generalization to both any human subject and any

trajectory appears to be more challenging with mitigated results, potentially due to the large variability of this complex problem relatively to the size of the training data set.

As a general remark, it can be noted that collisions are systematically the least well classified situation, because they are often interpreted as interactions, which reduces the overall success rate. Unlike *case study 1*, this cannot be explained by an imbalance in the sample distribution, since in this case study, interaction and collision situations are fairly represented in the training sets that have been designed to have as many samples of one type as the other. However, the conditions of the experiment simulating collisions may be questioned: it is likely that collisions with the hand did not generate undesired and unexpected contact situations that were sufficiently characteristic and distinct from the interactions. In any case, for more severe collisions (e. g. with other parts of the body that are stiffer or more sensitive than the hand), the contact profiles would potentially be more pronounced and therefore the results would probably be better.

Review of case studies 1 and 2

Final results are summarized in [Table 5.16](#). As a reference, the filtering-based approach in [\[Kouris 2018\]](#) that was tested on new human subjects but on the same robot trajectory obtained on average 90% of success rate for interactions, and from 53 to 100% of success rate for collisions depending on the body area in contact. For the same circumstances, the results obtained with our neural network-based approach is 95.75% of success rate for interactions and 91.30% for collisions, which validates the interest for this approach.

The main issue addressed was to study if spending more time in collecting data from several human subjects and robot trajectories to generate a general classifier is more worthwhile than reducing the pre-processing effort and get only a personalized model of classification.

At this stage, [Outcome 2](#) could be the most promising approach given the favorable results even when extended to new trajectories. However, for a realistic application, it would be necessary to reduce the amount of training data required. For this purpose, a comprehensive study could be carried out using for instance a PCA to determine which other signals may contain a relevant signature of the contact situation (e. g. the position-tracking error $\mathbf{q}_d - \mathbf{q}$, the joint deformation $\mathbf{q} - \boldsymbol{\theta}$, or frequency domain-related features) to be added to the network inputs. More complex neural network structures could also be studied, such as RNNs or CNNs, to allow a more in-depth and efficient extraction of the information needed for classification.

According to the tests performed so far, a general classifier ([Outcome 1](#)) could yield interesting results if used in combination with [Outcome 3](#) (a classifier trained over multiple candidates and trajectories and used after an adaptation phase). Some improvements could be proposed to achieve a more generalizing classifier (e. g. reconsidering the neural network structure, sorting out the training data to keep only the most representative contact profiles, using the force/torque sensor measurements as inputs for the training step, etc.). However, the limits of supervised learning techniques may be reached as it involves generalizing to a very large dimension (new human subjects and trajectories) from a limited data set (few candidates and trajectories recorded).

The size of data sets being limited by the time-consuming data acquisition step, a solution to overcome this problem would be to take advantage of simulation tools to generate a large amount of training data. For this purpose, a model of the human-robot contact situation would be required: for instance, an impedance control law could be identified for the human arm as proposed in [Lu 2005], using the extensive information collected during the *case study 2* and in particular from the force/torque and position sensors. Then we could potentially determine the intrinsic parameters that cause a change of behavior between interaction and collision cases. This could ultimately be used to generate an unlimited number of contact situations at several locations on the arm and on different robot trajectories, thus increasing the chances for a successful classification.

Finally, for a possible future deployment on several robots, the question of inter-robot variability is to be studied: is a contact characterization algorithm specific to the robot used for generating the training data, or can it be applied to other robots (of the same model at least) ? The ultimate objective would be to extract features that are general enough to be independent from the robot's choice.

Human subject	Trajectory	Experiment	Result on interactions / collisions
=	=	<i>Cast study 2</i> – Experiment A	98.78% / 95.64% on average over 16 human subjects
=	≠	<i>Cast study 1</i> – Experiment A	93.22% / 90.54% over 1 human subject
≠	=	<i>Cast study 2</i> – Experiment B	95.75 % / 91.30% on average over 16 human subjects with 3 candidates in the training data set
≠	≠	<i>Cast study 1</i> – Experiment B	80.25% / 83.33% on average over 2 human subjects after an adaptation phase of about a hundred trials
		<i>Cast study 2</i> – Experiment C	83.85% / 62.17% on average over 16 human subjects with 3 trajectories and 4 candidates per trajectory in the training data set

Table 5.16: Final results obtained for *case studies 1* and *2* depending on whether the same candidate and trajectory were considered for validation (=) or different ones (≠).

5.5 Conclusion

In this chapter, the contact characterization phase that takes place once the impact has been detected was investigated, so that ultimately, appropriate robot reactions could be triggered. In particular, two aspects were studied in the form of classification problems: the localization of the contact area on the robot arm and the underlying intent of the user when he or she comes into contact with the robot.

The proposed method applies supervised learning techniques by training a neural network, where the structure of the network is inspired by the physics of contact in order to increase data efficiency. Contrary to filtering-based approaches, in this case there is no need to manually tailor features that are to be used for classification. Although this is inevitably accompanied by a loss of transparency in the decision-making algorithm, the chances of generalization to different operating conditions of the robot are likely to be higher.

The relevance of this approach was explored through two case studies. The first study demonstrated that the localization of the robot's contact area (upper or lower arm) using a neural network can be very efficient. The next step would be to detect the specific axis where the contact was applied. Both studies addressed the issue of classifying the intention of contact, which is likely to be related to subject-specific characteristics. Generalization to any individual or robot trajectory appears to be achievable, but the performance on both fronts of a universal classifier such as the one developed seems limited. Future directions of work were proposed to overcome this obstacle.

Conclusions and outlooks

“ *There’s a difference between knowing the path,
and walking the path.* ”

Matrix (1999)

Contents

6.1	Conclusions	161
6.1.1	Development of a quantitative methodology rendering explicit the contribution of uncertainties	162
6.1.2	Design of novel adaptive impact detection strategies explicitly taking into account the contribution of uncertainties (rigid and flexible cases)	162
6.1.3	Characterization of the contact intention and localization	163
6.2	Outlooks	163
6.2.1	Validation of the impact detection algorithms in the flexible case	163
6.2.2	A greater efficiency in impact detection	164
6.2.3	Further improvements in contact situations characterization	165
6.2.4	Towards a complete control scheme	165

6.1 Conclusions

Physical collaboration between humans and robots is generating growing interest as evidenced by constantly evolving research work, particularly on safety issues associated with the recent adaptation of robotic standards in this field. Some limitations still need to be overcome in order to go beyond the framework of research laboratories for an application in open industrial environments or in service robotics. This thesis falls within the scope of the following issue: guaranteeing the operator’s safety by monitoring the contacts with the robot, and collecting as much information as possible during a contact in order to initiate an appropriate robot reaction. The challenge lies in achieving the dual objective of performance (in particular in terms of speed and dynamics) and safety in a context of reduced measurements, i. e. in the absence of force/torque sensor, while being subject to modeling uncertainties.

For this purpose, four contributions have been presented in this thesis:

- The development of a quantitative methodology rendering explicit the contribution of uncertainties,
- The design of novel adaptive impact detection strategies explicitly taking into account the contribution of uncertainties (rigid case),
- The design of novel adaptive impact detection strategies explicitly taking into account the contribution of uncertainties (flexible case),
- The characterization of the contact intention and localization on the robot arm.

6.1.1 Development of a quantitative methodology rendering explicit the contribution of uncertainties

Since impact detection methods based on the dynamical model of the robot are subject to the trade-off between detection sensitivity and robustness to modeling uncertainties, a thorough analysis of the uncertainties-induced errors involved has been conducted. In particular, two main types of errors have been considered: errors on the dynamic parameters of the robot (calculated by experimental identification) and errors induced by the calculation of the robot's state (obtained by numerical differentiation of the measured position). In each case, a stochastic characterization of the error distribution has been proposed, which has been applied to the ISYBOT prototype robot.

This quantitative, theoretical and experimental methodology has been applied to several impact detection algorithms to quantify the effects induced by uncertainties. By making explicit the errors involved in a given impact detection algorithm, the developed methodology has finally made it possible to:

- clarify which uncertainties are involved and how they are affecting the detection,
- propose new strategies of impact detection (see [Section 6.1.2](#)),
- compare these algorithms according to the type and amount of uncertainties involved.

6.1.2 Design of novel adaptive impact detection strategies explicitly taking into account the contribution of uncertainties (rigid and flexible cases)

New impact detection strategies have been designed based on the previous methodology. To this end, a probabilistic approach was adopted to determine the maximum contribution of modeling errors based on their explicit formulation. This maximum error margin then constitutes a relevant impact detection threshold, depending on the robot's trajectory, the level of parametric uncertainties, the noise on the position measurement and the numerical approximation method chosen for calculating speed and acceleration.

Two types of impact detection methods have been studied in the case of robots with infinitely stiff joints and rigid links: direct estimation of the external torque responsible for a contact and disturbance observer-based approach. With regard to the latter method, in addition to

the widely used technique based on the generalized momentum, another observer based on the joint position and velocity has been proposed. These three strategies have first been compared conceptually according to the structure of the uncertainties involved, then a frequency-domain analysis has been carried out in order to predict certain trends based on modeling errors and tuning parameters. Finally, these algorithms have been validated offline on the ISYBOT prototype robot and criteria for characterizing the resulting detection performance have been proposed, such as the energy transferred to the collided system during the contact.

Furthermore, these algorithms have also been derived in the case of robots with rigid links and elastic joints. For each method, two possible variants have been proposed, depending on whether the uncertainties on the motor friction model or on the joint stiffness are considered.

6.1.3 Characterization of the contact intention and localization

After the impact detection step, the characterization phase aims to reconstruct contextual elements of the contact, in order to trigger an appropriate robot reaction that, on the one hand, does not endanger the human operator, and on the other hand, ensures an efficient transition. In this thesis, we focused on determining the operator's intention to come into contact with the robot and on locating the area of the robot that was collided.

Given the complexity of the problem due to modeling uncertainties as well as additional uncertain parameters induced by the operator, an approach based on feed-forward neural network classifiers has been investigated. A "gray box" network structure guided by the physics of contact has been proposed to increase the efficiency of the classification. Two case studies were conducted to assess the generalizability to any human subject and any robot trajectory. Results have demonstrated that localizing the collided area on the robot arm can be very efficient using neural networks. Determining the intention of contact, however, has been more tedious since it may be related to subject-specific characteristics. Generalization to any human subject or robot trajectory has given promising results, but generalization to both factors at the same time seems limited by the elementary structure of the neural network considered. The adaptation of a human individual to a classifier trained on another person might be an alternative approach.

6.2 Outlooks

These results are a step towards a hand-to-hand human-robot collaboration. Interesting research directions could be explored for future work and are described below.

6.2.1 Validation of the impact detection algorithms in the flexible case

Impact detection strategies have been specifically designed in the flexible case for robots with rigid links and elastic joints. In this case, we expect the robot dynamic model to be more accurately identified, with reduced standard deviations on the parameters estimation errors.

This would not only lead to a more reliable external torque estimate (which would be exempt from discrepancies between the rigid and flexible models) but also to lower error margins, and therefore to improved detection performance.

A possible extension of this work would therefore consist in verifying this assumption in simulation and experimentally. This would allow to increase the dynamics of the robot's motion without the risk of stimulating the joint elasticities since the induced effects would be taken into account, while ensuring a safe detection of impacts.

6.2.2 A greater efficiency in impact detection

Above all, an extensive online validation of the detection algorithms on realistic operating scenarios (robot speeds and accelerations, contact times and locations) is essential for future use. As the frequency-domain analysis developed in this thesis has established the relation between modeling uncertainties and expected impact detection performance, it would be relevant to go one step further for an industrial application with a well-defined task, for example by:

- investigating the reverse approach: on the basis of safety requirements to be respected during the task (a priori imposed by robotic standards), determining which levers are available to improve the detection performance. The study of the evolution of the modeling errors according to the robot's trajectory would be a first approach: the trajectory could then be programmed according to a criterion minimizing the uncertainties-induced errors and thus enhancing the detection performance. In the case of a redundant robot, some configurations of the robotic arm may also be preferred over others in this respect. Another possibility in the case of disturbance observer-based methods would be to adjust the disturbance model parameters according to the maximum dissipated energy allowed by the standards. Indeed, based on the two-mass system connected by a spring, we could specify the evolution of the contact force and therefore the assumed external torque model.
- introducing contextual elements: so far in this thesis, a 3σ -confidence interval has been considered for the detection, but the adjustment of this parameter could be refined in order to avoid overly conservative detection results. Local reductions of this parameter could be considered, for example if we can identify sequences of the task during which a contact of the robot with its environment is expected. The adjustment of this parameter could also be determined by learning techniques or fuzzy logic, by providing the estimated external torque and the error margin of the associated model uncertainties as inputs. The speed of the robot could also be a determining criterion for adjusting this parameter.

In a more exploratory perspective, it would be interesting to compare the detection performance obtained with the detection strategies proposed in this thesis with learning-based techniques: these latter could be used in conjunction in order to possibly guarantee a finer detection of small-amplitude impacts (not detected by the developed strategies because within the error range of modeling errors). However, relying solely on such approaches seems disputable at first sight since there is no way to quantify the expected performance except by heuristic knowledge, unlike the proposed strategies, which has so far been an obstacle to the operator's safety.

6.2.3 Further improvements in contact situations characterization

In order to improve the generalizability of the classification of the contact intent to any human individual and any robot trajectory, two approaches are proposed:

- investigating other input choices: the choice of the estimated external torque and robot speed as network inputs was based on physical considerations, but other inputs may also be relevant. Indeed, if the objective is to keep a fairly simple neural network structure with a reduced number of neurons, then pre-processed inputs could improve the classification results. For this purpose, a PCA could be used to determine the influential variables of contact models as it is done in [Rodriguez 2010] for force signature models in assembly tasks.
- examining other neural network structures: more complex network structures may be required to deal more effectively with the complexity of the problem. On the one hand, RNNs would be appropriate to process the temporal evolution of the external torque, as proposed in [Kouris 2018] using a frequency-domain approach. On the other hand, CNNs would allow deeper contact characteristics to be extracted. However, it should be noted that more complex structures also require longer processing times, so the compatibility with a real-time implementation on the robot should be examined.

These advances could also make it possible to extract more information on the contact situation, such as the stiffness of the collided environment to distinguish for example between a human subject and a rigid part.

6.2.4 Towards a complete control scheme

The proposed detection and characterization methods should be integrated into a complete control scheme, which would include in particular post-impact strategies. To this end, the choice of a post-impact control scheme can be directed towards an impedance control law, which is widely recognized as being suitable for robots interacting with their environment.

More specifically, an adaptation of the control gains in impedance could be considered to obtain an efficient behavior in the post-impact phase (regarding passivity and transparency objectives), and taking into account the characteristics of the detected impact (intention, contact point, force amplitude, etc.). In this adaptive context, the issue of control stability will have to be examined.

APPENDIX A

Biomechanical constants of the human body

Body region	Specific body area	Effective spring constant (N/mm)	Effective mass (kg)
Skull and forehead	Middle of forehead Temple	150	4,4
Face	Masticory muscle	75	4,4
Neck	Neck muscle	50	1,2
	Seventh neck muscle		
Back and shoulders	Shoulder joint	35	40
	Fifth lumbar vertebra		
Chest	Sternum	25	40
	Pectoral muscle		
Abdomen	Abdominal muscle	10	40
Pelvis	Pelvic bone	25	40
Upper arms and elbow joints	Deltoid muscle	30	3
	Humerus		
Lower arms and wrist joints	Radial bone	40	2
	Forearm bone		
	Arm nerve		
Hands and fingers	Forefinger pad R	75	0,6
	Forefinger pad L		
	Forefinger end joint R		
	Forefinger end joint L		
	Thenar eminence		
	Palm R		
	Palm L		
	Back of the hand R		
	Back of the hand L		
Thighs and knees	Thigh muscle	50	75
	Kneecap		
Lower legs	Middle of shin	60	75
	Calf muscle		

Table A.1: Biomechanical constants of the human body from [ISO/TS 15066: 2016] (in grey: critical zone).

Applicative case of the ISYBOT prototype robot

B.1 Presentation of the robot

This thesis includes an experimental part that has been carried out using the ISYBOT prototype robot illustrated in [Figure B.1](#). This collaborative robot prototype is entirely designed and developed by the Interactive Robotics Laboratory of the CEA-LIST, in collaboration with the company ISYBOT[®]. It has been used to test and validate the proposed impact detection and classification algorithms.



Figure B.1: Prototype of the 6-DOF ISYBOT collaborative robot

This prototype is a lightweight robot manipulator with 6 DOF. Its anthropomorphic structure, similar to that of a human arm, is composed of an arm/forearm and a wrist. At each joint, the actuation and transmission system is based on a direct current motor driving a screw and cable actuator (see [Figure 1.11a](#)). This technology has the advantage of being compact and is characterized by good backdrivable properties and low friction levels [[Garrec 2010](#)]. Due to the reduced level of force required to drive the mechanism through the output and coupling this with the low inertia of the robot, the robot is easy to manipulate during co-manipulation tasks or for programming trajectories by demonstration. Moreover, these characteristics make it sensitive to any external contact and thereby particularly suitable for impact detection without additional force/torque sensor, but only by monitoring motor currents.

The motor currents and positions are measured before the gear reduction. The robotic arm is also equipped with incremental encoders measuring joint positions. The position sensors at motor and joint sides are identical for all the axes and have a resolution after gear reduction of order 10^{-5} and 10^{-7} rad respectively (thus joint measurement will be preferred when the choice is possible, e.g. in the rigid case). The knowledge of both positions gives information on the mechanical deformation due to joint elasticities. Finally, during the experiments, the robot was controlled in position either in the joint space or in the Cartesian space with a proportional-derivative (PD) control law using a real-time dedicated controller, with a sampling time of $T_s = 1\text{ms}$. A simulator of the robot dynamic behavior has been developed under Matlab/Simulink during the thesis.

B.2 Geometric model parameters

The attached frames and associated parameters of the ISYBOT prototype robot are defined according to the Khalil-Kleininger convention [Khalil 2004]. They are presented in Figure B.2 and Table B.1:

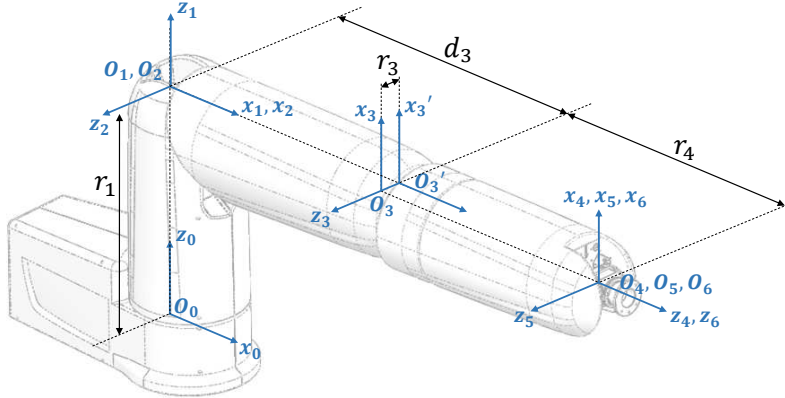


Figure B.2: Illustration of the attached frames of the ISYBOT prototype robot in the configuration $\mathbf{q} = (0\ 0\ 0\ 0\ 0\ 0)^T$.

axis j	σ_j	α_j	d_j	θ_j	r_j
1	0	0	0	q_1	0.582
2	0	$\pi/2$	0	q_2	0
3	0	0	0.600	$q_3 + \frac{\pi}{2}$	0.0135
4	0	$\pi/2$	0	$-q_4$	0.600
5	0	$-\pi/2$	0	q_5	0
6	0	$\pi/2$	0	$-q_6$	0

Table B.1: Table of the associated parameters of the ISYBOT prototype robot

B.3 Dynamic model parameters

First, the approach followed for the identification of rigid dynamic parameters is described and the subsequent results are presented. Finally, insights on the flexible identification are proposed.

The notations used for the rigid dynamic model parameters and their meanings are recalled in [Table B.2](#).

Parameter	Signification	Unit (SI)
$XX_j, XY_j, XZ_j, YY_j, YZ_j, ZZ_j$	components of the inertia matrix of link j	kg m^2
MX_j, MY_j, MZ_j	first moments of link j	kg m
M_{m_j}	mass of link j	kg
J_{m_j}	rotor inertia of the motor j	kg m^2
F_{v_j}	viscous friction coefficient of link j	$\text{kg m}^2 \text{ s}^{-1}$
F_{s_j}	dry friction coefficient of link j	$\text{kg m}^2 \text{ s}^{-2}$

Table B.2: Notations for the rigid dynamic model parameters of the ISYBOT prototype robot

Additional specific parameters are to be identified in the case of the ISYBOT prototype robot:

- Axes 5 and 6 being mechanically coupled, the actuator inertia matrix \mathbf{J}_m and the matrices of Coulomb friction coefficients \mathbf{F}_v and \mathbf{F}_s are non-diagonal of the form:

$$\mathbf{J}_m = \begin{pmatrix} J_{m1} & 0 & 0 & 0 & 0 & 0 \\ 0 & J_{m2} & 0 & 0 & 0 & 0 \\ 0 & 0 & J_{m3} & 0 & 0 & 0 \\ 0 & 0 & 0 & J_{m4} & 0 & 0 \\ 0 & 0 & 0 & 0 & J_{m5} & J_{m56} \\ 0 & 0 & 0 & 0 & J_{m56} & J_{m6} \end{pmatrix}$$

$$\mathbf{F}_v = \begin{pmatrix} F_{v1} & 0 & 0 & 0 & 0 & 0 \\ 0 & F_{v2} & 0 & 0 & 0 & 0 \\ 0 & 0 & F_{v3} & 0 & 0 & 0 \\ 0 & 0 & 0 & F_{v4} & 0 & 0 \\ 0 & 0 & 0 & 0 & F_{v5} & F_{v56} \\ 0 & 0 & 0 & 0 & F_{v56} & F_{v6} \end{pmatrix}, \quad \mathbf{F}_s = \begin{pmatrix} F_{s1} & 0 & 0 & 0 & 0 & 0 \\ 0 & F_{s2} & 0 & 0 & 0 & 0 \\ 0 & 0 & F_{s3} & 0 & 0 & 0 \\ 0 & 0 & 0 & F_{s4} & 0 & 0 \\ 0 & 0 & 0 & 0 & F_{s5} & F_{s56} \\ 0 & 0 & 0 & 0 & F_{s65} & F_{s6} \end{pmatrix}$$

Parameters J_{m56} , F_{v56} , F_{s56} and F_{s65} are added to the list of parameters to be identified.

- Constant offset parameters OFS_j are also included for each axis j , in order to take into account any asymmetry into the friction coefficients (see [Section B.3.2](#)),

- Due to the presence of a gravity-compensating spring on axis 2, an additional contribution $K_{r_2}(q_2 - q_{20})$ is added to the second component of the gravity torque of the IDM, with K_{r_2} the torsional stiffness and q_{20} the calibration angle. These two parameters are additional dynamic parameters to be identified.

The relations to obtain the base parameters from the physical parameters of the robot are calculated using SYMORO+ software [Khalil 2004]. In total, 63 rigid base parameters are to be identified for the ISYBOT prototype robot (see Table B.3, the grouped parameters being denoted with a superscript R).

B.3.1 Experimental protocol

Experimental measurements were performed on a set of exciting trajectories chosen to sequentially excite different groups of parameters: single-joint motion at constant velocities excites the gravity and friction parameters, while inertial parameters are excited by simultaneous high-velocity sinusoidal trajectories for all joints.

For the practical application of the identification methodology described in Chapter 2, Section 2.3.1.2, data processing is carried out according to the recommendations in [Khalil 2004]. More specifically, motor and joint position measurements are filtered by a low-pass Butterworth filter of order 7 in both the forward and reverse direction (`filtfilt` procedure in Matlab). Then velocities and accelerations are obtained by centered difference of filtered positions. In this way, any phase shift is avoided and amplitude distortion is limited in the bandwidth.

The applied motor torques are also necessary to evaluate the IDM. Owing to the high bandwidth of the current loop, the reference torques are used, which have the advantage of being less noisy than the actuator current measurements.

B.3.2 Validation of the friction model

A Coulomb friction model has been considered throughout the thesis. Experiments were carried out to verify the validity of this assumption in the case of the ISYBOT prototype robot. For each axis, measurements were collected on a triangular trajectory of increasing frequency, which corresponds to velocity steps of increasing magnitude.

Figure B.3 represents for each axis the motor torque with respect to the computed joint velocity. Only points at constant speeds are picked out to identify the friction model (in red in the figure): given the gravity component, either the robot is stimulated in configurations not subjected to gravity (axes 1 and 4 to 6), or points at a fixed position are selected (axes 2 and 3). A clear trend towards a model based on viscous and dry friction is recognizable, whose parameters can be retrieved by interpolation or LS minimization. For the global identification, symmetrical dry friction coefficients were considered, associated with an offset parameter for each axis.

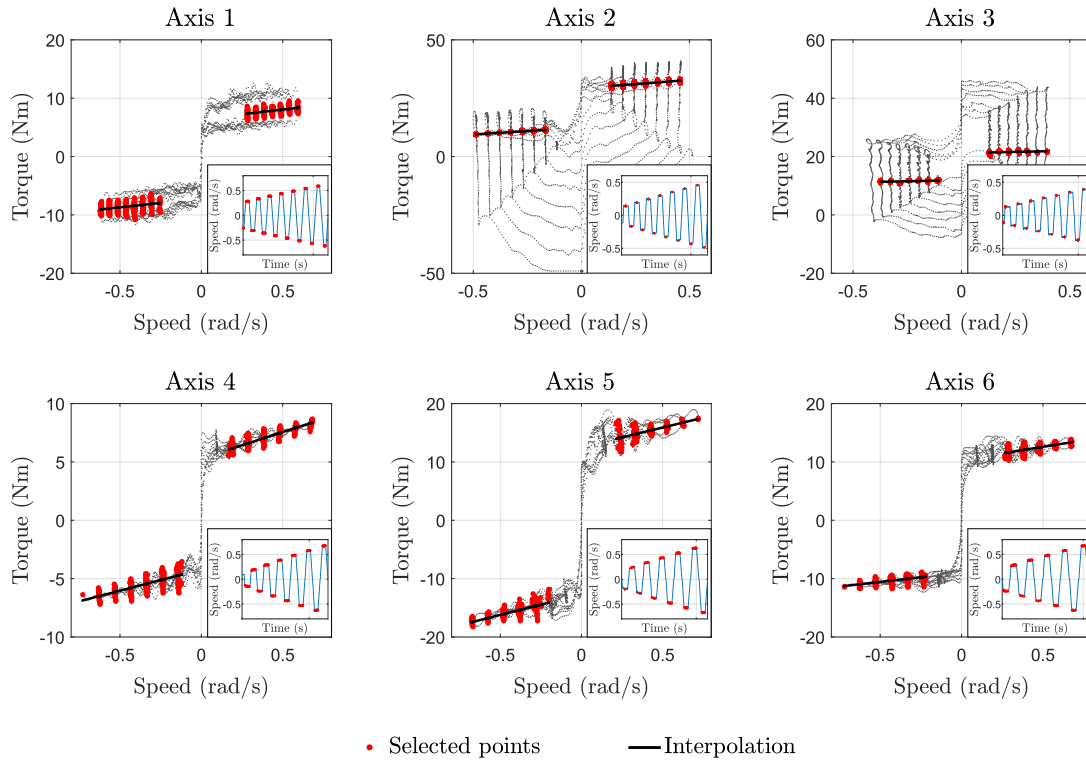


Figure B.3: Validation of the Coulomb friction model on triangular trajectories of increasing frequency.

B.3.3 Results and associated uncertainties

The global identification procedure is carried out on the concatenated system that gathers all the experimental measurements. The WLS resolution method is used. The identified dynamic parameters and their relative standard deviations are listed in [Table B.3](#), along with the CAD values when available. Some values are difficult to identify due to their low contribution to the total torque, thus their value are fixed to their CAD estimate (in green in the table). Although some parameters are poorly identified (XZ_4 , $, $in particular, and all the parameters previously fixed), the identification results at this stage were considered acceptable since all relative standard deviations are below 10% (except for the parameters previously fixed but which contribution is very small and therefore have little influence).$$

[Figure B.4](#) shows a comparison of the applied motor torques with the torques estimated using the identified dynamic parameters. The validation trajectory is a sinusoidal trajectory of increasing frequency simultaneously for each joint, and that is different from those included in the identification set. We observe that the motor torque is faithfully reconstructed for axes 1 to 4. Some error peaks can be noticed during changes in trajectory direction, which may reflect a significant flexible component. Axes 5 and 6, however, are less well identified due to noisy motor torques and particularly high friction on these axes. Poor detection performances are therefore to be expected on these last two axes.

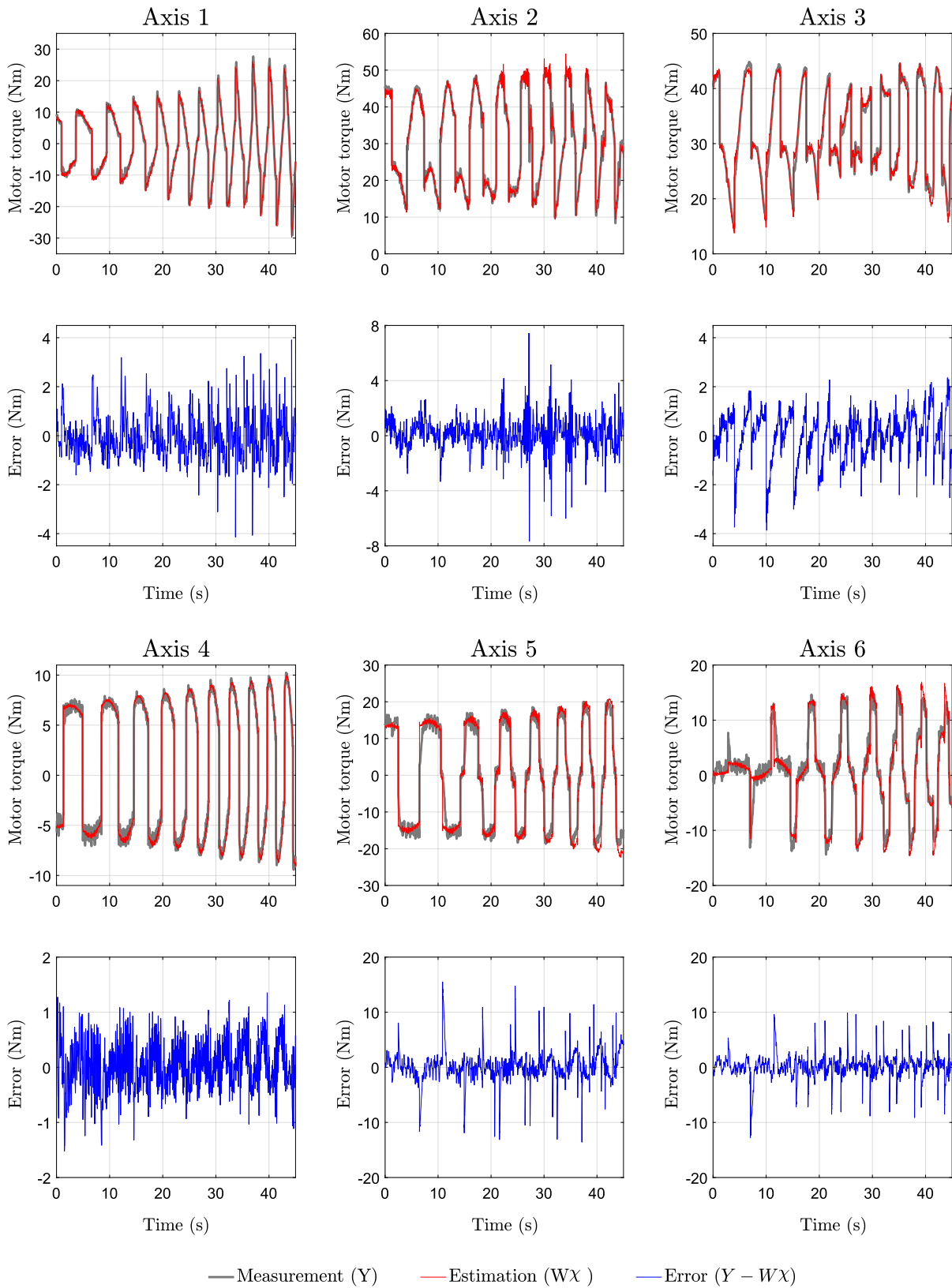


Figure B.4: Validation of the identification of the rigid dynamic model parameters

Parameter	CAD value	Identified value χ_{\star_i}	$\% \sigma_{\chi_i}$ (%)	Parameter	CAD value	Identified value χ_{\star_i}	$\% \sigma_{\chi_i}$ (%)
ZZ_1^R	5.279	10.961	0.14	MY_4^R	-0.002	0.007	6.74
F_{v1}	–	3.254	0.49	J_{m4}	0.047	1.329	0.35
F_{s1}	–	7.484	0.07	F_{v4}	–	3.299	0.24
OFS_1	0.000	-0.122	1.80	F_{s4}	–	5.176	0.06
XX_2^R	-4.782	-5.727	0.35	OFS_4	0.000	0.735	0.35
XY_2	-0.006	-0.006	215.40	XX_5^R	0.001	0.001	453.83
XZ_2^R	0.064	0.064	19.15	XY_5	0.000	0.000	–
YZ_2	-0.002	-0.002	569.61	XZ_5	0.000	0.000	–
ZZ_2^R	5.221	11.696	0.12	YZ_5	0.000	0.000	–
MX_2^R	8.637	9.192	0.10	ZZ_5^R	0.002	0.002	237.73
MY_2	-0.049	-0.621	2.14	MX_5	0.000	-0.044	0.99
F_{v2}	–	6.753	0.35	MY_5^R	-0.018	-0.031	1.13
F_{s2}	–	8.868	0.05	J_{m5}	0.055	2.570	0.40
K_{r2}	68.000	51.283	0.28	F_{v5}	–	8.168	0.32
OFS_2	-131.240	-107.483	0.08	F_{s5}	–	-5.819	0.22
XX_3^R	1.677	2.486	0.75	OFS_5	0.000	-0.093	4.22
XY_3	-0.001	-0.001	1723.47	XX_6^R	0.000	0.000	–
XZ_3	0.000	0.000	–	XY_6	0.000	0.000	–
YZ_3	0.000	0.000	–	XZ_6	0.000	0.000	–
ZZ_3^R	1.678	1.592	0.49	YZ_6	0.000	0.000	–
MX_3	0.007	-0.125	0.33	ZZ_6	0.000	0.000	–
MY_3^R	-3.580	-3.780	0.02	MX_6	0.000	0.000	–
J_{m3}	0.165	2.490	0.34	MY_6	0.000	0.007	4.52
F_{v3}	–	2.692	0.74	J_{m6}	0.027	1.959	0.48
F_{s3}	–	6.408	0.07	F_{v6}	–	4.410	0.35
OFS_3	0.000	1.213	0.48	F_{s6}	–	5.015	0.08
XX_4^R	0.001	0.001	768.69	OFS_6	0.000	0.946	0.31
XY_4	0.000	0.000	–	J_{m56}	0.000	0.000	–
XZ_4	-0.022	-0.025	8.59	F_{v56}	–	2.348	0.64
YZ_4	0.000	0.000	–	F_{s56}	–	6.765	0.18
ZZ_4^R	0.023	0.067	7.52	F_{s65}	–	5.180	0.11
MX_4	0.104	0.065	0.60				

Table B.3: Identified rigid dynamic model parameters of the ISYBOT prototype robot

B.3.4 Insights on the identification of flexible dynamic model parameters

The identification of the flexible dynamic model parameters has been carried out in two steps: in a preliminary stage, [Hypothesis 2.1](#) of constant linear stiffness has been verified by static methods, then a local identification of the dynamic behavior has been conducted. The post-processing phase of this second step was conducted as explained in [Section B.3.1](#).

Validation of the stiffness model

A constant linear stiffness K_j has been considered in the thesis to model the lumped elasticity of the j^{th} joint. Experiments were carried out to validate this assumption in the case of the ISYBOT prototype robot. The deformation $\mathbf{q} - \boldsymbol{\theta}$ was measured at several static positions of axis 2 around the “extended arm”-configuration $\mathbf{q}_0 = (0 \ 0 \ 0 \ 0 \ 0)^T$. In the absence of external torque and in static configurations, the link equation of the FDM yields:

$$\mathbf{G}(\mathbf{q}) + \mathbf{F}_{sa} \text{sign}(\dot{\mathbf{q}}) = -\mathbf{K}(\mathbf{q} - \boldsymbol{\theta}) + \boldsymbol{\tau}_k \mathbf{0} \quad (\text{B.1})$$

Considering that dry friction is mainly concentrated at the motor side ($\mathbf{F}_{sa} \approx \mathbf{0}$), the gravity torque computed with the rigid identified parameters is represented with respect to the measured deformation $\mathbf{q} - \boldsymbol{\theta}$ for axis 2 in [Figure B.5](#). A clear trend towards a linear model is recognizable. Parameters could be retrieved by interpolation or LS minimization, however, the stiffness varying locally, a local dynamic identification has been preferred to determine the stiffness constant.

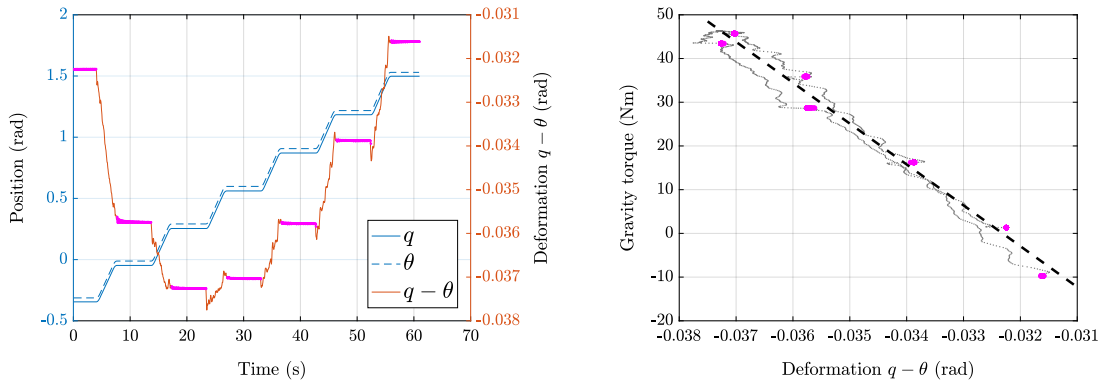


Figure B.5: Validation of the constant linear stiffness model for axis 2. The points corresponding to the static configurations and used to identify the stiffness model are in magenta.

Local identification of the flexible dynamic model parameters

The flexible dynamic model parameters have been identified locally on the trajectories without contact used in [Chapter 4: "Experimental validation of impact detection strategies"](#) – [Section 4.2](#). Given the limited use in the thesis, the results are not presented here.

B.4 State calculation

In this section, the distribution of the noise on the measured position is first examined. Then, the assumption that the error term on the numerically derived velocity and acceleration follow a normal distribution is verified below based on experimental data.

B.4.1 Position error distribution

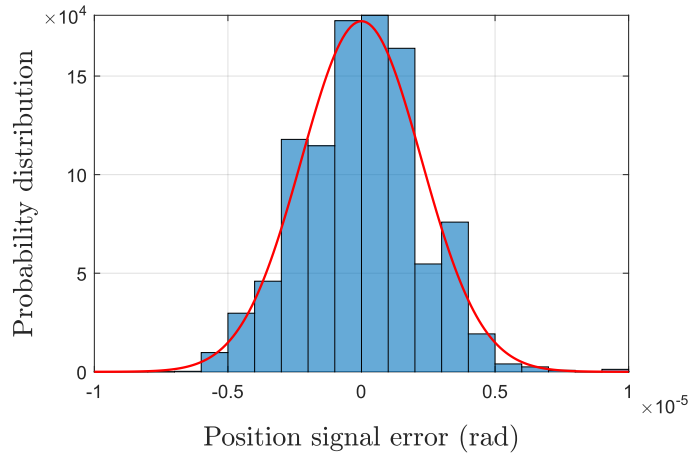
Experiments with the ISYBOT prototype robot have been conducted to analyze the measurement noise distribution in position signals. Therein, the joint position has been measured for each individual joint in different static robot configurations and the mean of the position measurement is subtracted for each configuration. As an example, [Figure B.6a](#) shows the empirical distribution of the position signal error for joint 2 (the joint position sensors being identical for all axes). As depicted, the measurement noise distribution can reasonably well be approximated by a Gaussian distribution. Indeed, in this case, the position measurement is slightly filtered, which explains why we observe a Gaussian distribution and not a uniform distribution as we would expect if the measurement noise was only due to the quantization noise (see [Section 2.3.2.3](#)). The covariance matrix Σ_q of the measurement noise is deduced from the standard deviations measured experimentally and is given by $\Sigma_q = 7.1506 \cdot 10^{-12} \mathbf{I}_6$.

B.4.2 Velocity error distribution

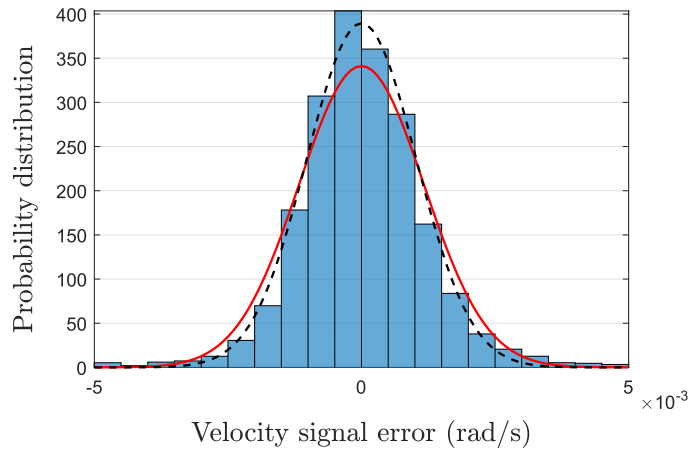
In this case, each joint is moved individually on a triangular trajectory of increasing frequency, which corresponds to velocity steps of increasing magnitude. Parts of the trajectory at different constant speed are extracted and for each part, the mean of the numerically derived velocity is subtracted. As an example, [Figure B.6b](#) shows the empirical distribution of the velocity signal error for joint 2. As depicted, the velocity error distribution can reasonably well be approximated by a Gaussian distribution. For comparison, the empirical and the theoretical PDF are displayed, where the variance of the theoretical one has been obtained from equation (2.52).

B.4.3 Acceleration error distribution

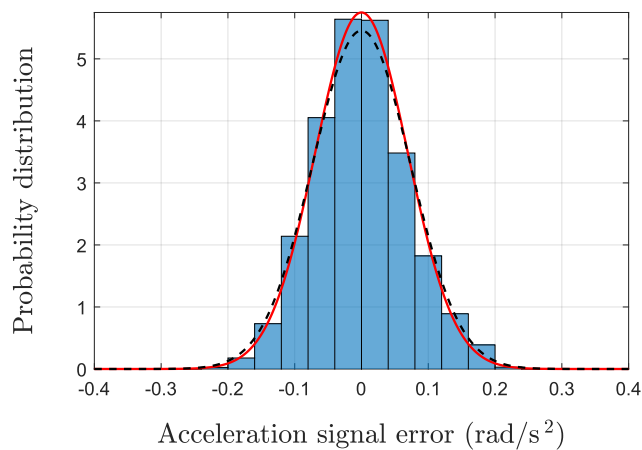
In this case, each joint is moved individually on a triangular trajectory of increasing frequency, which corresponds to velocity steps of increasing magnitude. This experiment is repeated for several maximal accelerations. For each experiment, parts of the trajectory at constant acceleration are extracted and for each part, the mean of the numerically derived acceleration is subtracted. As an example, [Figure B.6c](#) shows the empirical distribution of the acceleration signal error for joint 2. As depicted, the acceleration error distribution can reasonably well be approximated by a Gaussian distribution. For comparison, the empirical and the theoretical PDF are displayed, where the variance of the theoretical one has been obtained from equation (2.53).



(a) Position error distribution



(b) Velocity error distribution



(c) Acceleration error distribution

■ Empirical distribution
 — Empirical PDF
 - - - Theoretical PDF

Figure B.6: Empirical distribution of the mean-free error signals in position, velocity and acceleration for joint 2 (*histograms*). The corresponding PDF are calculated empirically (*red lines*) and theoretically (*dashed black lines*).

Further information on the characterization of Human-Robot contact situations

C.1 Experimental protocol

In order to record realistic but reproducible contact situations among the different subjects, the following instructions were given to the participants. These guidelines are intended to reproduce unexpected or intentional contact situations (*collisions* or *interactions* respectively):

- Collisions: the participant is blindfolded to simulate the effect of surprise produced by an unexpected contact. In addition, to avoid the apprehensive effect that could stiffen his muscles, he has to move his hand from one end of the rail to the other when a signal is given to him in order to distract him. At an undetermined moment during the movement of his hand, he will be unexpectedly in contact with the robot that moves back and forth in a straight line along the rail. The signal frequency is constantly changing to ensure that the participant does not anticipate the movements and the contacts with the robot.
- Interactions: with his eyes open in this case, the participant has to come into contact with the force/torque sensor placed on the robot end-effector when it is reachable, with the intention of slowing down the robot. The participant is warned that he would not be able to stop the robot due to the control loop, but that the robot would move in the opposite direction after a few seconds of contact.

Contact acquisitions were conducted in two phases, starting with collisions and then interactions. At the beginning of each phase, the instructions were given. Then participants were allowed to familiarize themselves with the experimental conditions before the recordings began.

The following sections describe the individual results obtained for each participant, in Experiment A (Section C.2), Experiment B (Section C.3) and Experiment C (Section C.4) for *case study 2*.

C.2 Experiment A: 1 candidate in the training

Candidate 1 - Trajectory 1

Percentage		Situation classified as			Total
		Non-contact	Interaction	Collision	
Actual situation	Non-contact	98.57	0.00	1.43	100.00
	Interaction	0.00	100.00	0.00	100.00
	Collision	0.00	5.88	94.12	100.00
Overall success rate					97.86

Candidate 2 - Trajectory 1

Percentage		Situation classified as			Total
		Non-contact	Interaction	Collision	
Actual situation	Non-contact	98.57	0.00	1.43	100.00
	Interaction	0.00	100.00	0.00	100.00
	Collision	0.00	5.88	94.12	100.00
Overall success rate					97.86

Candidate 3 - Trajectory 1

Percentage		Situation classified as			Total
		Non-contact	Interaction	Collision	
Actual situation	Non-contact	100.00	0.00	0.00	100.00
	Interaction	0.00	97.22	2.78	100.00
	Collision	0.00	0.00	100.00	100.00
Overall success rate					99.30

Candidate 4 - Trajectory 1

Percentage		Situation classified as			Total
		Non-contact	Interaction	Collision	
Actual situation	Non-contact	100.00	0.00	0.00	100.00
	Interaction	0.00	97.22	2.78	100.00
	Collision	0.00	6.06	93.94	100.00
Overall success rate					97.83

Candidate 5 - Trajectory 2

Percentage		Situation classified as			Total
		Non-contact	Interaction	Collision	
Actual situation	Non-contact	100.00	0.00	0.00	100.00
	Interaction	0.00	100.00	0.00	100.00
	Collision	2.94	0.00	97.06	100.00
Overall success rate					99.29

Candidate 6 - Trajectory 2

Percentage		Situation classified as			Total
		Non-contact	Interaction	Collision	
Actual situation	Non-contact	95.71	4.29	0.00	100.00
	Interaction	0.00	97.22	2.78	100.00
	Collision	0.00	11.76	88.24	100.00
Overall success rate					94.29

Candidate 7 - Trajectory 2

Percentage		Situation classified as			Total
		Non-contact	Interaction	Collision	
Actual situation	Non-contact	100.00	0.00	0.00	100.00
	Interaction	0.00	97.22	2.78	100.00
	Collision	0.00	5.71	94.29	100.00
Overall success rate					97.89

Candidate 8 - Trajectory 2

Percentage		Situation classified as			Total
		Non-contact	Interaction	Collision	
Actual situation	Non-contact	100.00	0.00	0.00	100.00
	Interaction	0.00	100.00	0.00	100.00
	Collision	0.00	6.06	93.94	100.00
Overall success rate					98.55

Candidate 9 - Trajectory 3

Percentage		Situation classified as			Total
		Non-contact	Interaction	Collision	
Actual situation	Non-contact	100.00	0.00	0.00	100.00
	Interaction	0.00	100.00	0.00	100.00
	Collision	0.00	0.00	100.00	100.00
Overall success rate					100.00

Candidate 10 - Trajectory 3

Percentage		Situation classified as			Total
		Non-contact	Interaction	Collision	
Actual situation	Non-contact	95.77	0.00	4.23	100.00
	Interaction	0.00	100.00	0.00	100.00
	Collision	0.00	5.71	94.29	100.00
Overall success rate					96.48

Candidate 11 - Trajectory 3

Percentage		Situation classified as			Total
		Non-contact	Interaction	Collision	
Actual situation	Non-contact	100.00	0.00	0.00	100.00
	Interaction	0.00	100.00	0.00	100.00
	Collision	0.00	2.78	97.22	100.00
Overall success rate					99.31

Candidate 12 - Trajectory 3

Percentage		Situation classified as			Total
		Non-contact	Interaction	Collision	
Actual situation	Non-contact	100.00	0.00	0.00	100.00
	Interaction	0.00	100.00	0.00	100.00
	Collision	0.00	2.78	97.22	100.00
Overall success rate					99.31

Candidate 13 - Trajectory 4

Percentage		Situation classified as			Total
		Non-contact	Interaction	Collision	
Actual situation	Non-contact	100.00	0.00	0.00	100.00
	Interaction	0.00	100.00	0.00	100.00
	Collision	0.00	3.23	96.77	100.00
Overall success rate					99.25

Candidate 14 - Trajectory 4

Percentage		Situation classified as			Total
		Non-contact	Interaction	Collision	
Actual situation	Non-contact	100.00	0.00	0.00	100.00
	Interaction	0.00	91.67	8.33	100.00
	Collision	0.00	3.03	96.97	100.00
Overall success rate					97.10

Candidate 15 - Trajectory 4

Percentage		Situation classified as			Total
		Non-contact	Interaction	Collision	
Actual situation	Non-contact	100.00	0.00	0.00	100.00
	Interaction	0.00	100.00	0.00	100.00
	Collision	0.00	2.78	97.22	100.00
Overall success rate					99.31

Candidate 16 - Trajectory 4

Percentage		Situation classified as			Total
		Non-contact	Interaction	Collision	
Actual situation	Non-contact	95.83	1.39	2.78	100.00
	Interaction	0.00	100.00	0.00	100.00
	Collision	0.00	5.56	94.44	100.00
Overall success rate					96.53

C.3 Experiment B: 3 candidates in the training

Candidate 1 - Trajectory 1

Percentage		Situation classified as			Total
		Non-contact	Interaction	Collision	
Actual situation	Non-contact	100.00	0.00	0.00	100.00
	Interaction	0.00	95.83	4.17	100.00
	Collision	0.00	1.43	98.57	100.00
Overall success rate					98.59

Candidate 2 - Trajectory 1

Percentage		Situation classified as			Total
		Non-contact	Interaction	Collision	
Actual situation	Non-contact	97.18	0.71	2.11	100.00
	Interaction	0.00	100.00	0.00	100.00
	Collision	0.00	4.29	95.71	100.00
Overall success rate					97.54

Candidate 3 - Trajectory 1

Percentage		Situation classified as			Total
		Non-contact	Interaction	Collision	
Actual situation	Non-contact	100.00	0.00	0.00	100.00
	Interaction	0.00	100.00	0.00	100.00
	Collision	0.00	0.00	100.00	100.00
Overall success rate					100.00

Candidate 4 - Trajectory 1

Percentage		Situation classified as			Total
		Non-contact	Interaction	Collision	
Actual situation	Non-contact	96.45	0.00	3.55	100.00
	Interaction	0.00	98.61	1.39	100.00
	Collision	0.00	5.80	94.20	100.00
Overall success rate					96.45

Candidate 5 - Trajectory 2

Percentage		Situation classified as			Total
		Non-contact	Interaction	Collision	
Actual situation	Non-contact	99.30	0.70	0.00	100.00
	Interaction	0.00	80.56	19.44	100.00
	Collision	1.43	2.86	95.71	100.00
Overall success rate					93.66

Candidate 6 - Trajectory 2

Percentage		Situation classified as			Total
		Non-contact	Interaction	Collision	
Actual situation	Non-contact	99.30	0.70	0.00	100.00
	Interaction	0.00	94.44	5.56	100.00
	Collision	0.00	10.00	90.00	100.00
Overall success rate					95.77

Candidate 7 - Trajectory 2

Percentage		Situation classified as			Total
		Non-contact	Interaction	Collision	
Actual situation	Non-contact	100.00	0.00	0.00	100.00
	Interaction	0.00	95.83	4.17	100.00
	Collision	0.00	12.68	87.32	100.00
Overall success rate					95.80

Candidate 8 - Trajectory 2

Percentage		Situation classified as			Total
		Non-contact	Interaction	Collision	
Actual situation	Non-contact	97.87	0.00	2.13	100.00
	Interaction	0.00	100.00	0.00	100.00
	Collision	0.00	57.97	42.03	100.00
Overall success rate					84.75

Candidate 9 - Trajectory 3

Percentage		Situation classified as			Total
		Non-contact	Interaction	Collision	
Actual situation	Non-contact	100.00	0.00	0.00	100.00
	Interaction	0.00	100.00	0.00	100.00
	Collision	0.00	0.00	100.00	100.00
Overall success rate					100.00

Candidate 10 - Trajectory 3

Percentage		Situation classified as			Total
		Non-contact	Interaction	Collision	
Actual situation	Non-contact	100.00	0.00	0.00	100.00
	Interaction	0.00	87.50	12.50	100.00
	Collision	0.00	14.08	85.92	100.00
Overall success rate					93.36

Candidate 11 - Trajectory 3

Percentage		Situation classified as			Total
		Non-contact	Interaction	Collision	
Actual situation	Non-contact	97.22	0.00	2.78	100.00
	Interaction	0.00	88.89	11.11	100.00
	Collision	0.00	0.00	100.00	100.00
Overall success rate					95.83

Candidate 12 - Trajectory 3

Percentage		Situation classified as			Total
		Non-contact	Interaction	Collision	
Actual situation	Non-contact	100.00	0.00	0.00	100.00
	Interaction	0.00	100.00	0.00	100.00
	Collision	0.00	9.72	90.28	100.00
Overall success rate					97.57

Candidate 13 - Trajectory 4

Percentage		Situation classified as			Total
		Non-contact	Interaction	Collision	
Actual situation	Non-contact	98.56	0.72	0.72	100.00
	Interaction	0.00	100.00	0.00	100.00
	Collision	0.00	2.99	97.01	100.00
Overall success rate					98.56

Candidate 14 - Trajectory 4

Percentage		Situation classified as			Total
		Non-contact	Interaction	Collision	
Actual situation	Non-contact	93.62	2.13	4.25	100.00
	Interaction	0.00	93.06	6.94	100.00
	Collision	0.00	1.45	98.55	100.00
Overall success rate					94.68

Candidate 15 - Trajectory 4

Percentage		Situation classified as			Total
		Non-contact	Interaction	Collision	
Actual situation	Non-contact	96.53	1.39	2.08	100.00
	Interaction	0.00	97.22	2.78	100.00
	Collision	0.00	12.50	87.50	100.00
Overall success rate					94.44

Candidate 16 - Trajectory 4

Percentage		Situation classified as			Total
		Non-contact	Interaction	Collision	
Actual situation	Non-contact	97.92	2.08	0.00	100.00
	Interaction	0.00	100.00	0.00	100.00
	Collision	1.39	1.39	97.22	100.00
Overall success rate					98.26

C.4 Experiment C: 3 trajectories in the training

Candidate 1 - Trajectory 1

Percentage		Situation classified as			Total
		Non-contact	Interaction	Collision	
Actual situation	Non-contact	90.85	0.00	9.15	100.00
	Interaction	0.00	33.33	66.67	100.00
	Collision	0.00	0.00	100.00	100.00
Overall success rate					78.52

Candidate 2 - Trajectory 1

Percentage		Situation classified as			Total
		Non-contact	Interaction	Collision	
Actual situation	Non-contact	85.92	4.93	9.15	100.00
	Interaction	0.00	69.44	30.56	100.00
	Collision	0.00	0.00	100.00	100.00
Overall success rate					85.21

Candidate 3 - Trajectory 1

Percentage		Situation classified as			Total
		Non-contact	Interaction	Collision	
Actual situation	Non-contact	94.41	0.00	5.59	100.00
	Interaction	0.00	86.11	13.89	100.00
	Collision	0.00	0.00	100.00	100.00
Overall success rate					93.71

Candidate 4 - Trajectory 1

Percentage		Situation classified as			Total
		Non-contact	Interaction	Collision	
Actual situation	Non-contact	92.20	0.00	7.80	100.00
	Interaction	0.00	54.17	45.83	100.00
	Collision	0.00	0.00	100.00	100.00
Overall success rate					84.40

Candidate 5 - Trajectory 2

Percentage		Situation classified as			Total
		Non-contact	Interaction	Collision	
Actual situation	Non-contact	89.44	0.00	10.56	100.00
	Interaction	0.00	88.89	11.11	100.00
	Collision	4.28	24.29	71.43	100.00
Overall success rate					84.86

Candidate 6 - Trajectory 2

Percentage		Situation classified as			Total
		Non-contact	Interaction	Collision	
Actual situation	Non-contact	88.73	0.00	11.27	100.00
	Interaction	0.00	87.50	12.50	100.00
	Collision	0.00	65.71	34.29	100.00
Overall success rate					75.00

Candidate 7 - Trajectory 2

Percentage		Situation classified as			Total
		Non-contact	Interaction	Collision	
Actual situation	Non-contact	92.31	0.00	7.69	100.00
	Interaction	0.00	98.61	1.39	100.00
	Collision	4.23	26.76	69.01	100.00
Overall success rate					88.11

Candidate 8 - Trajectory 2

Percentage		Situation classified as			Total
		Non-contact	Interaction	Collision	
Actual situation	Non-contact	96.45	0.00	3.55	100.00
	Interaction	0.00	95.83	4.17	100.00
	Collision	0.00	59.42	40.58	100.00
Overall success rate					82.62

Candidate 9 - Trajectory 3

Percentage		Situation classified as			Total
		Non-contact	Interaction	Collision	
Actual situation	Non-contact	72.03	16.78	11.19	100.00
	Interaction	0.00	88.89	11.11	100.00
	Collision	0.00	54.93	45.07	100.00
Overall success rate					69.58

Candidate 10 - Trajectory 3

Percentage		Situation classified as			Total
		Non-contact	Interaction	Collision	
Actual situation	Non-contact	71.33	13.99	14.68	100.00
	Interaction	0.00	95.83	4.17	100.00
	Collision	0.00	39.44	60.56	100.00
Overall success rate					74.83

Candidate 11 - Trajectory 3

Percentage		Situation classified as			Total
		Non-contact	Interaction	Collision	
Actual situation	Non-contact	59.72	7.64	32.64	100.00
	Interaction	0.00	54.17	45.83	100.00
	Collision	0.00	59.72	40.28	100.00
Overall success rate					53.47

Candidate 12 - Trajectory 3

Percentage		Situation classified as			Total
		Non-contact	Interaction	Collision	
Actual situation	Non-contact	73.61	9.03	17.36	100.00
	Interaction	0.00	88.89	11.11	100.00
	Collision	0.00	44.44	55.56	100.00
Overall success rate					72.92

Candidate 13 - Trajectory 4

Percentage		Situation classified as			Total
		Non-contact	Interaction	Collision	
Actual situation	Non-contact	97.12	1.44	1.44	100.00
	Interaction	0.00	100.00	0.00	100.00
	Collision	0.00	28.36	71.64	100.00
Overall success rate					91.73

Candidate 14 - Trajectory 4

Percentage		Situation classified as			Total
		Non-contact	Interaction	Collision	
Actual situation	Non-contact	99.29	0.71	0.00	100.00
	Interaction	0.00	100.00	0.00	100.00
	Collision	0.00	39.13	60.87	100.00
Overall success rate					90.07

Candidate 15 - Trajectory 4

Percentage		Situation classified as			Total
		Non-contact	Interaction	Collision	
Actual situation	Non-contact	94.44	5.56	0.00	100.00
	Interaction	0.00	100.00	0.00	100.00
	Collision	0.00	72.22	27.78	100.00
Overall success rate					79.17

Candidate 16 - Trajectory 4

Percentage		Situation classified as			Total
		Non-contact	Interaction	Collision	
Actual situation	Non-contact	96.53	2.78	0.69	100.00
	Interaction	0.00	100.00	0.00	100.00
	Collision	1.39	77.78	20.83	100.00
Overall success rate					78.47

Bibliography

- [ABB 2019] ABB. *YuMi[®] – IRB 14000 | Collaborative Robot*, 2019. <https://new.abb.com/products/robotics/industrial-robots/irb-14000-yumi>. (Cited on page 17.)
- [Alazard 2005] Daniel Alazard. *Introduction to Kalman filtering*. SUPAERO, 2005. (Cited on page 77.)
- [Albu-Schäffer 2001] Alin Albu-Schäffer and Gerd Hirzinger. *Parameter identification and passivity based joint control for a 7 DOF torque controlled light weight robot*. In IEEE International Conference on Robotics and Automation (ICRA), volume 3, pages 2852–2858, 2001. (Cited on page 38.)
- [ANSI R15.06 2012] ANSI R15.06. *American National Standard for Industrial Robots and Robot Systems – Safety Requirements*. Standard, American National Standards Institute/Robotics Industry Association, 2012. (Cited on page 8.)
- [Armstrong H elouvry 1994] Brian Armstrong H elouvry, Pierre Dupont and Carlos Canudas De Wit. *A survey of models, analysis tools and compensation methods for the control of machines with friction*. *Automatica*, vol. 30, no. 7, pages 1083 – 1138, 1994. (Cited on page 30.)
- [Armstrong 1986] Brian Armstrong, Oussama Khatib and Joel Burdick. *The explicit dynamic model and inertial parameters of the PUMA 560 arm*. In IEEE International Conference on Robotics and Automation (ICRA), volume 3, pages 510–518, Apr 1986. (Cited on page 38.)
- [Asimov 1950] Isaac Asimov. *I, robot*. Gnome Press, 1950. (Cited on page 8.)
- [Assurance Maladie 2017] Assurance Maladie. *Risques professionnels – Rapport annuel, 2017*. https://assurance-maladie.ameli.fr/sites/default/files/cnam-drp_rapport_de_gestion_2017_vdef_pour_mise_en_ligne_web.pdf. (Cited on page 3.)
- [Bagge Carlson 2015] Fredrik Bagge Carlson, Anders Robertsson and Rolf Johansson. *Modeling and identification of position and temperature dependent friction phenomena without temperature sensing*. In IEEE/RSJ International Conference on Intelligent Robots and Systems (IROS), pages 3045–3051, Sept 2015. (Cited on page 30.)
- [Barth 2011] Tim Barth. *A brief overview of uncertainty quantification and error estimation in numerical simulation*. NASA Ames Research Center, NASA Report, 2011. (Cited on page 34.)
- [Behrens 2014] Roland Behrens and Norbert Elkmann. *Study on meaningful and verified thresholds for minimizing the consequences of human-robot collisions*. In IEEE International Conference on Robotics and Automation (ICRA), pages 3378–3383, 2014. (Cited on page 12.)

- [Belanger 1992] Pierre R. Belanger. *Estimation of angular velocity and acceleration from shaft encoder measurements*. In IEEE International Conference on Robotics and Automation (ICRA), pages 585–592, 1992. (Cited on page 44.)
- [Bicchi 2008] Antonio Bicchi, Michael A. Peshkin and J. Edward Colgate. *Safety for physical human–robot interaction*. In Springer handbook of Robotics, pages 1335–1348. Springer, 2008. (Cited on page 7.)
- [Bishop 2007] Christopher M. Bishop. *Pattern Recognition and Machine Learning (Information Science and Statistics)*, 2007. (Cited on page 133.)
- [Bittencourt 2012] André Carvalho Bittencourt and Svante Gunnarsson. *Static friction in a robot joint-modeling and identification of load and temperature effects*. Journal of Dynamic Systems, Measurement, and Control, vol. 134, no. 5, page 051013, 2012. (Cited on page 30.)
- [Brown 1992] Ronald H. Brown, Susan C. Schneider and Michael G. Mulligan. *Analysis of algorithms for velocity estimation from discrete position versus time data*. IEEE Transactions on Industrial Electronics, vol. 39, no. 1, pages 11–19, 1992. (Cited on page 44.)
- [Brunot 2016] Mathieu Brunot, Alexandre Janot, Francisco Carrillo and Maxime Gautier. *State space estimation method for robot identification*. IFAC-PapersOnLine, vol. 49, no. 21, pages 228–233, 2016. (Cited on page 44.)
- [Camoriano 2016] Raffaello Camoriano, Silvio Traversaro, Lorenzo Rosasco, Giorgio Metta and Francesco Nori. *Incremental semiparametric inverse dynamics learning*. In IEEE International Conference on Robotics and Automation (ICRA), pages 544–550, 2016. (Cited on page 38.)
- [Capek 1920] Karel Capek. Rossum’s universal robots. Penguin Classics, 1920. (Cited on page 2.)
- [Chan 1998] S. P. Chan. *Velocity estimation for robot manipulators using neural network*. Journal of Intelligent and Robotic Systems, vol. 23, no. 2-4, pages 147–163, 1998. (Cited on page 44.)
- [Chen 2000] Wen-Hua Chen, Donald J. Ballance, Peter J. Gawthrop and John O’Reilly. *A nonlinear disturbance observer for robotic manipulators*. IEEE Transactions on Industrial Electronics, vol. 47, no. 4, pages 932–938, 2000. (Cited on page 54.)
- [Chen 2012] Jie Chen and Ron J. Patton. Robust model-based fault diagnosis for dynamic systems, volume 3. Springer Science & Business Media, 2012. (Cited on page 53.)
- [Chen 2016] Wen-Hua Chen, Jun Yang, Lei Guo and Shihua Li. *Disturbance-observer-based control and related methods – An overview*. IEEE Transactions on Industrial Electronics, vol. 63, no. 2, pages 1083–1095, 2016. (Cited on page 54.)

- [Cho 2012] Chang-Nho Cho, Joon-Hong Kim, Young-Loul Kim, Jae-Bok Song and Jin-Ho Kyung. *Collision Detection Algorithm to Distinguish Between Intended Contact and Unexpected Collision*. *Advanced Robotics*, vol. 26, no. 16, pages 1825–1840, 2012. (Cited on pages 128 and 129.)
- [Civil 1988] Ian D. Civil and C. William Schwab. *The Abbreviated Injury Scale, 1985 revision: a condensed chart for clinical use*. *The Journal of Trauma*, vol. 28, no. 1, pages 87–90, 1988. (Cited on page 11.)
- [De Luca 2003] Alessandro De Luca and Raffaella Mattone. *Actuator failure detection and isolation using generalized momenta*. In *IEEE International Conference on Robotics and Automation (ICRA)*, volume 1, pages 634–639, 2003. (Cited on page 54.)
- [De Luca 2004] Alessandro De Luca and Raffaella Mattone. *An adapt-and-detect actuator FDI scheme for robot manipulators*. In *IEEE International Conference on Robotics and Automation (ICRA)*, volume 5, pages 4975–4980, 2004. (Cited on page 56.)
- [De Luca 2006] Alessandro De Luca, Alin Albu-Schäffer, Sami Haddadin and Gerd Hirzinger. *Collision detection and safe reaction with the DLR-III lightweight manipulator arm*. In *IEEE/RSJ International Conference on Intelligent Robots and Systems (IROS)*, pages 1623–1630, 2006. (Cited on pages xvii, 18, 20, 33, 53, 87, 128 and 129.)
- [De Luca 2007] Alessandro De Luca, Dierk Schroder and Michael Thummel. *An acceleration-based state observer for robot manipulators with elastic joints*. In *IEEE International Conference on Robotics and Automation (ICRA)*, pages 3817–3823, 2007. (Cited on page 43.)
- [De Luca 2008] Alessandro De Luca and Lorenzo Ferrajoli. *Exploiting robot redundancy in collision detection and reaction*. In *IEEE/RSJ International Conference on Intelligent Robots and Systems (IROS)*, pages 3299–3305, 2008. (Cited on page 18.)
- [De Luca 2012] Alessandro De Luca and Fabrizio Flacco. *Integrated control for pHRI: Collision avoidance, detection, reaction and collaboration*. In *IEEE RAS & EMBS International Conference on Biomedical Robotics and Biomechatronics (BioRob)*, pages 288–295, 2012. (Cited on page 18.)
- [De Luca 2016] Alessandro De Luca and Wayne J. Book. *Robots with flexible elements*. In *Springer Handbook of Robotics*, pages 243–282. Springer, 2016. (Cited on pages 31 and 32.)
- [Desmoulin 2011] Geoffrey T. Desmoulin and Gail S. Anderson. *Method to investigate contusion mechanics in living humans*. *Journal of Forensic Biomechanics*, vol. 2, 2011. (Cited on page 12.)
- [Dhaouadi 2003] Rached Dhaouadi, Fathi H. Ghorbel and Prasanna S. Gandhi. *A new dynamic model of hysteresis in harmonic drives*. *IEEE Transactions on Industrial Electronics*, vol. 50, no. 6, pages 1165–1171, Dec 2003. (Cited on page 33.)

- [Dimeas 2015] Fotios Dimeas, Luis David Avendaño-Valencia and Nikos Aspragathos. *Human-robot collision detection and identification based on fuzzy and time series modelling*. *Robotica*, vol. 33, no. 9, pages 1886–1898, 2015. (Cited on page 56.)
- [Ding 2008] Steven X. Ding. *Model-based fault diagnosis techniques: design schemes, algorithms, and tools*. Springer Science & Business Media, 2008. (Cited on page 53.)
- [Dixon 2000] Warren E. Dixon, Ian D. Walker, Darren M. Dawson and John P. Hartranft. *Fault detection for robot manipulators with parametric uncertainty: A prediction-error-based approach*. *IEEE Transactions on Robotics and Automation*, vol. 16, no. 6, pages 689–699, 2000. (Cited on pages 56 and 69.)
- [Elfes 1990] Alberto Elfes. *Occupancy grids: A stochastic spatial representation for active robot perception*. In *Conference on Uncertainty in AI*, volume 2929, page 6, 1990. (Cited on page 36.)
- [FANUC 2018] FANUC. *Collaborative robot CR-35iA*, 2018. <https://www.fanuc.eu/fr/en/robots/robot-filter-page/collaborative-robots/collaborative-cr35ia>. (Cited on page 17.)
- [Fichera 2017] Francesco Fichera and Mathieu Grossard. *On the modeling and identification of stiffness in cable-based mechanical transmissions for robot manipulators*. *Mechanism and Machine Theory*, vol. 108, pages 176–190, 2017. (Cited on page 33.)
- [Flacco 2011] Fabrizio Flacco, Alessandro De Luca, Irene Sardellitti and Nikos G. Tsagarakis. *Robust estimation of variable stiffness in flexible joints*. In *IEEE/RSJ International Conference on Intelligent Robots and Systems (IROS)*, pages 4026–4033, 2011. (Cited on page 38.)
- [Flacco 2012a] Fabrizio Flacco, Torsten Kröger, Alessandro De Luca and Oussama Khatib. *A depth space approach to human-robot collision avoidance*. In *IEEE International Conference on Robotics and Automation (ICRA)*, pages 338–345, 2012. (Cited on page 15.)
- [Flacco 2012b] Fabrizio Flacco, Alessandro De Luca, Irene Sardellitti and Nikos G. Tsagarakis. *On-line estimation of variable stiffness in flexible robot joints*. *The International Journal of Robotics Research*, vol. 31, no. 13, pages 1556–1577, 2012. (Cited on page 33.)
- [Fostec & Company 2019] Fostec & Company. *Industrie 4.0*, 2019. <https://www.fostec.com/en/competences/digitalisation-strategy/industry-4-0/>. (Cited on pages v and 4.)
- [Frank 1997] Paul M. Frank and Xianchun Ding. *Survey of robust residual generation and evaluation methods in observer-based fault detection systems*. *Journal of Process Control*, vol. 7, no. 6, pages 403–424, 1997. (Cited on page 54.)
- [Garrec 2010] Phillipe Garrec. *Screw and Cable Actuators (SCS) and Their Applications to Force Feedback Teleoperation, Exoskeleton and Anthropomorphic Robotics*. In *Robotics 2010 Current and Future Challenges*. InTech, 2010. (Cited on pages 18 and 169.)

- [Gautier 1988] Maxime Gautier and Wisama Khalil. *On the identification of the inertial parameters of robots*. In IEEE Conference on Decision and Control (CDC), volume 3, pages 2264–2269, Dec 1988. (Cited on page 40.)
- [Gautier 1990] Maxime Gautier and Wisama Khalil. *Direct calculation of minimum set of inertial parameters of serial robots*. IEEE Transactions on Robotics and Automation, vol. 6, no. 3, pages 368–373, Jun 1990. (Cited on page 39.)
- [Gautier 2001] Maxime Gautier and Philippe Poignet. *Extended Kalman filtering and weighted least squares dynamic identification of robot*. Control Engineering Practice, vol. 9, no. 12, pages 1361 – 1372, 2001. (Cited on page 41.)
- [Gautier 2013a] Maxime Gautier and Sébastien Briot. *Dynamic parameter identification of a 6 DOF industrial robot using power model*. In IEEE International Conference on Robotics and Automation (ICRA), pages 2914–2920, May 2013. (Cited on page 40.)
- [Gautier 2013b] Maxime Gautier, Alexandre Janot and Pierre-Olivier Vandanjon. *A new closed-loop output error method for parameter identification of robot dynamics*. IEEE Transactions on Control Systems Technology, vol. 21, no. 2, pages 428–444, 2013. (Cited on page 38.)
- [Geffard 2000] Franck Geffard, Claude Andriot, Alain Micaelli and Guillaume Morel. *On the use of a base force/torque sensor in teleoperation*. In IEEE International Conference on Robotics and Automation (ICRA), volume 3, pages 2677–2683, 2000. (Cited on page 18.)
- [Geravand 2013] Milad Geravand, Fabrizio Flacco and Alessandro De Luca. *Human-robot physical interaction and collaboration using an industrial robot with a closed control architecture*. In IEEE International Conference on Robotics and Automation (ICRA), pages 4000–4007, 2013. (Cited on pages 53, 129, 131 and 135.)
- [Golz 2015] Saskia Golz, Christian Osendorfer and Sami Haddadin. *Using tactile sensation for learning contact knowledge: Discriminate collision from physical interaction*. In IEEE International Conference on Robotics and Automation (ICRA), pages 3788–3794, May 2015. (Cited on page 130.)
- [Haddadin 2007] Sami Haddadin, Alin Albu-Schäffer and Gerd Hirzinger. *Safety Evaluation of Physical Human-Robot Interaction via Crash-Testing*. In Robotics: Science and Systems, volume 3, pages 217–224, 2007. (Cited on page 11.)
- [Haddadin 2008a] Sami Haddadin, Alin Albu-Schäffer, Alessandro De Luca and Gerd Hirzinger. *Collision detection and reaction: A contribution to safe physical human-robot interaction*. In IEEE/RSJ International Conference on Intelligent Robots and Systems (IROS), pages 3356–3363, 2008. (Cited on pages 18, 53 and 128.)
- [Haddadin 2008b] Sami Haddadin, Alin Albu-Schäffer, Mirko Frommberger and Gerd Hirzinger. *The role of the robot mass and velocity in physical human-robot interaction - Part II: Constrained blunt impacts*. In IEEE International Conference on Robotics and Automation (ICRA), pages 1339–1345, May 2008. (Cited on pages 11 and 16.)

- [Haddadin 2008c] Sami Haddadin, Alin Albu-Schäffer and Gerd Hirzinger. *The role of the robot mass and velocity in physical human-robot interaction - Part I: Non-constrained blunt impacts*. In IEEE International Conference on Robotics and Automation (ICRA), pages 1331–1338, May 2008. (Cited on pages 11 and 16.)
- [Haddadin 2009] Sami Haddadin, Alin Albu-Schäffer and Gerd Hirzinger. *Requirements for safe robots: Measurements, analysis and new insights*. The International Journal of Robotics Research, vol. 28, no. 11-12, pages 1507–1527, 2009. (Cited on pages 10 and 11.)
- [Haddadin 2010a] Sami Haddadin, Alin Albu-Schäffer, Oliver Eiberger and Gerd Hirzinger. *New insights concerning intrinsic joint elasticity for safety*. In IEEE/RSJ International Conference on Intelligent Robots and Systems (IROS), pages 2181–2187, 2010. (Cited on page 16.)
- [Haddadin 2010b] Sami Haddadin, Alin Albu-Schäffer and Gerd Hirzinger. *Safety analysis for a human-friendly manipulator*. International Journal of Social Robotics, vol. 2, no. 3, pages 235–252, 2010. (Cited on page 11.)
- [Haddadin 2012] Sami Haddadin, Simon Haddadin, Augusto Khoury, Tim Rokahr, Sven Parusel, Rainer Burgkart, Antonio Bicchi and Alin Albu-Schäffer. *On making robots understand safety: Embedding injury knowledge into control*. The International Journal of Robotics Research, vol. 31, no. 13, pages 1578–1602, 2012. (Cited on page 11.)
- [Haddadin 2013] Sami Haddadin. *Towards safe robots: Approaching asimov’s 1st law*, volume 90. Springer, 2013. (Cited on pages v, 10, 11 and 12.)
- [Haddadin 2017] Sami Haddadin, Alessandro De Luca and Alin Albu-Schäffer. *Robot collisions: A survey on detection, isolation, and identification*. IEEE Transactions on Robotics, vol. 33, no. 6, pages 1292–1312, 2017. (Cited on pages v, xvi, xvii, 19, 20, 53, 54 and 87.)
- [Hägele 2002] Martin Hägele, Walter Schaaf and Evert Helms. *Robot assistants at manual workplaces: Effective co-operation and safety aspects*. In International Symposium on Robotics (ISR), volume 7, 2002. (Cited on pages v and 3.)
- [Hamon 2010] Pauline Hamon, Maxime Gautier and Philippe Garrec. *Dynamic identification of robots with a dry friction model depending on load and velocity*. In IEEE/RSJ International Conference on Intelligent Robots and Systems (IROS), pages 6187–6193, 2010. (Cited on page 30.)
- [Helms 2002] Evert Helms, Rolf Dieter Schraft and Martin Hägele. *rob@work: Robot assistant in industrial environments*. In IEEE International Workshop on Robot and Human Interactive Communication, pages 399–404, 2002. (Cited on pages v and 6.)
- [Hu 2018] Jin Hu and Rong Xiong. *Contact Force Estimation for Robot Manipulator Using Semiparametric Model and Disturbance Kalman Filter*. IEEE Transactions on Industrial Electronics, vol. 65, no. 4, pages 3365–3375, 2018. (Cited on page 56.)

- [IEC 60204-1: 2016] IEC 60204-1: *Safety of machinery – Electrical equipment of machines – Part 1: General requirements*. Standard, International Electrotechnical Commission (IEC), 2016. (Cited on page 8.)
- [ISO 10218-1: 2011] ISO 10218-1: *Robots and robotic devices – Safety requirements for industrial robots – Part 1: Robots*. Standard, International Organization for Standardization (ISO), 2011. (Cited on pages ix, 8 and 9.)
- [ISO 10218-2: 2011] ISO 10218-2: *Robots and robotic devices – Safety requirements for industrial robots – Part 2: Robot systems and integration*. Standard, International Organization for Standardization (ISO), 2011. (Cited on pages ix, 8 and 9.)
- [ISO 12100: 2010] ISO 12100: *Safety of machinery – General principles for design – Risk assessment and risk reduction*. Standard, International Organization for Standardization (ISO), 2010. (Cited on page 8.)
- [ISO 13850: 2015] ISO 13850: *Safety of machinery – Emergency stop function – Principles for design*. Standard, International Organization for Standardization (ISO), 2015. (Cited on page 8.)
- [ISO 13855: 2010] ISO 13855: *Safety of machinery – Positioning of safeguards with respect to the approach speeds of parts of the human body*. Standard, International Organization for Standardization (ISO), 2010. (Cited on page 8.)
- [ISO 8373: 2012] ISO 8373: *Robots and robotic devices – Vocabulary*. Standard, International Organization for Standardization (ISO), 2012. (Cited on page 2.)
- [ISO/TS 15066: 2016] ISO/TS 15066: *Robots and robotic devices – Collaborative robots*. Standard, International Organization for Standardization (ISO), 2016. (Cited on pages x, 12, 13, 123 and 167.)
- [Janabi-Sharifi 2000] Farrokh Janabi-Sharifi, Vincent Hayward and Chung-Shin J. Chen. *Discrete-time adaptive windowing for velocity estimation*. IEEE Transactions on Control Systems Technology, vol. 8, no. 6, pages 1003–1009, 2000. (Cited on page 44.)
- [Janot 2011] Alexandre Janot, Maxime Gautier, Anthony Jubien and Pierre-Olivier Vandanjon. *Experimental joint stiffness identification depending on measurements availability*. In IEEE Conference on Decision and Control (CDC) and European Control Conference (ECC), pages 5112–5117, 2011. (Cited on page 38.)
- [Jaulin 2001] Luc Jaulin. *Applied interval analysis, volume 1*. Springer Science & Business Media, 2001. (Cited on page 36.)
- [Jeon 2010] Soo Jeon. *State estimation based on kinematic models considering characteristics of sensors*. In IEEE American Control Conference (ACC), pages 640–645, 2010. (Cited on page 44.)

- [Jiang 2012] Allen Jiang, Joao Bimbo, Simon Goulder, Hongbin Liu, Xiaojing Song, Prokar Dasgupta, Kaspar Althoefer and Thrishantha Nanayakkara. *Adaptive grip control on an uncertain object*. In IEEE/RSJ International Conference on Intelligent Robots and Systems (IROS), pages 1161–1166, Oct 2012. (Cited on page 36.)
- [Johnson 2004] Oliver Thomas Johnson. *Information theory and the central limit theorem*. World Scientific, 2004. (Cited on page 36.)
- [Joseph 2018] Lucas Joseph, Vincent Padois and Guillaume Morel. *Experimental validation of an energy constraint for a safer collaboration with robots*. In International Symposium on Experimental Robotics (ISER), 2018. (Cited on page 15.)
- [Judd 1990] Robert P. Judd and Al B. Knasinski. *A technique to calibrate industrial robots with experimental verification*. IEEE Transactions on Robotics and Automation, vol. 6, no. 1, pages 20–30, 1990. (Cited on page 49.)
- [Jung 2006] J. Jung, J. Lee and K. Huh. *Robust contact force estimation for robot manipulators in three-dimensional space*. Institution of Mechanical Engineers, Part C: Journal of Mechanical Engineering Science, vol. 220, no. 9, pages 1317–1327, 2006. (Cited on page 56.)
- [Jung 2014] Byung-jin Jung, Ja Choon Koo, Hyouk Ryeol Choi and Hyungpil Moon. *Human-robot collision detection under modeling uncertainty using frequency boundary of manipulator dynamics*. Journal of Mechanical Science and Technology, vol. 28, no. 11, pages 4389–4395, 2014. (Cited on page 69.)
- [Karlsson 2018] Martin Karlsson, Anders Robertsson and Rolf Johansson. *Detection and Control of Contact Force Transients in Robotic Manipulation without a Force Sensor*. In IEEE International Conference on Robotics and Automation (ICRA), pages 21–25, May 2018. (Cited on pages 130 and 141.)
- [Kermani 2007] Mehrdad R. Kermani, Rajnikant V. Patel and Mehrdad Moallem. *Friction identification and compensation in robotic manipulators*. IEEE Transactions on Instrumentation and Measurement, vol. 56, no. 6, pages 2346–2353, 2007. (Cited on page 38.)
- [Khalil 2000a] Wisama Khalil, Sébastien Besnard and Philippe Lemoine. *Comparison study of the geometric parameters calibration methods*. International Journal of Robotics and Automation, vol. 15, no. 2, pages pp–56, 2000. (Cited on page 50.)
- [Khalil 2000b] Wisama Khalil and Maxime Gautier. *Modeling of mechanical systems with lumped elasticity*. In IEEE International Conference on Robotics and Automation (ICRA), volume 4, pages 3964–3969, 2000. (Cited on page 31.)
- [Khalil 2002] Wisama Khalil and Sébastien Besnard. *Geometric calibration of robots with flexible joints and links*. Journal of Intelligent and Robotic Systems, vol. 34, no. 4, pages 357–379, 2002. (Cited on page 50.)

- [Khalil 2004] Wisama Khalil and Etienne Dombre. Modeling, identification and control of robots. Butterworth-Heinemann, 2004. (Cited on pages 27, 28, 30, 37, 39, 42, 50, 170 and 172.)
- [Khalil 2010] Wisama Khalil. *Dynamic modeling of robots using recursive Newton-Euler techniques*. In International Conference on Informatics in Control, Automation and Robotics (ICINCO), 2010. (Cited on page 28.)
- [Kilic 2010] Ergin Kilic, Ozgur Baser, Melik Dolen and E. Ilhan Konukseven. *An enhanced adaptive windowing technique for velocity and acceleration estimation using incremental position encoders*. In IEEE International Conference on Signals and Electronic Systems (ICSSES), pages 61–64, 2010. (Cited on page 44.)
- [Kim 2001] Seong-Hwan Kim, Tae-Sik Park, Ji-Yoon Yoo and Gwi-Tae Park. *Speed-sensorless vector control of an induction motor using neural network speed estimation*. IEEE Transactions on Industrial Electronics, vol. 48, no. 3, pages 609–614, Jun 2001. (Cited on page 44.)
- [Kirchhoff 2018] Jérôme Kirchhoff and Oskar von Stryk. *Velocity estimation for ultra lightweight tendon driven series elastic robots*. IEEE Robotics and Automation Letters, 2018. (Cited on page 44.)
- [Klir 1995] George J. Klir and Baozung Yuan. Fuzzy sets and fuzzy logic: theory and applications, volume 574. Prentice Hall PTR New Jersey, 1995. (Cited on page 35.)
- [Kouris 2016] Alexandros Kouris, Fotios Dimeas and Nikos Aspragathos. *Contact distinction in human-robot cooperation with admittance control*. In IEEE International Conference on Systems, Man, and Cybernetics (SMC), pages 001951–001956, Oct 2016. (Cited on pages vii, 128 and 129.)
- [Kouris 2018] Alexandros Kouris, Fotios Dimeas and Nikos Aspragathos. *A Frequency Domain Approach for Contact Type Distinction in Human-Robot Collaboration*. IEEE Robotics and Automation Letters, vol. 3, no. 2, pages 720–727, April 2018. (Cited on pages vii, xxii, 129, 130, 131, 157 and 165.)
- [Krizhevsky 2012] Alex Krizhevsky, Ilya Sutskever and Geoffrey E. Hinton. *ImageNet Classification with Deep Convolutional Neural Networks*. In Neural Information Processing Systems (NIPS), 2012. (Cited on page 130.)
- [Kröse 1993] Ben Kröse, Ben Krose, Patrick van der Smagt and Patrick Smagt. An introduction to neural networks. Citeseer, 1993. (Cited on page 133.)
- [KUKA 2017] KUKA. *LBR iiwa*, 2017. <https://www.kuka.com/en-us/products/robotics-systems/industrial-robots/lbr-iiwa>. (Cited on page 17.)
- [Kulić 2005] Dana Kulić and Elizabeth A. Croft. *Real-time safety for human-robot interaction*. In IEEE International Conference on Advanced Robotics (ICAR), pages 719–724, July 2005. (Cited on page 15.)

- [Labarrère 1993] Marc Labarrère, Jean-Pierre Krief and Bernard Gimonet. *Le filtrage et ses applications*. Cepadues-editions, 1993. (Cited on page 72.)
- [Lee 2009] Hyung-Jik Lee and Seul Jung. *Gyro sensor drift compensation by Kalman filter to control a mobile inverted pendulum robot system*. In IEEE International Conference on Industrial Technology, pages 1–6, 2009. (Cited on page 43.)
- [Leonard 1990] James Leonard and M.A. Kramer. *Improvement of the backpropagation algorithm for training neural networks*. Computers & Chemical Engineering, vol. 14, no. 3, pages 337 – 341, 1990. (Cited on page 138.)
- [Li 2016] Miao Li, Kaiyu Hang, Danica Kragic and Aude Billard. *Dexterous grasping under shape uncertainty*. Robotics and Autonomous Systems, vol. 75, pages 352 – 364, 2016. (Cited on page 36.)
- [Lightcap 2010] Chris A Lightcap and Scott A Banks. *An extended Kalman filter for real-time estimation and control of a rigid-link flexible-joint manipulator*. IEEE Transactions on Control Systems Technology, vol. 18, no. 1, pages 91–103, 2010. (Cited on page 44.)
- [Linderoth 2013] Magnus Linderoth, Andreas Stolt, Anders Robertsson and Rolf Johansson. *Robotic force estimation using motor torques and modeling of low velocity friction disturbances*. In IEEE/RSJ International Conference on Intelligent Robots and Systems (IROS), pages 3550–3556, 2013. (Cited on pages 55 and 57.)
- [Lippmann 1987] Richard P. Lippmann. *An introduction to computing with neural nets*. IEEE ASSP Magazine, vol. 4, no. 2, pages 4–22, Apr 1987. (Cited on page 133.)
- [Liu 2017] Yuqiang Liu, Chunlin Tan, Yang Zhao, Liu Huawei and Liu Yongjian. *Nonlinear attributes modeling and analysis of harmonic drive manipulator joint*. In IEEE International Conference on Control, Automation and Robotics (ICCAR), pages 256–264, April 2017. (Cited on page 33.)
- [Lu 2005] Shujun Lu, Jae Heon Chung and Steven A Velinsky. *Human-robot collision detection and identification based on wrist and base force/torque sensors*. In IEEE International Conference on Robotics and Automation (ICRA), pages 3796–3801, 2005. (Cited on pages 18, 132 and 158.)
- [Maddern 2016] Will Maddern and Paul Newman. *Real-time probabilistic fusion of sparse 3D LIDAR and dense stereo*. In IEEE/RSJ International Conference on Intelligent Robots and Systems (IROS), pages 2181–2188, 2016. (Cited on page 15.)
- [Mainprice 2013] Jim Mainprice and Dmitry Berenson. *Human-robot collaborative manipulation planning using early prediction of human motion*. In IEEE/RSJ International Conference on Intelligent Robots and Systems (IROS), pages 299–306, 2013. (Cited on page 15.)
- [Makarov 2012] Maria Makarov, Mathieu Grossard, Pedro Rodriguez-Ayerbe and Didier Dumur. *A frequency-domain approach for flexible-joint robot modeling and identification*. IFAC Proceedings Volumes, vol. 45, no. 16, pages 583–588, 2012. (Cited on page 38.)

- [Makarov 2014] Maria Makarov, Alex Caldas, Mathieu Grossard, Pedro Rodriguez-Ayerbe and Didier Dumur. *Adaptive filtering for robust proprioceptive robot impact detection under model uncertainties*. IEEE/ASME Transactions on Mechatronics, vol. 19, no. 6, pages 1917–1928, 2014. (Cited on page 56.)
- [Mansfeld 2017] Nico Mansfeld, Badis Djellab, Jaime Raldúa Veuthey, Fabian Beck, Christian Ott and Sami Haddadin. *Improving the performance of biomechanically safe velocity control for redundant robots through reflected mass minimization*. In IEEE/RSJ International Conference on Intelligent Robots and Systems (IROS), pages 5390–5397, 2017. (Cited on page 16.)
- [Mansfeld 2018] Nico Mansfeld, Mazin Hamad, Marvin Becker, Antonio Gonzales Marin and Sami Haddadin. *Safety map: A unified representation for biomechanics impact data and robot instantaneous dynamic properties*. IEEE Robotics and Automation Letters, vol. 3, no. 3, pages 1880–1887, 2018. (Cited on page 14.)
- [Marvel 2015] Jeremy A. Marvel, Joe Falco and Ilari Marstio. *Characterizing task-based human-robot collaboration safety in manufacturing*. IEEE Transactions on Systems, Man, and Cybernetics: Systems, vol. 45, no. 2, pages 260–275, 2015. (Cited on page 9.)
- [Matthias 2016] Björn Matthias and Thomas Reisinger. *Example application of ISO/TS 15066 to a collaborative assembly scenario*. In International Symposium on Robotics (ISR), pages 1–5. VDE, 2016. (Cited on page 13.)
- [Meguenani 2016] Anis Meguenani, Vincent Padois, Jimmy Da Silva, Antoine Hoarau and Philippe Bidaud. *Energy based control for safe human-robot physical interaction*. In International Symposium on Experimental Robotics (ISER), pages 809–818. Springer, 2016. (Cited on page 15.)
- [Melia 2015] Michael Melia, Martin Schmidt, Britta Geissler, Jochem König, Ulrike Krahn, Hans Jürgen Ottersbach, Stephan Letzel and Axel Muttray. *Measuring mechanical pain: the refinement and standardization of pressure pain threshold measurements*. Behavior research methods, vol. 47, no. 1, pages 216–227, 2015. (Cited on page 12.)
- [Mendel 2001] Jerry M. Mendel. Uncertain rule-based fuzzy logic systems: introduction and new directions. Prentice Hall PTR Upper Saddle River, 2001. (Cited on page 35.)
- [Merlet 2004] J.-P. Merlet. *Solving the forward kinematics of a Gough-type parallel manipulator with interval analysis*. The International Journal of Robotics Research, vol. 23, no. 3, pages 221–235, 2004. (Cited on page 36.)
- [Merry 2010] Roel J.E. Merry, Marinus J.G. Van de Molengraft and Maarten Steinbuch. *Velocity and acceleration estimation for optical incremental encoders*. Mechatronics, vol. 20, no. 1, pages 20–26, 2010. (Cited on page 44.)
- [Mikhel 2018] Stanislav Mikhel, Dmitry Popov and Alexandr Klimchik. *Collision Driven Multi Scenario Approach for Human Collaboration with Industrial Robot*. In International

- Conference on Mechatronics and Robotics Engineering, pages 78–84. ACM, 2018. (Cited on page 128.)
- [Min 2019] Feiyan Min, Gao Wang and Ning Liu. *Collision Detection and Identification on Robot Manipulators Based on Vibration Analysis*. *Sensors*, vol. 19, no. 5, 2019. (Cited on page 18.)
- [Ministère du travail 2017] Ministère du travail. *Pour la mise en œuvre des applications collaboratives robotisées*, 2017. https://travail-emploi.gouv.fr/IMG/pdf/guide_de_prevention_25_aout_2017.pdf. (Cited on pages v and 6.)
- [Mittendorfer 2015] Philipp Mittendorfer, Eiichi Yoshida and Gordon Cheng. *Realizing whole-body tactile interactions with a self-organizing, multi-modal artificial skin on a humanoid robot*. *Advanced Robotics*, vol. 29, no. 1, pages 51–67, 2015. (Cited on page 18.)
- [Møller 1990] Martin Møller. *A Scaled Conjugate Gradient Algorithm for Fast Supervised Learning*. DAIMI Report Series, vol. 19, no. 339, 1990. (Cited on page 138.)
- [Moore 1979] Ramon E. Moore. *Methods and applications of interval analysis*, volume 2. Siam, 1979. (Cited on page 36.)
- [Morinaga 2003] Shinya Morinaga and Kazuhiro Kosuge. *Collision detection system for manipulator based on adaptive impedance control law*. In *IEEE International Conference on Robotics and Automation (ICRA)*, volume 1, pages 1080–1085, 2003. (Cited on page 56.)
- [Nakamoto 2017] Hideichi Nakamoto and Nobuto Matsuhira. *Safety evaluation method of robot arm considering energy of contact*. In *IEEE International Conference on Advanced Robotics (ICAR)*, pages 438–443, 2017. (Cited on page 14.)
- [National Science Foundation 2019] National Science Foundation. *Cyber-Physical Systems (CPS)*, 2019. <https://www.nsf.gov/pubs/2019/nsf19553/nsf19553.pdf>. (Cited on page 4.)
- [Oberer 2007] Susanne Oberer and Rolf Dieter Schraft. *Robot-dummy crash tests for robot safety assessment*. In *IEEE International Conference on Robotics and Automation (ICRA)*, pages 2934–2939, 2007. (Cited on page 11.)
- [Ogorodnikova 2009] Olesya Ogorodnikova. *How safe the human-robot coexistence is? Theoretical presentation*. *Acta Polytechnica Hungarica*, vol. 6, no. 4, pages 51–74, 2009. (Cited on page 11.)
- [Olsson 1998] Henrik Olsson, Karl Johan Åström, Carlos Canudas De Wit, Magnus Gäfvert and Pablo Lischinsky. *Friction models and friction compensation*. *European Journal of Control*, vol. 4, no. 3, pages 176–195, 1998. (Cited on page 30.)
- [Park 2011] Jung-Jun Park, Sami Haddadin, Jae-Bok Song and Alin Albu-Schäffer. *Designing optimally safe robot surface properties for minimizing the stress characteristics of human-robot collisions*. In *IEEE International Conference on Robotics and Automation (ICRA)*, pages 5413–5420, 2011. (Cited on page 16.)

- [Parusel 2011] Sven Parusel, Sami Haddadin and Alin Albu-Schäffer. *Modular state-based behavior control for safe human-robot interaction: A lightweight control architecture for a lightweight robot*. In IEEE International Conference on Robotics and Automation (ICRA), pages 4298–4305, 2011. (Cited on page 18.)
- [Petrov 1995] Valentin V. Petrov. *Limit theorems of probability theory: sequences of independent random variables*. Technical report, Oxford, New York, 1995. (Cited on page 36.)
- [Pham 2001] Minh Tu Pham, Maxime Gautier and Philippe Poignet. *Identification of joint stiffness with bandpass filtering*. In IEEE International Conference on Robotics and Automation (ICRA), volume 3, pages 2867–2872, 2001. (Cited on page 38.)
- [Popov 2017] Dmitry Popov, Alexandr Klimchik and Nikolaos Mavridis. *Collision detection, localization & classification for industrial robots with joint torque sensors*. In IEEE International Symposium on Robot and Human Interactive Communication (RO-MAN), pages 838–843, 2017. (Cited on pages 56, 130 and 132.)
- [Povse 2010] Borut Povse, Darko Koritnik, Tadej Bajd and Marko Munih. *Correlation between impact-energy density and pain intensity during robot-man collision*. In IEEE RAS & EMBS International Conference on Biomedical Robotics and Biomechatronics (BioRob), pages 179–183, 2010. (Cited on page 12.)
- [Pratt 1995] Gill A. Pratt and Matthew M. Williamson. *Series elastic actuators*. In IEEE/RSJ International Conference on Intelligent Robots and Systems (IROS), volume 1, pages 399–406, 1995. (Cited on page 16.)
- [Press 2007] W.H. Press, S.A. Teukolsky, W.T. Vetterling and B.P. Flannery. *Confidence limits on estimated model parameters*. Numerical Recipes: The Art of Scientific Computing. Cambridge University Press, Cambridge, pages 807–818, 2007. (Cited on page 64.)
- [Presse 1993] C. Presse and Maxime Gautier. *New criteria of exciting trajectories for robot identification*. In IEEE International Conference on Robotics and Automation (ICRA), pages 907–912 vol.3, May 1993. (Cited on page 41.)
- [Puglisi 2015] Lisandro José Puglisi. *On the velocity and acceleration estimation from discrete time-position signal of linear encoders*. Journal of Control Engineering and Applied Informatics, vol. 17, no. 3, pages 30–40, 2015. (Cited on page 45.)
- [Rethink Robotics 2018] Rethink Robotics. *Sawyer – High performance collaborative robot*, 2018. <https://www.rethinkrobotics.com/sawyer/>. (Cited on page 17.)
- [Robotiq 2018] Robotiq. *COBOTS EBOOK*, 2018. <https://blog.robotiq.com/collaborative-robot-ebook>. (Cited on page 17.)
- [Rodriguez 2010] Alberto Rodriguez, David Bourne, Mathew Mason, Gregory F. Rossano and JianJun Wang. *Failure detection in assembly: Force signature analysis*. In IEEE Conference on Automation Science and Engineering (CASE), pages 210–215, 2010. (Cited on pages 56 and 165.)

- [Rosenstrauch 2017] Martin J. Rosenstrauch and Jörg Krüger. *Safe human-robot-collaboration-introduction and experiment using ISO/TS 15066*. In IEEE International Conference on Control, Automation and Robotics (ICCAR), pages 740–744, 2017. (Cited on page 13.)
- [Roy 2011] Christopher J. Roy and William L. Oberkampf. *A comprehensive framework for verification, validation, and uncertainty quantification in scientific computing*. Computer methods in applied Mechanics and Engineering, vol. 200, no. 25-28, pages 2131–2144, 2011. (Cited on page 34.)
- [Schmidhuber 2015] Jürgen Schmidhuber. *Deep learning in neural networks: An overview*. Neural Networks, vol. 61, pages 85 – 117, 2015. (Cited on page 133.)
- [Shelley 1818] Mary Wollstonecraft Shelley. *Frankenstein*. Lackington, Allen & Co., 1818. (Cited on page 2.)
- [Smith 1990] Randall Smith, Matthew Self and Peter Cheeseman. *Estimating uncertain spatial relationships in robotics*. In Autonomous Robot Vehicles, pages 167–193. Springer, 1990. (Cited on page 36.)
- [Smith 2013] Ralph C. Smith. *Uncertainty quantification: theory, implementation, and applications*, volume 12. Siam, 2013. (Cited on page 34.)
- [Sneider 1996] H. Sneider and Paul M. Frank. *Observer-based supervision and fault detection in robots using nonlinear and fuzzy logic residual evaluation*. IEEE Transactions on Control Systems Technology, vol. 4, no. 3, pages 274–282, 1996. (Cited on pages v, 56 and 57.)
- [Song 2005] Zuoshi Song, Jianqiang Yi, Dongbin Zhao and Xinchun Li. *A computed torque controller for uncertain robotic manipulator systems: Fuzzy approach*. Fuzzy Sets and Systems, vol. 154, no. 2, pages 208 – 226, 2005. (Cited on page 35.)
- [Song 2013] Jae-Bok Song. *Collision detection algorithm robust to model uncertainty*. International Journal of Control, Automation and Systems, vol. 11, no. 4, pages 776–781, 2013. (Cited on pages v, 54 and 55.)
- [Sotoudehnejad 2012] Vahid Sotoudehnejad, Amir Takhmar, Mehrdad R. Kermani and Ilia G. Polushin. *Counteracting modeling errors for sensitive observer-based manipulator collision detection*. In IEEE/RSJ International Conference on Intelligent Robots and Systems (IROS), pages 4315–4320, 2012. (Cited on page 56.)
- [Sousa 2014] Cristóvão D. Sousa and Rui Cortesão. *Physical feasibility of robot base inertial parameter identification: A linear matrix inequality approach*. The International Journal of Robotics Research, vol. 33, no. 6, pages 931–944, 2014. (Cited on page 41.)
- [Spong 1987] Mark W. Spong. *Modeling and control of elastic joint robots*. Journal of Dynamic Systems, Measurement, and Control, vol. 109, no. 4, pages 310–318, 1987. (Cited on page 31.)
- [Spong 2006] Mark W. Spong, Seth Hutchinson and Mathukumalli Vidyasagar. *Robot modeling and control*, volume 3. Wiley New York, 2006. (Cited on page 28.)

- [Stolt 2012] Andreas Stolt, Magnus Linderöth, Anders Robertsson and Rolf Johansson. *Force controlled robotic assembly without a force sensor*. In IEEE International Conference on Robotics and Automation (ICRA), pages 1538–1543, 2012. (Cited on page 55.)
- [Stolt 2015] Andreas Stolt, Magnus Linderöth, Anders Robertsson and Rolf Johansson. *Detection of contact force transients in robotic assembly*. In IEEE International Conference on Robotics and Automation (ICRA), pages 962–968, 2015. (Cited on page 56.)
- [Suita 1995] Kazutsugu Suita, Yoji Yamada, Nuiro Tsuchida, Koji Imai, Hiroyasu Ikeda and Noboru Sugimoto. *A failure-to-safety "Kyozon" system with simple contact detection and stop capabilities for safe human-autonomous robot coexistence*. In IEEE International Conference on Robotics and Automation (ICRA), volume 3, pages 3089–3096, 1995. (Cited on page 11.)
- [Swevers 1997] Jan Swevers, Chris Ganseman, D. Bilgin Tükel, Joris De Schutter and Hendrik Van Brussel. *Optimal robot excitation and identification*. IEEE Transactions on Robotics and Automation, vol. 13, no. 5, pages 730–740, Oct 1997. (Cited on page 41.)
- [Swevers 2007] Jan Swevers, Walter Verdonck and Joris De Schutter. *Dynamic Model Identification for Industrial Robots*. IEEE Control Systems, vol. 27, no. 5, pages 58–71, Oct 2007. (Cited on page 44.)
- [Tan 2009] Jeffrey Too Chuan Tan, Feng Duan, Ye Zhang, Kei Watanabe, Ryu Kato and Tamio Arai. *Human-robot collaboration in cellular manufacturing: Design and development*. In IEEE/RSJ International Conference on Intelligent Robots and Systems (IROS), pages 29–34, Oct 2009. (Cited on page 15.)
- [Tu 2018] Xiao Tu, YunFei Zhou, Pu Zhao and Xin Cheng. *Modeling the Static Friction in a Robot Joint by Genetically Optimized BP Neural Network*. Journal of Intelligent & Robotic Systems, pages 1–13, 2018. (Cited on page 41.)
- [Unfallversicherung 2009] Deutsche Gesetzliche Unfallversicherung. *BG/BGIA risk assessment recommendations according to machinery directive, design of workplaces with collaborative robots*. Technical report, Report, 2009. (Cited on page 12.)
- [Universal Robots 2017] Universal Robots. *Collaborative robots from Universal Robots*, 2017. <https://www.universal-robots.com/products/>. (Cited on page 17.)
- [Van Damme 2011] Michaël Van Damme, Pieter Beyl, Bram Vanderborght, Victor Grosu, Ronald Van Ham, Innes Vanderniepen, Arnout Matthys and Dirk Lefeber. *Estimating robot end-effector force from noisy actuator torque measurements*. In IEEE International Conference on Robotics and Automation (ICRA), pages 1108–1113, 2011. (Cited on page 54.)
- [Vandanjon 1995] Pierre-Olivier Vandanjon, Maxime Gautier and P. Desbats. *Identification of robots inertial parameters by means of spectrum analysis*. In IEEE International Conference on Robotics and Automation (ICRA), volume 3, pages 3033–3038 vol.3, May 1995. (Cited on page 41.)

- [Vemula 2018] Bhanoday Vemula, Björn Matthias and Aftab Ahmad. *A design metric for safety assessment of industrial robot design suitable for power- and force-limited collaborative operation*. International Journal of Intelligent Robotics and Applications, pages 1–9, 2018. (Cited on pages 12, 13 and 16.)
- [Venkatasubramanian 2003] Venkat Venkatasubramanian, Raghunathan Rengaswamy, Surya N. Kavuri and Kewen Yin. *A review of process fault detection and diagnosis: Part III: Process history based methods*. Computers & chemical engineering, vol. 27, no. 3, pages 327–346, 2003. (Cited on page 53.)
- [Versace 1971] John Versace. *A review of the severity index*. Technical report, SAE Technical Paper, 1971. (Cited on page 11.)
- [Villagrossi 2013] Enrico Villagrossi, Nicola Pedrocchi, Federico Vicentini and Lorenzo Molinari Tosatti. *Optimal robot dynamics local identification using genetic-based path planning in workspace subregions*. In IEEE/ASME International Conference on Advanced Intelligent Mechatronics, pages 932–937, 2013. (Cited on page 38.)
- [Wagner 2018] Michael Wagner, Stefan Liu, Andrea Giusti and Matthias Althoff. *Interval-Arithmetic-Based Trajectory Scaling and Collision Detection for Robots with Uncertain Dynamics*. In IEEE International Conference on Robotic Computing (IRC), pages 41–48, 2018. (Cited on page 56.)
- [Wahrburg 2014] Arne Wahrburg, Stefan Zeiss, Björn Matthias and Hao Ding. *Contact force estimation for robotic assembly using motor torques*. In IEEE International Conference on Automation Science and Engineering (CASE), pages 1252–1257, 2014. (Cited on page 55.)
- [Wahrburg 2015a] Arne Wahrburg, Björn Matthias and Hao Ding. *Cartesian contact force estimation for robotic manipulators – A fault isolation perspective*. IFAC-PapersOnLine, vol. 48, no. 21, pages 1232–1237, 2015. (Cited on page 54.)
- [Wahrburg 2015b] Arne Wahrburg, Elena Morara, Gianluca Cesari, Björn Matthias and Hao Ding. *Cartesian contact force estimation for robotic manipulators using Kalman filters and the generalized momentum*. In IEEE International Conference on Automation Science and Engineering (CASE), pages 1230–1235, 2015. (Cited on pages 54 and 55.)
- [Wahrburg 2018] Arne Wahrburg, Johannes Bös, Kim D. Listmann, Fan Dai, Björn Matthias and Hao Ding. *Motor-Current-Based estimation of Cartesian contact forces and torques for robotic manipulators and its application to force control*. IEEE Transactions on Automation Science and Engineering, vol. 15, no. 2, pages 879–886, 2018. (Cited on pages xvii, 20, 55, 57, 58 and 74.)
- [Walker 1994] Ian D. Walker. *Impact configurations and measures for kinematically redundant and multiple armed robot systems*. IEEE Transactions on Robotics and Automation, vol. 10, no. 5, pages 670–683, Oct 1994. (Cited on page 27.)

- [Wallén 2008] Johanna Wallén. The history of the industrial robot. Linköping University Electronic Press, 2008. (Cited on pages [v](#) and [2](#).)
- [Wang 2018] Yiwei Wang, Yixuan Sheng, Ji Wang and Wenlong Zhang. *Optimal Collision-Free Robot Trajectory Generation Based on Time Series Prediction of Human Motion*. IEEE Robotics and Automation Letters, vol. 3, no. 1, pages 226–233, 2018. (Cited on page [15](#).)
- [Wernholt 2011] Erik Wernholt and Stig Moberg. *Nonlinear gray-box identification using local models applied to industrial robots*. Automatica, vol. 47, no. 4, pages 650–660, 2011. (Cited on page [38](#).)
- [Wolf 2016] Sebastian Wolf, Giorgio Grioli, Oliver Eiberger, Werner Friedl, Markus Grebenstein, Hannes Höppner, Etienne Burdet, Darwin G. Caldwell, Raffaella Carloni and Manuel G. Catalano. *Variable stiffness actuators: Review on design and components*. IEEE/ASME Transactions on Mechatronics, vol. 21, no. 5, pages 2418–2430, 2016. (Cited on page [16](#).)
- [Wu 2007] Weidong Wu and Singiresu S. Rao. *Uncertainty analysis and allocation of joint tolerances in robot manipulators based on interval analysis*. Reliability Engineering & System Safety, vol. 92, no. 1, pages 54 – 64, 2007. (Cited on page [36](#).)
- [Yamada 1997] Yoji Yamada, Yasuhiro Hirasawa, Shengyang Huang, Yoji Umetani and Kazutsugu Suita. *Human-robot contact in the safeguarding space*. IEEE/ASME Transactions on Mechatronics, vol. 2, no. 4, pages 230–236, 1997. (Cited on page [11](#).)
- [Yang 2000] Sheng-Ming Yang and Shuenn-Jenn Ke. *Performance evaluation of a velocity observer for accurate velocity estimation of servo motor drives*. IEEE Transactions on Industry Applications, vol. 36, no. 1, pages 98–104, Jan 2000. (Cited on page [44](#).)
- [Yusivar 1999] Feri Yusivar, Daisuke Hamada, Kenji Uchida, Shinji Wakao and Takashi Onuki. *A new method of motor speed estimation using fuzzy logic algorithm*. In IEEE International Conference on Electric Machines and Drives, pages 278–280, 1999. (Cited on page [44](#).)
- [Zube 2015] Angelika Zube. *Combined workspace monitoring and collision avoidance for mobile manipulators*. In IEEE Conference on Emerging Technologies & Factory Automation (ETFAs), pages 1–8, 2015. (Cited on page [14](#).)
- [Zwiener 2018] Adrian Zwiener, Christian Geckeler and Andreas Zell. *Contact Point Localization for Articulated Manipulators with Proprioceptive Sensors and Machine Learning*. In IEEE International Conference on Robotics and Automation (ICRA), pages 323–329, 2018. (Cited on page [132](#).)

List of Publications

International journal

N. Briquet-Kerestedjian, M. Makarov, M. Grossard, P. Rodriguez-Ayerbe. *Performance quantification of observer-based robot impact detection under modeling uncertainties*, International Journal of Intelligent Robotics and Applications (IJIRA), 2018.

International conferences

N. Briquet-Kerestedjian, A. Wahrburg, M. Grossard, M. Makarov, P. Rodriguez-Ayerbe. *Using Neural Networks for Classifying Human-Robot Contact Situations*, IEEE European Control Conference (ECC), Naples, Italy, June 2019.

N. Briquet-Kerestedjian, M. Makarov, M. Grossard, P. Rodriguez-Ayerbe. *Generalized Momentum based-Observer for Robot Impact Detection – Insights and Guidelines under Characterized Uncertainties*, IEEE Conference on Control Technology and Applications (CCTA), Hawaii, United-States of America, August 2017.

N. Briquet-Kerestedjian, M. Makarov, M. Grossard, P. Rodriguez-Ayerbe. *Stochastic observer design for robot impact detection based on inverse dynamic model under uncertainties*, International Federation of Automatic Control (IFAC), Toulouse, France, July 2017.

N. Briquet-Kerestedjian, M. Makarov, M. Grossard, P. Rodriguez-Ayerbe. *Quantifying the Uncertainties-Induced Errors in Robot Impact Detection Methods*, IEEE Industrial Electronics Society (IECON), Firenze, Italy, October 2016.

National communications

N. Briquet-Kerestedjian. *Stratégies pour la détection d'impact : application à l'interaction homme-robot sûre*, Journée Fédération Demeny-Vaucanson (FéDeV) 2017, oral presentation, Paris, France, November 2017, [link](#).

N. Briquet-Kerestedjian. *Stratégies adaptatives pour la détection d'impact : application à l'interaction homme-robot sûre*, GT3/GT6: Conception mécatronique pour l'interaction robot-environnement, oral presentation, Paris, France, January 2017, [link](#).

Patent

A. Wahburg, N. Briquet-Kerestedjian, M. Grossard, M. Makarov, P. Rodriguez-Ayerbe, P17456
Robot system and operation method.

Titre : Détection et classification d'impact pour l'interaction physique Homme-Robot sûre en présence d'incertitudes

Mots clés : Systèmes incertains, robots manipulateurs, détection de défaut, observateurs, filtrage adaptatif, réseaux de neurones.

Résumé : La problématique traitée dans cette thèse vise à développer une stratégie efficace de détection et de classification des impacts en présence d'incertitudes de modélisation du robot et de son environnement et en utilisant un nombre minimal de capteurs, notamment en l'absence de capteur d'effort.

La première partie de la thèse porte sur la détection d'un impact pouvant avoir lieu à n'importe quel endroit du bras robotique et à n'importe quel moment de sa trajectoire. Les méthodes de détection d'impacts sont généralement basées sur un modèle dynamique du système, ce qui les rend sujettes au compromis entre sensibilité de détection et robustesse aux incertitudes de modélisation. A cet égard, une méthodologie quantitative a d'abord été mise au point pour rendre explicite la contribution des erreurs induites par les incertitudes de modèle. Cette méthodologie a été appliquée à différentes stratégies de détection, basées soit sur une estimation directe du couple extérieur, soit sur l'utilisation d'observateurs de perturbation, dans le cas d'une modélisation parfaitement rigide ou à articulations flexibles. Une comparaison du type et

de la structure des erreurs qui en découlent et de leurs conséquences sur la détection d'impacts en a été déduite. Dans une deuxième étape, de nouvelles stratégies de détection d'impacts ont été conçues: les effets dynamiques des impacts sont isolés en déterminant la marge d'erreur maximale due aux incertitudes de modèle à l'aide d'une approche stochastique.

Une fois l'impact détecté et afin de déclencher la réaction post-impact du robot la plus appropriée, la deuxième partie de la thèse aborde l'étape de classification. En particulier, la distinction entre un contact intentionnel (l'opérateur interagit intentionnellement avec le robot, par exemple pour reconfigurer la tâche) et un contact non-désiré (un sujet humain heurte accidentellement le robot), ainsi que la localisation du contact sur le robot, est étudiée en utilisant des techniques d'apprentissage supervisé et plus spécifiquement des réseaux de neurones *feed-forward*. La généralisation à plusieurs sujets humains et à différentes trajectoires du robot a été étudiée.

Title : Impact detection and classification for safe physical Human-Robot Interaction under uncertainties

Keywords : Uncertain systems, robot manipulators, fault detection, observers, adaptive filtering, neural networks.

Abstract : The present thesis aims to develop an efficient strategy for impact detection and classification in the presence of modeling uncertainties of the robot and its environment and using a minimum number of sensors, in particular in the absence of force/torque sensor.

The first part of the thesis deals with the detection of an impact that can occur at any location along the robot arm and at any moment during the robot trajectory. Impact detection methods are commonly based on a dynamic model of the system, making them subject to the trade-off between sensitivity of detection and robustness to modeling uncertainties. In this respect, a quantitative methodology has first been developed to make explicit the contribution of the errors induced by model uncertainties. This methodology has been applied to various detection strategies, based either on a direct estimate of the external torque or using disturbance observers, in the perfectly rigid case or in the elastic-joint case. A comparison of the type and struc-

ture of the errors involved and their consequences on the impact detection has been deduced. In a second step, novel impact detection strategies have been designed: the dynamic effects of the impacts are isolated by determining the maximal error range due to modeling uncertainties using a stochastic approach.

Once the impact has been detected and in order to trigger the most appropriate post-impact robot reaction, the second part of the thesis focuses on the classification step. In particular, the distinction between an intentional contact (the human operator intentionally interacts with the robot, for example to reconfigure the task) and an undesired contact (a human subject accidentally runs into the robot), as well as the localization of the contact on the robot, is investigated using supervised learning techniques and more specifically feedforward neural networks. The challenge of generalizing to several human subjects and robot trajectories has been investigated.

